INEXTRICABLE TIES BETWEEN CHEMICAL COMPLEXITY AND DYNAMICS OF EMBEDDED PROTOSTELLAR REGIONS

MARIA NIKOLAYEVNA DROZDOVSKAYA

Inextricable Ties between Chemical Complexity and Dynamics of Embedded Protostellar Regions, PhD Thesis, Leiden University

Outer cover and bookmark image: iStockphoto.com/Cappan (Stock photo ID: 62958243).
Inner cover images: iStockphoto.com/VladNikon (Stock photo ID: 70821061) and iStockphoto.com/Lubushka (Stock photo ID: 87709453).
Outer, inner cover and bookmark design: Maria Nikolayevna Drozdovskaya.

ISBN/EAN: 978-94-028-0328-0

Printed by Ipskamp Printing, Enschede, The Netherlands.

INEXTRICABLE TIES BETWEEN CHEMICAL COMPLEXITY AND DYNAMICS OF EMBEDDED PROTOSTELLAR REGIONS

PROEFSCHRIFT

ter verkrijging van
de graad van Doctor aan de Universiteit Leiden,
op gezag van de Rector Magnificus Prof. mr. C.J.J.M. Stolker
volgens besluit van het College voor Promoties
te verdedigen op donderdag 6 oktober, 2016
klokke 11.15 uur

door

MARIA NIKOLAYEVNA DROZDOVSKAYA
Мария Николаевна Дроздовская
geboren te Moskou, USSR
op 14 september, 1989

PROMOTIECOMMISSIE

PROMOTOR:
Prof. Dr. E. F. van Dishoeck

CO-PROMOTOR:
Dr. C. Walsh

OVERIGE LEDEN:

Prof. Dr. Y. Aikawa	University of Tsukuba
Prof. Dr. E. Herbst	University of Virginia
Prof. Dr. H. V. J. Linnartz	
Prof. Dr. H. J. A. Röttgering	
Dr. M. R. Hogerheijde	

For my parents
I am eternally grateful that you gave me the impossible

Для моих родителей
Я бесконечно благодарна за то что вы мне дали невозможное

CONTENTS

1 INTRODUCTION

1.1 ASTROCHEMICAL SPRING

The study of chemical species and reactions in space constitutes the astrochemical field of research. It is one of the most interdisciplinary topics in astronomy and chemistry based on work that is theoretical, experimental and observational in nature. The footing of the field relies on the initial cosmochemical nucleosynthesis of light elements (hydrogen, H, and helium, He; see Galli and Palla 2013 for a review) and the subsequent stellar nucleosynthesis of heavy elements (such as carbon, C, oxygen, O, and nitrogen, N; see Nomoto et al. 2013 for a review). All the subsequent chemical evolution of ions, atoms, radicals and molecules is studied by astrochemists. The research field blends with the field of astrobiology, which covers the largest biocompounds and habitability conditions for life. Although, the definition of life itself is an actively debated topic[1]. The main goal of this thesis is to start putting together our 'astrochemical ancestral tree', i.e., to go after the simplest building blocks to life at the earliest phases of star and planet formation.

Some of the first interstellar polyatomic molecules detected in space were inorganic ammonia (NH_3, towards Sgr A and B2; Cheung et al. 1968) and water (H_2O, towards Sgr B2, the Orion Nebula and W39; Cheung et al. 1969), and the first organic polyatomic - formaldehyde (H_2CO, in numerous sources including Sgr A and B2; Snyder et al. 1969). A molecule is defined as organic if it contains at least one carbon atom. These earliest detections were made in the microwave range (wavelengths, λ, of $\sim 1-1.5$ cm; or frequencies, ν, of $\sim 20-30$ GHz) of the radio regime of the electromagnetic spectrum and paved the way to modern astrochemistry. Soon thereafter, in the 1970s, when dedicated millimeter ($\lambda \sim 1$ cm -1 mm; $\nu \sim 30-300$ GHz) telescopes became available, the list of observed species quickly expanded with many being detected towards high-mass star forming regions (e.g., Blake et al. 1987; Lovas et al. 1979; see Herbst and van Dishoeck 2009 for the most recent review on interstellar chemical complexity). Now, almost 50 years later, ever more complex compounds are being detected under interstellar conditions. The most recent highlights include the detection of the simplest sugar towards the low-mass protostar IRAS 16293-2422, glycoladehyde ($HOCH_2CHO$; Jørgensen et al. 2012); the first detection of a branched alkyl molecule towards Sgr B2(N), *iso*-propyl cyanide (i-C_3H_7CN; Belloche et al. 2014); and the first chiral molecule, propylene oxide towards the same star-forming region (CH_3CHCH_2O; McGuire et al. 2016). These discoveries indicate the presence of biologically relevant molecules in systems analogous in mass to our primitive Solar System and the existence of side-chain structures under interstellar conditions, which are characteristic to amino acids - the building blocks of life.

Gaseous molecules are not the end of the story for astrochemistry. Cold interstellar regions are also rich in various ices. Water ice was first detected towards the Orion Nebula via its very strong absorption feature at 3.1 μm caused by the O-H vibration

1 ESA definition http://sci.esa.int/home/30551-what-is-life/; NASA definition http://www.nasa.gov/vision/universe/starsgalaxies/life's_working_definition.html; ROSCOSMOS definition http://www.federalspace.ru/1305/ (all as seen on June 14, 2016).

band (Gillett and Forrest 1973; see Dishoeck et al. 2013 and Dishoeck et al. 2014 for detailed reviews on interstellar water). Other confirmed solid-phase molecules include carbon monoxide (CO), carbon dioxide (CO_2), methane (CH_4) and methanol (CH_3OH; Whittet et al. 1996). Ices more complex than methanol, specifically formic acid (HCOOH), ethanol (C_2H_5OH) and the formate ion ($HCOO^-$), have only been tentatively detected, because it has been difficult to identify a single carrier (Schutte et al. 1999; see Boogert et al. 2015 for the latest review on interstellar ices). These findings signify that solid-phase molecules from the earliest coldest stages of star formation could potentially be incorporated into the building blocks of comets and planets as the ice-covered dust grains assemble to form larger bodies.

Astrochemistry is also booming in our Solar System. Thanks to flyby missions, remote observations and in situ measurements, the chemical inventory of several comets has now been probed and shown to be complex (as reviewed in Mumma and Charnley 2011). Until recently, the most complex cometary molecule detected was ethylene glycol towards C/1995 O1 (Hale-Bopp; Crovisier et al. 2004). Since then, ethylene glycol has also been detected towards comets C/2012 F6 (Lemmon) and C/2013 R1 (Lovejoy; Biver et al. 2014). The picture has just changed even further, with the *Rosetta* mission detecting a whole zoo of molecules towards 67P/Churyumov–Gerasimenko (67P hereafter; Le Roy et al. 2015), including glycine (Altwegg et al., 2016). Glycine (NH_2CH_2COOH) is the simplest amino acid with a disputed interstellar detection (Kuan et al., 2003; Snyder et al., 2005), which remains to be confirmed with ALMA (Kuan and Chuang, 2014). Complex organic molecules have also been found in other Solar System bodies. Ethyl cyanide (C_2H_5CN; Cordiner et al. 2015) and vinyl cyanide (CH_2CHCN; Palmer et al. 2016 subm.) have been detected in Titan's atmosphere (also see the review of Cable et al. 2012). Diacetylene (C_4H_2) and methylacetylene (CH_3C_2H) have been measured in Saturn's atmosphere (Guerlet et al., 2010), as examples.

The *Rosetta* mission is a unique endeavor to study 67P, as it is capable of performing in situ measurements of the gas and dust in its coma. The orbiter has been following the comet from the 6th of August, 2014 and will still orbit it until September 30th, 2016. This also includes the period of highest activity at perihelium on the 13th of August, 2015. The Rosetta Orbiter Spectrometer for Ion and Neutral Analysis (ROSINA) instrument aboard *Rosetta* is of particular interest to astrochemistry thanks to its high mass resolution. The orbiter was also paired with the lander *Philae*, which executed a historic landing on a comet on November 12th, 2014. Even if for a short while, Philae was able to obtain the only currently available data set from the surface of the comet. As more data are being processed, further discoveries about 67P and its role as a probe of the initial makeup of our Solar System are anticipated.

Two schemes towards interstellar chemical complexity have been postulated (see Tielens 2013 for a review). The first is that of 'bottom-up chemistry' when large complex organics form from small simple species via various reactions in the gas and in the solid phase (Charnley et al., 1992; Herbst and van Dishoeck, 2009; Tielens and Charnley, 1997; Tielens and Hagen, 1982). The second is that of 'top-down chemistry', which starts with polycyclic aromatic hydrocarbons (PAHs) - organic compounds composed of hydrogen and carbon and that include aromatic rings (see Tielens 2008 for a review). As a result of photodissociation by ultraviolet (UV) photos, PAHs undergo dehydrogenation and fragmentation giving rise to flat carbon sheets, rings, chains and fragments, which are then free to assemble and combine with various functional groups (Allamandola et al., 1989). In reality, it is likely both schemes are active in different interstellar environments.

Bottom-up chemistry is supported by observations of complex organics (such as ketene, CH_2CO, formic acid, HCOOH, methyl formate, $HCOOCH_3$, acetaldehyde, CH_3CHO, dimethyl ether, CH_3OCH_3) under dark cold conditions of prestellar cores (in L1689B, L183 and L1544; Bacmann et al. 2012; Requena-Torres et al. 2007; Vastel et al. 2014) and laboratory experiments showing the formation of similar species under analogous conditions (see, e.g., Linnartz et al. 2015 for a review). Meanwhile, top-down chemistry is reinforced by the detection of interstellar fullerenes (spherical carbon cages, e.g., C_{60} and C_{70}; Cami et al. 2010), which theoretical models and laboratory experiments have shown to be formed via isomerization of dehydrated PAHs (Berné and Tielens, 2012).

Currently several facilities with unprecedented capabilities are in operation, including the Atacama Large Millimeter/submillimeter Array (ALMA) and *Rosetta*. The list will be extended in 2018 with the *James Webb Space Telescope* (*JWST*) and the Square Kilometre Array (SKA) in 2025 (tentatively). The JWST will be capable of exposing interstellar ices and key gas-phase molecules (such as CO_2, acetylene (C_2H_2), CH_4), while the SKA has the capability of accessing low-excitation rotational transitions of prebiotic compounds, both at much higher sensitivities than previously possible. Furthermore, several spectral surveys have been attempting to assemble the complete chemical inventory of star-forming regions. Recent examples include the Herschel observations of EXtra-Ordinary Sources (HEXOS) of Orion KL (Phillips et al., 2010)[2]; Exploring Molecular Complexity with ALMA (EMoCA) in Sagittarius B2(N2) (Belloche et al., 2014); the Protostellar Interferometric Line Survey (PILS) with ALMA of IRAS 16293-2422 (Jørgensen and et al., 2016)[3]; and Seeds Of Life In Space (SOLIS) survey of multiple targets with the NOrthern Extended Millimeter Array (NOEMA)[4]. The stream of major astrochemical discoveries in the last 5 years alone, and the state-of-the-art observing facilities at the disposal of scientists now and in the near future, implies that this is just the astrochemical spring.

1.2 MAKINGS OF PLANETARY SYSTEMS

Galaxies are characterized by strongly varying amounts of gas by mass depending on their stage of evolution from those that are gas-rich with high rates of star formation (such as spirals and irregulars) to those devoid of gas and newly formed stars (ellipticals; see (Courteau et al., 2014) for a review). On smaller scales of the interstellar medium (ISM), the gas is organized into ionized (gas temperatures, T_{gas}, of several thousand K), atomic ($T_{gas} \sim 1000$ K) and molecular phases (T_{gas} on the order of several hundred K and colder). Upon cooling, the diffuse atomic medium gives rise to dense giant molecular clouds, which are home to ongoing star formation. On the scales of these giant molecular clouds (~ 100 pc), physical phenomena such as gravitational collapse, pressure confinement, magnetic fields, turbulence, galactic sheer motions and various forms of feedback (e.g., HII regions and supernova) shape the internal structure of the gas in these clouds (see Dobbs et al. 2014 for a review). Observations have shown that the internal structure is complex and filamentary in nature. The filaments are long, but typically have widths of ~ 0.1 pc. They tend to be structured into dominating 'ridges' and disorganized networks or 'nests'. Dense cores ($\sim 0.01 - 0.1$ pc or $\sim 2000 - 20\,000$ AU) form primarily along filaments likely as a result of fragmentation through gravitational instability, and consequently, are clustered together. The cores are classified into 'starless', i.e., lacking

2 http://www.submm.caltech.edu/hexos/
3 http://youngstars.nbi.dk/PILS/
4 http://solis.osug.fr/

a central protostar, and 'prestellar', defined as gravitationally bound and starless, but likely to collapse in the future (see André et al. 2014a for a review). In prestellar cores, the initial physical and chemical conditions for individual star and planetary system formation are set.

The process of star formation is thought to be better understood for the case of low-mass than for high-mass stars. Under the influence of gravity, the prestellar core is expected to undergo uniform, spherically symmetric Larson-Penston collapse with a flat density distribution at the center (Larson, 1969; Penston, 1969). This gives rise to the first hydrostatic Larson core (Larson, 1969). Thereafter, inside-out collapse of an isothermal sphere in isolation with an associated expansion wave and an initial central singularity (Shu, 1977) gives rise to the protostar (see Dunham et al. 2014a for a review). Initially, the protostar is deeply embedded in the remnant material of its parent core - the so-called envelope. This corresponds to the Class 0/I phases of protostellar evolution. Prestellar cores have an inherent initial rotation rate, and the conservation of angular momentum gives rise to a disk around the central object. Depending on the scientific community, this disk can be called an accretion disk (for those studying the growth of the protostars via accretion of material from the envelope and the disk), a circumstellar disk, a protostellar disk or a protoplanetary disk (for those researching planet and comet formation). Although there is much debate about the timing and formation mechanisms of rotationally supported disks (see Li et al. 2014, Turner et al. 2014 and Williams and Cieza 2011 for reviews), observations show that such disks are common in the Class II phase. Detections of flattened disk-like structure in earlier phases have recently been increasing (e.g., Ohashi et al. 2014; Tobin et al. 2012, 2015). The system further powers bipolar outflows along the axis of its angular momentum with opening angles that increase with time and become less collimated (see Frank et al. 2014 for a review). Accretion of material onto the protostar and the disk, in combination with the widening of the outflows, clear out the surrounding envelope material. Eventually, the central protostar and its protoplanetary disk are fully revealed, which corresponds to the Class II phase. In reality, however, many stars form in clustered environments and as binaries (see Krumholz et al. 2014; Luhman 2012; Reipurth et al. 2014 for reviews), thus smearing the idyllic scenario. Furthermore, the accretion of material by the protostar may occur through episodic events rather than as a continuous process as suggested by outflow and FU Ori observations (e.g., Plunkett et al. 2015; as reviewed in Audard et al. 2014; Hartmann and Kenyon 1996).

As the star-disk system evolves, the protoplanetary disk disperses via processes such as accretion onto the protostar, photoevaporation, stellar and disk winds, leaving behind a transitional and, subsequently, a gas-poor debris disk (see Alexander et al. 2014; Espaillat et al. 2014; Matthews et al. 2014 for reviews). Such disks are classified as Class III. The final phase of the evolutionary sequence corresponds to a mature star with a planetary system. Initially, in prestellar cores and Class 0-II protoplanetary disks, the dust is thought to constitute a mere $\sim$ 1% by mass ($\sim$ 99% of mass as gas; Williams and Cieza 2011). However, the gas to dust mass ratio decreases with time, as the dust becomes the only remaining disk constituent. From the onset of collapse in the prestellar phase, the micron-sized dust particles undergo grain growth processing (see Testi et al. 2014 for a review), which results in km-sized planetesimals and several thousand km-sized rocky planets. The various mechanisms of planet formation have a few Myr to build a gaseous giant, which is the typical lifetime of a gas-rich protoplanetary disk (Alexander et al., 2014; Williams and Cieza, 2011). The formation of such large bodies in turn contributes to the dispersal of the disk and has been suggested to erode gaps as early as in the Class I

phase, based on high spatial resolution ALMA data (e.g., ALMA Partnership et al. 2015). Along with the same processes that build protoplanets or planetary embryos, comets are also formed. The reasons behind certain bodies growing to planets, while others remain small, are most likely correlated with the availability of dust and pebbles for accretion, and the destruction processes. Comets are also thought to spend most of their lifetime in the most distant regions of planetary systems, and hence are considered the most pristine tracers of the parent protoplanetary disk (see A'Hearn 2011 for a review). However, at the very least, their surfaces are subject to continuous space-weathering (as reviewed in Bennett et al. 2013). It remains to be modeled where exactly they are assembled in protoplanetary disks, which are thought to be subject to various internal dynamic processes especially in the Class II phase (see Armitage 2011 for a review).

The constraints on high-mass star formation are weaker than those on low-mass star formation, which in part has to do with larger distances to these sources, making spatially resolved studies more difficult. Several formation theories have been postulated (as reviewed in Tan et al. 2014). One of them is that of scaled-up low-mass star formation. However, high-mass protostars are associated with a significantly stronger radiation field, which gives rise to a (hyper or ultra) compact HII region and to radiation pressure that is capable of preventing accretion. This sets them apart from the weaker low-mass counterparts. The existence and survival of disks around such high-mass objects is currently in the early stages of verification (as reviewed in Beltrán and de Wit 2016). Multiple intermediate-mass A-type stars and high-mass B-type stars have been shown to have Keplerian disks (e.g., Cesaroni et al. 1999; Ilee et al. 2013; Kraus et al. 2010), while AFGL 4176 is for now the sole high-mass O-type star displaying a 'Keplerian-like disk' (Johnston et al., 2015). Whether such disks are able to form planets is currently entirely unknown.

1.3 THE CHEMICAL CONNECTION

The highest known level of chemical complexity is found here, on Earth. It appears that within our Solar System, complex organic molecules are also readily available in numerous comets and some of the atmospheres of our planets and moons (e.g., Saturn and Titan). Beyond our Solar System, the highest degree of complexity is found towards young star-forming regions. They are most easily detectable as gases in the hot inner regions of such systems - the so-called hot cores or hot corinos in the case of high- and low-mass star formation, respectively. It is currently still unclear which zone gives rise to this emission, whether this is thermally desorbed envelope ices, or outflow cavity wall-related emission (e.g., Dishoeck et al. 1995a), or ring-shaped emission associated with the centrifugal barrier (e.g., Oya et al. 2016). However, this may also depend on the mass regime. Nevertheless, the chemical links between a mature planetary system, such as our own, and the younger phases of extrasolar systems are intriguing. Chemical processes are expected to be universal; however, the commonality of conditions for efficient pathways towards chemical complexity is yet unknown.

The molecular inventory of protoplanetary disks can be probed via near-infrared (near-IR) in the inner 1 AU, mid-infrared (mid-IR) in the surface layers of the disk and millimeter/submillimeter in the outer disk (see e.g., fig. 1 of Dullemond and Monnier 2010). The midplane, where most of the dust and icy volatiles reside, is unfortunately obscured from direct observations. However, indirect chemical tracers can potentially be used to trace the major volatile reservoirs. For example, rings of gas-phase DCO^+ and N_2H^+ have re-

vealed where gas-phase CO is enhanced in the midplane, i.e., where the temperature for its efficient thermal desorption is exceeded (also known as a 'snowline' or 'iceline'; Mathews et al. 2013; Öberg et al. 2015a; Qi et al. 2015a; Schwarz et al. 2016). The first complex organic molecule, gaseous methyl cyanide (CH_3CN), has been detected with ALMA in 2015 in a Class II disk around MWC480 (Öberg et al., 2015b). In 2016, ALMA revealed gas-phase methanol in the Class II disk around TW Hya (Walsh et al., 2016). These are the first observational signals that chemical complexity persists in protoplanetary disks, which has long been predicted by models (see Dutrey et al. 2014 and Henning and Semenov 2013 for reviews). These two detections pertain to molecules made available in the gas-phase in the cold outer disk regions via non-thermal desorption processes.

Although refractories (the silicates and carbonaceous compounds that make up interstellar dust particles) build up the rocky component of planets and comets, it is the volatiles (all the species that thermally desorb at temperatures below a few 100 K) that set the scene for prebiotically-relevant chemistry. In order to understand the chemical connection between the various phases of star and planet formation, it is necessary to piece together the transport and degree of processing from the initial prestellar core to the protoplanetary disk and into the protoplanetary and cometary bodies. For comets, this link can be studied via icy volatiles, since they do not retain any disk gases. For the case of gas giant planets, either the gases of the protoplanetary disk are needed to assemble their atmospheres or their atmospheres can be built up via accretion of icy pebbles. However, atmospheric physical conditions enable efficient two- and three-body gas-phase reactions due to high densities and temperatures. This implies that their composition is likely highly modified from the initially accreted gases, breaking the link with earlier phases of evolution.

The two extreme scenarios for the history of icy volatiles are that of *inheritance*, when the prestellar ices remain entirely unaltered and are incorporated into protoplanets and comets as such, and that of *reset*, when ices need to reform at some point between the prestellar phase and the incorporation into large bodies (Pontoppidan et al., 2014). Inheritance is tentatively supported by rough similarities in abundance ratios between prestellar cores and comets (Mumma and Charnley, 2011; Öberg et al., 2011c); while reset is founded on the presence of calcium-aluminium-rich inclusions (CAIs) in meteorites that require high-temperature processing. Since observations will always be snapshots of various stages of evolution of different systems due to the long astronomical timescales involved, models are the key to providing an answer to this question.

Some of the largest variations in terms of physical conditions are experienced by the volatiles during the initial collapse of the system. The typical dark, cold prestellar core conditions are replaced by a central irradiating and heating source, while densities range across many orders of magnitude. In the star formation community, it is thought that the temperatures are elevated from $\sim$ 10 K to several tens of K closer to the central source, and to several hundred K in the inner $\sim$ 1 AU for low-mass protostars (inner $\sim$ 100 AU for high-mass protostars; Fig. 1.3; see Henning and Semenov 2013 for a review). Furthermore, simulations show the newly formed protoplanetary disk is to be warm ($20 - 80$ K; e.g., Visser et al. 2009a). This implies that during the transport from core to disk, icy volatiles are only selectively stripped from the grain surfaces via thermal (and non-thermal) desorption. This is considered the 'cold cloud start' perspective.

The Solar System community, on the contrary, typically favors the 'hot disk start' scenario. It is believed that the primitive Solar System formed from an initially hot (several hundred to several thousand K) Solar Nebula as evidenced by meteoritic samples and

Table 1.1: Summary of the assumptions made by the Solar System and star- and planet formation communities on the evolution of volatiles in the primitive Solar Nebula

Solar System	Star- and planet-formation
$T\,(\mathrm{disk}) > 100$ K $\forall R$	$T\,(\mathrm{disk}) \in [20, 80]$ K for $R > 1$ AU
inheritance of prestellar ices as gases and subsequent adsorption	transport of prestellar ices into the disk as ices during collapse
chemical equilibrium	non-equilibrium chemistry

the detections of crystalline sillicates out to tens of AU. However, this is not observed for extrasolar disks and likely does not imply these hot conditions for the entire innate protosolar disk. It is not excluded that certain regions may be hot enough for the production of CAIs and crystalline syllicates via shocks and viscous heating of the densest inner regions, for example. The unique cometary in situ measurements by the *Rosetta* mission promise to resolve these conflicting views (as summarized in Table 1.1) by providing one of the best data sets on cometary composition, which can then be compared and related to that of extrasolar analogues.

1.4 OBSERVING ASTROCHEMISTRY

Astrochemical questions can be targeted from three interconnected directions. The first approach is observational, which allows the determination of abundances, ratios and spatial distributions of various species under a range of different physical conditions. The second method involves laboratory studies, which are designed to mimic interstellar conditions under a controlled environment thereby permitting various processes to be disentangled. Alternatively, such studies are performed under conditions that can be extrapolated to those of the ISM, e.g., as done for the determination of rate coefficients for gas-phase reactions. The third technique is that of theoretical models, which incorporate experimental results and attempt to reproduce observations.

Gaseous molecules can be observed via electronic transitions in the UV and visible part of the electromagnetic spectrum, vibrational transitions in the IR, rotational transitions in the microwave or combinations thereof (rovibrational, vibronic and rovibronic transitions). Many astrochemical studies today are carried out in the millimeter/submillimeter regime, pushing from the radio into the far-infrared (FIR) range. Furthermore, smaller dishes are being incorporated into interferometric arrays, leading to a much larger synthesized antenna and very high angular resolution. Unfortunately, observations at mid- and far-IR wavelengths are difficult from the ground, since the atmosphere is strongly opaque in that range. Ground-based millimeter/submillimeter facilities such as the 100-m Robert C. Byrd Green Bank Telescope (GBT), the 15-m single-dish James Clerk Maxwell Telescope (JCMT), the single-dish Institute for Radio Astronomy in the Millimeter Range (IRAM) 30-m telescope, the single-dish 12-m telescope on Kitt Peak (as of 2013 operating with the European ALMA prototype antenna), the Nobeyama 45-m Radio Telescope and the recently upgraded eight 15-m antenna NOEMA (previously known as the Plateau de Bure Interferometer, PdBI) have consequently carried out much of the astrochemical observations. Additional progress has been made with the *Herschel Space Observatory* with a top spectral resolution, $R = \Delta\lambda/\lambda$, of $\sim 10^7$ for $\lambda \sim 150 - 600$ μm.

Currently in operation is the Stratospheric Observatory for Infrared Astronomy (SOFIA), which is an airborne observatory. At its cruising altitudes of $12-14$ km, only $\sim 1\%$ of the Earth's atmospheric water vapor remains, hence a larger fraction of the IR window is open for observations, albeit at a much lower sensitivity than *Herschel*[4]. SOFIA carries several instruments onboard, covering the $\sim 1-240$ μm range.

In 2016, ALMA is the most state-of-the-art interferometer in operation with fifty 12-m antennas in the main array (the 12-m Array), twelve 7-m antennas in the Atacama Compact Array (ACA or the 7-m Array) and four 12-m antennas in the Total Power Array (TP Array; ALMA Partnership et al. 2016). ALMA covers the $\lambda \sim 0.4-3$ mm ($\nu \sim 84-950$ GHz) range with resolutions ranging from $0.7''$ at 675 GHz to $4.8''$ at 110 GHz in the most compact configuration (~ 150 m) and from $0''.006$ at 675 GHz to $0''.037$ at 110 GHz in the most extended configuration (~ 16 km). ALMA Science Verification (SV) data with baselines of ~ 15 km reached unprecedented angular resolutions of $0''.075$ (10 AU) to $0''.025$ (3.5 AU) for continuum images at wavelengths of 2.9, 1.3 and 0.87 mm for the low-mass HL Tau star-forming region at a distance of 140 pc and revealed detailed ring structures (ALMA Partnership et al., 2015), which are currently a topic of heated debates (e.g., Dipierro et al. 2015; Okuzumi et al. 2016; Zhang et al. 2015). Thereby ALMA is zooming in on the dust evolution in the planet-forming region of disks and signaling that the processes of planetesimal formation are initiated very early on in the embedded phase.

Observations of solid phase molecules are more challenging from the ground. Only the strongest transitions of the most abundant solids can be studied, since solely vibrational transitions are possible in this phase, which correspond to the low atmospheric transmission region in the IR. However, the first ice detection was made with a 152-cm ground-based Mount Lemmon Observing Facility of the University of Minnesota with $R \approx 100$ at $\lambda \sim 2.8-5.6$ μm. The Very Large Telescope (VLT) consists of four 8-m telescopes that are used individually and cover the visible and IR ranges with subarcsecond capability and $R \approx 10^4$. It has been used, for example, to map the distribution of methanol ice and to study solid CO and OCN^- towards low-mass protostars (Broekhuizen et al. 2005; Pontoppidan et al. 2003a,b). Much progress has been made with spaceborne facilities, which included the *Infrared Space Observatory* (*ISO*) with peak $R \sim 1\,000$ (for ices) for λ in the $\sim 10-40$ μm range and the *Spitzer Space Telescope* with a maximum of $R \sim 600$ for a similar λ range (e.g., Boogert et al. 2013; Öberg et al. 2011). The difficulty with such space missions is not only the cost of construction and launch, but also the limited lifespan of infrared operations. Such instruments must be cryogenically cooled to just a few K in order to limit their own thermal radiation and become sensitive to IR emission from targeted sources; thus, once the coolant runs out, IR observations are no longer possible. The much anticipated JWST will once again open up the IR regime in the $0.6-28.5$ μm range for ice observations.

1.5 MODELING ASTROCHEMISTRY

Many different types of chemical and physical models are currently available. The choice of an appropriate model depends on the goal that one wishes to attain. Fig. 1.1 organizes the types of chemical models based on their microchemical accuracy and the feasibility of simulating the largest complex organic molecules. Quantum chemical calculations are used to precisely describe the state of a small system, for example that of a potential

4 SOFIA technical brochure, https://www.sofia.usra.edu/sites/default/files/SOFIAtech2016.pdf

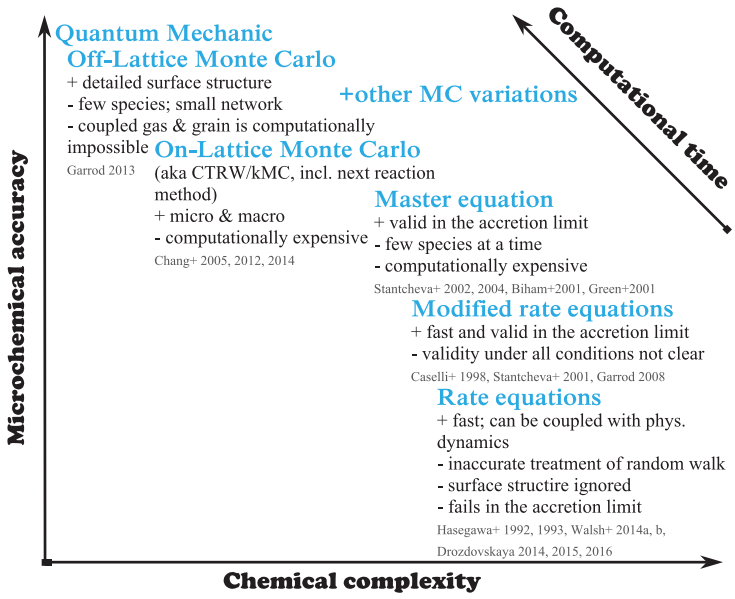

Figure 1.1: A summary of the types of chemical models available and their organization in terms of chemical complexity and microchemical accuracy.

well associated with a single binding site on the surface of a grain. The various types of Monte Carlo simulations can describe a larger section of a surface, but can only be coupled with a small set of species (see Cuppen et al. 2013 for a review). The rate equations method (Hasegawa and Herbst 1993; Hasegawa et al. 1992; see Herbst 1995 and Garrod and Widicus Weaver 2013 for reviews) is the computationally quickest approach available, thereby making it possible to compute the chemistry of complex organics, which require a large chemical network of several hundred species and several thousand reactions. Unfortunately, the speed comes at a price of chemical accuracy, because the detailed structure of the surface is completely neglected, for example. The modified rate equations and the master equation methods have the advantage of accounting for the case of single-monolayer chemistry; however, are also computationally slower.

In order to model the chemistry under interstellar conditions or for a certain source, the chemical model needs to be coupled with a physical framework (see Wakelam et al. 2013 for a review of the workflow). Fig. 1.2 thus adds two additional axis to the model space, in which the available physical models are organized in terms of complexity of physics that they account for and their computationally feasible run time, which corresponds to the age of the simulated target. The highest degree of detail is accounted for in hydrodynamic and magnetohydrodynamic models; however, they are also the most computationally expensive and not necessary more realistic than other types of models available. This implies that, in the context of star forming systems, they can typically be run only for the protoplanetary disk (e.g., Evans et al. 2015; Ilee et al. 2011) or the initial collapsing core (e.g., Aikawa et al. 2001, 2008; Furuya et al. 2012; Hincelin et al. 2013, 2016; Lee and Bergin 2015) separately. The simplest and quickest models are static and at most 2D in nature, i.e., no time-dependent physics (e.g., Aikawa et al. 1997, 2002). In such simulations the chemistry can be run for any desired amount of time, but are also

an oversimplification of the physics involved. Semi-analytic models, in which physics change in time, have the advantage of accounting for macroscopic physical processes, while remaining computationally feasible in combination with chemical networks. Such are the models of Harsono et al., (2013), Visser and Dullemond, (2010), and Visser et al., (2009a, 2011), which compute the Shu collapse of an initial spherically symmetric core to an embedded star-disk system. The evolutionary nature of these simulations allows the reconstruction of the dynamic transport of the material into the protoplanetary disk and the computation of the physical conditions encountered en route.

Chemistry of prestellar cores is typically simulated within the simplest physical frameworks - single point models, since the physical conditions do not vary significantly within the cores (such efforts are reviewed in Agúndez and Wakelam 2013). Chemical networks are compiled based on the number of phases they account for and the types of chemical reactions included. For example, two-phase models account for the gas and solid phases, while three-phase models treat the surface and bulk of the ice separately. Gas-phase chemistry includes ion-neutral, neutral-neutral, photodissociation and ionization reactions (as reviewed in Smith 2011). In the context of complex organic chemistry, it has been demonstrated that most gas-phase reactions are not sufficiently efficient at producing observable abundances of such molecules (see the review of Geppert and Larsson 2013 on ionic reactions). Although, some neutral-neutral reactions and ion-neutral reactions with NH_3 may produce appreciable abundances of some complex organics under certain conditions (Balucani et al., 2015; Taquet et al., 2016). Typically, grain-surface chemistry that occurs directly in the solid phase has been invoked to reproduce the complex organic budget. This realm comes with many more processes and free parameters than gas-phase chemistry. Additionally, much depends on the detailed structure of the surface, and efficiencies of processes are typically species-dependent. The processes of adsorption, surface diffusion, quantum tunneling through diffusion barriers and nuclear spin conversion are reviewed in Hama and Watanabe, (2013) on the surface of amorphous water ice. It is thought that complex organics can form via radical-radical reactions and hydrogenations on the grain. Such chemistry can be UV-induced (see Öberg 2016 for a review), but can also occur under dark (in the absence of UV) conditions (Chuang et al., 2016; Fedoseev et al., 2015).

The solid and gaseous phases are coupled through the processes of thermal and non-thermal desorption. Non-thermal processes such as photodesorption due to UV irradiation (of internal protostellar, external or cosmic-ray induced origins) and reactive desorption are responsible for the gaseous abundances of volatiles at conditions cooler than the respective desorption temperatures (e.g., Vasyunin and Herbst 2013b). Quantum chemistry and molecular dynamics have helped to understand exactly how photodissociation and subsequent reactions lead to the expulsion of a gaseous molecule from different layers of the icy mantle (e.g., Andersson and van Dishoeck 2008; Andersson et al. 2006; Arasa et al. 2011) and how photodesorption of CO occurs ().

From that perspective, the chemistry of hot cores is anticipated to be simpler, since all volatiles are thermally desorbed. In hot cores is also where gaseous complex organics are most abundant and they have been modeled with some of the largest chemical networks (see Garrod and Widicus Weaver 2013 for a review). However, other work suggests that this later phase of star formation is not decoupled from the chemistry that occurs earlier. The duration of the prestellar phase is thought to play a role. If it is short, then warm carbon chain chemistry occurs and complex organic formation is impeded, resulting

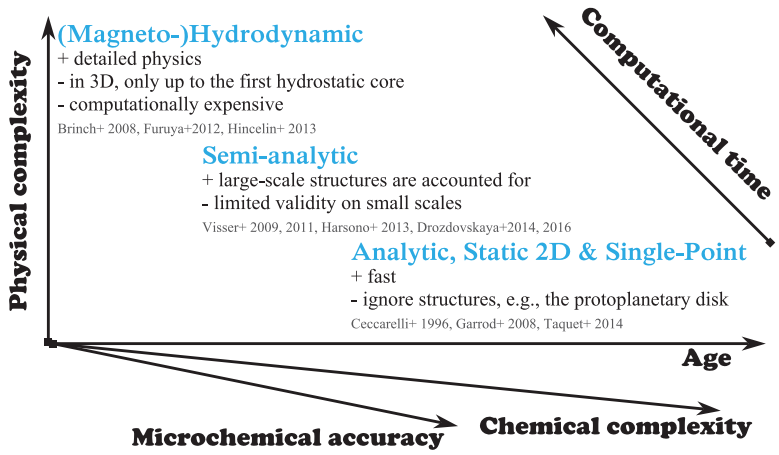

Figure 1.2: A summary of the types of physical models available and their organization in terms of physical complexity and the simulated age of the system.

predominantly in carbon chain molecules in the hot core (see Sakai and Yamamoto 2013 for a review).

Extensive astrochemical modeling effort has gone into protoplanetary disk models, which include static set ups, those that follow accretion flows within the disks and disks with turbulent mixing (e.g., Furuya and Aikawa 2014; Furuya et al. 2013; Semenov et al. 2006, 2010; Walsh et al. 2010, 2012, 2014a,b, 2015; Woitke et al. 2016). Such models have been successful at reproducing the observed molecules in the surface layers of disks and have raised questions on the chemical effects of mixing, turbulence and dust settling (e.g., Akimkin et al. 2013; Lee et al. 2010). Furthermore, dynamic processes may result in additional chemical modification (e.g., Aikawa et al. 1998; as reviewed in Aikawa 2013). Those can be accounted for in either the Lagrangian of the Eulerian specification of the flow field. In this thesis, the role of the earlier prestellar phase and the subsequent collapse to build a Class 0/I protoplanetary disk in the embedded phase is investigated. Thus, the output of the disk models discussed in subsequent chapters may be used as initial conditions for subsequent Class II disk models.

1.6 EXPERIMENTING ASTROCHEMISTRY

The idea of getting a handle on interstellar chemistry under controlled experimental conditions came about just as soon as the flood of molecules started to be detected and dates back to 1937 (see, e.g., Hagen et al. 1979). In a laboratory setup, it is possible to regulate the availability of reactants and the physical conditions that they are exposed to, such as the temperature and UV flux. The methodology then allows the study of individual processes in a species-dependent fashion (see Linnartz et al. 2015 for a review). The most challenging aspect of experimental work is the detection of the products, in particular for solid phase experiments. It used to be necessary to transfer the more complex refractory products into a detector, such as a mass spectrometer, without inducing any additional chemical processing. Furthermore, the question of the extrapolation of experimental results to astronomical timescales remains to be tested with models.

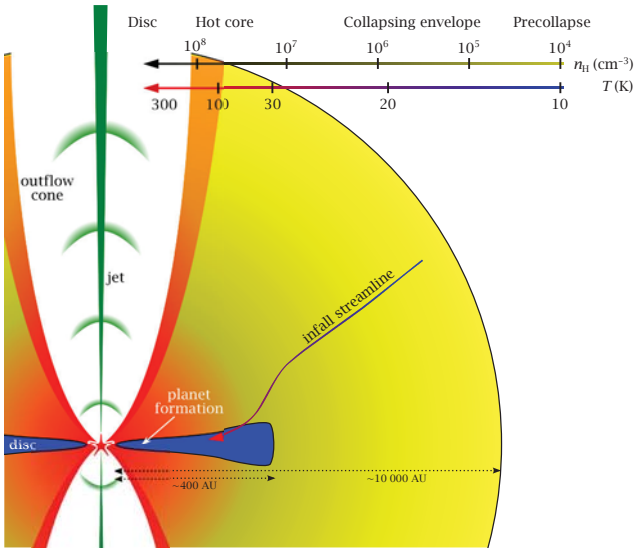

Figure 1.3: A schematic of the trail of collapsing material from the prestellar phase to their incorporation into planetesimals in the planet- and comet-forming region of the protoplanetary disk midplane in the embedded phase of star formation. Chemistry en route is pivotal for the main volatile species and the trace complex organics as a result of elevated temperatures and enhanced UV irradiation in the envelope. (Adapted from Drozdovskaya et al. 2014.)

On the other hand, laboratory experiments are the only way to disentangle on a reaction by reaction basis the intertwined reaction networks that operate under interstellar conditions. They are also key at providing crucial reaction rates and process efficiencies for use in chemical models. For example, the highly unconstrained processes of reactive desorption has been shown to be quite efficient on bare grain-like surface, but less so beyond a single monolayer coverage (Minissale et al., 2016b). Also, surface diffusion appears to be atom-dependent (Minissale et al., 2016a). Laboratory experiments are also capable of investigating the competition of a small network of reactions, such as that of the sequence of hydrogenation reactions of CO leading to CH_3OH. The most recent results are indicating that the various intermediate reactions are competitive and back reactions may also be important (Chuang et al., 2016; Minissale et al., 2016c). These results are yet to be incorporated into astrochemical models and are critical parameters for some of the model results presented in this thesis.

1.7 THIS THESIS: INFANT CHEMICAL COMPLEXITY

Astrochemistry has been a fundamental research topic at Leiden Observatory within Leiden University for several decades and is facilitated by several staff members from the observational, theoretical and laboratory perspectives under one roof. This thesis is centered around the embedded phase of star formation and the chemical links between the various stages of evolution. The primary goal of this work is to pinpoint the origins of cometary complex organic molecules in the proceeding protoplanetary disk and prestellar stages, both in the gas and solid phases. The grand motivation is to identify

our interstellar roots. This work is unique in comparison to earlier publications due to the dynamic nature of the models used in combination with the large comprehensive chemical network. Three subsequent chapters pertain to physicochemical models and another is of observational nature. Main results of this thesis are given as bullet points below.

Chapter 2 The chemistry of methanol, a key precursor to complex organics, is studied as material undergoes dynamic transport from the prestellar phase to the protoplanetary disk. A 2D, semi-analytical collapse model by Visser et al., (2009a, 2011) is combined with a two-phase chemical network of Walsh et al., (2014a,b) and abundances are computed along trajectories that trace the assembly of a Class I protoplanetary disk around a low-mass protostar. Two disks on scales of several hundred AU are studied, which differ in the dominant large-scale motions that assemble them.

- *The results show that additional methanol ice is formed in the envelope en route to the disk; however, the net effect is that of reduction relative to the initial prestellar abundance due to destruction prior to disk entry.*

Chapter 3 The same two-phase chemical network is combined with a static, 2D physical framework mimicking the Class I phase of low-mass star formation on scales of several thousand AU. The chemistry of a set of oxygen-bearing complex organic species and their spatial distribution is modeled in the envelope, including the outflow cavity wall region. Outflow cavities enhance the FUV flux penetrating the envelope and thereby trigger frequent photodissociation within the ices, leading to active radical-radical chemistry.

- *Complex organic molecules are found to be abundant in the gas phase along cavity walls, if reactive desorption is efficient at a level of* 1%*, and in the solid phase at lukewarm dust temperatures in a toroidal region around the protostar.*

Chapter 4 The midplanes of the two disks studied in Chapter 2 are analyzed with high sampling in combination with an updated version of the same two-phase chemical network (Walsh et al., 2015) with the aim of obtaining detailed information on the comet- and planet-forming zone. This time, all the main volatile carriers and a set of complex organics are studied in order to obtain the dominant volatile and minor prebiotically-significant composition of the protoplanetary and cometary building blocks in Class I disks. The results support the 'cold cloud start' perspective based cometary correlations rather than the 'hot disk start' stance of the Solar System community. Additionally, the C/O and C/N ratios in gaseous and solid phases are derived based upon a full chemical network.

- *Model results indicate that volatiles are not simply inherited from the prestellar phase: the abundance of carbon dioxide ice can increase at the expensive of water ice, and complex organic ices form at the cost of methanol ice. The overall C/O and C/N ratios in the solid phase do not vary significantly in the planet- and comet-forming zone and models reproduce solar values within the assumed framework.*

Chapter 5 Sulfur-bearing species towards IRAS 16293-2422, the most chemically rich Solar System analogue, are analyzed based on ALMA data from the Protostellar Interferometric Line Survey (PILS). Abundances and upper limits are derived for molecules such as SO_2, OCS, CS, H_2CS and H_2S via multiple isotopologues. The results include a firm first-time detection of $OC^{33}S$ towards this source and a tentative first-time detection of $C^{36}S$ towards a low-mass protostar.

- A comparison of the PILS and ROSINA data on 67P/C-G in terms of ratios in sulfur-bearing molecules reveals that the comet is much richer in H_2S rather than OCS, which is the case of the protostellar Solar analogue. This potentially suggests that our Solar System formed in a warmer, CO ice-poor environment that inhibits efficient OCS formation via grain-surface chemistry.

Altogether, this thesis is an attempt to piece together the chemical connection between the prestellar core, the protoplanetary disk and the protoplanetary- and cometary materials, as illustrated in Fig. 1.3. The main take-home message is that the seeding of infant Solar System building blocks with complex organic molecules is unavoidable as a result of chemistry during protoplanetary disk assembly.

1.8 OUTLOOK: MATURE CHEMICAL COMPLEXITY

The suggested links between interstellar molecules and cometary chemical inventories are intriguing and require the extension of the work presented in this thesis. This connection must be thoroughly quantified, which is finally possible in light of the data from the *Rosetta* mission on 67P, which has the unique ability to probe the coma in situ. Future work will include the extension of the current chemical network with newly detected species in the coma of 67P. The physical model will be tailored to represent the innate Solar protoplanetary disk more closely, for example, by accounting for the Solar System environment (as reviewed in Adams 2010). In order to further extrapolate the connection, it is also necessary to accurately simulate the incorporation of ice volatiles into large bodies (e.g., Ciesla et al. 2015). Additionally, isotopic ratios acqross varies stages of evolution as measured in various species will be studied, as they could be an important tracer of the temperature during evolution. Potentially the first steps towards bridging the gap with astrobiology can also be made.

This research will be continued at the Center for Space and Habitability (CSH) at the University of Bern. The topic is timely with the current stream of astrochemical and cometary discoveries. The strong cometary and (exo-)planetary expertise at the CSH should yield fruitful interactions and depend our understanding of the chemical links from infancy to maturity of star- and planet-forming systems.

2

METHANOL ALONG THE PATH FROM ENVELOPE TO PROTOPLANETARY DISC

Maria N. Drozdovskaya, Catherine Walsh, Ruud Visser, Daniel Harsono, and Ewine F. van Dishoeck
MNRAS, 2014, 445, 913

ABSTRACT

Interstellar methanol is considered to be a parent species of larger, more complex organic molecules. A physicochemical simulation of infalling parcels of matter is performed for a low-mass star-forming system to trace the chemical evolution from cloud to disc. An axisymmetric 2D semi-analytic model generates the time-dependent density and velocity distributions, and full continuum radiative transfer is performed to calculate the dust temperature and the UV radiation field at each position as a function of time. A comprehensive gas-grain chemical network is employed to compute the chemical abundances along infall trajectories. Two physical scenarios are studied, one in which the dominant disc growth mechanism is viscous spreading, and another in which continuous infall of matter prevails. The results show that the infall path influences the abundance of methanol entering each type of disc, ranging from complete loss of methanol to an enhancement by a factor of > 1 relative to the prestellar phase. Critical chemical processes and parameters for the methanol chemistry under different physical conditions are identified. The exact abundance and distribution of methanol is important for the budget of complex organic molecules in discs, which will be incorporated into forming planetary system objects such as protoplanets and comets. These simulations show that the comet-forming zone contains less methanol than in the precollapse phase, which is dominantly of prestellar origin, but also with additional layers built up in the envelope during infall. Such intriguing links will soon be tested by upcoming data from the *Rosetta* mission.

2.1 INTRODUCTION

The birth of a star is accompanied by the emergence of a protoplanetary disc, which serves as a nursery for young planets. These systems are formed from dense, cold cores (Shu et al., 1987). With time, a rotating core evolves into the constituents of a protostar and a protoplanetary disc, to conserve angular momentum, leaving behind a remnant envelope. Young star-forming systems set the initial conditions for planet and comet formation, but it remains unclear what level of chemical complexity is attained in the early protoplanetary and cometary material. It is necessary to consider the chemical evolution as the envelope collapses in order to know the chemical composition of the regions in which protoplanets emerge. Complex organics formed at the early stages of star formation are likely important ingredients for the prebiotic chemistry of planetary systems.

Starting from simple chemical ingredients, such as water (H_2O) and carbon monoxide (CO), star-forming systems flourish in chemical complexity. Complex organic molecules

have been observed in high-mass and low-mass protostars, as discussed in reviews by Herbst and van Dishoeck, (2009) and Caselli and Ceccarelli, (2012). However, the mechanism for their formation remains a puzzle. Laboratory experiments of UV-irradiated methanol (CH_3OH) ice have shown that the radicals produced by the photodissociation of CH_3OH go on to produce species that are more complex, such as glycolaldehyde (CH_2OHCHO) and methyl formate ($HCOOCH_3$) (see, e.g., Öberg et al. 2009a). Methanol is thus considered to be a vital precursor of complex organic molecules. Furthermore, laboratory studies demonstrate that CH_3OH can easily form under conditions as cold as 12 K via grain-surface hydrogenation reactions (Fuchs et al., 2009; Watanabe and Kouchi, 2002), making it abundant ($\sim 1-10$ per cent of water ice) under prestellar conditions (Dartois et al., 1999; Gibb et al., 2004; Öberg et al., 2011c; Pontoppidan et al., 2004). This suggests that methanol is readily available in prestellar environments to provide the key radicals to form larger, more complex organic molecules.

This paper explores the chemical history of the material that enters a protoplanetary disc by tracing the chemical evolution of infalling parcels of matter along trajectories from the early envelope into the disc. The aim is to gain insight into the evolving chemistry with changing physical conditions along infall paths. Visser et al., (2009a), henceforth referred to as V09, studied the chemical evolution of H_2O and CO ices in a similar manner. Their key conclusion was that large outer regions of the disc contain pristine water, i.e. H_2O that has never been sublimated, dissociated, reformed, nor refrozen on its path from cloud to disc. A follow-up study, Visser et al., (2011), henceforth referred to as V11, discussed the full gas-phase chemistry. They concluded that comets form from material with different chemical histories. The physical model of V09 and V11 is a 2D, semi-analytic simulation and is also the model used in this work. The motivation for 2D physicochemical collapse models spawns from the successes of 2D disc models (see, e.g., Aikawa and Herbst 1999).

Over the years, a number of other codes have also been developed with their own advantages and disadvantages. 1D physicochemical models (e.g., Ceccarelli et al. 1996; Garrod et al. 2008) are not able to treat the vertical structure of the disc realistically, while 3D hydrodynamic simulations including radiative transfer and chemistry are computationally challenging. In fact, this has only been attempted recently up to the first hydrostatic core phase (Furuya et al., 2012; Hincelin et al., 2013), which is a transient pressure-supported stage with a lifetime of a few thousand years, after the onset of collapse, and prior to the formation of a true protostar (Larson, 1969). The results of this work are explicitly compared to the conclusions drawn by Hincelin et al., (2013) later in this paper, since both works analyse the survival of molecules with individual methods, but up to different stages of evolution.

In recent years, large data sets on ice observations in low-mass protostars have become available from dedicated *Spitzer Space Telescope* and ground-based surveys. From these bigger samples, Öberg et al., (2011c) made an inventory of the major ice components and their variations from source to source. For the case of methanol, variations from $\lesssim 1-25$ per cent with respect to H_2O ice are found, but the mean values and their spread are within a factor of two of those found in comets. Observational surveys have also been carried out for quiescent clouds prior to star formation (Boogert et al., 2011, 2013), which have demonstrated that methanol ice is now commonly detected at the level of a few per cent with respect to water ice in cold clouds that have never been heated. Recently, a signpost of active methanol chemistry, the methoxy radical (CH_3O), was detected in a cold dark cloud (Cernicharo et al., 2012). Finally, an intriguing link between interstellar

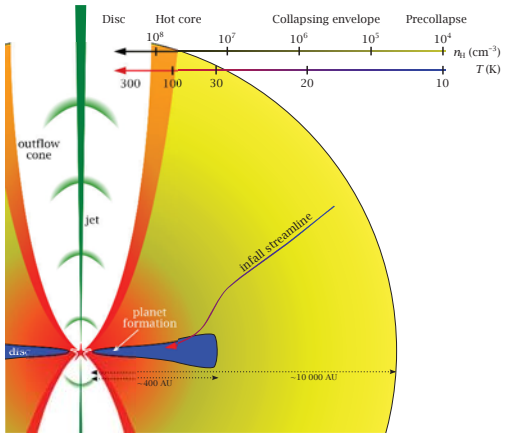

Figure 2.1: A cartoon depicting the physical components of an embedded phase of star formation, the planet-forming zone, and a trajectory of an infalling parcel. Typical gas densities, n_H (cm^{-3}), and the dust temperatures, T_{dust} (K), are also indicated. Figure not to scale (by R. Visser, adapted from Herbst and van Dishoeck 2009).

and cometary chemistry is suggested based on other data such as chemical complexity and observed isotope fractionations (Mumma and Charnley, 2011).

This work expands upon V11 by considering the evolution of more complex ices, using a significantly larger and more comprehensive gas-grain chemical network. The work presented here focuses on methanol to probe the budget of complex organic compounds for two different sets of initial physical conditions. The critical steps and processes in the methanol chemistry are also investigated.

The paper is structured as follows. The physical and chemical models and methods employed are described in Section 2.2. The simulated physical and chemical results are shown in Section 2.3. Three different infall trajectories per physical scenario are discussed in detail, and the methanol ice budgets and histories for both discs are investigated. The astrophysical implications of the obtained results are addressed in Section 2.4. Finally, the concluding remarks can be found in Section 2.5.

2.2 MODELS

2.2.1 *Physical framework*

The process of star formation is simulated using the model developed by V09 and V11, and further advanced by Visser and Dullemond, (2010) and Harsono et al., (2013). This scheme is an axisymmetric 2D, semi-analytic computation of the physical structure throughout the collapse and the disc formation stages. The collapse dynamics in the model are taken from Shu, (1977). The effects of rotation are incorporated (Cassen and Moosman, 1981; Terebey et al., 1984) and evolving outflow cavities are included. Magnetic fields are not considered.

The effects of any accretion shock at the disc surface are not taken into account, following the discussion in V09 (section 2.5). Neufeld and Hollenbach, (1994) investigated how interstellar dust is processed as it passes through an accretion shock. Vapourisation was determined to be the dominant mechanism of ice and grain destruction. They showed

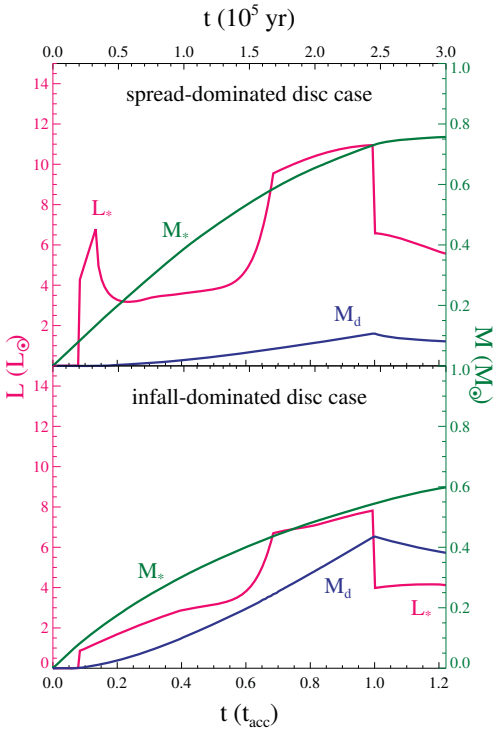

Figure 2.2: The time evolution of physical properties for the two cases studied. Each panel shows its respective evolution of stellar luminosity, L_* ($L_\odot$), stellar mass, M_* ($M_\odot$), and disc mass, M_d ($M_\odot$). The top panel displays the data for the spread-dominated disc case, i.e. case 3 from V09. The bottom panel corresponds to the infall-dominated disc case, i.e. case 7 from V09.

Table 2.1: Initial physical conditions[a]

Disc Case		spread-dominated[b]	infall-dominated[c]
Ω_0	(s^{-1})	10^{-14}	10^{-13}
c_s	(km s^{-1})	0.26	0.26
M_0	($M_\odot$)	1.0	1.0
t_{acc}	(yr)	2.46×10^5	2.46×10^5
M_d	($M_\odot$)	0.11	0.44
R_{out}	(AU)	51	294

[a] Ω_0: solid-body rotation rate; c_s: effective sound speed; M_0: initial core mass; t_{acc}: accretion time; M_d: disc mass at t_{acc}; R_{out}: outer disc radius at t_{acc}.

[b] case 3 from V09

[c] case 7 from V09

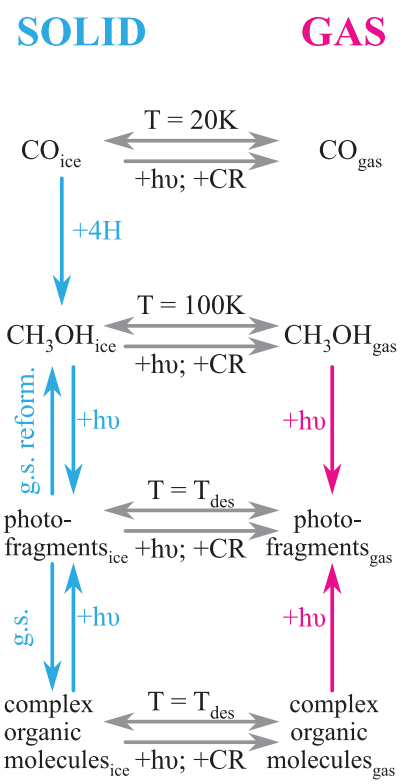

Figure 2.3: A schematic chemical network for methanol, summarizing the key reactions and processes at low temperatures ($T_{dust} \lesssim 100$ K). In the illustration, $h\nu$ corresponds to the energy of a photon, CR stands for a cosmic ray, g. s. - for grain surface, g. s. reform. - for grain-surface reformation, and T_{des} is the desorption temperature.

Table 2.2: The precollapse physical and chemical conditions[d]

n_H (cm^{-3})	4×10^4
T_{dust} (K)	10
F_{UV} (erg cm^{-2} s^{-1})	0
$n(H)/n_H$	5.0×10^{-5}
$n(H_2)/n_H$	5.0×10^{-1}
$n(He)/n_H$	9.8×10^{-2}
$n(C)/n_H$	1.4×10^{-4}
$n(N)/n_H$	7.5×10^{-5}
$n(O)/n_H$	3.2×10^{-4}

[d] Initial abundances of F, Na, Mg, Si, P, S, Cl and Fe are all in the $10^{-8} - 10^{-9}$ range relative to n_H, see table 3 of McElroy et al., (2013) and the references therein.

Table 2.3: Select molecular abundances at the end of the precollapse phase of 3×10^5 yr and their binding energies

Species	$n(X_{gas})/n_H$	$n(X_{ice})/n_H$	$E_{des}(X)$ (K)
H_2	5.0×10^{-1}	9.0×10^{-7}	430[e]
CO	3.7×10^{-5}	8.2×10^{-5}	1150[e]
H_2O	5.1×10^{-8}	1.8×10^{-4}	5773[f]
H_2CO	7.8×10^{-9}	6.9×10^{-6}	2050[e]
CH_3OH	8.3×10^{-11}	8.0×10^{-7}	4930[g]

[e] Garrod and Herbst, (2006) - estimate

[f] Fraser et al., (2001) - measurement for pure ice

[g] Brown and Bolina, (2007) - measurement for pure ice

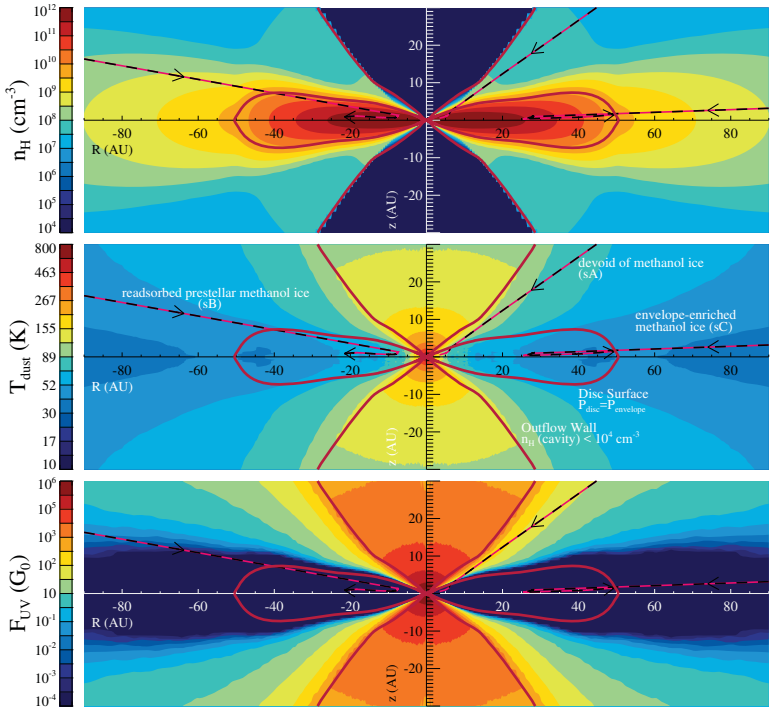

Figure 2.4: For the spread-dominated disc case from top to bottom: the gas density, n_H (cm^{-3}), the dust temperature, T_{dust} (K), and the combined field of the shielded stellar radiation and the cosmic-ray-induced UV field, F_{UV} (G_0). All these panels are at $\sim$ t_{acc} for the spread-dominated disc case. The disc surface and the outflow walls are labelled. Furthermore, three infall trajectories are depicted with black and pink lines as they move inwards from the far-out envelope at $t = 0$ to the protoplanetary disc by t_{acc}.

that the maximum grain temperature reached depends on the pre-shock velocities and densities. In the models presented here, the highest velocities and densities are reached at the earliest times, when the material accretes close to the protostar. At such positions, all ices would thermally desorb anyhow. Furthermore, this material is incorporated into the star before the end of collapse of the system. Sputtering of ices can also occur (Jones et al., 1994). The gas and dust that make up the disc experience a shock of at most 10 km s^{-1}, which is not energetic enough to release strongly bound ices such as H_2O and CH_3OH. For the grain sizes assumed here, heating of the dust grains by the stellar UV photons dominantes over the accretion shock heating (V09). Thus, the release of weakly bound molecules, like CO, is still treated correctly in the formulation employed here.

With this model, 2D time-dependent density and velocity distributions are obtained, with a self-consistent treatment of large-scale physical structures. The evolution of the central overdensity is simulated up to the formation of the first hydrostatic core for 2×10^4 yr and thereafter treated as a protostar (hereafter, the central overdensity throughout its evolution will be referred to as the star for simplicity). This allows for the determination of the stellar UV radiation field and thus the reaction rates of processes such as photodesorption, photodissociation, and photoionization. No external sources of radiation are included in this work since most star-forming regions are deeply embedded and thus shielded from external sources of UV photons. Accretion shocks onto the star, which are believed to be the source of excess UV around T Tauri stars (Bertout et al., 1988), are not considered. The central star thus solely controls the dust temperature, another important parameter for the chemistry. For further details, the reader should refer to the original publications on this model (Harsono et al., 2013; Visser and Dullemond, 2010; Visser et al., 2009a, 2011).

This model is used to simulate the system up to the accretion time, t_{acc}, defined as when the primary accretion phase onto the star ends and the outer shell of the envelope reaches the protoplanetary disc. This parameter is defined as:

$$t_{acc} = \frac{M_0 G}{m_0 c_s^3}, \tag{2.1}$$

where M_0 is the initial core mass, G is Newton's gravitational constant, $m_0 = 0.975$ is a constant coming from the analytical solution of the hydrodynamics equations of a collapsing isothermal sphere (Shu, 1977) and c_s is the effective sound speed.

The 3D continuum radiative transfer code RADMC-3D[3] is used to compute the dust temperature and the shielded stellar radiation in 2D as a function of time based on the output of the collapse model. As a first-order approximation, it is assumed that the gas and dust are coupled, and thus the temperatures of both are equal. This assumption is most likely false for the outflow cavities, because the density is too low for gas-grain collisions to cool the gas efficiently, while the dust can still cool radiatively (Draine, 1978; Weingartner and Draine, 2001). The UV radiation calculated with RADMC-3D accounts for shielding and scattering by the material located between the star and the point of interest. A gas to dust mass ratio of 100 is assumed. Opacity tables for icy grains from Crapsi et al., (2008) are used. In this work opacities for bare grains, dependent upon the dust temperature, are not incorporated. This is expected to cause temperature variations of at most ~ 10 K around the ~ 100 K zones, which is where the dominant ice component, H_2O ice, is sublimated for both the midplane and the surface layers of a disc (M.K. McClure, priv. comm.).

3 http://www.ita.uni-heidelberg.de/~dullemond/software/radmc-3d/

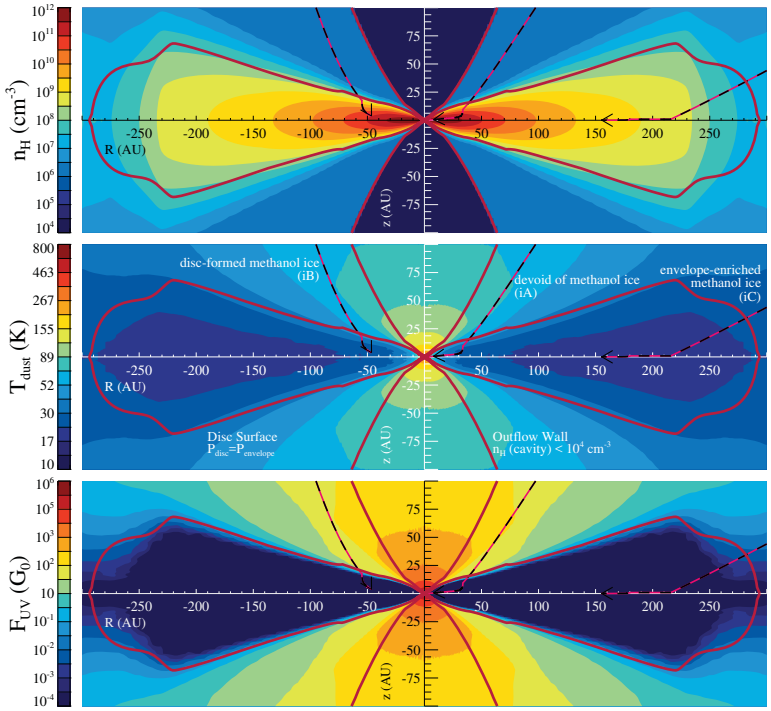

Figure 2.5: As Fig. 2.4, but for the infall-dominated disc case.

The collapse model computes trajectories of parcels of gas and dust as they fall in towards the star and into the protoplanetary disc, as illustrated in Fig. 2.1. Using the time-dependent velocity distribution, it is possible to follow material along infall streamlines. Each parcel's temporal and spatial coordinates can then be coupled to the corresponding values for physical parameters, such as density, dust temperature and stellar radiation, to which the parcels are exposed. With a sample of trajectories it is thus possible to trace the physical and chemical histories of various regions in the envelope and the protoplanetary disc. The motion of a large number of parcels from early to late times is shown in fig. 7 of V09.

The initial physical conditions control the subsequent evolution of the system. Here, two sets of initial parameters are considered, based on cases 3 and 7 from V09, respectively termed 'spread-dominated' and 'infall-dominated', and summarised in Table 2.1. Figure 2.2 shows select physical properties of the two scenarios. The two cases studied differ in the solid-body rotation rate, Ω_0, by an order of magnitude. Since t_{acc} is independent of Ω_0, t_{acc} is equal for the two cases under consideration in this work, at a value of 2.46×10^5 yr (Table 2.1). A slower solid-body rotation rate implies that more envelope material will be incorporated into the star and the disc will be less massive. Furthermore, since most of the material is used to build up the star, viscous spreading is the dominant mechanism of disc growth. As a result, the star formed in the spread-dominated disc case (case 3 from V09) is of higher mass and more luminous than that of the infall-dominated disc case (case 7 from V09), as shown in Fig. 2.2.

On the other hand, the disc formed in the infall-dominated case is more massive than that formed in the spread-dominated case. The sizes of the discs vary by a factor of ~ 4 at t_{acc} and the dominant motions that build the discs are not the same, which is reflected by the disc radial velocity profiles. This affects the trajectories of incoming parcels and the chemistry along them. For case 3 from Vo9, which was also central to V11, the disc has an outer radius of 51 AU and mainly grows by viscous spreading, thus termed 'spread-dominated'. For case 7 from Vo9 the disc has an outer radius of 294 AU and primarily grows by the accretion of more envelope material onto it, thus termed 'infall-dominated'. Due to the modifications between Vo9 and V11, the modelled protoplanetary disc sizes have decreased significantly (a factor $2-3$ difference in the outer disc radii for reasons explained in detail in Visser and Dullemond 2010 and Harsono et al. 2013). Due to the modifications in the model, it became necessary to modify the equation for the outflow cavity wall to:

$$z = 0.98 \left(\frac{t}{t_{acc}} \right)^{-3} R^{1.5},$$

where R and z are cylindrical coordinates in AU. The full opening angle in our situation at t_{acc} is 11.58° at $z = 1000$ AU and 5.39° at $z = 10000$ AU, both of which are approximately a factor 3 smaller than that in V11.

In this work the embedded phase of low-mass star formation is modelled, that is while the remnant envelope is still present. Few observations of such early discs are available, which makes it hard to constrain their dimensions. For example, the Keplerian disc in L1527 has been estimated to have an outer radius of ~ 125 AU (Sakai et al., 2014; Tobin et al., 2012, 2013). The set of Keplerian discs discussed in Harsono et al., (2014) have outer radii in the $\sim 50-310$ AU range and masses varying from several thousandths to several tenths $M_\odot$. By considering two different cases in this work with disc parameters in these ranges, future measurements are anticipated for confirmation.

2.2.2 *Chemical network*

The physical model described above yields trajectories that trace streamlines of material infalling from the envelope into the protoplanetary disc. For simplicity, the chemical calculations are performed independently from the physical computations. The physical conditions (density, dust temperature, radiation field) at various time steps along the trajectories are used as input for the chemical code, which computes chemical abundances at each step. The procedure yields chemical abundances as a function of physical evolution for parcels probing various regions in the envelope and the protoplanetary disc, and is pictorially summarised in fig. 1 in V11.

The chemical model contains 666 species and 8759 reactions. The gas-phase network is the Rate12 release of the UMIST Database for Astrochemsitry (UDfA[5], McElroy et al. 2013). The network accounts for gas-phase two-body reactions. Three-body reactions are not considered, as they only become important at densities higher than $\sim 10^{10}$ cm^{-3}, which are only attained briefly at the latest time steps in the evolution. Photoreactions (photoionization and photodissociation) by stellar and cosmic-ray-induced UV photons (generated by the cosmic-ray excitation of H_2, taken to be 10^4 photons cm^{-2} s^{-1}), and direct cosmic-ray ionization (with a rate of 5.0×10^{-17} s^{-1}) for gas-phase species, are

5 http://www.udfa.net

also included in RATE12. Photoreactions are computed according to equation 2 from V11, which takes the evolving stellar temperature into account. Self- and mutual shielding are taken into account for H_2, CO, and N_2 based on recent work (Li et al., 2013; Visser et al., 2009b). Grain-cation recombination is also included.

The model is supplemented with gas-grain interactions and grain-surface chemistry (and several additional reactions for complex organic molecules) extracted from the Ohio State University (OSU) network[6] (Garrod et al., 2008) and are calculated according to the detailed description in Walsh et al., (2014b) and the references therein. The chemistry is described by a two-phase model, i.e. gaseous and solid phases solely: that is, the ice surface and bulk are not treated as distinct phases. The rate equation approach is adopted for grain-surface reactions, based on Hasegawa et al., (1992) and Hasegawa and Herbst, (1993). If one of the reactants is either an H or a He atom, then quantum tunnelling is allowed through the activation energy for a reaction and through diffusion barriers on the grains (Cazaux and Tielens, 2004; Watanabe et al., 2010). For all other species, only classical hopping is permitted. The relation between the diffusion barrier (E_{diff}) and the binding energy of a molecule to the surface (E_{des}, which is also sometimes called the desorption energy) is taken to be $E_{diff} = 0.3 \times E_{des}$. The set of binding energies compiled for use in conjunction with RATE12 is used with the exception of water ice. A higher value of 5773 K from Fraser et al., (2001) for pure water ice is adopted instead.

The gas-grain interactions included are adsorption onto grain surfaces (also known as freeze-out) and thermal desorption (Hasegawa and Herbst, 1993; Hasegawa et al., 1992). Ices can also desorb non-thermally. Photodesorption (either by stellar or cosmic-ray-induced UV photons), cosmic-ray-induced thermal desorption (via heating of grains), and reactive desorption are all taken into account. The most recent experimental values for the photodesorption yields are adopted for the photodesorption rates (Öberg et al., 2009b,c). Furthermore, a coverage factor is used in light of recent experiments, which suggest that photodesorption occurs only from the top two monolayers (Bertin et al., 2012). The efficiency of reactive desorption is set to 1 per cent (Garrod et al., 2007; Vasyunin and Herbst, 2013b), but the efficiency of this process is not yet constrained by experiments and is likely variable, dependent on the reaction and the substrate (see e.g. Dulieu et al. 2013).

Finally, grain-surface photoionization and photodissociation by stellar and cosmic-ray-induced UV photons are included. As a first order approximation, the equivalent rates for the gas phase are used. This is likely over-estimating the grain-surface photodissociation rates, since the mechanisms for UV photodissociation and photodesorption of ices are now understood to be related as demonstrated in molecular dynamics studies (Andersson and van Dishoeck, 2008; Andersson et al., 2006; Arasa et al., 2010, 2011, 2013; Koning et al., 2013) and experimental work (Bertin et al., 2012; Fayolle et al., 2013).

The grains are assumed to have a radius of 0.1 μm and $n(\text{grains})/n_H = 2.2 \times 10^{-12}$, where by definition: $n_H = n(H) + 2 \times n(H_2)$. The density of grain surface sites is 1.5×10^{15} cm^{-2} and the barrier thickness for quantum tunnelling between grain surface sites is taken to be 1 Å, assuming a rectangular barrier (Hasegawa et al., 1992).

Prior to running the chemical model on a set of trajectories, it is necessary to obtain the initial chemical conditions at the onset of collapse. Assuming that the precollapse conditions are identical for the entire 2D plane, the precollapse phase for a single point is simulated at constant physical conditions for 3×10^5 yr. The precollapse physical and chemical conditions are tabulated in Table 2.2. The chemical abundances obtained at

6 http://www.physics.ohio-state.edu/~eric/research.html

the end of the precollapse phase are used as initial chemical abundances for the trajectories. For reference, Table 2.3 tabulates select molecular abundances at the end of the precollapse phase with their respective binding energies.

2.2.3 *Methanol chemistry*

The key chemical reactions involving CH_3OH are summarised in Fig. 2.3. Early models suggested that methanol could form in the gas phase via ion-molecule reactions under dark cloud conditions (Herbst and Leung, 1986; Millar and Nejad, 1985). This is thought to be a two-step process invoking initially radiative association (Blake et al., 1987; Luca et al., 2002), followed by dissociative recombination (Geppert et al., 2006). However, it was quickly suspected that this formation route is inefficient at low temperatures (Millar et al., 1987). Later it was experimentally shown that, although fast, only 3 per cent of the product channels of dissociative recombination lead to methanol (Geppert et al., 2006). Moreover, radiative association has to compete with other ion-molecule processes that have much larger rate coefficients resulting in too low gas-phase production of CH_3OH to explain dark cloud observations (Garrod et al., 2006).

Currently it is accepted that at low dust temperatures ($<$ 100 K and when external UV is negligible), grain-surface chemistry is responsible for the production of methanol via the sequential hydrogenation of CO:

$$CO \overset{H}{\rightarrow} HCO \overset{H}{\rightarrow} H_2CO \overset{H}{\rightarrow} H_3CO/H_2COH \overset{H}{\rightarrow} CH_3OH,$$

as first proposed by Tielens and Hagen, (1982). This mechanism has been extensively studied experimentally by various groups (Hidaka et al., 2004; Hiraoka et al., 2002; Watanabe and Kouchi, 2002; Watanabe et al., 2004) and confirmed for $12\ K \leqslant T_{dust} \leqslant 20\ K$ (Fuchs et al., 2009). The second and fourth steps in the above mechanism are barrierless, because the H atoms are reacting with radicals. CO and H_2CO do not have unpaired valence electrons, thus the additions of H atoms are endothermic reactions. A reaction barrier of $E_A = 2500$ K for step one and for both routes (leading to either methoxy or hydromethoxy) of step three is adopted (Garrod and Herbst, 2006; Ruffle and Herbst, 2001; Woon, 2002). This formation route is possible for dust temperatures as low as 10 K, because quantum tunnelling allows the H atom to overcome this 'large' barrier (Cuppen and Herbst, 2007). These processes are also reflected in the temperature-dependent 'effective' reaction barrier measured in the laboratory, which are on the order of $\sim 400 - 500$ K (Fuchs et al., 2009), i.e. much lower than the theoretical value of 2500 K. Above $\sim$ 20 K, the parent CO molecule sublimates from the grains and the residence time of the H atom on grain surfaces is too short for this reaction sequence to occur efficiently. As a result, methanol production significantly slows.

Similar to water and carbon monoxide, methanol can undergo thermal and non-thermal desorption, as shown in laboratory experiments. This work assumes $E_{des} = 4930$ K for CH_3OH, as stated in Table 2.3, which is the value measured for pure methanol ice (Brown and Bolina, 2007). At low temperatures ($T_{dust} \lesssim 100$ K) thermal desorption is inefficient for methanol, therefore under prestellar conditions it can only desorb non-thermally from the grains. Under dark conditions non-thermal desorption is sparked by the absorption of UV photons generated by the cosmic ray excitation of H_2 molecules. Weakly bound molecules like CO (see Table 2.3) are thought to be thermally desorbed due to the cosmic-ray heating of dust grains (at temperatures lower than their respective

desorption temperatures). However, CH_3OH is a strongly bound species and its primary mechanism of coming off the grains is cosmic-ray-induced photodesorption (Hasegawa et al., 1992; Roberts et al., 2007; Shen et al., 2004).

Currently the chemical network includes the gas-phase and, in turn, the grain-surface photodissociation rates from RATE12. It is the photodissociation products of CH_3OH ice that are thought to pave the way to more complex species, such as glycolaldehyde and methyl formate, making this process and its parameters crucial for the chemistry. The photodissociation pathways of CH_3OH are:

$$CH_3OH + h\nu \rightarrow CH_3 + OH,$$

$$CH_3OH + h\nu \rightarrow CH_2OH + H,$$

$$CH_3OH + h\nu \rightarrow CH_3O + H,$$

as investigated by Garrod and Herbst, (2006), Öberg et al., (2009a), and Laas et al., (2011). These studies have analysed how the chemistry of methyl (CH_3), hydromethoxy (CH_2OH) and methoxy (CH_3O) radicals leads to complex species. In this work the 'standard' branching ratios are adopted, namely 60 : 20 : 20 per cent for the reactions in the order given above (table 1 in Laas et al. 2011). The exploration of the dependence of the formation of complex organics on the branching ratios in this model is a topic of upcoming work.

2.2.4 *Caveats*

Certain crucial chemical parameters affect the key chemical processes that govern the methanol abundance under different physical conditions. The first key aspect is the availability of reactant species (H, CO, HCO, H_2CO, CH_3O, CH_2OH) on the grains, which is determined by their binding energies. Methanol can only be formed if those species are present on the grains, and a change in the binding energies can influence the dominance of thermal and non-thermal desorption mechanisms. Secondly, these species need to be mobile in order to meet and react. The relation between E_{diff} and E_{des} is crucial here. In this work a factor of 0.3 is used (Hasegawa et al., 1992), but other values also appear in the literature, e.g. 0.5 in Garrod and Herbst, (2006). Hence, the mobility of individual species is related to the binding energy. Under cold conditions ($T_{dust} \lesssim 20$ K), greater mobility could enhance the amount of methanol formed. However, under warmer conditions (20 K $\lesssim T_{dust} \lesssim$ 100 K), the amount of methanol formed could be reduced if the photoproducts efficiently diffuse to form other species, rather than recombine immediately. This means that values of E_{des} for the photoproducts (CH_3, CH_3O, CH_2OH, OH) of methanol also need to be constrained. Thirdly, the efficiencies of the first and third hydrogenation steps en route to CH3OH, set by the value of E_A, affect its production. The large difference between the theoretical and experimental ('effective') values has been pointed out in the previous section, and it is not clear how to treat this properly in models. Finally, the binding energy of methanol itself determines where it survives upon formation.

There are also two physical parameters that can have profound significance for the chemistry of methanol. The first one is the assumed dust model. Different values for the grain radius, the number density, the number of surface sites and the quantum barrier heights can affect adsorption rates of species onto the grains and the grain-surface diffusion rates (Hasegawa et al., 1992). Currently the dust grains are assumed to consist of

Table 2.4: Final parcel positions (at t_{acc})

Case	Label	Parcel behaviour	R (AU)	z (AU)
spread-dominated disc	sA	devoid of CH_3OH_{ice}	3.4	0.55
	sB	readsorbed prestellar CH_3OH_{ice}	21.6	0.89
	sC	envelope-enriched CH_3OH_{ice}	49.4	1.44
infall-dominated disc	iA	devoid of CH_3OH_{ice}	1.3	0.03
	iB	disc-formed CH_3OH_{ice}	46.4	3.75
	iC	envelope-enriched CH_3OH_{ice}	155.3	0.06

compact spheres that are well-mixed with the gas. Aspects such as settling and dust coagulation have not been accounted for; however, they may be very important for adsorption and grain-surface associations due to the reduction of the grain surface area available for freeze-out and increased shielding from UV irradiation in the midplane (Aikawa and Nomura, 2006; Akimkin et al., 2013; Fogel et al., 2011; Vasyunin et al., 2011). The other important physical parameter is the assumed ice model. Currently, frozen-out species are considered as a single entity, while it is known that ices are actually layered and that the mantle and the surface monolayers have different chemistry (see, e.g., Ehrenfreund et al. 1998; Taquet et al. 2012). For example, in clouds water freezes out first, followed by CO at later times. Methanol ice is thus expected to be sequestered and associated with CO rather than water ice (Boogert et al., 2011). Furthermore, accounting for the ice composition and structure would affect all of the chemical parameters mentioned above.

2.3 RESULTS

In this work there are two discs with different dominant disc growth mechanisms, one that is spread-dominated and another that is infall-dominated. In Section 2.3.1 the physical evolution for these two cases is presented. In Section 2.3.2 the chemical evolution is analysed. In each scenario, three trajectories entering the disc are studied in detail. Each disc has two trajectories with different methanol ice behaviours that are common to both cases, and one trajectory that is unique to its scenario. Finally, the methanol ice budget and history are presented for both cases at $\sim t_{acc}$ in Section 2.3.3.

2.3.1 *Physical evolution*

2.3.1.1 *Spread-dominated disc case*

The top panel of Fig. 2.4 shows the physical structure at the end of the simulation, at $\sim t_{acc}$, for the spread-dominated case. The star is at the origin and is surrounded by a protoplanetary disc with midplane densities of $\sim 10^{12}$ cm^{-3} at 8 AU. The outflow cavities are identified as the regions where $n_H < 10^4$ cm^{-3}. The remnant envelope has densities in the $\sim 10^6 - 10^{10}$ cm^{-3} range. The disc surface is defined along the points where the envelope and disc pressures are equal, $P_{envelope} = P_{disc}$ (Visser and Dullemond, 2010).

The middle panel of Fig. 2.4 shows the dust temperature at the same time step for the spread-dominated disc case, as computed with RADMC-3D (Section 2.2.1). The highest temperatures are found within the outflow cavities, since this is where the density is lowest, and it is thus easier for the radiation to permeate and heat the dust. The central temperature (inner 0.1 AU) exceeds 850 K, while the midplane of the protoplanetary disc remains in the $\sim 40-70$ K range depending on the radial distance from the star. Within 5 AU, the dust temperatures in the disc exceed 100 K. The envelope temperature varies in the $\sim 20-110$ K range on larger scales and increases with proximity to the star. Due to the fact that the disc is only 51 AU in radial size, it is easily heated passively by reprocessed stellar radiation and, consequently, is fairly warm (above 40 K) in its entirety.

The bottom panel of Fig. 2.4 shows the total strength of the far-UV $912-2066$ Å ($6-13.6$ eV) flux, which has contributions from the shielded stellar radiation field and the cosmic-ray-induced UV field, at the same time step for the spread-dominated disc case. The strength of the interstellar UV radiation field, G_0, is 1.6×10^{-3} erg cm^{-2} s^{-1} (Habing, 1968). The envelope regions closest to the outflow walls are subjected to a UV radiation field that is $1-100$ times stronger than the interstellar field and the outflow cavities are exposed to even stronger radiation (> 100 G_0). The protoplanetary disc remains fully shielded from the stellar radiation ($A_V \gtrsim 10$ mag). Other regions are subject to weak UV irradiation, below the interstellar value. All zones of the system, even the midplane of the disc, are subject to a weak, but constant, cosmic-ray-induced UV radiation, which is assumed to be the typical $\sim 10^{-7}$ erg cm^{-2} s^{-1} (Prasad and Tarafdar, 1983).

All panels of Fig. 2.4 depict three infall trajectories with black and pink lines as they move inwards from the far-out envelope at $t = 0$ and into the protoplanetary disc by t_{acc}. These three trajectories are representative of the key methanol ice behaviours encountered in the spread-dominated disc case and are labelled accordingly. This is further elaborated upon in Section 2.3.2. Table 2.4 lists the final positions of the three parcels at t_{acc}, which are all within the protoplanetary disc. This disc grows primarily by viscous spreading, as reflected in the outward motion for two of the three trajectories after they enter the disc. A total of 250 trajectories were calculated for the spread-dominated disc case, sampling the full spatial extent of the disc at t_{acc}, and most of them embark on an outward path upon disc entry.

2.3.1.2 *Infall-dominated disc case*

The physical parameters for the infall-dominated disc case vary from those for the spread-dominated case presented previously. The top panel of Fig. 2.5 shows the density distribution at $\sim t_{acc}$ for the infall-dominated disc case (on a much larger spatial scale than in Fig. 2.4 due to the difference in disc sizes). The midplane densities of this much larger disc vary from $\sim 10^{11}$ cm^{-3} within the inner 30 AU to $\sim 10^{8}$ cm^{-3} beyond 250 AU. The outflow cavities are again low-density zones of $< 10^{4}$ cm^{-3}. Note that the outflow cavities appear of different sizes between Fig. 2.4 and Fig. 2.5 only due to the difference in scales on the two figures. For this case the remnant envelope is of a lower density, $\sim 10^{5}$ cm^{-3}, which peaks at $\sim 10^{8}$ cm^{-3} close to the disc boundary.

The middle panel of Fig. 2.5 displays the dust temperature at the same time step for the infall-dominated disc case. Overall this system is colder than the spread-dominated disc case, which correlates with this being a less massive star, and the disc being larger in size and mass. The disc has a large outer zone ($\gtrsim 70$ AU) that is at ~ 20 K. The temperature exceeds 100 K only within 5 AU, similar to the spread-dominated case, despite this disc

having lower temperatures otherwise. The remnant envelope is generally cool and a dust temperature of ~ 100 K is exceeded only within ~ 30 AU in R and z. The outflow cavities are again the hottest regions with temperatures > 150 K close to the star (z < 23 AU) and a central peak temperature (inner 0.1 AU) of just under 800 K.

The bottom panel of Fig. 2.5 portrays the total strength of the far-UV flux at the same time step for the infall-dominated disc case. The outflow cavities are subject to the strongest radiation, > 1000 G_0 within z ~ 60 AU. The disc remains shielded from the stellar UV flux and again subject only to the cosmic-ray-induced UV photon flux. However, in this case, a small disc surface layer exists, immediately below the labelled disc surface, that encounters UV flux at the interstellar level. Furthermore, larger regions of the envelope experience a UV flux ~ 10 G_0. Both effects are a consequence of the lower densities along the line of sight between the star and the remnant envelope (as seen in the top panel of Fig. 2.5). Additionally, this disc has a larger geometrical height due to its larger mass.

All panels of Fig. 2.5 show three infall trajectories that are representative of the dominant methanol ice behaviours encountered for the infall-dominated disc case and are labelled as such. This is further discussed in Section 2.3.2. Table 2.4 lists the final positions of these parcels at t_{acc}. This disc grows primarily by infall of matter as opposed to viscous spreading. Hence, none of the three trajectories have an outward component, and viscous spreading is observed only for a handful of parcels from the other 250 trajectories calculated for this case.

2.3.2 *Chemical evolution*

During the precollapse phase, CO forms via ion-molecule chemistry, reaching a peak canonical gas-phase abundance of ~ 10^{-4} relative to n_H. (All abundances discussed hereafter are relative to n_H unless stated otherwise.) CO subsequently adsorbs onto the grains on a time-scale of ~ 10^5 yr. Upon CO freeze-out, CH_3OH is efficiently formed on the grains from CO via sequential hydrogenation, as discussed in Section 2.2.3 (Tielens and Hagen, 1982). This persists for 3×10^5 yr, the duration of the precollapse phase in the simulation. At the onset of collapse, the modelled methanol ice abundance is 8.0×10^{-7}, corresponding to 0.44 per cent of water ice, which is consistent with observations of quiescent clouds without star formation (Boogert et al., 2013). Photodesorption by cosmic-ray-induced UV photons strips some of the ice from the dust grains, yielding a gas-phase methanol abundance of 8.3×10^{-11}, which is in agreement with ~ 10^{-10} from Garrod and Herbst, (2006) and on the lower end of observed values ~ $10^{-8} - 10^{-9}$ (Friberg et al., 1988; Gómez et al., 2011). Although, extraction of gas-phase abundances from observations remains challenging and needs to be approached cautiously.

The precollapse abundances obtained are used as the initial conditions for the computation of the chemical evolution along infall trajectories. Figure 2.6 shows select molecular abundances for the three parcels introduced in the previous sections for the spread-dominated disc case and Fig. 2.7 shows the same for the infall-dominated disc case. The figures should be read from right to left along the abscissa, which corresponds to decreasing time steps from early to late times. All six parcels start out with the same precollapse methanol abundance. As they undergo infall, the physical evolution they experience varies, which includes radically different temperatures, FUV fluxes and densities. These physical parameters are crucial for the chemistry and, as a result, the parcels obtain unique molecular abundance profiles. The figures should be analysed with the

key reactions and processes, as depicted in the network in Fig. 2.3, in mind. The timescales of various processes are also of importance. For example, thermal desorption is very fast (on the order of 10^3 yr for $n_H \sim 10^{12}$ cm^{-3}, $T_{dust} \sim 150$ K), while methanol ice grain-surface formation is slow (on the order of 10^5 yr for $n_H \sim 10^4$ cm^{-3}, $T_{dust} \sim 10$ K). Besides methanol, Figs. 2.6 and 2.7 shows the abundance of CO, H_2O and formaldehyde (H_2CO) for reference. Next, the chemical evolution is discussed for each characteristic methanol ice behaviour encountered.

2.3.2.1 *Enrichment of methanol ice*

For the spread-dominated disc case the parcel with envelope-enriched methanol ice is depicted in the right column of Fig. 2.6 and labelled sC. It encounters densities in the $2.1 \times 10^5 - 7.1 \times 10^{10}$ cm^{-3} range along its infall path with a steep jump of several orders of magnitude around 10^5 yr before the end of the simulation, which corresponds to the parcel's entry into the disc. The temperature varies from 10 K to its maximum value of 54 K, followed by a decrease to 40 K. The UV radiation encountered by the parcel briefly spikes up to a maximum of 2.6×10^{-3} G_0. The temperature and the UV flux peak around the density peak, because immediately prior to disc entry is also where the parcel is closest to the star sans the shielding effects of the disc. Similar spikes in the physical parameters occur for all of the parcels considered; however at different times depending on when they enter the disc. After the disc entry, parcel sC remains inside the warm and heavily UV shielded disc, while moving outwards as the disc spreads viscously (Fig. 2.4).

Prior to the temperature reaching 20 K, methanol ice continues to be formed efficiently on the grains via sequential hydrogenation of CO, which explains the initial rise in the methanol ice abundance. This occurs while the parcel is still infalling through the envelope, therefore the methanol in parcel sC is envelope-enriched. Once the temperature surpasses 20 K, CO thermally desorbs off the grains and the formation of methanol slows down. Soon thereafter the temperature increases further, however it remains well below 100 K, so methanol does not thermally desorb along this trajectory. The UV flux is also briefly elevated, however since its peak value is approximately four orders of magnitude lower than the interstellar value, neither photodesorption nor photodissociation remove significant amounts of methanol ice from the grains.

Upon disc entry, the rapid and large density increase to $\sim 10^{10}$ cm^{-3} leads to the adsorption of gaseous methanol, which is reflected by a bump in the solid methanol abundance profile. The bump is levelled within $\sim 10^4$ yr by the cosmic-ray-induced UV photons. Thereafter, the methanol ice abundance is preserved at the envelope-enriched level along the parcel's path through the disc. This is because the disc zones that the parcel encounters are all at temperatures below the desorption temperature of methanol and above the desorption temperature of CO. Furthermore, little stellar UV penetrates the disc. As a result, inefficient non-thermal destruction by the cosmic-ray-induced UV photons balances the slow formation of methanol ice via the OH and CH_3 route (whose abundance is very low due to the absence of stellar UV photons), the photodissociation (by the cosmic-ray-induced UV photons) of more complex species into CH_3OH and adsorption.

For the infall-dominated disc case the parcel with envelope-enriched methanol ice is depicted in the right column of Fig. 2.7 and is labelled iC. The density for this parcel is in the $9.5 \times 10^4 - 4.3 \times 10^9$ cm^{-3} range. The temperature increases from 10 K to a peak value of 31 K, then decreases to 20 K. The UV flux peaks at a value of 0.7 G_0. This parcel

encounters the lowest densities and temperatures, as it enters the outermost disc region considered (see, e.g., Fig. 2.4 and Fig. 2.5).

The methanol ice profile of this parcel is very similar to that of parcel sC. In fact, the same processes are at play here. That is also the reason for this parcel being the envelope-enriched methanol ice analog for the infall-dominated disc case, although the parcel motion is very different. However, there is one key difference between parcels iC and sC, namely that for parcel iC the temperature drops below the desorption temperature of CO towards its final position. Once CO is again frozen out on the grains, methanol formation can occur. This is not seen here, because the simulation only runs for approximately another 10^4 yr upon the readsorption of CO, which is not long enough for the grain-surface chemistry to produce a significant amount of methanol. In other words, parcels enter the outer disc later in the evolution and do not have enough time to form methanol within the disc.

2.3.2.2 *Destruction of methanol ice*

The left column of Fig. 2.6 depicts the parcel that is devoid of methanol ice for the spread-dominated disc case and labelled sA. It undergoes an increase in density in the $6.9 \times 10^4 - 1.0 \times 10^{13}$ cm^{-3} range with a spike that coincides with a brief strong burst of UV radiation with a maximum value of 901 G_0. The temperature again peaks prior to disc entry, but keeps rising to reach its maximum value of 161 K at its final position. This is explained by the parcel's motion in the disc, which is inward in its entirety for all times, which, in turn, is a result of this parcel entering the disc within 10 AU.

While the temperature is below 20 K, more methanol is formed as was the case for parcels sC and iC with envelope-enriched methanol ice. However this parcel approaches the star much closer than the previous parcels and the temperature prior to disc entry peaks at 130 K. Methanol ice is thereby rapidly removed by thermal desorption. Furthermore, the UV flux exceeds the interstellar value causing, not only photodesorption of methanol ice, but also photodissociation of both solid and gaseous methanol. This explains why the gas-phase methanol is also destroyed prior to disc entry. Once in the disc, the temperatures remain too high for any methanol to form. This parcel is devoid of not only methanol ice, but also of methanol gas.

The left column of Fig. 2.7 illustrates a parcel that is devoid of methanol ice for the infall-dominated disc case and labelled iA. The densities are in the $2.3 \times 10^5 - 7.7 \times 10^{13}$ cm^{-3} range. The temperature, although containing certain spikes, tends to increase from 10 K to higher values with the final point attaining the maximum of 444 K. The UV spikes with a peak value of 2.5 G_0.

This parcel is similar to parcel sA in the sense that they both have no solid methanol left at their final positions. However for parcel sA, thermal desorption, photodesorption and photodissociation ensured the destruction of methanol ice. Gaseous methanol was also photodissociated at the same time. In parcel iA, methanol ice undergoes pure thermal desorption, since the disc fully shields from stellar UV. As a result, gaseous methanol survives in the inner disc at the abundance level close to that of prestellar methanol ice.

2.3.2.3 *Readsorption of prestellar methanol ice*

The parcel containing readsorbed prestellar methanol ice is depicted in the middle column of Fig. 2.6 and labelled sB. It is unique to the spread-dominated disc case. The density curve lies in the $8.4 \times 10^5 - 1.8 \times 10^{12}$ cm^{-3} range. The temperature similarly

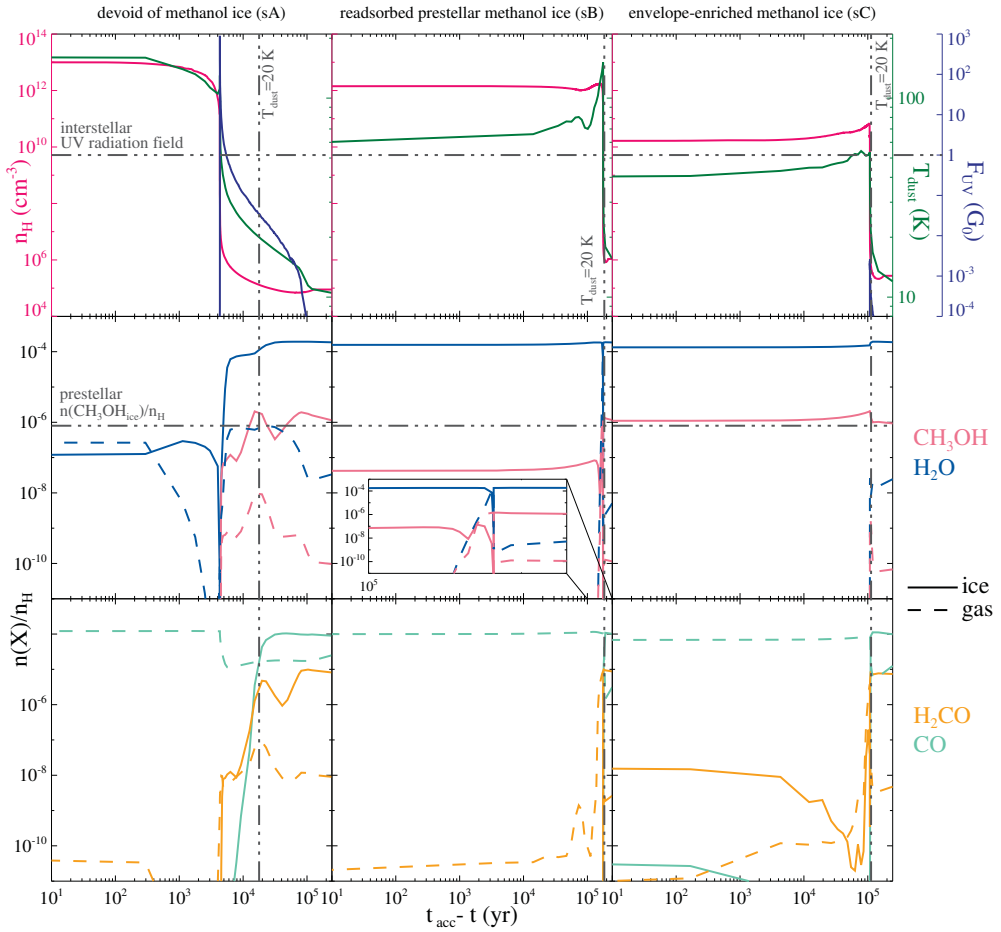

Figure 2.6: Physical conditions and molecular abundances as a function of time for the three parcels for the spread-dominated disc case. The figures should be read from right to left along the abscissa, which corresponds to going from early to late times. In the top three panels, the pink curves are the gas densities, n_H (cm^{-3}), the green curves are the dust temperatures, T_{dust} (K), and the dark blue curves are the combined fields of the shielded stellar radiation and the cosmic-ray-induced UV field, F_{UV} (G_0). The level of the interstellar UV radiation field is labelled, as are the points at which the $T_{dust} = 20$ K limit is surpassed, where CO ice desorbs. The lower six panels display the chemical abundances relative to n_H (see text). The colours correspond to different species, solid lines are used for the solid phase and dashed line for the gas phase. The initial prestellar methanol ice abundance is labelled as well. The center middle panel includes a blow-up of the critical transition region.

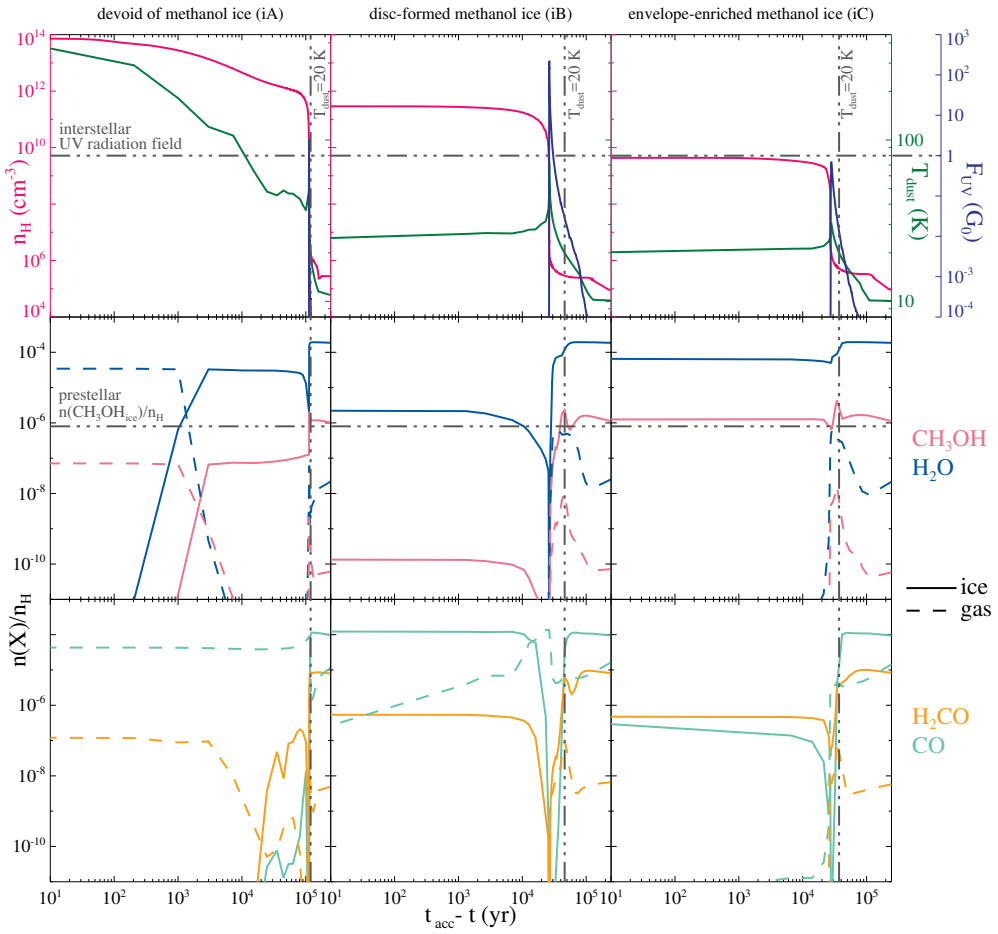

Figure 2.7: As Fig. 2.6, but for the infall-dominated disc case.

rapidly spikes from 10 to 151 K, then gradually decreases to 59 K. This parcel enters the disc earlier than parcel sC and also far away from the star (R $>$ 25 AU for both). This ensures that the UV flux remains at the cosmic-ray-induced level at all times. Contrary to the path of parcel sC, which initiates outward motion upon entry into the disc, this parcel first continues to move inwards, encountering high temperatures within the inner disc ($\lesssim$ 10 AU), while staying fully shielded from stellar UV, to only later embark on an outward journey.

Parcel sB spends little time below 20 K due to its early disc entry. As a result, CO does not stay on the grains sufficiently long for any significant amount of additional methanol to be formed. The prestellar methanol is carried straight into the disc. However, once the parcel enters disc zones with temperatures higher than 100 K, rapid thermal desorption of methanol occurs and all the ice is released into the gas. Once the parcel migrates outwards and the temperature drops again, methanol rapidly adsorbs onto the grains due to the high densities. The methanol molecules are still of prestellar origins hereafter; however, the abundance is lower than the initial prestellar value. This is due to the fact that some methanol was destroyed while it was in the gas-phase in the hot inner zones of the disc. The readsorbed prestellar methanol ice is preserved towards the final position of this parcel for the same reasons as it was preserved in parcel sC.

2.3.2.4 *Disc-formation of methanol ice*

The middle column of Fig. 2.7 depicts the parcel that contains disc-formed methanol ice and labelled iB. It is unique to the infall-dominated disc case. The densities lie in the $9.3 \times 10^4 - 2.9 \times 10^{11}$ cm^{-3} range. The temperatures rise from 10 K to a peak value of 73 K, then decrease down to 24 K. The UV flux briefly spikes at 215 G_0.

Initially the methanol profile is similar to that seen for parcels sC and iC that contain envelope-enriched methanol ice, however before the disc entry the UV flux is 2 orders of magnitude higher for this parcel. As a result, methanol gas is rapidly photodissociated. Methanol ice undergoes photodesorption, but most importantly also more frequent photodissociation. At the point of this strong UV spike, the temperature rises to 73 K, therefore once a methanol ice molecule dissociates, it is much more likely that the photofragments thermally desorb off the grains rather than recombine. This leads to the rapid destruction of methanol ice, which is seen in the figure as a deep dip in the solid methanol abundance. The exact depth of the dip depends on the combination of the UV flux and the temperature. Once the parcel enters the disc, it is fully shielded from the stellar UV photons and the temperature decreases. In fact, the temperature drops to the level of $\sim$ 20 K and CO once again freezes out onto the grains. This in turn allows methanol formation via sequential hydrogenation of CO, but now within the disc. Due to the short time of $\sim 10^4$ yr, the increase in methanol ice seen in the figure is slow and at a low abundance. The methanol ice found at the final position of this parcel is, in fact, partially disc-formed methanol ice.

2.3.3 *Methanol ice in discs*

2.3.3.1 *Methanol ice budget*

To sample the two discs studied, around 250 trajectories per case were computed. From this information approximate zones can be delineated in the discs based on the amount of methanol ice that they contain. This is done by means of schematics in the top panel

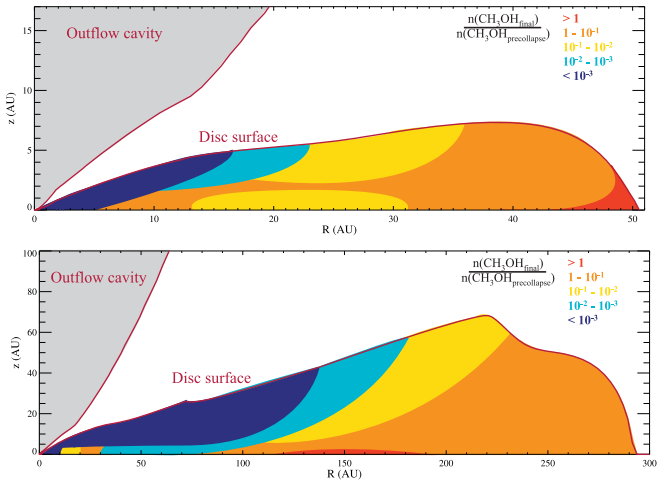

Figure 2.8: Methanol ice budget schematic for the spread-dominated disc case in the top panel and for the infall-dominated disc case in the bottom panel. The colours represent the value of the ratio of the methanol ice abundance at $\sim$ t_{acc} to the value at the onset of collapse (end of prestellar core phase) in the zones. The outflow cavity and the disc surface are also labelled. The zonal divisions are based on $\sim$ 250 trajectories per case.

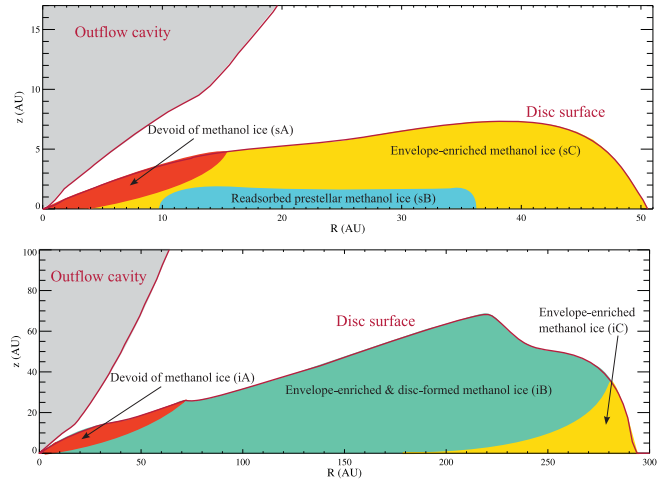

Figure 2.9: Methanol ice history schematic for the spread-dominated disc case in the top panel and for the infall-dominated disc case in the bottom panel. The zones are coloured depending on the characteristic methanol ice profiles for parcels building up those zones (see text) and are labelled accordingly. The zonal divisions are based on $\sim$ 250 trajectories per case.

for the spread-dominated disc case and in the bottom panel for the infall-dominated disc case in Fig. 2.8. The zones are coloured depending on the value of the ratio of the methanol ice abundance at $\sim t_{acc}$ to the constant value at the onset of collapse (end of the prestellar core phase, Table 2.3).

For the spread-dominated disc case in the top panel of Fig. 2.8, the inner ~ 5 AU (in the midplane) is devoid of methanol ice, which is around the methanol snowline. Further out, there is radially dependent layering in the upper parts of the disc. The further away from the star, the less harsh the conditions (in terms of temperature and UV radiation) that parcels encounter upon infall and therefore, the more methanol ice is preserved on the grains. The outer zones of the disc lose the least methanol ice compared with that injected at the onset of collapse. (This holds for the precollapse abundances computed here.) The striking feature of this figure is the midplane, which contains less methanol ice than the prestellar core. This demonstrates the effect of the physics of the system on its chemistry. The trajectory undertaken by the parcels to get to the midplane in that radial range is by first approaching the star, and then viscously spreading outwards with the growing disc. For example, for a final position of ~ 20 AU in the midplane, the approach must be as far in as ~ 8 AU. Therefore, the parcels making up the midplane lose methanol ice during their approach by rapid thermal desorption. Once under methanol-ice preserving conditions again, methanol is quickly readsorbed onto the grains; however, at abundances lower than the initial prestellar value. Since the disc formed in this spread-dominated scenario is warm (above ~ 40 K) methanol is not formed in the disc itself via the CO hydrogenation route. The CH_3 and OH route is viable at this temperature; however, these transient species are not efficiently formed due to the strong shielding from stellar radiation by the disc. The methanol ice formed via this route, the photodissociation (by the cosmic-ray-induced UV photons) of more complex species into CH_3OH and adsorption are balanced out by the inefficient non-thermal destruction of CH_3OH by the cosmic-ray-induced UV photons. It is the most outer disc zones that are rich in methanol ice due to cold, shielded conditions and further production in the envelope.

Comparing to the infall-dominated disc case in the bottom panel of Fig. 2.8, similarities and differences are present. Due to the lower remnant envelope densities in this case and therefore stronger UV flux at larger radii close to the disc surface, a much larger zone is methanol-ice poor. The methanol snowline still lies around ~ 5 AU at the midplane. However, in this case the disc surface layers as far out as ~ 100 AU lack solid methanol due to the strong FUV radiation, and thus due to rapid photodissociation, encountered immediately prior to entering the disc. Otherwise, a similar radially dependent layering still perseveres in the disc. The large outer zones of this infall-dominated disc contain more methanol ice than initially present in the system, as is the case for the spread-dominated disc for the same reasons. Contrary to the spread-dominated disc case, in this case, the disc is cold enough for CO to freeze out and methanol ice formation to initiate within the disc. Additionally, no methanol-ice poor midplane is seen. Here the midplane is populated by infalling parcels that are still methanol-ice rich, rather than those that have suffered methanol ice loss close to the star. Within the inner ~ 50 AU the picture is more complicated, since different types of parcels flow inwards into that area. There are those from the surface layers that are methanol-ice poor, but there are also those from the outer zones, which are methanol-ice rich.

2.3.3.2 *Methanol ice history*

From the sets of trajectories computed, it is not only possible to compute the methanol budget, but also to deduce the methanol history in the disc. The select parcels discussed in Section 2.3.2, namely in Figs. 2.6 and 2.7, display methanol ice profiles characteristic of various zones of the two discs. By classifying the profiles from all the parcels computed, the history of zones in the discs can be understood. The coloured regions are dominated by trajectories with the respective characteristic methanol ice profile, however this division is approximate.

The top panel of Fig. 2.9 shows the methanol ice history for the spread-dominated disc case. The inner ~ 5 AU midplane zone, containing parcels of type sA, is devoid of methanol ice, as anticipated from Fig. 2.8. The dominant portion of this disc contains envelope-enriched methanol ice, which is built up from parcels of type sC. Although all the parcels of this zone undergo methanol ice formation during infall, they do not necessarily contain more than the prestellar amount. Prior to entering the disc, some of them still lose methanol ice due to the temperatures and UV fluxes encountered, which is reflected in the budget schematic in Fig. 2.8. The third and final zone of this disc is the one containing readsorbed prestellar methanol ice and parcels of type sB. This zone corresponds to the methanol-ice poor midplane seen in Fig. 2.8.

In comparison to the conclusions drawn in V11 for water in their figs. 4 and 6, for the spread-dominated case, methanol is also absent within a similar inner disc zone. Furthermore, the readsorbed prestellar methanol ice in the midplane corresponds with the same behaviour seen for water by Visser et al. for a comparible region. The unique aspect of methanol ice is however the enrichment in the envelope en route to the disc, thanks to the formation pathway via CO. There are no analogous low-temperature formation pathways for water, and thus it is simply preserved from the prestellar phase into the outer disc zones, as seen in V11.

The bottom panel of Fig. 2.9 depicts the methanol ice history for the infall-dominated disc case. Similar to the spread-dominated case and once again anticipated from the respective methanol budget figure, the inner ~ 5 AU comprise the zone that is devoid of methanol ice and that contains parcels of type iA. The largest zone in this disc is that containing a mixture of disc-formed and envelope-enriched methanol ice, which is built up from parcels of type iB. This zone exists uniquely in this colder disc. The disc-formation and envelope-enhancement of methanol ice does not imply that there is more than the prestellar value. The methanol budget is not the same across this zone, as seen in Fig. 2.8. The last zone of this disc is associated with envelope-enriched methanol ice, which is where parcels of type iC come to reside.

2.4 ASTROPHYSICAL IMPLICATIONS

Figures 2.6-2.9 show that the different physical conditions encountered along the various infall trajectories affect the chemical composition of the infalling material and set its history. The dust temperature and the UV radiation, in particular, drive the chemical changes. These two physical parameters determine the feasibility of critical chemical processes. Large variations in the density affect all processes and may result in, for example, rapid freeze-out. As a result, the material that enters a protoplanetary disc shows strong chemical differentiation according to regions. The inner ~ 4 AU zone is expected to be methanol-ice poor in both discs studied and the prestellar fingerprint completely erased. Gas-phase preservation of the fingerprint is case-dependent. The

extended outer regions, on the contrary, are methanol-ice rich and enriched during infall. In the case of the colder, infall-dominated disc, further enrichment occurs thanks to methanol ice formation within the disc itself. In the spread-dominated disc case, the midplane is methanol-ice poor, but does contain readsorbed prestellar methanol ice. In the infall-dominated disc case, the midplane is methanol-ice rich and contains both envelope-enriched and disc-formed methanol ice, depending on the time spent by each parcel in the disc.

In this work, regions have been identified where methanol is abundant. Methanol is thought to be a key precursor to larger, more complex organic molecules (Laas et al., 2011; Öberg et al., 2009a; Walsh et al., 2014b). This means that one of the main ingredients is readily available in the extended outer regions of discs and in the midplane in the infall-dominated disc case. The formation and distribution of complex organic molecules during disc formation and envelope dissipation will be investigated in future work.

Several limitations and uncertainties in the chemical model were identified in Section 2.2.4. The qualitative results presented are robust against chemical uncertainties, which are expected to have quantitative effects only. It is certain that the inner disc is methanol-ice poor, while the outer regions are methanol-ice rich. However, to what exact radial ranges the two belong is not definite. In addition, the physical model does not account for all known physical parameters, e.g., magnetic fields, viscous heating, and mixing are not included. It is also important to realise that the physical model is most useful for understanding what type of material is delivered to the early discs, and thus primarily serves for obtaining the initial conditions for other disc models that include more complete disc physics.

2.4.1 *Comparisons to previous works*

In comparison with the 3D work of Hincelin et al., (2013), our model runs up to $t_{acc} = 2.46 \times 10^5$ yr, while their simulations stop at the first hydrostatic core stage, namely at $\sim 3.8 \times 10^4$ yr. As can be seen from Figs. 2.6 and 2.7, prior to $(t_{acc} - 38 \times 10^3 \text{ yr}) = 2.08 \times 10^5$ yr profound chemical changes that occur thereafter are not probed. Hincelin et al. concluded that the chemical composition in the outer disc is pristine while the temperature in the disc remains below the respective desorption temperatures. In this work, the outer parts of each disc have also been shown to preserve the prestellar methanol ice, but it is also further enriched en route through the envelope. Furthermore, it is found that photodesorption and photodissociation, in addition to thermal desorption, cause the destruction of methanol ice in the inner region of the spread-dominated disc. The UV field is also strong enough to destroy gas-phase methanol in that case. Thermal desorption is responsible for stripping methanol in the inner zone of the infall-dominated disc (since these parcels drift inwards along the shielded midplane rather than infalling into the disc under irradiated conditions). In the simulations of Hincelin et al., regions of the disc attain temperatures higher than the desorption temperature of methanol already as early as the first hydrostatic core. This is not the case in this work. Here the desorption temperature of methanol is only exceeded within the inner ~ 5 AU at t_{acc}. The reason for this is most likely the radiative transfer method. Hincelin et al. make use of the flux-limited diffusion approximation, while here full continuum radiative transfer is performed.

The 2D hydrodynamical work of Brinch et al., (2008) obtained density and temperature profiles similar to those obtained in this work; however, their model did not include

outflow cavities and was primarily focused on the envelope rather than the disc. The duration of their simulation is equal to that used here, namely 2.5×10^5 yr. The code of Yorke and Bodenheimer, (1999) adopted by Brinch et al. used flux-limited diffusion, which results in a temperature difference of a few Kelvin in the envelope. The differences in disc temperatures, in comparison to the full continuum RADMC-3D calculation, cannot be quantified. Brinch et al. also included accretion shocks onto the disc, which results in elevated temperatures ($\sim$ 60 K) along the disc surface. Their model was coupled with chemistry by Weeren et al., (2009), in a similar approach to that performed here.

Van Weeren et al. used the RATE06 release of the UMIST database as their gas-phase network, i.e. the predecessor of the gas-phase network used here. For the surface reactions, Weeren et al. used the network assembled in Hasegawa et al., (1992) and Hasegawa and Herbst, (1993) in conjunction with the modified reaction rates approach. Here, the larger, more up-to-date OSU network Garrod et al., (2008) is employed in combination with the classical rate equation method. The majority of the results presented in Weeren et al. pertain to gaseous methanol, which becomes readily abundant at later times in the inner $\sim$ 100 AU at an abundance of $\sim 10^{-5}$ due to thermal desorption. The only zone rich in gas-phase methanol seen in this work is the inner disc ($\sim$ 5 AU) in the infall-dominated disc case. This could be due to Weeren et al. assuming $A_V = 15$ for all times and all positions, thereby completely excluding photodesorption and photodissociation. In this work, these processes are carefully accounted for and are shown to play a crucial role. Alternatively, this could be due to their temperature structure in the disk, which must be much hotter than here in order to thermally desorb methanol from $\sim$ 100 AU inwards in the midpplane. According to table 2 of Weeren et al., the amount of methanol ice decreases with time, but this work shows that this is only true for certain zones of the disc. Finally, their fig. 19 shows that methanol is not formed at any radial position in their simulation, which has, on the contrary, been seen for an array of positions in this work.

It was mentioned earlier that the results of this work are most useful in understanding the nature of the material entering the disc, rather than its composition as it evolves. As a result, the final abundances obtained are suitable as initial conditions for other more detailed disc models (e.g., Walsh et al. 2014b). In comparison to that work, which also looked at gas-phase and solid-state methanol among many other more complex species, there is agreement within an order of magnitude for the methanol ice abundance $\sim 10^{-6}$. The main differences occur for the surface layers of the disc. In our models, the disc is still surrounded by remnant envelope material, which makes the surface layers less distinct, in particular for the spread-dominated disc case. In the work of Walsh et al. thermal and non-thermal processes result in a drop of around two orders of magnitude in the methanol ice abundance between the midplane and the disc surface (for R $\sim$ 100 AU). As for the midplane, Walsh et al. demonstrate the survival of methanol ice up to $\sim$ 2 AU, which then crosses over into a gas-phase methanol rich zone between 1 and 2 AU. This is similar to what is seen in this work for the infall-dominated case, however the methanol snowline lies around $\sim$ 5 AU here, which is the set by the adopted star-disc parameters. This is on the other hand contrary to what is seen with the spread-dominated case, in which gas-phase methanol is photodissociated once it comes off the grains. The stellar properties of Walsh et al. are that of a more mature system than the ones studied here, namely a 0.5 $M_\odot$ T Tauri star with an accretion rate of 10^{-8} $M_\odot$ yr^{-1}.

Nomura et al., (2009) modelled the chemistry along accretion flows in the inner disc around a low-mass protostar. For the stream line shown in their work, which runs

through the disc ($z = 1.2H$, where H is the disc scale height), a gas-phase methanol-rich zone is seen between $\sim$ 5.5 and $\sim$ 6.5 AU for an accretion rate of 1.0×10^{-8} $M_\odot$ yr^{-1}. Nomura et al. concluded that for all species the existence of such gas-rich zones depends on the assumed accretion rate. In their models, gas-phase methanol is destroyed by reactions with ionised species or atomic hydrogen on time-scales of $\sim 10^4$ yr. Thus, the size of the zone rich in gaseous methanol depends on whether the accretion flow is faster than this destruction time. For example, the gas-phase methanol-rich zone extends between $\sim$ 2 and $\sim$ 6.5 AU for a higher accretion rate of 5.0×10^{-8} $M_\odot$ yr^{-1} (fig. 3 in Nomura et al. 2009). This is roughly in agreement with the infall-dominated disc case in this work, although their star is more massive and less luminous (1.5 $M_\odot$ and $\sim$ 5 $L_\odot$ vs. Fig. 2.2). Here, the accretion rate is time-dependent and decreases from $\sim 4 \times 10^{-6}$ $M_\odot$ yr^{-1} at the beginning of the simulation to $\sim 2 \times 10^{-6}$ $M_\odot$ yr^{-1} at $\sim t_{acc}$ for the infall-dominated case. This is around 2 orders of magnitude higher than in the work of Nomura et al., however their accretion rates are for the disc alone, while the rates here pertain to the embedded phase, which includes the envelope. The discs presented in our work are inherently different from that of Nomura et al., since these discs are still forming. Therefore, the parcels tend to move quickly within the discs and material does not stay in the inner gas-phase rich zone long enough. Furthermore, Nomura et al. used the variable Eddington factor method to calculate dust temperatures. It is not clear what the temperature differences are in comparison with this work, since only one stream line is published. In addition, Nomura et al. and Walsh et al., (2014b) include viscous dissipation in the disc, which provides extra heating in the inner few AU.

More recently, Walsh et al., (2014a) modelled the abundances of complex organic molecules along multiple streamlines in a disc. The authors found that methanol was preserved along the midplane, prior to crossing of its snowline. At larger scale heights, a balance of photodesorption and photodissociation determines the fate of methanol molecules. Their findings are consistent with the conclusion reached in this work.

2.4.2 *Application to comets*

A key application of the results obtained in this work is towards comets, especially in light of upcoming data from the *Rosetta* mission. Comets likely form in young protoplanetary discs, and therefore may probe physical and chemical conditions in the early Solar Nebula. Efforts have been made to compare the abundances of various solid species relative to water ice in comets and towards young protostars. An example of such work is fig. 13 in Öberg et al., (2011c), using cometary data from Mumma and Charnley, (2011), where cometary methanol abundances are shown to overlap with observations of methanol towards low-mass protostars. These simularities have also been demonstrated by Bockelée-Morvan et al., (2000). It is not clear whether this is just a coincidence or if most of the cometary methanol is still prestellar from the cloud, out of which our Solar System formed. This point is also strongly dependent on how much methanol ice is built up during in the precollapse phase. Walsh et al., (2014b) concluded based on their fig. 10 that further disc formation is necessary to reproduce the observed cometary abundances of complex organic molecules, including methanol, as modelled cloud values are too low.

Öberg et al. concluded that the spreads in cometary and prestellar methanol ice abundances are comparable, with roughly a factor of 2 difference in logarithmic space relative to water ice. Recalling Fig. 2.8, in the spread-dominated case, $10 \lesssim R \lesssim 30$ and $z \lesssim 2$

is the zone with $\sim 1 - 10^{-2}$ times less methanol ice than in the precollapse phase. In the infall-dominated case, a similar level of methanol ice loss is seen for the same R and z range. This implies that the factor of 2 found by Öberg et al. is also found in these discs, and is a result of ice processing en route into the protoplanetary disc. Other zones in these discs allow for a loss greater than this factor of 2, which is in agreement with methanol-poor cometary observations (Mumma and Charnley, 2011).

2.5 CONCLUSIONS

This work employs an axisymmetric 2D semi-analytical physical model to simulate the formation of a low-mass protostar (Visser et al., 2009a, 2011). Infall trajectories of parcels of matter are computed so that the material that makes up the protoplanetary disc can be sampled. A chemical model with a large gas-grain network is then applied to compute the chemical evolution of the system (Garrod et al., 2008; McElroy et al., 2013; Walsh et al., 2014b). First, the quiescent prestellar phase is simulated, and then the chemistry is computed along infall trajectories terminating at different points in the disc. By combining the two models into a physicochemical simulation, the chemical evolution as a function of physical evolution is studied for a star-forming system. Furthermore, two physical scenarios that vary in their respective dominant disc growth mechanism are studied side by side.

The main conclusion obtained in this work are as follows.

- The infall path sets the dust temperature and the UV flux, thus thermal desorption, photodesorption and photodissociation rates are trajectory-dependent. Methanol ice is stripped from the grains, if the dust temperature exceeds $\sim$ 100 K. If the UV flux is on the order of the interstellar field strength, methanol is rapidly destroyed both in the gas and solid phases. The abundance of methanol entering protoplanetary discs depends on how it is transported.

- In the spread-dominated disc case, the inner $\sim$ 5 AU along the midplane is devoid of methanol ice and gas, since, en route, it is thermally desorbed, or photodissociated in the ice followed by thermal desorption of its photofragments, or photodissociated in the gas. Conversely, gas-phase methanol is plentiful for the infall-dominated disc case in the same region and methanol ice is lost solely due to thermal desorption.

- The extended outer disc regions are rich in methanol ice that has been enhanced in the envelope.

- The fate of the midplane depends on the mechanism, by which the disc grows. In the spread-dominated scenario, the midplane is methanol-ice poor and is built up of readsorbed prestellar methanol ice. In the infall-dominated disc case, the midplane is methanol-ice rich. It contains envelope-enriched and disc-formed methanol ice, which is unique to this colder disc, in addition to the preserved prestellar layers.

The simulations show that the abundance and history of one of the key precursors for complex organic molecules, methanol, varies across protoplanetary discs, the physical structure of which is heavily influenced by the initial cloud rotation from which the star-disk system forms. The complex organics budget is directly affected by the availability of methanol, because it dissociates into radicals that are needed for synthesising

larger, more complex species. The formation and survival of the latter will be studied in future work. The presence or absence of methanol and complex organic molecules determines the initial chemical composition of early protoplanetary and cometary material. The results obtained in this work are able to replicate the observed methanol cometary abundances and are also not inconsistent with the scenario of comets containing mostly prestellar methanol ice with some loss along the way.

2.6 ACKNOWLEDGEMENTS

This work is supported by a Huygens fellowship from Leiden University, by the Netherlands Research School for Astronomy (NOVA), by a Royal Netherlands Academy of Arts and Sciences (KNAW) professor prize, by European Union A-ERC grant 291141 CHEMPLAN, and by the Netherlands Organization for Scientific Research (NWO, grant 639.041.335). R.V. is supported by NASA through an award issued by JPL/Caltech and by the National Science Foundation under grant 1008800.

3

THE COMPLEX CHEMISTRY OF OUTFLOW CAVITY WALLS EXPOSED: THE CASE OF LOW-MASS PROTOSTARS

Maria N. Drozdovskaya, Catherine Walsh, Ruud Visser, Daniel Harsono, and Ewine F. van Dishoeck
MNRAS, 2015, 451, 3836

ABSTRACT

Complex organic molecules are ubiquitous companions of young low-mass protostars. Recent observations suggest that their emission stems, not only from the traditional hot corino, but also from offset positions. In this work, 2D physicochemical modelling of an envelope-cavity system is carried out. Wavelength-dependent radiative transfer calculations are performed and a comprehensive gas-grain chemical network is used to simulate the physical and chemical structure. The morphology of the system delineates three distinct regions: the cavity wall layer with time-dependent and species-variant enhancements; a torus rich in complex organic ices, but not reflected in gas-phase abundances; and the remaining outer envelope abundant in simpler solid and gaseous molecules. Strongly irradiated regions, such as the cavity wall layer, are subject to frequent photodissociation in the solid phase. Subsequent recombination of the photoproducts leads to frequent reactive desorption, causing gas-phase enhancements of several orders of magnitude. This mechanism remains to be quantified with laboratory experiments. Direct photodesorption is found to be relatively inefficient. If radicals are not produced directly in the icy mantle, the formation of complex organics is impeded. For efficiency, a sufficient number of FUV photons needs to penetrate the envelope; and elevated cool dust temperatures need to enable grain-surface radical mobility. As a result, a high stellar luminosity and a sufficiently wide cavity favor chemical complexity. Furthermore within this paradigm, complex organics are demonstrated to have unique lifetimes and be grouped into early (formaldehyde, ketene, methanol, formic acid, methyl formate, acetic acid, glycolaldehyde) and late (acetaldehyde, dimethyl ether, ethanol) species.

3.1 INTRODUCTION

Young, forming stars emerge in regions seeded with diverse molecules. From highly abundant deuterated species in prestellar cores (see Ceccarelli et al. 2014 for a review) to complex organic molecules in hot cores and corinos (see Herbst and van Dishoeck 2009 for a review), chemical variety spans the entire lifetime of a protostar. Complex organic species are particularly alluring due to their potential astrobiological implications.

Complex organic compounds are loosely defined in both chemistry and astronomy, but typically mean large ($\geqslant$ 6 atoms) carbon-containing species (Herbst and van Dishoeck, 2009). They were first observed in hot cores surrounding high-mass protostars (e.g., Blake et al. 1987; Kuan and Chuang 2014; Lovas et al. 1979), but have since also been detected in the environs of several low-mass counterparts (e.g., Bottinelli et al. 2004a,b; Cazaux et al. 2003; Dishoeck et al. 1995b; Jørgensen et al. 2012; Maury et al. 2014; Sakai et

al. 2013). The proximity of low-mass protostars facilitates spatially resolved studies. So far, single-dish telescopes have not revealed the origin of complex organics conclusively, but this is changing – progress is being made with powerful interferometers, such as the Submillimeter Array (SMA), the Plateau de Bure Interferometer (PdBI) and the Atacama Large Millimeter/submillimeter Array (ALMA).

It is well established that hot corinos (defined as the inner warm zones where $T_{dust} \geqslant$ 100 K) are chemically rich; however, several studies have shown that colder envelopes and positions with impinging outflows may also glow with emission from complex organic molecules. Formic acid (HCOOH), methyl formate ($HCOOCH_3$), acetaldehyde (CH_3CHO), methyl cyanide (CH_3CN) and ethanol (C_2H_5OH) were detected at a distance of $\sim 10^4$ AU from the L1157–mm low-mass protostar ($\sim$ 11 $L_\odot$, Sugimura et al. 2011) – towards the B1 position in the brightest carbon monoxide (CO) clump in the blue outflow lobe (Arce et al., 2008; Codella et al., 2009, 2015; Sugimura et al., 2011). The authors suggest that some species are already present on the grain surfaces and are subsequently liberated as gases by passing shocks, while others (e.g., methyl cyanide and acetaldehyde) form in the gas phase.

An outflow-affected position in the Perseus B1-b dust core (near a namefellow $\sim$ 3 $L_\odot$ protostar) and another in the Serpens core (specifically, SMM4-W, separated by $\sim$ 3000 AU from SMM4, which has a luminosity of $\sim$ 5 $L_\odot$) were studied by Öberg et al., (2010a) and Öberg et al., (2011a), respectively. The former did not show emission from complex organic species in contrast to the latter, which was bright in acetaldehyde and dimethyl ether (CH_3OCH_3). The envelopes of B1-b, SMM4, and SMM1 ($\sim$ 30 $L_\odot$) contain lines from ketene (H_2CCO), formic acid, methyl formate, acetaldehyde, dimethyl ether, methyl mercaptan (CH_3SH), propynal (HCCCHO), methoxy (CH_3O) and potentially oxirane (CH_2OCH_2) (Cernicharo et al., 2012; Öberg et al., 2010a, 2011a). The envelope encompassing the most luminous target, SMM1, has the highest overall abundance of complex molecules. It was proposed that the ice content was revealed thanks to photodesorption, which may be efficient on larger scales due to the presence of outflow cavities, through which FUV photons can escape.

Jaber et al., (2014) presented data from The IRAS16293 Millimeter and Submillimeter Spectral Survey (TIMASS, Caux et al. 2011). Detections of ketene, methyl formate, acetaldehyde, dimethyl ether, methyl cyanide and formamide (NH_2CHO) in the cold ($\lesssim$ 50 K) envelope (spanning $\sim$ 6000 AU) surrounding IRAS16293-2422 A and B (combined $\sim$ 22 $L_\odot$) were asserted. This is supported by earlier work on this source, which showed spatial segregation for various species (e.g., Bisschop et al. 2008; Ceccarelli et al. 2000; Dishoeck et al. 1995b; Schöier et al. 2002).

Öberg et al., (2011a), based on their observations and laboratory experiments (Öberg et al., 2009a), argued that complex organics form sequentially. While CO is frozen out, HCO-rich chemistry prevails, leading to 'cold' species like methyl formate and acetaldehyde. Upon warm up, $CH_{3/2}$-rich molecules are formed, building 'hot' species like dimethyl ether. However, observations of ketene, methyl formate, acetaldehyde, and dimethyl ether in the prestellar core L1689B (Bacmann et al., 2012), and formic acid towards the dark cloud L183 (Requena-Torres et al., 2007), argue against this sequential chemistry scenario due to the lack of elevated temperatures in these cold ($\sim 11-12$ K) sources.

A third prestellar core, L1544, was observed to show emission from ketene, formic acid, acetaldehyde, and propyne (CH_3CCH), but not from other species (such as methyl formate and dimethyl ether) found towards L1689B (Vastel et al., 2014). Cernicharo et al.,

(2012) secured a detection of the methoxy radical towards B1-b in Perseus and, based on laboratory data, argued that it is most likely produced in the gas phase from reactions between CH_3OH and OH - a reaction which has since been calculated to have a significantly larger rate coefficient at low temperatures than previously thought (Shannon et al., 2013). In summary, complex organic molecules are associated with outflow cavity walls, envelopes and even cold, dark cores, but it remains unclear when and how the various species form.

The complete chemistry of complex organics has been eluding astrochemists. Models have shown that gas-phase pathways contribute to the complex organic budget only under hot core-like conditions, when the densities and gas temperatures are high ($\sim 10^7$ cm^{-3} and > 100 K, e.g., Charnley et al. 1992; Rodgers and Charnley 2001). Instead, complexity could be built up in the ices. One solid-phase scenario is based on atom addition reactions (Tielens and Charnley, 1997). This has been experimentally proven for the sequential hydrogenation chain leading to methanol (Fuchs et al., 2009; Tielens and Hagen, 1982; Watanabe et al., 2004). An alternative scenario is that of processed 'zeroth generation' ices (i.e., simple ices like CO, methane (CH_4) and CH_3OH), which have been subjected to far-ultraviolet (FUV) irradiation, heating and/or cosmic rays (CRs, e.g., Garrod et al. 2008). Experimentally, an array of species is produced upon FUV irradiation of CH_3OH and CO mixtures (Öberg et al., 2009a). Recent ideas include combinations of radical-radical and hydrogenation reactions (Fedoseev et al., 2015), and revisions of gas-phase reaction rates, potentially making gas-phase chemistry non-negligible at lower temperatures (Balucani et al., 2015). In addition, alternative mechanisms, like Eley–Rideal and complex-induced reactions (Ruaud et al., 2015), or CR-induced diffusion (Reboussin et al., 2014), have also been invoked to pave the way to complexity. However, efficient mechanisms that couple ices to the gas phase resulting in appreciable observed abundances remain challenging.

To obtain more insight, this paper offers physicochemical models of envelopes harboring low-mass protostars, including the impact of outflow cavities. Previously, Bruderer et al., (2009, 2010) modelled a high-mass young stellar object (YSO) with an outflow cavity with a focus on ions and diatomic hydrides. The authors pre-calculated chemical abundances with a gas-phase network at a given time, which saves computational time. Instead, here, a two-phase chemical network is used for time-dependent calculations on a cell-by-cell basis. Visser et al., (2012) simulated the low-mass analogue of Bruderer et al., (2009, 2010), but focused on a thin warm/hot layer along the cavity wall, from which the far-infrared CO and water emission originate, rather than the larger cooler layers of the envelope that are central to this work.

In this work, the dust temperature and the stellar radiation field of the system are computed with RADMC – a 2D wavelength-dependent radiative transfer module. A comprehensive gas-grain chemical model is employed in order to simulate the distribution of complex organic molecules across the envelope as a function of time. The major upgrade in this paper, in comparison to the setup of Visser et al., (2012), is the inclusion of various grain-surface processes. Our models test the hypothesis that enhanced irradiation of the envelope, due to outflow cavities, stimulates the observed appearance of complex organic molecules in the gas phase in the colder offset positions from the protostar. The physicochemical models are described in Section 3.2. The results are presented in Section 3.3 and discussed in Section 3.4. The main findings are summarised in Section 3.5.

Table 3.1: Density distribution, outflow cavity, and stellar parameters (fiducial model setup).

Parameter	Units	Value
p		-1.7
r_{in}	AU	35.9
$n_{H_2;\,in}$	cm^{-3}	4.9×10^8
a_{cav}	AU	4.3×10^4
b_{cav}	AU	6.5×10^3
$\alpha\,(z = 1000\text{AU})$	deg	109
$\alpha\,(z = 10\,000\text{AU})$	deg	45
T_*	K	10 000
L_*	$L_\odot$	35.7

3.2 PHYSICOCHEMICAL MODEL

3.2.1 *Physical setup*

The goal of this work is to model the physical structure and the chemical composition of the envelope affected by outflow cavities on scales of 10 000 AU. A static setup is adopted, representative of a low-mass embedded protostar (Class 0/I). The chemistry is then computed in time at each point under constant physical conditions.

The gas density distribution (n_H) sets the underlying dust distribution upon the assumption of a gas to dust mass ratio (r_{gd}). Once the dust distribution is coupled with a set of stellar variables, the temperature and radiation field distributions are defined. Jørgensen et al., (2002) and Kristensen et al., (2010) fitted dust continuum emission stemming from envelopes with the DUSTY code (Ivezic and Elitzur, 1997). DUSTY models are spherically symmetric power law density distributions. The authors imposed the spectral energy distributions (SEDs) and continuum radial profiles at 450 and 850 μm from the JCMT as restrictions on these models to arrive at a set of best-fitting parameters. Those results were updated in Kristensen et al., (2012) based on new *Herschel* fluxes. In this work, the density distribution derived with the DUSTY model of NGC 1333-IRAS2A is taken as a test case for low-mass protostars with strong emission from complex organics.

In the modelling work of Kristensen et al., (2010, 2012), outflow cavities were neglected. Here, their presence is simulated by carving out ellipsoidal cavities from the DUSTY density distribution. This has previously been done in the work of Bruderer et al., (2009, 2010) and Visser et al., (2012) with two slightly different parameterisations. In this work, equation 1 from Visser et al., (2012) is used,

$$R_{cav} = b_{cav}\sqrt{1 - \left(\frac{z}{a_{cav}} - 1\right)^2}, \tag{3.1}$$

where (R_{cav}, z_{cav}) are the cylindrical coordinates of the cavity wall, and a_{cav} and b_{cav} are the semimajor and semiminor axes, respectively. Within the outflow cavity a comparatively low constant density is assumed,

$$n_H\,(\text{cavity}) = 2 \times 10^4 \text{cm}^{-3}, \tag{3.2}$$

and elsewhere,

$$n_H\,(\text{elsewhere}) = n_{H;\,in} \times \left(\frac{r}{r_{in}}\right)^p, \tag{3.3}$$

where r is the radial spherical coordinate, p is the power index of the density profile, r_{in} is the inner boundary of the envelope and $n_{H;\,in}$ is the H nuclei number density at r_{in}. It is assumed that $n_H = 2 \times n_{H_2}$ (at all positions). With the selected values of a_{cav} and b_{cav}, the full opening angle of the outflow cavity is 109° at $z = 1000$ AU and 45° at $z = 10\,000$ AU. Plunkett et al., (2013) tabulated the full opening angles for this source (table 4, although it is unclear at what distance from the source the values are derived), and find 30° and 56° for the two outflows in the blue lobe, and 32° and 93° for the two in the red lobe. These values are comparable to the full opening angles in this model. For other sources, wider angles have also been measured, e.g., 110° for HH46/47 (Velusamy et al., 2007).

The amount of radiation stemming from a star depends on its blackbody temperature and the size of the emitting surface, i.e., on the stellar temperature (T_*) and radius (R_*). The bolometric luminosity of NGC 1333-IRAS2A is 35.7 $L_\odot$ (Karska et al., 2013; Kristensen et al., 2012). Protostars are thought to have an ultraviolet (UV) excess due to accretion of material from the disc onto the star (e.g., Spaans et al. 1995). FUV photons are particularly efficient at photodissociating and photodesorbing molecules. Therefore in this work, a stellar temperature of 10 000 K is adopted in order to account for the anticipated UV excess. From the definition of stellar luminosity (L_*), the following parameterization is used to obtain the stellar radius:

$$R_* = \sqrt{\frac{L_*/L_\odot}{\left(T_*/T_\odot\right)^4}} R_\odot. \tag{3.4}$$

Although parameters derived for NGC 1333-IRAS2A are used, our aim is not to model this particular source, but instead to build a template for a Class 0 protostar (see, e.g., fig. 13 in Evans et al. 2009 for statistics per Class). The set of adopted parameters is summarized in Table 3.1.

Once the dust density distribution and stellar properties are prescribed, RADMC[1] (Dullemond and Dominik, 2004) is employed to calculate the temperature and radiation field distributions. An r_{gd} of 100 is assumed and the dust mass density (ρ_{dust}) is given by:

$$\rho_{dust} = 0.5 \times n_H \times \mu \times m_p / r_{gd}, \tag{3.5}$$

where m_p is the proton mass and μ is the mean molecular mass of the gas (taken to be 2.3). The dust is assumed to be a mixture of carbonaceous material (25 per cent) and silicates (75 per cent). Opacity tables for bare grains covering a range of grain sizes from Pontoppidan et al., (2007) are adopted. Modifications of the opacities to include icy mantles are expected to alter the dust temperatures (T_{dust}) by, at most, a few K (M.K. McClure, priv. comm.). Computations are carried out over frequencies in the $2.998 \times 10^{10} - 3.288 \times 10^{15}$ Hz (0.09 – 1000 μm) range, ensuring coverage of the dust's crystalline silicate features and the FUV range. The FUV radiation field (F_{FUV}) distribution is obtained via integration over the 912 – 2066 Å (6.0 – 13.6 eV) range at every grid point. Isotropic scattering is included in the model. In this way, thanks to the

1 http://www.ita.uni-heidelberg.de/~dullemond/software/RADMC/index.shtml

curved cavity rims, direct irradiation of the envelope by the protostar is also simulated (as illustrated in fig. 5 of Bruderer et al. 2009). Each setup was computed 10 times and the median F_{FUV} was adopted for each grid cell, in order to minimize the numerical noise stemming from the Monte–Carlo nature of RADMC, while remaining computationally economic.

3.2.2 *Complex organic molecule chemistry*

The evolving composition of the system is computed with a two-phase (gaseous and solid) chemistry code designed to solve for the abundances of species in time. The reaction rates depend on the physical conditions and the chemical network, as detailed in Walsh et al., (2014a,b). The network has also been used previously in Drozdovskaya et al., (2014), with only minor updates incorporated into the version used here. The chemical network is a compilation of the RATE12 release of the UMIST Database for Astrochemsitry (UDfA[2], McElroy et al. 2013) and the Ohio State University (OSU) network (Garrod et al., 2008), with a total of 668 species and 8764 reactions.

The chemical model includes gas-phase two-body associations, recombination of cations on grain surfaces, adsorption, thermal desorption, CR-induced thermal desorption (i.e., spot heating), photodesorption, photodissociation and ionization in the gas and solid phases, grain-surface two-body reactions, and reactive desorption with an efficiency of 1 per cent (Garrod et al., 2007; Vasyunin and Herbst, 2013b). Two sources of FUV photons are accounted for: the protostar with the attenuated F_{FUV} computed from RADMC, and the CRs, which produce FUV photons through excitation of H_2 (the most abundant molecule). Within the code, F_{FUV} is converted to visual extinction (A_V) via

$$A_V = \tau/3.02, \tag{3.6}$$

where τ is the UV extinction (Bohlin et al., 1978) given by:

$$\tau = -\ln\left(\frac{F_{FUV}}{\pi \times \int_{FUV} B_\lambda\left(T_*\right) d\lambda \times R_*^2/\left(R^2+z^2\right)}\right), \tag{3.7}$$

where the denominator is the blackbody radiation for T_* over the same FUV wavelength range as the numerator, with the inclusion of geometrical dilution, and where π accounts for radiation stemming from one hemisphere towards a point in the envelope. A similar concept was applied in Visser et al., (2011) and Drozdovskaya et al., (2014). A CR ionization rate (ζ_{CR}) of 5×10^{-17} s^{-1} is used (Dalgarno, 2006), which is slightly higher than the traditional dark cloud value ($\zeta_{ISM} = 1.3 \times 10^{-17}$ s^{-1}). FUV photons stemming from CR excitation of H_2 (with a flux of 10^4 photons cm^{-2} s^{-1} for ζ_{ISM}, Shen et al. 2004) are produced internally, and are thus available in the most dense and shielded regions. The elevated ζ_{CR} favors chemical complexity, although recent work suggests that the ionization rate may be as much as 3 orders of magnitude lower (e.g., Cleeves et al. 2013, 2015; Padovani et al. 2013). It is assumed that CRs penetrate the entire system uniformly, since even the maximum gas column density ($\sim 1-2$ g cm^{-2}) is too low for CR attenuation. Furthermore, magnetic fields are not modelled in this work; and stellar winds are expected to be important only in the innermost regions (Cleeves et al., 2013). External irradiation is not considered, since it strongly varies from source to source and is expected to affect only the very outermost envelope. H_2, CO and N_2 self- and mutual

2 http://www.udfa.net

shielding is accounted for in the calculation of the respective photodissociation rates (Li et al., 2013; Visser et al., 2009b). The main difference between the chemical setup in Drozdovskaya et al., (2014) and the one here, is the use of photorates[3] for a 10 000 K rather than a 4000 K blackbody (Dishoeck et al., 2006; Hemert and van Dishoeck, 2008).

To decrease the computational weight of the chemistry module, all grains are assumed to be 0.1 μm in radius (a), which is near the peak of typical dust populations. The number density of grain surface sites (N_{sites}) is 1.5×10^{15} cm^{-2} with a barrier thickness of 1 Å, under the assumption of a rectangular barrier (Hasegawa et al., 1992). Grains are considered to be either neutral or negatively charged, with a total, temporally and spatially constant number density (x_{grains}) relative to n_H. It is assumed that the gas temperatures equal the dust temperatures derived with RADMC. This should only break down at the lowest densities ($10^3 - 10^4$ cm^{-3}), e.g., within the outflow cavities themselves (where the chemistry is disregarded in this work) and in a thin layer along the cavity walls (Visser et al., 2012). Furthermore, gas temperature is of limited influence on the abundance of complex organics, because grain-surface associations and thermal desorption both depend solely on the dust temperature. Grain-surface reaction rates are computed assuming the Langmuir-Hinshelwood mechanism only and using the rate-equation method (Hasegawa et al., 1992).

Currently, in the chemical network, the formation of complex organic molecules relies primarily on associations of radicals upon FUV irradiation and the warm-up of icy mantles. At the lowest temperatures, hydrogenation is assisted by quantum tunneling of H and H_2 between grain surface sites, which becomes faster than classical thermal hopping. Quantum tunneling through reaction barriers is also allowed for these two species. The mobility of any species on the grain surface depends on its binding energy (E_{des}, also called its desorption energy). Here, the diffusion barrier (E_{diff}) is set by:

$$E_{diff} = 0.3 \times E_{des}, \tag{3.8}$$

as in Hasegawa et al., (1992). This allows higher mobility at low temperatures ($\sim 15 - 20$ K) in comparison to the factor of 0.5 used in Garrod and Herbst, (2006). Off-lattice kinetic Monte Carlo techniques suggest that the value is species-dependent, e.g., 0.31 for CO and 0.39 for CO_2 have been determined on the surface of crystalline water ice (Karssemeijer and Cuppen, 2014) – values which are in line with that assumed in this work. The set of adopted E_{des} values is the one supplied with RATE12, with the exception of water, for which a higher value of 5773 K for pure water ice is used instead (Fraser et al., 2001). These values can vary significantly depending on the surface composition, which may vary with the formation sequence of icy mantles and eventual segregation of solid species within the mantle.

FUV photons are responsible for photodissociating molecules and producing radicals, which may go on to make larger species. Radicals can be formed directly in the ice or in the gas phase, followed by subsequent adsorption or gas-phase reactions. However, FUV photolysis is a delicate balance. A strong FUV radiation field breaks molecules apart and favorably produces photofragments (like CH_3 and C_2H_5). In this work, an elevated ζ_{CR} favors radical production in strongly attenuated regions ($A_V \gtrsim 5$ mag) by CR-induced FUV photons (e.g., Gerakines et al. 1996; Palumbo et al. 2008), which has been seen to enhance complexity in experiments (Maity et al., 2015). Elsewhere, the stellar FUV field dominates. Other mechanisms for producing radicals have been postulated in the

3 http://home.strw.leidenuniv.nl/~ewine/photo/

literature and supported by experiments, e.g., low-energy electron radiolysis (Boamah et al., 2014), but they are not taken into account in this work.

The assumed grain properties are highly simplified in this chemical setup. Grain sizes and their distribution change with time, although theory suggests that this is most prominent for protoplanetary discs (see Testi et al. 2014 for a review; however there is also accumulating observational evidence for grain growth in the embedded phase, e.g., Jørgensen et al. 2009; Lommen et al. 2010; Miotello et al. 2014; Pagani et al. 2010; Ricci et al. 2010). The grains are also not necessarily spherical, and their surfaces may be highly irregular. All these parameters will change the surface area available for grain-surface chemistry and the number of binding sites that are available per unit volume. Under the current assumptions, the key parameter is the total density of sites (n_{sites}), given by:

$$n_{sites} = 4\pi \times a^2 \times N_{sites} \times x_{grains} \times n_H. \tag{3.9}$$

Here, $x_{grains} = 2.2 \times 10^{-12}$ is assumed. Decreasing this number by a factor of ~ 2, for example, results in abundances of gaseous and solid species changing by a factor of $\sim 2-3$ non-linearly.

Finally, time is also an important parameter. Grain-surface radical-radical association reaction rates are highly temperature-dependent and may require a long time to build up appreciable product abundances. Thermal desorption, on the other hand, can be very rapid if the dust temperature is sufficiently high. Radicals may thus be lost to the gas phase before a reaction can take place. In this work, the chemical evolution of the system is computed up to 3×10^6 yr, which corresponds to the upper limits on the age of embedded sources (see table 1 in Dunham et al. 2014b).

3.3 RESULTS

3.3.1 *Physical structure*

The physical structure of the system is displayed in Fig. 3.1. In the top panel, the number density of H nuclei follows the adopted power law throughout the envelope, $n_H \propto r^{-1.7}$ (equation 3.3 and Table 3.1). The outflow cavity has a fixed low density of 2×10^4 cm^{-3} (equation 3.2). The ellipsoidal cavity wall, as specified by equation 3.1 for the parameters given in Table 3.1, separates the zone carved out by the outflow from the envelope. The middle panel shows the dust temperature as obtained with RADMC. The cavity is the warmest region with $T_{dust} > 100$ K within the inner ~ 300 AU of the protostar, as a result of its low density and thus low extinction. The envelope is predominantly cold, $T_{dust} \lesssim 25$ K. Only a thin strip of material along the cavity wall (for $z \lesssim 8000$ AU) attains lukewarm conditions, $\sim 30-40$ K. Along the midplane, the $T_{dust} = 100$ K threshold is exceeded at $R \approx 38$ AU. This, in combination with our exclusion of the cavity itself, implies that the traditional hot corino is not treated in this work. The bottom panel displays the visual extinction, which is computed with equations 3.6 and 3.7 based on the stellar FUV radiation field calculated with RADMC. Again due to its low density, the cavity is subject to the strongest irradiation, $A_V < 2$ mag. The envelope zones closest to the radial axis are fully shielded from stellar FUV photons, $A_V > 10$ mag, thanks to the large dust column density separating them from the protostar. The rest of the envelope is subject to weak FUV irradiation, $A_V \lesssim 3$ mag.

The inner 35.9 AU around the protostar are excluded from this setup (Table 3.1), where the physical conditions need to be adjusted for the presence of a protoplanetary disc. The

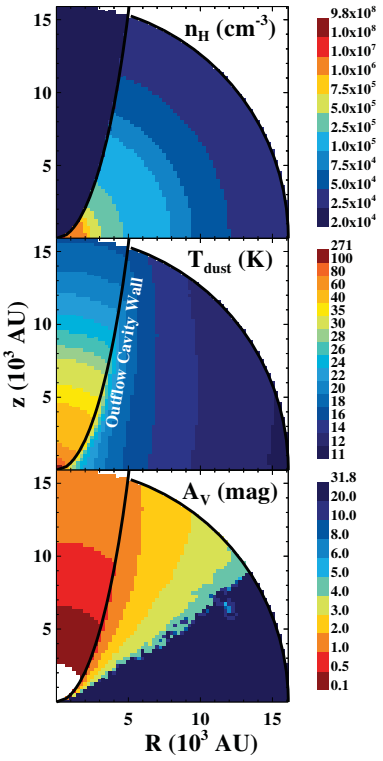

Figure 3.1: The physical structure of the system, from top to bottom: the gas density, n_H (cm^{-3}), the dust temperature, T_{dust} (K) and the visual extinction, A_V (mag). The outflow cavity wall is shown with a black curve. Data points only within a fixed radius (16 100 AU) of the protostar are considered.

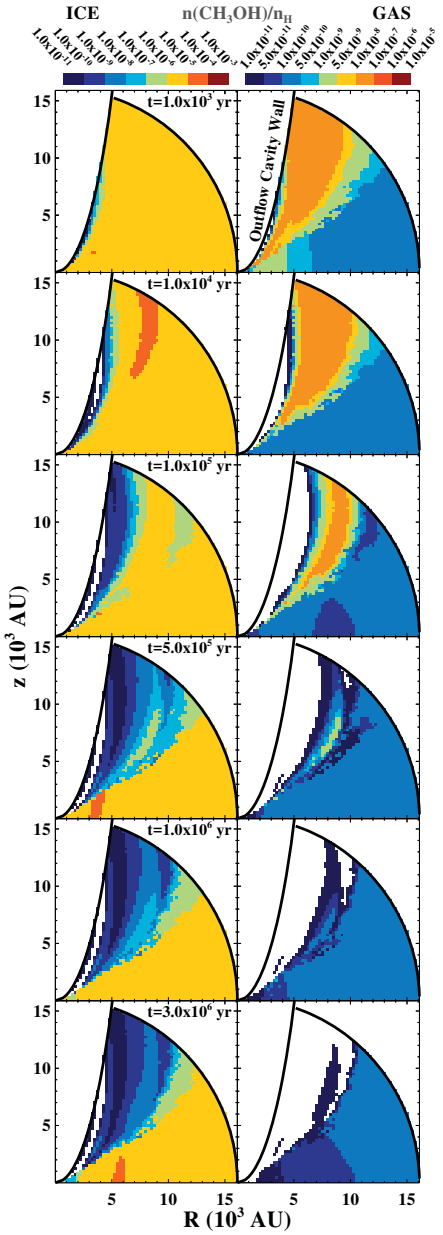

Figure 3.2: The abundance of methanol in the solid (left column) and gas (right column) phases at six different time steps across the envelope-cavity system. The outflow cavity wall is shown with a black curve. White cells correspond to either being outside of the area being considered or to having values outside of the range of the colour bar. The range of the gas colour bar is different from the range of that of the ice.

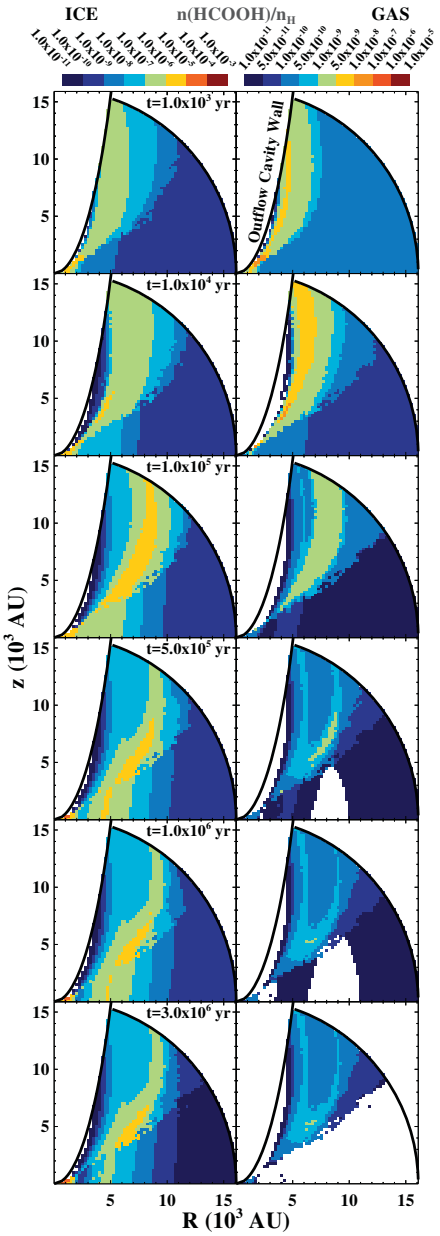

Figure 3.3: Same as Fig. 3.2, but for formic acid.

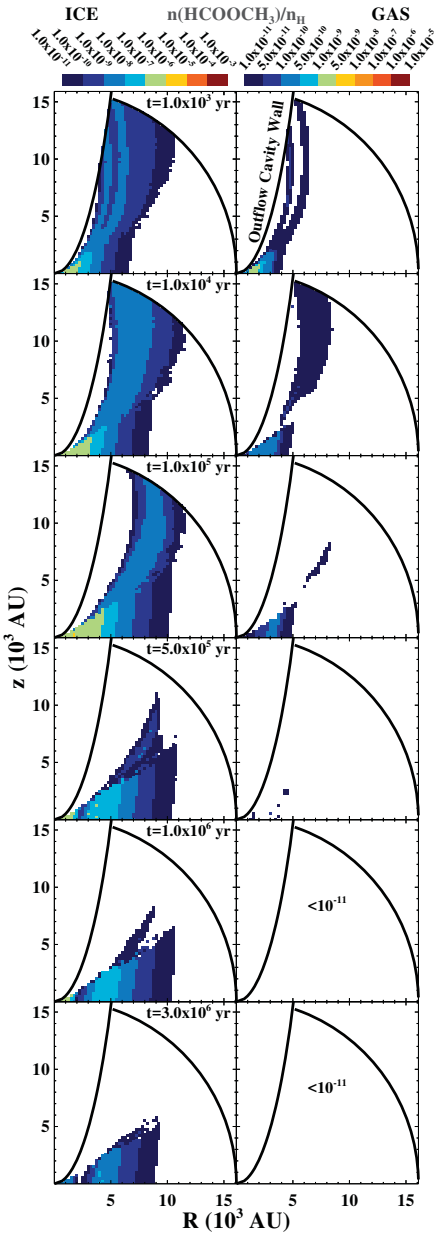

Figure 3.4: Same as Fig. 3.2, but for methyl formate.

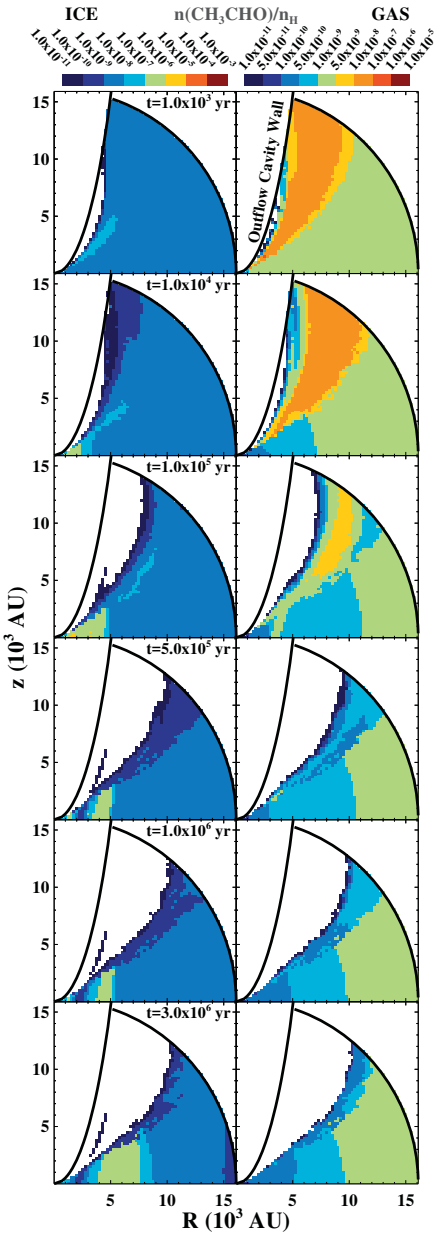

Figure 3.5: Same as Fig. 3.2, but for acetaldehyde.

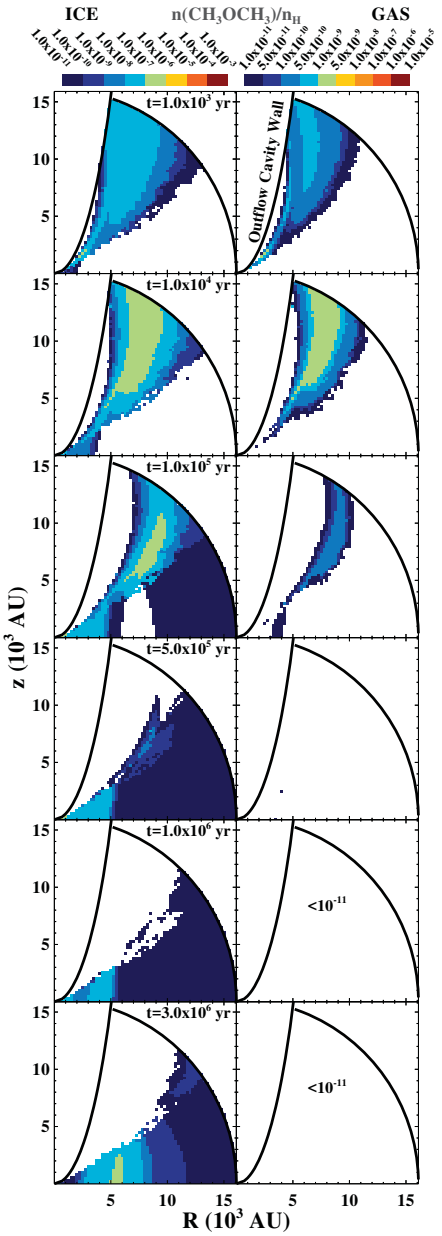

Figure 3.6: Same as Fig. 3.2, but for dimethyl ether.

Table 3.2: Abundances at the end of the prestellar core phase[a].

Species	Name	$n(X_{gas})/n_H$	$n(X_{ice})/n_H$
CO	carbon monoxide	3.5×10^{-5}	5.6×10^{-5}
H_2O	water	5.7×10^{-8}	2.0×10^{-4}
H_2CO	formaldehyde	6.0×10^{-8}	1.4×10^{-5}
CH_2CO	ketene	6.7×10^{-9}	1.7×10^{-8}
CH_3OH	methanol	1.3×10^{-10}	9.2×10^{-6}
HCOOH	formic acid	1.1×10^{-10}	4.4×10^{-10}
$HCOOCH_3$	methyl formate	3.2×10^{-15}	4.4×10^{-15}
CH_3CHO	acetaldehyde	2.1×10^{-9}	1.1×10^{-9}
CH_3OCH_3	dimethyl ether	3.1×10^{-15}	3.2×10^{-12}
C_2H_5OH	ethanol	5.1×10^{-12}	4.3×10^{-12}
CH_3COOH	acetic acid	2.7×10^{-21}	5.5×10^{-18}
$HOCH_2CHO$	glycolaldehyde	8.6×10^{-21}	2.4×10^{-17}

[a] The physical conditions of the prestellar core phase are assumed to be $n_H = 4 \times 10^4$ cm^{-3}, $T_{dust} = 10$ K, $F_{FUV} = 0$ erg cm^{-2} s^{-1} and $t = 3 \times 10^5$ yr.

RADMC calculations are performed on a much finer grid than that used for plotting in Fig. 3.1, which is the adopted grid for time-consuming chemical computations (4290 points in total). All cells are treated individually in the subsequent chemical calculations, i.e., as in a static model (in contrast with a dynamic evolutionary setup, as in Drozdovskaya et al. 2014). This maximizes the time spent in each temperature regime.

3.3.2 *Initial abundances*

The output of a single-point model of the prestellar core phase under constant physical conditions is assumed to be representative of the envelope material and therefore, is adopted as the set of initial molecular abundances. This scheme was also followed by Visser et al., (2011) and Drozdovskaya et al., (2014). The assumed physical parameters of the prestellar core are $n_H = 4 \times 10^4$ cm^{-3}, $T_{dust} = 10$ K, negligible stellar FUV flux and an age of 3×10^5 yr. André et al., (2014b) (in their section 3.3) estimated that the average lifetime of a starless core with a typical density of $\sim 10^4$ cm^{-3} is $\sim 10^6$ yr. A selection of the obtained abundances is provided in Table 3.2. Dark core observations of L1689B (Bacmann et al., 2012), L1544 (Vastel et al., 2014) and observations towards the 'core' position in B1-b of Öberg et al., (2010b) (and data from Cernicharo et al. 2012), derive column densities on the order of $\sim 10^{12}$ cm^{-2} for ketene, formic acid, methyl formate, acetaldehyde and dimethyl ether. If a typical H_2 column density of $\sim 10^{23}$ cm^{-2} is used, then the observed abundances of these species in prestellar cores are $\sim 10^{-11}$ within an order of magnitude. A comparison with the values in Table 3.2 reveals that from the aforementioned list only gas-phase methyl formate and dimethyl ether are underestimated in this prestellar core model. On the other hand, the modelled abundances of simpler ices, like water, carbon monoxide and methanol, are close to the observed ice

abundances against background stars (e.g., Boogert et al. 2011, 2013, 2015; Knez et al. 2005).

3.3.3 *Abundance maps*

Figs 3.2-3.6 show the abundance maps of five different molecules at six different time steps. The left six panels display the solid phase and the right six panels show the gas phase. For completeness, the abundance maps of five additional molecules (water, formaldehyde, ketene, ethanol, acetic acid) are provided in Appendix 3.7 (and glycolaldehyde is discussed in Section 3.3.4.3).

3.3.3.1 *Methanol*

Fig. 3.2 shows that the methanol ice abundance remains predominantly unchanged from its initial abundance (9.2×10^{-6}, Table 3.2) for the first 10^3 yr. With time, the abundance drops outwards from the cavity wall and eventually methanol ice is abundant ($\sim 10^{-6}$) only in the lower half of the envelope. This is the effect of photodissociation of methanol ice by stellar FUV photons (recall the A_V map from Fig. 3.1). At 10^4 yr, the upper cavity wall layer displays a small enhancement (within an order of magnitude). Stellar FUV photons do not only destroy methanol ice, but they also produce CH_3 and OH radicals by photodissociating other species (like H_2O ice), providing an additional formation channel for methanol ice (besides sequential hydrogenation of CO, which is efficient across the entire envelope). This enhancement along the wall survives until 10^5 yr, when the more distant zone (at $z \sim 12\,000$ AU and $R \sim 14\,000$ AU) starts to show a lower abundance ($\sim 10^{-7}$) by an order of magnitude, indicating favouritism towards destruction in that region.

Another methanol ice-rich zone is formed around $z \sim 500$ AU and $R \sim 5000$ AU. It will be shown in subsequent maps (Fig. 3.3-3.6) that this small area is rich in all complex organic ices, and for that reason this area is referred to as the 'complex organic molecule torus'. Methanol, being a key parent species, is also abundant here. As it is converted to larger species, the enhancement is subdued at 10^6 yr. At longer time-scales, $\sim 3 \times 10^6$ yr, CR-induced FUV photons start to dominate and photodissociate larger molecules to remake methanol, leading to the regaining of the enhancement and a resetting of the ice chemical complexity.

The distribution of gas-phase methanol is closely related to the abundance of methanol ice. In the regions furthest away from the cavity, where methanol ice is abundant ($\sim 10^{-6}$) for all times, the abundance of methanol gas is low ($\lesssim 5 \times 10^{-10}$). The entire envelope is colder than the thermal desorption temperature of methanol (~ 90 K), and there are no efficient gas-phase routes to methanol, therefore the amount of gaseous methanol relies purely on non-thermal desorption. In the furthest regions, extinction is high, so photodesorption with stellar FUV photons is insignificant. Gas-phase methanol is obtained through weak photodesorption by CR-induced FUV photons and reactive desorption stemming from hydrogenation reactions with CO. The cavity walls, on the other hand, light up in gaseous methanol for the first $\sim 10^5$ yr. This corresponds to the zone showing the methanol ice enhancement. There, enough stellar FUV photons penetrate to allow more efficient photodesorption, but more importantly, to dissociate methanol ice. Upon the subsequently recombination of the photoproducts, reactive desorption is assumed to occur in 1 per cent of such reactions, enhancing the gas-phase methanol abundance.

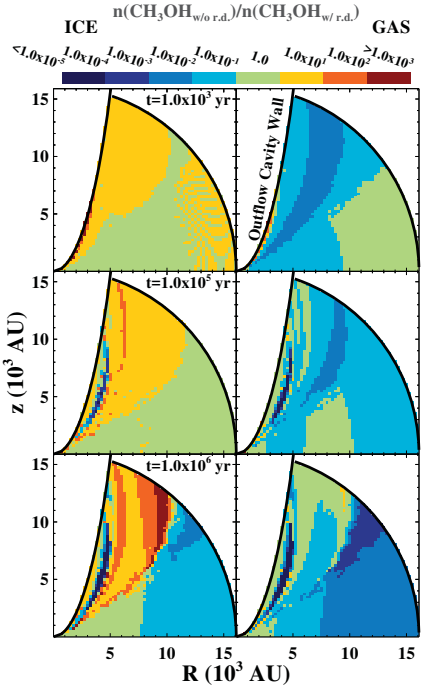

Figure 3.7: The ratio of the methanol abundance with reactive desorption switched off to that with an efficiency of 1 per cent. Three time steps are shown with the solid-phase and the gas-phase ratios in the left and right columns, respectively. The outflow cavity wall is shown with a black curve. A certain colour corresponds to a range of values between the two labeled bounds, e.g., yellow corresponds to any value between 1 and 10.

3.3.3.2 *Formic acid*

Formic acid has an initial abundance of $\sim 10^{-10}$ in both phases. There are several key grain-surface pathways leading to its formation, specifically hydrogenation (H + COOH) and associations of OH either with H_2CO or HCO. Solid formic acid is clearly enhanced along the cavity wall at all time steps in Fig. 3.3. This occurs due to elevated radical-radical association rates thanks to stellar FUV photons, as was the case with methanol ice. The enhancement moves further away from the cavity rim with time with the separation between the two being largest ($\sim$ 4000 AU) at highest z values ($\sim$ 10 000 AU), which is a result of the formation-destruction balance shifting. The zone with the highest abundances ($> 10^{-6}$) is maximized at 10^5 yr. Gas-phase formic acid illuminates the cavity wall primarily at the earlier times ($\leqslant 10^5$ yr). Its abundance peaks ($> 5 \times 10^{-9}$) at 10^4 yr, before that of the ice. This corresponds to the time when radical-radical chemistry is most active. On the longest time-scales, CR-induced FUV photons destroy formic acid in both phases.

3.3.3.3 *Methyl formate*

Fig. 3.4 shows the distribution of methyl formate. Its ice reaches abundances of $\sim 10^{-9}$ along the cavity wall, which is a large increase from its initial abundance of $\sim 10^{-15}$. Peak abundances $> 10^{-7}$ are reached at 10^5 yr in the complex organic molecule torus. Gaseous methyl formate exceeds the $\sim 10^{-11}$ abundance level at early times along the cavity wall, but mostly remains at a low abundance ($< 10^{-11}$). The enhancement of the ice in the complex organic molecule torus is not reflected in the gas-phase abundance, because at its location, there are no efficient routes to liberate the icy mantle species. This was also the case with methanol and formic acid in Figs 3.2 and 3.3, respectively. The formation of methyl formate predominantly occurs either via the association of methoxy with HCO or with CO followed by hydrogenation.

3.3.3.4 *Acetaldehyde*

Acetaldehyde ice remains at its initial abundance of $\sim 10^{-9}$ throughout the envelope. With time, photodissociation by stellar FUV photons depletes it in the vicinity of the cavity wall (Fig. 3.5). An appreciable enhancement is built up in the torus with an abundance of $\sim 10^{-7} - 10^{-6}$. Gaseous acetaldehyde appears to be highly decoupled from its ice due to a strong enhancement ($> 10^{-8}$) along the wall for $\lesssim 10^5$ yr, which is not seen in the solid phase. This feature appears due to a single gas-phase reaction, namely $O + C_2H_5$ (with a rate coefficient of 1.33×10^{-10} cm^3 s^{-1} upon extrapolation from Tsang and Hampson 1986). Atomic O is highest in abundance towards zones with the stronger irradiation, i.e., towards the cavity, while C_2H_5 is most abundant towards zones with the least irradiation, i.e., towards the radial axis. This results that in the 'overlap region', the cavity wall layer, the reaction is very efficient at producing acetaldehyde. Grain-surface production of acetaldehyde proceeds via CH_3 + HCO and CH_3 + CO followed by a hydrogenation.

3.3.3.5 *Dimethyl ether*

For the first $\sim 10^5$ yr, dimethyl ether strongly highlights the cavity wall with solid and gaseous abundances higher than 10^{-7} and 10^{-9}, respectively (Fig. 3.6). This is the result of active grain-surface chemistry and concomitant reactive desorption. At longer times

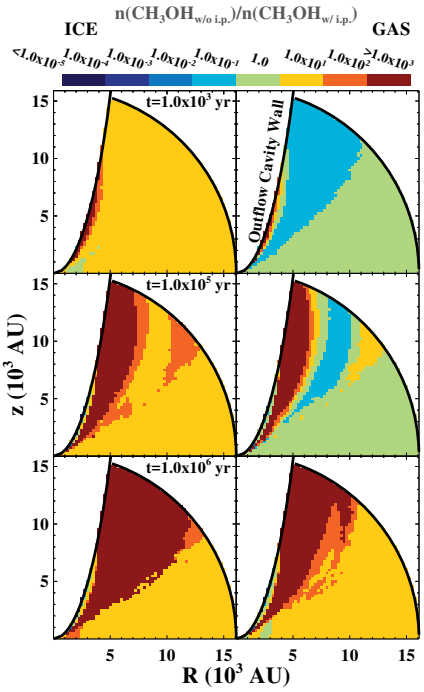

Figure 3.8: The ratio of the methanol abundance with ice photodissociation (by stellar and CR-induced FUV photons) switched off to that with it on. Three time steps are shown with the solid-phase and the gas-phase ratios in the left and right columns, respectively. The outflow cavity wall is shown with a black curve.

($> 10^5$ yr), the enhancement is destroyed due to the domination of photodissociation by stellar FUV photons. However, at those times dimethyl ether ice is built up in the torus at an abundance of 10^{-7}, which is hidden from the gas phase for the above-stated reasons. The only grain-surface pathway towards dimethyl ether included in the network is the association of CH_3 with methoxy.

3.3.4 *Parameter study*

3.3.4.1 *Reactive desorption*

During the above analysis of abundance maps, the importance of reactive desorption is readily seen, even with a mere 1 per cent efficiency. This has also been reported in previous publications. Vasyunin and Herbst, (2013b) saw variations of several orders of magnitude in gas-phase abundances and differences of 10 per cent in ice abundances for a dark core model ($T = 10$ K, $n_H = 10^5$ cm^{-3}, $A_V = 10$ mag, $t = 10^5 - 10^6$ yr) upon varying reactive desorption efficiency from 0 to 10 per cent. Wakelam et al., (2014) noted that gas-phase water abundances can change by a factor of 10 upon exclusion of reactive desorption (for various single point models with $T = 15 - 30$ K, $n_H = 2 \times 10^4 - 2 \times 10^5$ cm^{-3}, $A_V = 2 - 4$ mag, $t = 10^4 - 10^6$ yr). Experiments constraining this process are scarce. Recently, Dulieu et al., (2013) and Minissale and Dulieu, (2014) suggested that the efficiency of reactive desorption can vary greatly per reaction and per surface, from very efficient on bare grains to completely inefficient as soon as the first monolayer is built up.

Fig. 3.7 shows the ratio of the methanol abundance with reactive desorption switched off to that with an efficiency of 1 per cent, i.e., comparing with Fig. 3.2. Gas-phase abundances decrease over almost the entire envelope for all times once reactive desorption is excluded. The decrease is $1 - 3$ orders of magnitude for the largest portions of the envelope, and is explained by the exclusion of the most efficient mechanism for the population of the gas phase by the methanol-rich ices. In strongly irradiated areas, $A_V < 3$ mag, the abundance of solid methanol is as much as 3 orders of magnitude higher when reactive desorption is not included, which is an ice destruction mechanism. However, in zones where CR-induced FUV photons dominate, $A_V > 3$ mag, there is less solid methanol when reactive desorption is excluded. Reactive desorption elevates the gas-phase abundance not only of methanol and complex organic molecules, but also of simpler species, like CH_4. Gas-phase ion-molecule reactions then lead to an enhancement of gas-phase radicals, most notably CH_3. Higher gaseous radical abundances imply greater availability of these species on the grains (transiently) as well, thus allowing more efficient formation of methanol via the $OH + CH_3$ route.

Acetaldehyde and dimethyl ether follow a trend very similar to that seen with methanol in Fig. 3.7. Formic acid and methyl formate differ by not showing a decrease in the zone with high extinction when reactive desorption is switched off. This is linked to them being less reliant on the availability of CH_3.

3.3.4.2 *Ice photodissociation*

Another poorly constrained process is the photodissociation of solid species. UV photons can penetrate as deep as 100 monolayers into the icy mantle; however, what happens with the photofragments thereafter remains unclear. They may recombine immediately or diffuse away through the ice, if they have sufficient translational energy after photodis-

sociation (e.g., Andersson and van Dishoeck 2008). In the current setup, it is assumed that the entire mantle may be dissociated; however, by making all those radicals equally available for further grain-surface reactions, the chemistry of the solid phase is potentially overestimated, because the diffusion rates within the bulk ice mantle are likely slower than those across the surface.

To test the significance of ice photodissociation by stellar and CR-induced FUV photons, a control simulation is carried out with those processes turned off. Photodesorption and reactive desorption are still included. Fig. 3.8 shows the ratio of the methanol abundance with ice photodissociation excluded to that with it included, i.e., again comparing with Fig. 3.2. The amount of methanol ice is increased roughly by an order of magnitude in zones with the highest extinction ($A_V > 3$), and in the cavity wall by 3 orders of magnitude. This corresponds to where photodissociation is dominated by stellar UV photons and is the primary ice destruction pathway. For $t \leqslant 10^5$ yr, the gas-phase methanol abundance is reduced, since less ice photodissociation implies less radical recombinations, and thus less gas-phase methanol due to reactive desorption. However, at later time steps and in the cavity walls, a much larger abundance of ice leads to more gaseous methanol via photodesorption, CR-induced thermal desorption, and reactive desorption associated with slow formation pathways. At the final time step, the gas-phase methanol abundance starts to decrease in the most shielded zone, since CR-induced FUV photons are still photodissociating in the gas-phase, but efficient mechanisms (in particular, reactive desorption, in comparison to the fiducial setup) to replenish the gas from the ice are absent.

Other complex organics, i.e., formic acid, methyl formate, acetaldehyde and dimethyl ether, show a decrease by several orders of magnitude in both phases once ice photodissociation is switched off. In this control simulation, the radical production is limited to the gas phase, while key radical sources, such as methanol, are most abundant in the solid phase. The reduction of radicals drastically obstructs efficient formation of complex organic molecules. Only along the cavity wall, are the abundances higher than fiducially. Ice photodissociation dominates there and in the standard case efficiently destroys complex organics.

3.3.4.3 *An additional route to glycolaldehyde*

The chemistry explored in this work is limited by the reactions and the species included in our chemical network. In order to investigate this limitation, an additional formation pathway for glycolaldehyde is introduced, namely:

$$\dot{\mathrm{H}}\mathrm{CO}_{\mathrm{ice}} + \dot{\mathrm{H}}\mathrm{CO}_{\mathrm{ice}} \rightarrow \mathrm{OCHCHO}_{\mathrm{ice}},$$

$$\mathrm{OCHCHO}_{\mathrm{ice}} \overset{\mathrm{H}}{\rightarrow} \begin{matrix} \mathrm{HO}\dot{\mathrm{C}}\mathrm{HCHO}_{\mathrm{ice}} \\ \dot{\mathrm{O}}\mathrm{CH}_2\mathrm{CHO}_{\mathrm{ice}} \end{matrix} \overset{\mathrm{H}}{\rightarrow} \mathrm{HOCH}_2\mathrm{CHO}_{\mathrm{ice}}.$$

This scheme was suggested by Woods et al., (2013) and experimentally proven for ices by Fedoseev et al., (2015). In total, 68 reactions are added to the existing chemical network and are detailed upon in Appendix 3.7.

The same initial conditions are used as in the fiducial case (which also holds for all other test cases discussed), so that the dependence of the results purely on the inclusion of the additional pathway is explored. The abundance of gaseous and solid glycoladehyde increases by an order of magnitude across the system when the additional

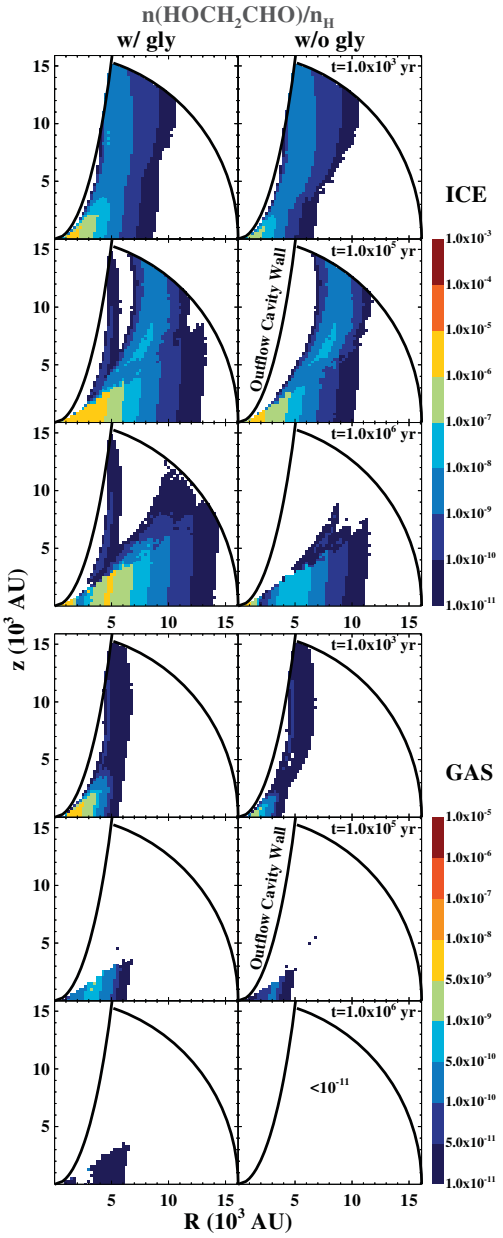

Figure 3.9: The abundance of glycolaldehyde in the solid (upper six panels) and gas (lower six panels) phases at three different time steps across the envelope-cavity system. The right column corresponds to the fiducial model. The left column is the model output upon the inclusion of the additional formation pathway via glyoxal. The outflow cavity wall is shown with a black curve. White cells correspond to either being outside of the area being considered or to having values outside of the range of the colour bar. The range of the gas colour bar is different from the range of that of the ice.

formation route is included, as Fig. 3.9 shows (the difference is larger in areas where the abundance of glycolaldehyde is very low ($n(HOCH_2CHO_{ice})/n_H < 10^{-11}$), but that is not significant). This is consistent with the upper limit derived by Woods et al., (2013), where destruction of glycolaldehyde and competitive routes are not considered. Adding an extra route for forming a molecule is expected to boost its abundance. The boost is larger in highly extincted and, in turn, cold ($T_{dust} \lesssim 20$ K) zones, where hydrogenation dominates over radical-radical associations. This enhancement also prolongs the lifetime of glycolaldehyde, and it is still found at appreciable ice abundances ($\sim 10^{-8}$) in the COM torus at 10^6 yr, which was not the case previously. All other species show differences by a factor of a few or less (any modification of a chemical network results in non-linear effects on all species due to competing pathways, e.g., the inclusion of HCO + HCO competes with HCO + H, HCO + CH_3O, etc.), which is consistent with the findings of Fedoseev et al., (2015) using Monte Carlo models. This exercise shows that there may remain important routes to the formation of complex organics that have not yet been included in models.

Glycolaldehyde and methyl formate (and acetic acid) are isomers and may be intriguing probes of the physics and chemistry of a system. Recent observations have estimated the methyl formate to glycoladehyde ratio to be ~ 13 for IRAS16293-2422 (Coutens et al., 2015; Jørgensen et al., 2012), $\sim 12-20$ for NGC 1333-IRAS2A (Coutens et al., 2015; Taquet et al., 2015) and ~ 10 for NGC 1333-IRAS4A (Taquet et al., 2015). Averaging over 10 points in the COM torus (along $z = 500$ AU and for $3756 \lesssim R \lesssim 6006$ AU) gives a ratio in the ice of 0.84 fiducially and of 0.04 after the route via glyoxal is introduced. The models indicate that there is more glycolaldehyde than methyl formate, while observations suggest the contrary. This may be explained by the fact that the observations probe predominantly the hot core regions, where gas-phase reactions become important (Taquet et al., 2015). They may drive chemistry that is different from that occuring in the solid phase. This may include gas-phase reactions with formic acid (Taquet et al., 2015), production of methoxy from OH+CH_3OH and hydrogen-abstraction reactions with F and Cl (Balucani et al., 2015).

3.3.4.4 *Stellar luminosity*

Young Class 0 and I protostars cover a range of luminosities from fractions of $L_\odot$ to more than an order of magnitude higher (Dunham et al., 2014b; Evans et al., 2009). The dependence of these models on the luminosity is investigated by computing the chemistry for the case of 1 $L_\odot$ and 15 $L_\odot$. Our adopted luminosity of 35.7 $L_\odot$ for NGC 1333-IRAS2A is on the higher side of the bulk of the low-mass protostars. Since the density is fixed, and both F_{FUV} and the geometric dilution of the blackbody radiation scale with L_* (see equation 3.7), the A_V map remains unchanged for different luminosities. However, the number of FUV photons reaching a certain grid cell does change. Fig. 3.17 in Appendix 3.7 shows the difference in the dust temperature between the fiducial 35.7 $L_\odot$ model and the two with lower luminosities. In the case of 15 $L_\odot$, the envelope dust temperatures are cooler by at most 5 K. For 1 $L_\odot$, the differences are larger, and the cavity wall can be as much as $10-15$ K colder than in the original case.

Fig. 3.18 shows the methanol abundance in the case of 15 $L_\odot$ and 1 $L_\odot$ in comparison to the fiducial setup. For solid and gaseous methanol (with both phases displaying strong coupling), the abundances for 15 $L_\odot$ and the fiducial run are very similar with differences predominantly within 1 order of magnitude. Only small regions show an increase in methanol by $2-3$ orders of magnitude in the 15 $L_\odot$ case. The enhancement

Table 3.3: Outflow cavity parameters (additional model setups).

Parameter	Units	Narrow	Wide
a_{cav}	AU	4.5×10^4	3.4×10^4
b_{cav}	AU	2.0×10^3	8.0×10^3
$\alpha\,(z = 1000\text{AU})$	deg	45	125
$\alpha\,(z = 10\,000\text{AU})$	deg	14	59

along the cavity wall is explained by the shift of the temperature regime most favorable for grain-surface chemistry due to enhanced mobility prior to thermal desorption of radicals and the decrease of FUV photons making radical production inefficient. Other species (formic acid, methyl formate, acetaldehyde and dimethyl ether) predominantly show a decrease in abundance by an order of magnitude, leading to the increase in simpler species, like methanol and formaldehyde.

For the 1 $L_\odot$ case (left column of Fig. 3.18), the trends seen with 15 $L_\odot$ are dramatized. The formation of complex organics is significantly impeded with gaseous and solid abundances of $\sim 10^{-11}$ or lower in the entire envelope. This results in an increase of solid, and in turn gaseous, methanol, by as much as 3 orders of magnitude in a broad zone along the cavity. In conclusion, the original model with the highest luminosity of 35.7 $L_\odot$ has been identified as most efficient for chemical complexity within this paradigm, while lower luminosities support stronger enhancement or retainment of simpler species, such as methanol. The morphology of the region, including the highlighting of the cavity wall, is preserved upon varying L_*, although the sizes of these regions change as do the peak abundances.

3.3.4.5 *Outflow cavity full opening angle*

The shape of the outflow cavities and the cavity full opening angle set the flux of stellar photons penetrating the envelope, as mentioned in Section 3.2.1. To test the importance of the full opening angle, two additional simulations have been executed, one with a narrower and another with a wider full opening angle (Table 3.3). Fig. 3.19 in Appendix 3.7 shows the difference in the dust temperature between the fiducial case and the two additional models, as well as the ratios in extinction. The temperature variations are largest in the zone that in one model is part of the cavity and not in the other, as well as in the cavity wall. The variations can exceed 20 K close to the star, and are a result of the change in the density from the radial profile of the envelope to a fixed low value of the cavity. When comparing the three extinction maps, the pattern from narrow to fiducial to wide angle is that of an opening flower blossom. In the ratio plot, that is reflected by a large scale decrease in extinction of $7-25$ times in the cavity wall when going from the small cavity to the fiducial setup. When switching from the fiducial to the large cavity, a further decrease by a factor of $7-10$ is seen in an area immediately after the zone with the previous weakening. Furthermore, there is also a change in extinction in the zone that is switching from envelope to cavity area, as was the case with the dust temperature.

Fig. 3.20 shows the methanol abundance in the case of a wider and a narrower full opening angle in comparison to the fiducial cavity. The most prominent change is the enhancement by $2-3$ orders of magnitude ~ 5000 AU away from the cavity wall, which is preceded by a decrease of $2-5$ orders of magnitude. This is due to the shift of the

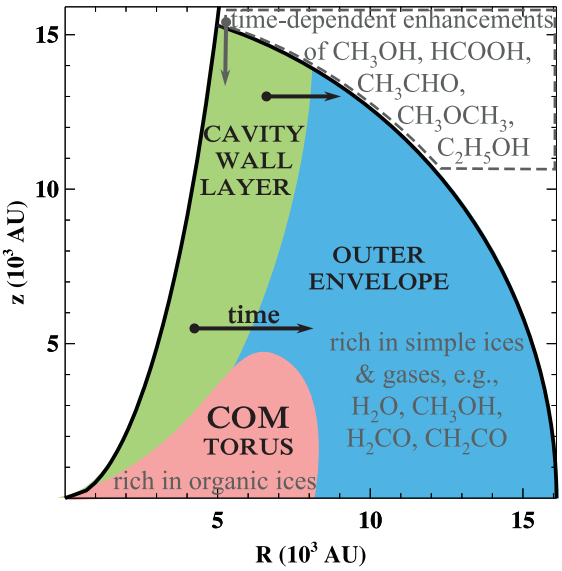

Figure 3.10: An illustration summarizing the key zones of the envelope-cavity system, and the major species and their phases therein. The motion of the cavity wall layer with time is indicated with two arrows. COM stands for complex organic molecules.

zone with efficient reactive desorption with the widening of the cavity. Other regions and other species predominantly show variations within an order of magnitude. The morphology of the system and highlighting of the cavity walls is preserved. Only the COM torus, still rich in complex organic species, is slightly reduced in size.

In the case of a small cavity (left column of Fig. 3.20), complex organic molecules are only produced in a narrow strip in the immediate vicinity of the cavity wall, because in all other regions of the system, very few FUV photons penetrate making radical production inefficient. Methanol benefits from this and an enhancement in both solid and gas-phase abundances is seen for a much thicker layer along the cavity wall. In the fiducial setup, stellar FUV photons would actively photodissociate methanol in that zone. In essence, the full opening angle of a cavity determines primarily the amount of FUV radiation entering the envelope. The morphological structure of the system remains comparable, but enhancements in methanol and other complex organic molecules shift angularly with the migration of the regions with optimal temperature and extinction combinations.

3.4 DISCUSSION

3.4.1 *Morphology*

The abundance maps in Figs 3.2-3.6 suggest an evolving chemical morphology of the envelope-cavity system. The representation in Fig. 3.10 summarises all the information from the individual species in one global picture. First, there is the outflow cavity wall layer, which lights up in various species at different times. This region corresponds to

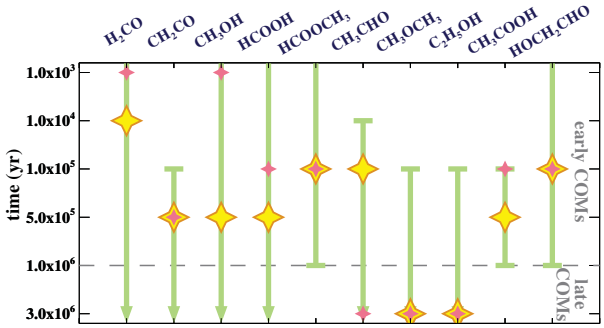

Figure 3.11: Lifetimes of complex organic ices in the COM torus (at $z = 500$ AU). The green bars indicate when the abundance of the specified molecule is above 5×10^{-8}. The filled pink stars mark the time when the zone (in R) above this cut off value is maximized. The larger orange-yellow stars mark when the peak abundance is highest.

where photodissociation by stellar UV photons leads preferentially to the formation of various large solid species via radical-radical associations on the grain. Reactive desorption stemming from many recombinations of photoproducts leads to an enhancement of methanol and complex organics in the gas phase. Acetaldehyde is an exception to this, due to an efficient gas-phase pathway (O + C_2H_5) leading to a large gas-phase abundance, but not in the solid phase. Such exceptional behaviour was also seen in and suggested by Codella et al., (2015).

Secondly, there is the COM torus with the largest diversity of complex organic ices at abundances several orders of magnitude higher than initially injected into the system. The largest, most complex species (e.g., dimethyl ether in contrast to formic acid) appear later in time in the torus than in the cavity wall layer, but also survive much longer due to the mild radiation. This zone probes the time-scales of cool ($15 - 25$ K) quiescent ($A_V \sim 10$ mag) grain-surface chemistry with CR-induced FUV photons being the only source of radicals. In essence, the cavity wall layer is the scaled-up version of the torus, based on the scaling of the FUV radiation fields. A stronger stellar FUV radiation field builds complex organics faster and in a larger zone, but for a short period of prosperity. A weaker CR-induced FUV radiation field builds complexity more slowly, in a smaller zone that is shielded from powerful dissociating stellar radiation. Both require cool dust temperatures (the distinguishing feature from the prestellar phase), and both eventually destroy complexity via photodissociation.

Finally, the rest of the envelope is where only relatively simple ices and gases reside. This pertains to species like water, methanol, formaldehyde, and ketene among others. Few changes happen in this zone compared with the initial conditions, because the temperature is low ($\lesssim 15$ K) and shielding is high ($A_V \gtrsim 3$ mag). The chemical composition of the outer region remains similar to the prestellar phase.

Several important lessons can be learned from the abundance maps, besides the chemical morphology of the system. As is seen for the COM torus, gases do not always reflect the composition of the ices. Effective non-thermal desorption mechanisms are needed to couple the two phases in the predominantly cold (< 100 K) envelope. Furthermore, there may be exceptional species, like acetaldehyde, that have an efficient gas-phase route at particular physical conditions (like that of the cavity wall layer), which would result in an inferred ice abundance that is several orders of magnitude too high. Observations

of solids are needed to accurately constrain the icy content, which remains a challenging task for solid complex organic molecules. Some species with isolated features in the $5-10$ μm range can be searched for with future missions like the *James Webb Space Telescope* (*JWST*).

3.4.2 *Comparison with observations*

From Fig. 3.2 it can be seen that gaseous methanol illuminates the cavity wall as early as 10^3 yr with abundances of $\sim 10^{-8}$. Formic acid, acetaldehyde, dimethyl ether and ethanol reach gas-phase abundances of $\sim 10^{-9}$, 10^{-8}, 10^{-9} and 10^{-9}, respectively, in the cavity wall layer. These values are in rough agreement with the column densities derived by Arce et al., (2008) for formic acid and ethanol at the B1 position ($\sim 10^{13}-10^{14}$ cm^{-2} giving abundances $\sim 10^{-10}-10^{-9}$ cm^{-3}), as well as those for acetaldehyde and dimethyl ether ($\sim 10^{13}$ cm^{-2}) from Öberg et al., (2011a) towards Serpens. This implies that thermal desorption (for $T_{dust} \gtrsim 100$ K) and sputtering with the passage of shocks along cavity walls do not need to be invoked when interpreting observations on these scales (several thousand AU). These processes are more likely to be efficient on smaller (several hundred AU) scales and shorter time-scales ($\sim 10^3$ yr). The enhancements seen in the cavity wall layer rely heavily on reactive desorption, which dominates over much less efficient direct photodesorption. This highlights the need for further laboratory studies quantifying the efficacy of reactive desorption as a mechanism for releasing complex organic ices into the gas phase at low temperatures. If it is inefficient, then shocks may once again be necessary to explain observations. Methyl formate does not follow the observed abundances of Arce et al., (2008) and Öberg et al., (2011a) in our models, and in fact, is only efficiently made in the COM torus.

By design of the chemical network used in this work, methanol plays a central role in the synthesis of larger, more complex species. However, it appears not only as a precursor, but also as a descendent (or postcursor), once CR-induced FUV photons dominate and destroy complexity at longer time-scales ($\gtrsim 3 \times 10^6$ yr). This scenario may be challenged as more atom addition reactions are included into the chemical network.

Our models predict the COM torus – a solid-state sweet spot, which has not been seen observationally. The abundances in this zone may still change due to influences of the protoplanetary disk and other dynamical effects (Section 3.4.4). For NGC 7538 IRS9 – a massive YSO, Öberg et al., (2013) reported a change in chemistry within 8000 AU of the protostar, which potentially links with efficient grain-surface chemistry. It remains unclear whether a high-mass source would be associated with more efficient pathways towards enriching the gas phase from the ices rich in complex organics, in comparison to the low-mass case modelled in this work. Although, recent ALMA observations towards the high-mass IRAS16547-4247 by Higuchi et al., (2015) suggest that methanol emission follows an hourglass morphology.

3.4.3 *Lifetimes of complex organics*

From the abundance maps it was seen that species peak at different times. Motivated by this, the ordering of complex organic species in time is shown in Fig. 3.11 as they appear in the COM torus (a slice at $z = 500$ AU is assumed to be representative, which covers $R \in [1006, 16\,100]$ AU). The green bars show when the abundance of an ice is above 5×10^{-8}, i.e., when the solid phase is enhanced. The time of maximal spatial extent of

this enhancement along R is marked with a filled pink star. When the peak ice abundance is reached, this is indicated with a larger orange-yellow star. The two do not necessarily overlap for all species considered. As was hinted earlier, Figs 3.4, 3.5, 3.6 and 3.11 do not support the partition of methyl formate with acetaldehyde into the group of 'cold' organics, contrasting dimethyl ether as a 'hot' species. Instead, acetaldehyde appears to have more in common with the morphology and lifetime of dimethyl ether. Yet, all three are formed in the COM torus at cool temperatures. A different organization of complex organic molecules by their lifetimes and times of peak abundance is attempted in Fig. 3.11. This would imply that species like formaldehyde, ketene, methanol, formic acid, methyl formate, acetic acid and glycolaldehyde are 'early' types; while acetaldehyde, dimethyl ether and ethanol are 'late' types. Fig. 3.11 indicates a chemical pattern that is consistent with the chemistry invoked in our model. Ketene, dimethyl ether and ethanol reach abundances $> 5 \times 10^{-8}$ only at 10^5 yr, while acetic acid abundances do not stay high outside of the $10^5 - 10^6$ yr range. This implies that simple ices, like methanol and ketene, are converted into more complex organic ices with the evolutionary stage of the source (Class 0 to Class I). Öberg et al., (2013) proposed that ketene, methanol and acetaldehyde belong to 'zeroth-generation' molecules, which is supported in this work for the former two species, but not for the latter (although the abundance of acetaldehyde peaks earlier than the maximization of the spatial extent of its enhancement).

3.4.4 *Episodic accretion and dynamics*

A potential caveat to the modelling presented thus far is episodic accretion. Visser and Bergin, (2012) and Visser et al., (2015) performed the first studies towards understanding the chemical implications of an accretion burst. The authors estimated that the effects should remain observable up to 10^4 yr after such an event and that there should be an excess of gaseous CO. A factor 10 increase in stellar luminosity (typical for a moderately strong burst) is expected to push the 100 K radius in the envelope out from $\sim$ 38 to $\sim$ 114 AU and the 20 K radius from $\sim$ 3300 to $\sim$ 10 000 AU for our setup (Visser and Bergin, 2012). Thus strong heating of the dust leading to thermal desorption of all species, in turn transferring the complexity from the solid phase into the gas, only occurs for the inner envelope and does not influence the large scales studied here. However, if episodic accretion is accompanied by sufficiently strong FUV irradiation (stronger than the typical interstellar UV field), which would photodissociate complex organic molecules, complexity may be reset for regions of the system. Alternatively, if FUV irradiation and/or dust heating are mild, then complexity may be enhanced, especially now that the 20 K radius lies much further out. The effects of episodic accretion must strongly depend on the exact physical properties of such an event, which is beyond the scope of this paper.

In addition, the static model used in this work neglects the dynamical effects of the system. On smaller scales, such as the inner $\sim$ 500 AU studied in Drozdovskaya et al., (2014), dynamics definitely play a crucial role due to the proximity to the growing protostar and the expanding protoplanetary disc, which is also where material moves through regions with high temperatures. However, on much larger scales of several thousand AU that are focused on in this work, a static model may be sufficient as the physical conditions have a shallower gradient with distance through the envelope. Furthermore, Jørgensen et al., (2002) and Kristensen et al., (2012) suggest that although Class 0 envelopes are infalling, by the Class I phase some envelopes are already showing expansion.

3.5 CONCLUSIONS

The envelopes encompassing young low-mass protostars are successively eroded by bipolar outflows, resulting in cavities that grow with time. These outflow cavities allow additional photons to penetrate the envelope, thus enhancing the heating of the dust and the irradiation of the material therein. Various observations (e.g., Arce et al. 2008; Öberg et al. 2011) have hinted that this results in unique morphological features and gas-phase detections of complex organic molecules. This paper describes a 2D physicochemical model of such an envelope-cavity system (excluding a traditional hot corino), including wavelength-dependent radiative transfer calculations and a comprehensive gas-grain chemical network. The main results of our modelling are:

1. An envelope-cavity system has three distinct regions. Firstly, the cavity wall layer, which displays time-dependent enhancements in solid and gaseous abundances of methanol, formic acid, acetaldehyde, dimethyl ether and ethanol. Secondly, closer to the star, a 'COM torus' – a zone rich in complex organic ices. Thirdly, the remaining outer envelope, which is predominantly comprised of simpler ices and gases, like water, methanol, formaldehyde and ketene.

2. Gases do not always reflect the ice composition – the COM torus is poor in gaseous complex organics, while having the highest solid abundances of the entire system. The division between the two phases depends on the relative efficiencies of non-thermal desorption mechanisms in different regions.

3. Complex organic ices peak in the COM torus at different times suggesting unique molecular lifetimes.

4. The gas-phase enhancements along cavity walls in select molecules are consistent with observations. In strongly irradiated regions ($A_V < 3$ mag), such as the cavity wall layer, photodissociation in the solid phase is frequent. Subsequent recombination of the photoproducts leads to frequent reactive desorption. Although the poorly constrained efficiency is assumed to be a mere 1 per cent, the high frequency of reactive desorption leads to gas-phase enhancements of several orders of magnitude. Direct photodesorption (using the laboratory constrained yield of 10^{-3} molecules per photon) is found to be inefficient in comparison, indicating the need for experimental quantification of the rates for reactive desorption.

5. Photodissociation directly in the solid phase produces radicals in the icy mantle, the absence of which impedes the formation of complex organic molecules. For efficiency, a sufficient number of FUV photons needs to penetrate the envelope and elevated cool dust temperatures enable radical mobility on the grain surface.

6. Consequently, a high stellar luminosity (~ 35 $L_\odot$) favours chemical complexity. A low stellar luminosity (~ 1 $L_\odot$) results in negligible complex organic abundances ($< 10^{-11}$).

7. Also, a sufficiently wide cavity (for example, $\alpha\,(z = 10\,000\text{AU}) = 45°$) is needed to directly irradiate the envelope.

This work has shown that low-mass protostars have gas-phase enhancements in complex organic molecules when outflow cavities are present, as well as hidden zones that

are rich in complex organic ices. Future research will explore the intriguing extrapolation of this to the high-mass case, especially in light of recent ALMA observations of methanol emission with an hourglass morphology towards IRAS16547-4247 (Higuchi et al., 2015).

3.6 ACKNOWLEDGEMENTS

This work is supported by a Huygens fellowship from Leiden University, by the European Union A-ERC grant 291141 CHEMPLAN, by the Netherlands Research School for Astronomy (NOVA) and by a Royal Netherlands Academy of Arts and Sciences (KNAW) professor prize. C.W. acknowledges support from the Netherlands Organisation for Scientific Research (NWO, program number 639.041.335).

3.7 APPENDIX

ADDITIONAL ABUNDANCE MAPS

In addition to the five sets of abundance maps shown in the main text of the paper, another five molecules are presented here for completeness.

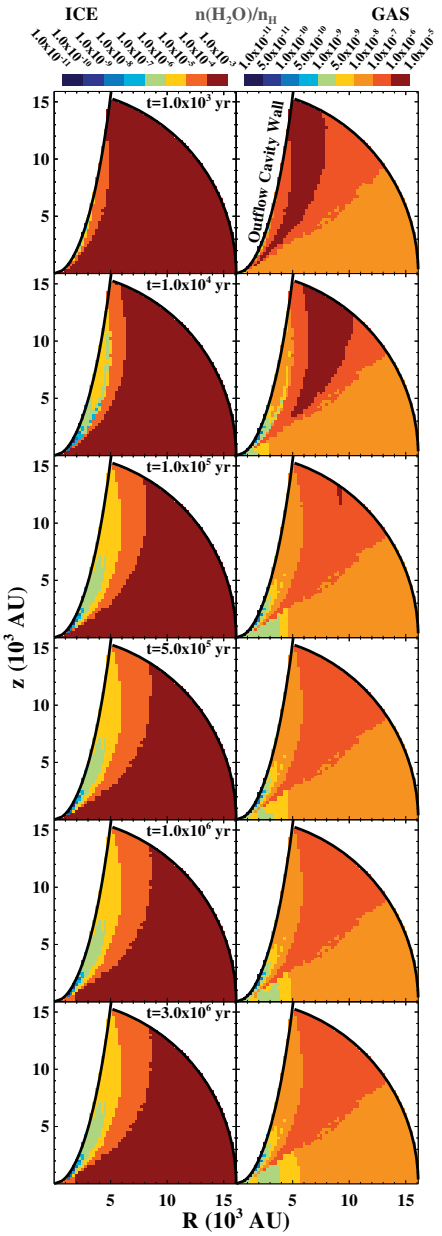

Figure 3.12: Same as Fig. 3.2, but for water.

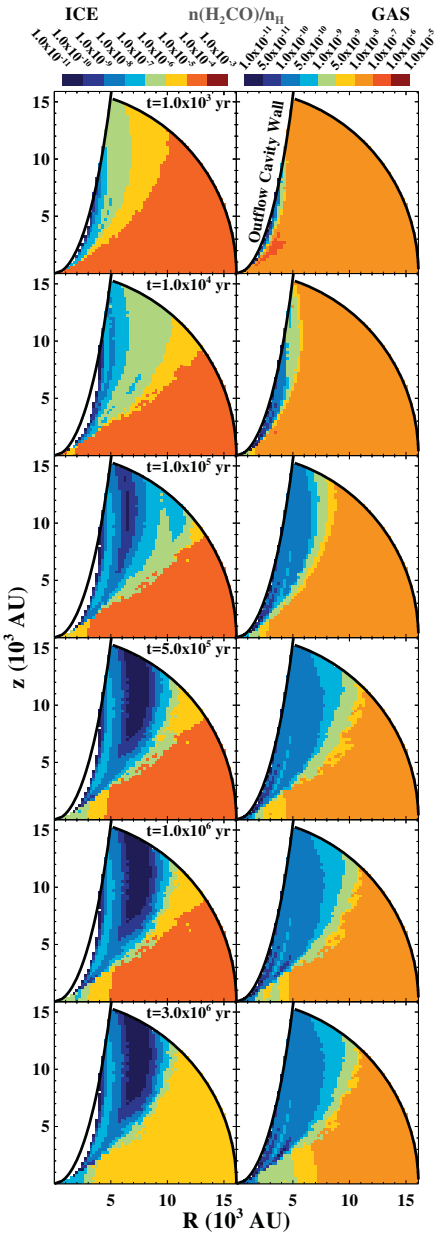

Figure 3.13: Same as Fig. 3.2, but for formaldehyde.

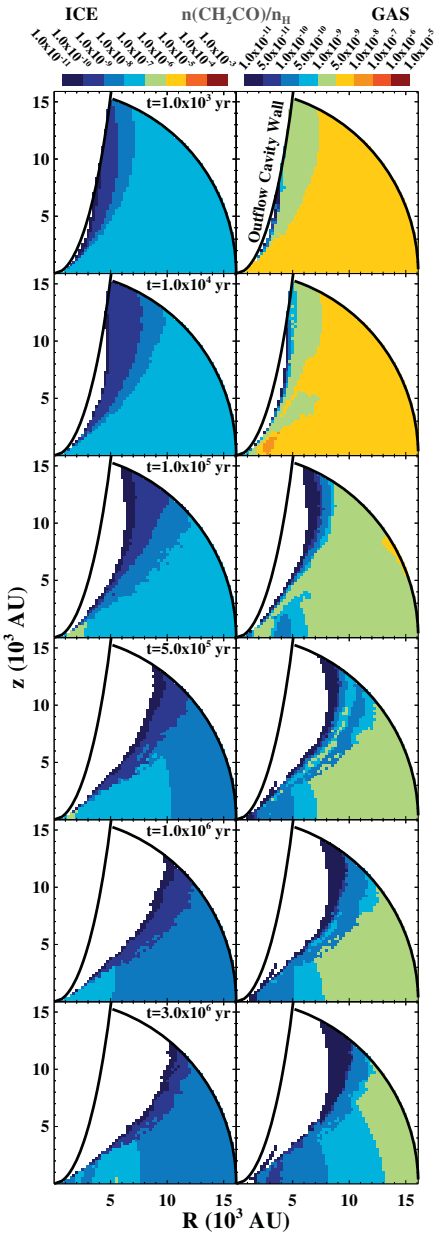

Figure 3.14: Same as Fig. 3.2, but for ketene.

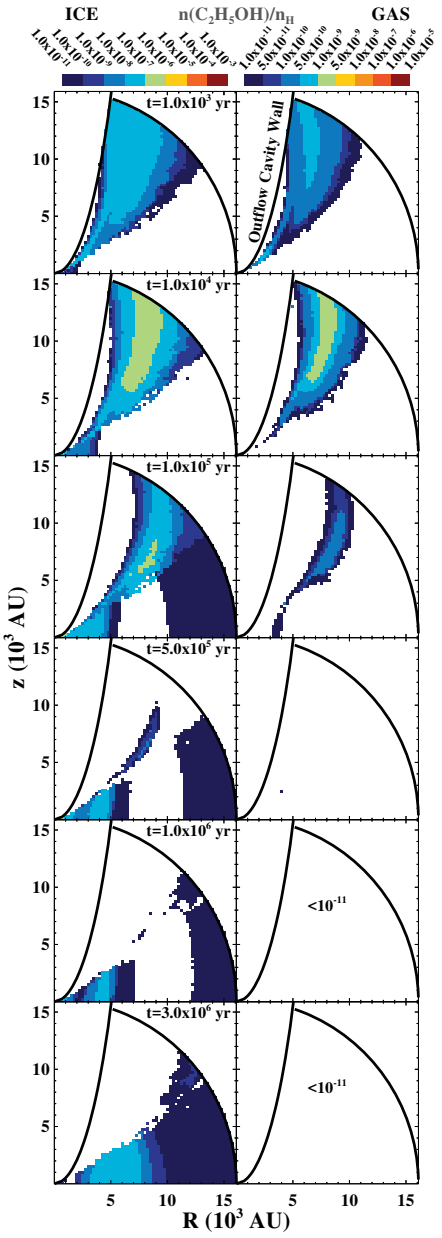

Figure 3.15: Same as Fig. 3.2, but for ethanol.

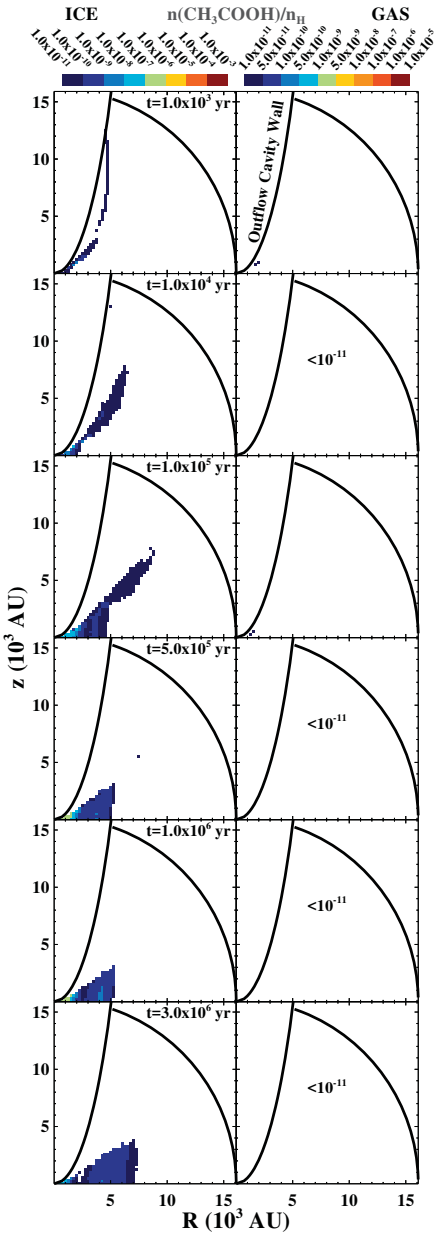

Figure 3.16: Same as Fig. 3.2, but for acetic acid.

DETAILS OF THE ROUTE TO GLYCOLALDEHYDE VIA GLYOXAL

The details of the added route to glycolaldehyde via glyoxal are described in this appendix. In this work, the route is only added for the solid phase (unlike in Woods et al. 2013), since three-body gas phase reactions require a radiative association mechanism, which is slow by nature. Associations of radicals are assumed to be barrierless, which includes the reaction between the two formyl radicals ($\dot{H}CO$) and the second hydrogenation. Hydrogenation of glyoxal (OCHCHO) has an adopted activation energy (E_A) of $\sim$ 1100 K, based on quantum chemical calculations of Woods et al., (2013).

The chemical network used is thereby expanded by 10 new species: gaseous and solid glyoxal, the cation of glyoxal ($OCHCHO^+$), the protonated glyoxal ($OCHCH_2O^+$), the gaseous and solid two intermediate species ($HO\dot{C}HCHO$, $\dot{O}CH_2CHO$), a joint cation ($C_2O_2H_3^+$), and a joint protonated form of the intermediates ($C_2O_2H_4^+$). The gas-phase chemistry of glyoxal is extracted from the OSU network (Garrod et al., 2008). The gas-phase chemistry of the two intermediate species is assumed to be similar to that of other large hydrogenated radicals and glyoxal itself, from which the gas-phase reaction rate coefficients are adopted. The dissociative reaction channels with He^+ and photodissociation channels are assumed to be 2HCO + H for $HO\dot{C}HCHO$ and H_2CO + HCO for $\dot{O}CH_2CHO$. Grain-surface chemistry of glyoxal and the two intermediates is not expanded further than the scheme provided above, with the exception of one competing reaction, namely:

$$OCHCHO_{ice} \xrightarrow{H} H_2CO_{ice} + HCO_{ice},$$

which is included in the OSU network (again $E_A = 1108$ K). The binding energy of glyoxal is taken to be 3200 K (OSU network, Garrod et al. 2008) and for the two intermediates calculated according to the prescription in Garrod et al., (2008) to be $E_{des}(HO\dot{C}HCHO_{ice}) = 6080$ K and $E_{des}(\dot{O}CH_2CHO) = 3800$ K (which accounts for the former molecule being able to H-bond due to the presence of an OH functional group).

SUPPORTING PARAMETER STUDY FIGURES

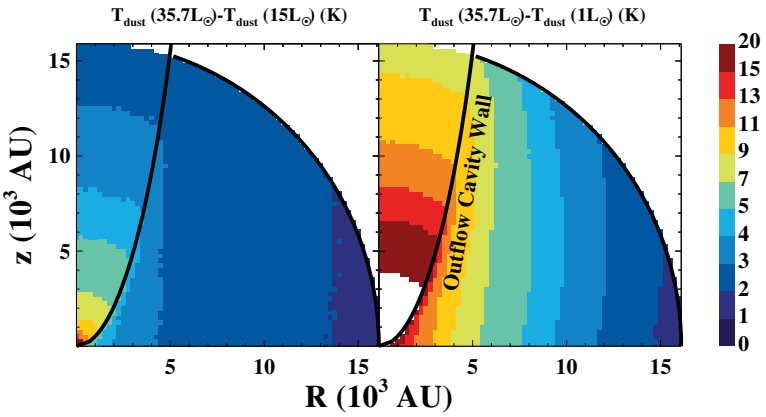

Figure 3.17: The difference in the dust temperature between the fiducial, 35.7 $L_\odot$ model, and the two with smaller luminosities (15 $L_\odot$ and 1 $L_\odot$). The outflow cavity wall is shown with a black curve.

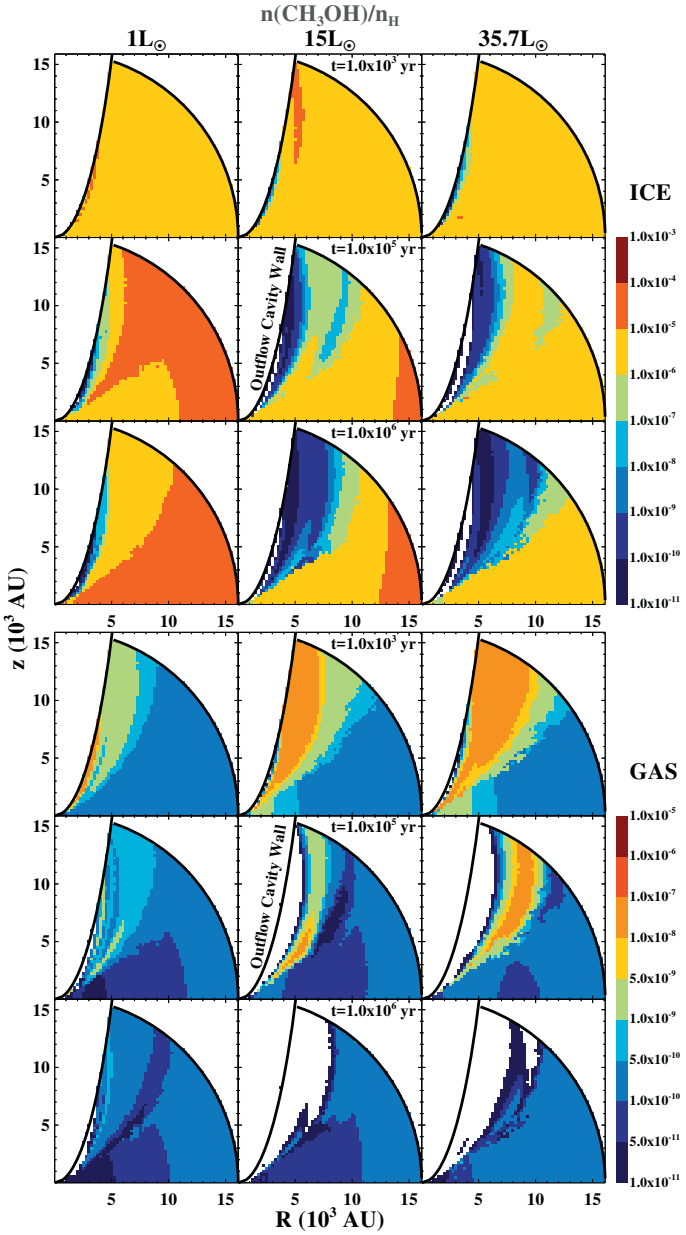

Figure 3.18: The abundance of methanol in the solid (upper nine figures) and gas (lower nine figures) phases at three different time steps across the envelope-cavity system. The left, middle and right columns correspond to the cases of 1 $L_{\odot}$, 15 $L_{\odot}$ and 35.7 $L_{\odot}$ (the fiducial model), respectively. The outflow cavity wall is shown with a black curve. White cells correspond to either being outside of the area being considered or to having values outside of the range of the colour bar.

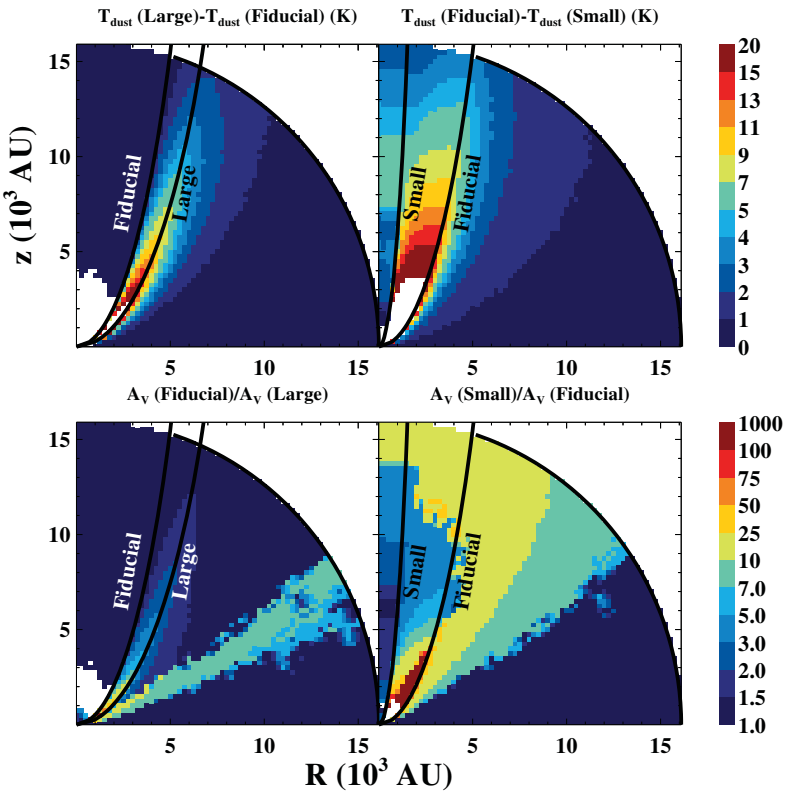

Figure 3.19: The difference in the dust temperature between the fiducial model and the two additional models, one with a larger cavity (upper left panel) and another with a smaller cavity (upper right panel), as well as the ratios in extinction (lower left and right panels, respectively). The different outflow cavity walls are shown and labeled.

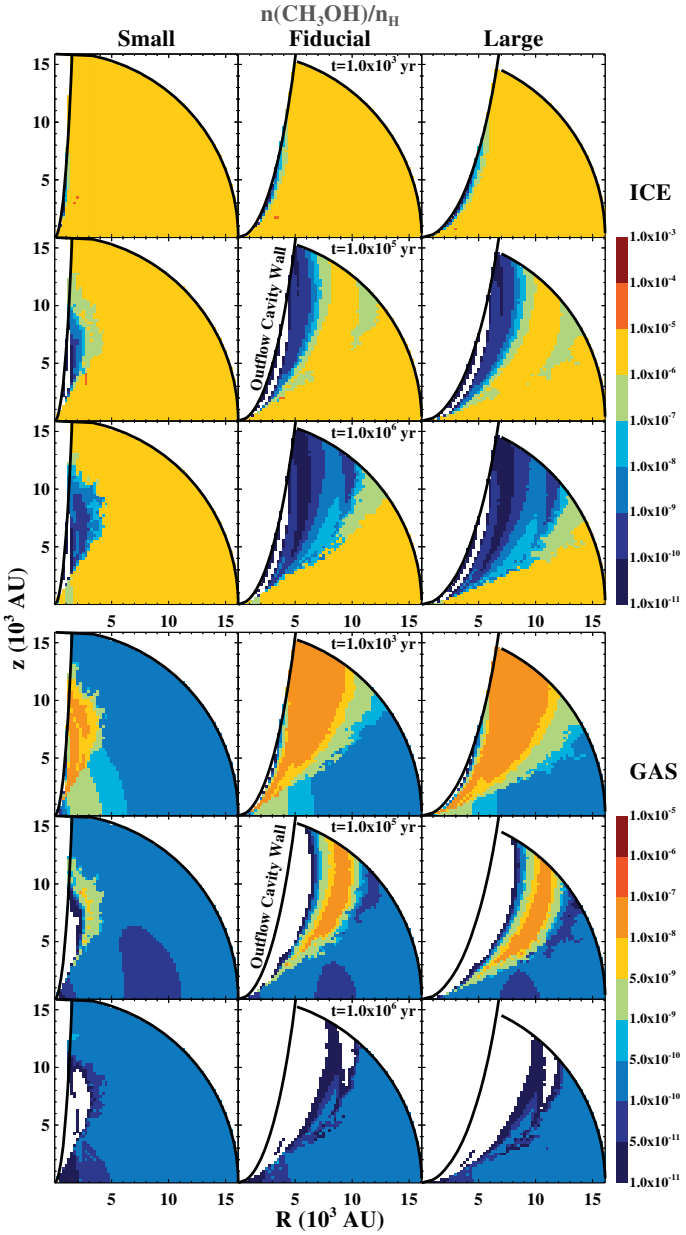

Figure 3.20: The abundance of methanol in the solid (upper nine figures) and gas (lower nine figures) phases at three different time steps across the envelope-cavity system. The left, middle and right columns correspond to the cases of a small, fiducial and large cavities, respectively. The outflow cavity wall is shown with a black curve. White cells correspond to either being outside of the area being considered or to having values outside of the range of the colour bar.

4

COMETARY ICES IN FORMING PROTOPLANETARY DISC MIDPLANES

Maria N. Drozdovskaya, Catherine Walsh, Ewine F. van Dishoeck, Kenji Furuya, Ulysse Marboeuf, Amaury Thiabaud, Daniel Harsono, and Ruud Visser
MNRAS, 2016a, 462, 977

ABSTRACT

Low-mass protostars are the extrasolar analogues of the natal Solar System. Sophisticated physicochemical models are used to simulate the formation of two protoplanetary discs from the initial prestellar phase, one dominated by viscous spreading and the other by pure infall. The results show that the volatile prestellar fingerprint is modified by the chemistry en route into the disc. This holds relatively independent of initial abundances and chemical parameters: physical conditions are more important. The amount of CO_2 increases via the grain-surface reaction of OH with CO, which is enhanced by photodissociation of H_2O ice. Complex organic molecules are produced during transport through the envelope at the expense of CH_3OH ice. Their abundances can be comparable to that of methanol ice (few % of water ice) at large disc radii ($R > 30$ AU). Current Class II disc models may be underestimating the complex organic content. Planet population synthesis models may underestimate the amount of CO_2 and overestimate CH_3OH ices in planetesimals by disregarding chemical processing between the cloud and disc phases. The overall C/O and C/N ratios differ between the gas and solid phases. The two ice ratios show little variation beyond the inner 10 AU and both are nearly solar in the case of pure infall, but both are sub-solar when viscous spreading dominates. Chemistry in the protostellar envelope en route to the protoplanetary disc sets the initial volatile and prebiotically-significant content of icy planetesimals and cometary bodies. Comets are thus potentially reflecting the provenances of the midplane ices in the Solar Nebula.

4.1 INTRODUCTION

Protoplanetary discs encircling young protostars are the birth locations of future mature planetary systems (see Johansen et al. 2014 for a review). Past observations have suggested that dust growth from micron sizes may begin as early as the prestellar core stage and dust grains may reach millimetre dimensions during infall in the envelopes of protostars (Jones et al. 2016; Miotello et al. 2014; Pagani et al. 2010; Ysard et al. 2016, see Testi et al. 2014 for a review). Recent ALMA data have shown strongly defined ring structures in the disc around the Class I–II protostar HL Tau, which is thought to be younger than $\leqslant 1-2$ Myr and still embedded in a large envelope (ALMA Partnership et al., 2015). Models have suggested that these rings may be caused by several planets of at least 0.2 M_J in mass clearing gaps in the dust distribution (Dipierro et al., 2015; Dong et al., 2015; Pinte et al., 2016). An alternative hypothesis is that the contrast reflects enhanced dust growth to centimeter sizes behind various snowlines, leading to a change in opacity in the emitting dust (Zhang et al., 2015). This is potentially aided by sintering close to

the snowlines of the volatiles (Okuzumi et al., 2016). These findings are pushing the onset of planetesimal formation much earlier along the star-disc evolutionary sequence than previously thought, perhaps even as early as the embedded phase.

At the same time, the exoplanet community has demonstrated the diverse outcomes of planet formation (see, e.g., www.exoplanet.eu, Schneider et al. 2011). Planet population synthesis modellers have carried out pioneering work in linking protoplanetary disc theory with the final architecture of planetary systems. Such models take the key physical processes across all these evolutionary stages into account, and with large sets of initial conditions, to make statistical predictions on the exoplanet population (see Benz et al. 2014 for a review). It has been postulated that planetary atmospheres form initially via pebble accretion and heating from this assembly prior to runaway gas accretion (Bitsch et al., 2015; Inaba and Ikoma, 2003; Ormel and Klahr, 2010). Based on the newest results from the star formation community, it may be necessary to use the initial conditions from the earlier embedded phase rather than the classical T Tauri (Class II) stage.

Typically, the constituents of planetesimals that feed protoplanets are grouped into volatiles (H, O, C, N and S containing molecules) and refractories/rocks (minerals/inorganic refractories and complex organic refractory components such as PAHs and macromolecular complex organic matter). For regions of a protoplanetary disc where most volatiles are frozen out as solids, an ice/rock mass ratio of $\sim 2-4$ is suggested (Pontoppidan et al., 2014). Various instruments aboard the *Rosetta* mission are attempting to constrain the the icy and dusty contents of comet 67P/Churyumov-Gerasimenko to an unprecedented precision. The RSI experiment indicates a ice/dust mass of ratio of ~ 4 based on the gravity field of the comet (Pätzold et al., 2016). CONSERT measurements of an ice/dust volumetric ratio of $\sim 0.4-2.5$ (Kofman et al., 2015) imply a ice/dust mass ratio of $\sim 0.1-0.9$, assuming an average dust density of 2 600 kg m^{-3} and an ice density of 940 kg m^{-3} as in Pätzold et al., (2016). These ratios mean that the solid-phase chemical composition is a pivotal parameter for the subsequent protoplanet makeup. The density is highest in the midplane of a protoplanetary disc, thus harbouring the bulk of the mass and implying that predominantly the ices in that region will likely shape the chemical composition of the atmospheres of the exoplanets that are observed today.

The chemical composition of discs in the embedded phase has been probed by models of Visser et al., (2009a), Visser et al., (2011), Drozdovskaya et al., (2014), Harsono et al., (2015). Observational evidence for them is scarce, because high spatial resolution ($\lesssim$ 30 AU) is necessary to get spatial information for a small ($\sim$ 100 AU) target,whose emission is easily overwhelmed by that of the more massive envelope, making it hard to constrain their physical parameters. Only recently, observations have shown embedded Keplerian discs of $\sim 50-300$ AU in radius in embedded protostars (Brinch and Jørgensen, 2013; Chou et al., 2014; Harsono et al., 2014; Murillo et al., 2013; Sakai et al., 2014; Tobin et al., 2012, 2013, 2015). Instead, significant modelling effort has focused on discs in the Class II/III stages of star formation (see, e.g., Henning and Semenov, (2013) and table 1 in Woitke et al. 2016 and the references therein). The chemistry in such Class II discs has been modelled by means of gas-grain models with grain-surface reactions, e.g., Akimkin et al., (2013), Henning et al., (2010), Hersant et al., (2009), Semenov et al., (2006, 2010), Vasyunin et al., (2011), Walsh et al., (2010, 2012), and Willacy et al., (2006). Only recently complex organics (loosely defined in both chemistry and astronomy as large, $\geqslant 6$ atoms, carbon-containing species, Herbst and van Dishoeck 2009) have also been considered by Semenov and Wiebe, (2011), Furuya and Aikawa, (2014), Walsh et al., (2014b), Walsh et al., (2014a), see also Henning and Semenov, (2013) for a review. Meanwhile, such

molecules have been frequently observed towards protostars and in Solar System bodies (Herbst and van Dishoeck, 2009).

The aim of this work is to compute the chemical composition of planetesimals and cometary materials in the midplanes of protoplanetary discs in the embedded phase of star formation. This is done using state-of-the-art physicochemical models that are dynamic in nature and include chemical kinetics, building upon the work in Drozdovskaya et al., (2014), which studied the discs as a whole. Main volatiles that are expected to dominate the icy component of plantesimals in the midplanes of protoplanetary discs are considered first. Trace complex organic species are also analysed in this work, since they are potentially the earliest precursors to prebiotic molecules. The dynamic nature of the model allows the study of the chemical effects stemming from the transport from the prestellar cloud through the envelope and into the disc. The key model features are highlighted in Section 4.2. The results are shown in Section 4.3 and are discussed in Section 4.4, including all the derived implications for the population synthesis models and the Solar System community. The conclusions are presented in Section 4.5.

4.2 MODELS

Models simulating the formation of protostars typically start from the so-called prestellar core/cloud phase, which undergoes spherical collapse. Cloud rotation leads to the formation of a protoplanetary disc and associated bipolar outflows due to the conservation of angular momentum. This work and the preceding publication by Drozdovskaya et al., (2014) use the axisymmetric, 2D semi-analytic physical model developed by Visser et al., (2009a) (and Harsono et al. 2013; Visser and Dullemond 2010; Visser et al. 2011), which describes the density and velocity of the collapsing material. Wavelength-dependent radiative transfer calculations are performed with RADMC-3D[2] to compute the dust temperature and far-ultraviolet radiation field (FUV; $912 - 2066$ Å; $6.0 - 13.6$ eV). Thereafter, the physical parameters are coupled with a large chemical network in the framework of a two-phase (gas and solid) model solved using the rate-equation method, including grain-surface chemistry and the chemistry of several families of complex organic molecules (Garrod and Herbst, 2006; McElroy et al., 2013; Walsh et al., 2014a,b, 2015). Initial atomic abundances are evolved under constant prestellar cloud conditions ($n_H = 4 \times 10^4$ cm^{-3}, $T_{dust} = 10$ K and cosmic ray-interaction with H_2 as the only source of FUV photons; assuming a cosmic ray ionisation rate $\zeta_0 = 5 \times 10^{-17}$ s^{-1}) for 3×10^5 yr (table 2 of Drozdovskaya et al. 2014) to obtain initial molecular abundances at the onset of collapse (Table 4.1). Chemical abundances are computed along evolutionary infall trajectories that are obtained from the physical model with path-dependent physical conditions. The collapse of the system takes an additional 2.46×10^5 yr, which corresponds to the time it takes for the envelope to accrete on to the star-disc system for the initial physical conditions chosen for this work.

In this paper, as in Drozdovskaya et al., (2014), two discs are studied. One is the so-called spread-dominated case, with a lower initial cloud rotation rate, in which the disc primarily grows via viscous spreading and has a final outer radius of ~ 50 AU. The second is the infall-dominated case, in which the disc is assembled predominantly via pure infall of material and has a final outer radius of ~ 300 AU (table 1 of Drozdovskaya et al. 2014). The reason for studying both discs is that their unique large-scale dynamics result in different dust temperature and FUV flux profiles along the trajectories, i.e., they

2 http://www.ita.uni-heidelberg.de/~dullemond/software/radmc-3d/

Table 4.1: Molecular abundances at the end of the prestellar phase[a] and their binding energies[b].

Species	Name	$n(X_{gas})/n_H$	$n(X_{ice})/n_H$	$\frac{n(X_{ice})}{n(H_2O_{ice})}$	$E_{des}(X)$ (K)
H_2O	water	7.7×10^{-8}	1.9×10^{-4}	1.0×10^{0}	5773[c]
CO	carbon monoxide	1.4×10^{-5}	5.9×10^{-5}	3.1×10^{-1}	1150[d]
CO_2	carbon dioxide	7.9×10^{-8}	1.9×10^{-5}	1.0×10^{-1}	2990[e]
NH_3	ammonia	2.1×10^{-7}	4.8×10^{-6}	2.5×10^{-2}	5534[d]
CH_4	methane	1.2×10^{-7}	1.5×10^{-5}	7.9×10^{-2}	1090[f]
CH_3OH	methanol	2.0×10^{-10}	3.7×10^{-6}	1.9×10^{-2}	4930[g]
H_2S	hydrogen sulfide	5.3×10^{-10}	8.1×10^{-9}	4.3×10^{-5}	2743[d]
N_2	nitrogen	1.3×10^{-5}	1.1×10^{-5}	5.8×10^{-2}	790[h]
H_2CO	formaldehyde	9.7×10^{-9}	2.3×10^{-6}	1.2×10^{-2}	2050[i]
CH_2CO	ketene	4.6×10^{-10}	8.0×10^{-8}	4.2×10^{-4}	2200[i]
HCOOH	formic acid	2.4×10^{-11}	4.9×10^{-11}	2.6×10^{-7}	5000[j]
$HCOOCH_3$	methyl formate	1.1×10^{-10}	6.4×10^{-14}	3.4×10^{-10}	4000[j]
CH_3CHO	acetaldehyde	1.0×10^{-9}	1.5×10^{-6}	7.9×10^{-3}	3800[j]
CH_3OCH_3	dimethyl ether	2.4×10^{-11}	9.2×10^{-8}	4.8×10^{-4}	3300[j]
C_2H_5OH	ethanol	2.2×10^{-11}	4.7×10^{-8}	2.5×10^{-4}	5200[j]
CH_3COOH	acetic acid	2.2×10^{-17}	9.7×10^{-14}	5.1×10^{-10}	6300[j]
$HOCH_2CHO$	glycolaldehyde	2.2×10^{-12}	5.3×10^{-9}	2.8×10^{-5}	6680[k]

[a] The constant physical conditions of the prestellar phase are: $n_H = 4 \times 10^4$ cm^{-3}, $T_{dust} = 10$ K and only cosmic ray-induced FUV photons, $\zeta = 5 \times 10^{-17}$ s^{-1}. The duration is taken to be 3×10^5 yr.

[b] The differences between this table and table 2 of Drozdovskaya et al. 2015 are due to this work including the glycolaldehyde formation via glyoxal, reaction-diffusion competition, a coverage factor for dust grains (limiting the number of reactive layers) and a higher barrier thickness between grain surface sites.

[c] Fraser et al., (2001) - measurement for pure water ice in the thin films ($\ll 50$ monolayers) regime (within errors of measurements of Collings et al., (2015) for pure water ice in the multilayer regime)

[d] Collings et al., (2004) and Garrod and Herbst, (2006) - measurement for CO on H_2O ice (to account for the deep trapping in the inner layers seen with multilayer models of (Taquet et al., 2012) and for the trapping in pores of amorphous water ice seen in the experiments of Collings et al., (2003a)); and measurements for NH_3 and H_2S on H_2O ice

[e] Edridge, (2010) - measured average for pure carbon dioxide ice in the multilayer regime

[f] Herrero et al., (2010) - measurement for CH_4 on H_2O ice (to account for the diffusion of methane molecules into the micropores of amorphous solid water (ASW) seen in these experiments)

[g] Brown and Bolina, (2007) - measurement for pure methanol ice in the multilayer regime

[h] Öberg et al., (2005) - measurement for pure N_2 ice in the multilayer regime (within errors of measurements of Bisschop et al., (2006), Collings et al., (2015), and Fayolle et al., (2016) for $^{15}N_2$, for pure ices in the multilayer regime)

[i] Garrod and Herbst, (2006)

[j] Öberg et al., (2009a) - measurements for pure ices in the multilayer regime

[k] Garrod, (2013)

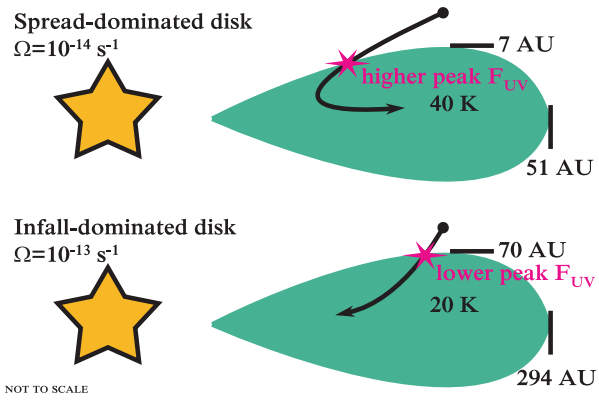

Figure 4.1: An illustration of the key parameters (such as the midplane dust temperature, outer radius and predominant parcel motion) of the two discs that are central to this work and Drozdovskaya et al., (2014).

have different physical histories for the protoplanetary disc material (this is pictorially illustrated in Fig. 4.1). At ~ 40 K, the smaller spread-dominated disc is warmer than the more massive infall-dominated disc, which is ~ 20 K close to the midplane (middle panels of figs. 4 and 5 of Drozdovskaya et al. 2014). A larger disc mass hinders passive heating by reprocessed stellar radiation. These models exclude viscous heating and its effects, such as those discussed in (Harsono et al., 2015); however, this is most important only very close to the star. These models do not consider magnetic field effects and dust growth, as discussed in, e.g., (Zhao et al., 2016) and (Pauly and Garrod, 2016).

Once collapse is initiated, the central protostar is the dominant source of FUV photons. Its luminosity, which varies with time and peaks at ~ 11 $L_\odot$ for the spread-dominated case (fig. 2 of Drozdovskaya et al. 2014), is given by the sum of the accretion luminosity (Adams and Shu, 1986) and the photospheric luminosity (due to gravitational contraction and deuterium burning; D'Antona and Mazzitelli 1994; Visser et al. 2009a). Excess UV observed for classical T Tauri stars (effective temperatures of ~ 10 000 K) as a result of boundary layer accretion from the disk onto the star (Bertout et al., 1988) is not accounted for in this work. External sources of FUV are excluded, since such young objects are expected to be deeply embedded in molecular clouds and hence highly shielded. The maximal FUV flux experienced by a parcel is set by the $1/r^2$ dependence of the flux and the corresponding decrease in the attenuating column as the parcel moves closer to the star. Once the parcel enters the disk, the attenuating column increases substantially, leading to an almost instantaneous reduction in FUV flux. The material entering the spread-dominated disc experiences higher peak FUV irradiation, because many of the parcels pass closer to the protostar prior to disc entry than in the infall-dominated case. The smaller disc also exerts less attenuation of cosmic rays, thus there are less internally produced cosmic ray-induced FUV photons in the infall-dominated disc. Both, the dust temperature and FUV flux, are crucial parameters for chemical grain-surface reactions controlling the mobility and availability of radicals.

All further details on the physical and chemical model and the radiative transfer setup can be found in Drozdovskaya et al., (2014, 2015). In this work, a different set of parcels is considered - more than 100 for each disc, all with final positions at $z = 0.01$ AU and

R in the $\sim 1-50$ AU range for the spread-dominated disc ($\sim 1-300$ AU range for the infall-dominated disc) to better sample the two midplanes. For the spread-dominated case at $R = 5.2$ AU, $\sim$ 90 per cent of the mass lies below 1 AU in height, while the disc surface extends up to $\sim$ 2 AU. This work includes the experimentally suggested glycolaldehyde formation via glyoxal (Fedoseev et al. 2015, as described in section 3.4.3 of Drozdovskaya et al. 2015). Furthermore, diffusion-reaction competition is now accounted for via the formulation of Garrod and Pauly, (2011) (equation 6). This enhances the probability of reactions with activation barriers (E_A) when thermal diffusion rates are low. A larger 1.5 Å barrier thickness (a) between grain surface sites is assumed to decrease the efficiency of quantum tunnelling reactions involving atomic and molecular hydrogen. The effects of varying the barrier to quantum tunneling are investigated in Section 4.3.2.1. Furthermore, a 'coverage factor' of 2 ice monolayers has been imposed. This parameter implies that grain-surface associations can occur only in the two upper most monolayers. However, in a two-phase model the surface is not distinguished from the bulk in terms of composition; therefore, the composition of these two chemically active layers is averaged together with that of the non-chemically active bulk. Finally, since gas column densities at positions along the midplane mostly exceed 100 g cm^{-2}, cosmic ray attenuation is now accounted for according to

$$\zeta = \zeta_0 \exp\left(\frac{-\Sigma_{(R,z)}}{96 \text{ g cm}^{-2}}\right), \tag{4.1}$$

where $\Sigma_{(R,z)}$ is the column density between the position of interest (R, z) and the disc surface at that time ($\Sigma_{(R,z)} = \mu m_u \int_z^{\text{surface}} n_{\text{gas}} dz$, where $\mu = 2.3$ is the mean molecular mass of the gas, m_u is the atomic mass unit, n_{gas} is the gas particle number density; fully molecular gas is assumed for simplicity, i.e., $n_{\text{gas}} = n_{H_2}$ and $n_H = 2n_{H_2}$). A lower limit of 7.3×10^{-19} s^{-1} is imposed, which stems from ^{26}Al radionuclide decay (Cleeves et al., 2013; Umebayashi and Nakano, 1981).

4.2.1 *Initial conditions: 'hot' disc start versus 'cold' cloud start scenarios*

The typical initial assumption of the solar system community and population synthesis models is that the initial conditions of the Solar Nebula are hot, i.e., all disc material (whether volatile or refractory) is in the gas phase. The disc is thought to be small, dense and hot (heated by viscous dissipation, initially), and subsequently to expand in radius and cool. Typically, to bypass this evolution, the initial temperature is simply assumed high ($\gg$ 300 K) out to at least 30 AU. For planet population synthesis statistics, disc models provide radial pressure, temperature and surface density profiles (Alibert et al., 2005, 2013; Marboeuf et al., 2014a,b; Thiabaud et al., 2014, 2015). Individual volatiles are then allowed to condense instantaneously at their respective temperature-pressure of condensation (and also be trapped in clathrates, so-called water cages that form from crystalline water ice, the importance of which is still under debate, e.g., Lunine and Stevenson 1985; Mousis et al. 2012; Thürmer et al. 2015), assuming thermodynamic equilibrium. This forms the ice and rock components of small grains as a function of disc radius (R). It is assumed that the composition of 300 m planetesimals at a certain R in the disc is identical to that of the small grain composition. The population synthesis model then describes how 10 planetary Lunar-sized embryos (of the same composition as the planetesimals at a certain R) grow through planetesimal accretion during migration, while the disc evolves and disperses by photoevaporation. By running a very large

number of disc models with varying initial conditions, general trends in planet populations are studied (Marboeuf et al., 2014a,b; Thiabaud et al., 2014). No chemistry occurs in these models; variations in the ice composition are set by the locations of snowlines (condensation fronts) at the start ($t = 0$). In contrast, the chemical models of the star formation community include a kinetic chemical network and many, if not all, of the possible chemical processes at play.

The initially hot Solar Nebula ('hot' disc start scenario) versus the cold prestellar phase and warm protoplanetary disc ('cold' cloud start scenario) is one of the major differences between the approaches of the Solar System and star plus disc formation communities. Under the 'cold' start scenario, a large icy reservoir is initially in place, which is not necessarily mimicked by the gas. Meanwhile, for the 'hot' start, only gases are available at the start. It remains unclear if potentially both scenarios are valid in different regions of the disc (see the review of Davis et al. 2014). Calcium-aluminium-rich inclusions (CAIs) are typically presented as evidence for the 'hot' scenario, since their production occurs at temperatures > 1300 K. CAIs are found in meteorites, which mostly originate from the asteroids in the inner Solar System, but have also been detected in comet 81P/Wild 2 with the Stardust mission (Brownlee et al., 2006). High temperature-processing is also suggested by the presence of crystalline silicates in protoplanetary discs and comets, which can only form by annealing at temperatures of $800 - 1000$ K or via condensation upon cooling below $\sim 1200 - 1500$ K. However, all observations of prestellar and protostellar sources point towards the 'cold' and 'warm' set of conditions. Localized temperature enhancement could occur via accretion shocks at the disc surface or via episodic accretion with subsequent spreading of crystalline silicates by radial or vertical large-range mixing throughout the protoplanetary disc (e.g., Ciesla 2011; Visser and Dullemond 2010). It is still debated whether either of these processes can reach high enough temperatures, but if so, strongly heated materials would be available at the largest disc radii for incorporation into distant larger bodies.

The models of Marboeuf et al., (2014a,b) and Thiabaud et al., (2014, 2015) impose initial gas-phase abundances based on observations of prestellar cores and protostellar sources, assuming complete inheritance without modification of the prestellar icy composition by discs upon formation. In other words, they are a hybrid of the two scenarios just discussed. This is visually summarized in Fig. 4.2. This work tests the simplified approach of phase diagrams under the assumption of complete prestellar inheritance to obtain the volatile composition of discs by comparing with the output obtained from a full kinetic chemical model, which also takes dynamic collapse into account. The focus lies on the disk beyond the inner few AU.

4.3 RESULTS

In Fig. 4.3, the midplane conditions for both the spread- and infall-dominated discs are shown (disc slice at $z \approx 0.01$ AU). These are the physical conditions that the parcels reach at the final timestep of the evolution, depending on their final radial coordinate.

The inner few AU of each midplane, close to the protostar, has the highest final dust temperature ($T_{dust} > 200$ K) and density ($n_H > 10^{14}$ cm^{-3}). The smaller spread-dominated disc tends to be warmer (~ 40 K for $R > 25$ AU) than the more massive infall-dominated disc (~ 20 K for $R > 30$ AU) due to more efficient passive heating. For $R \gtrsim 25$ AU, the density, surface density ($\Sigma = 2\mu m_u \int_{0.01\ \mathrm{AU}}^{\mathrm{surface}} n_{gas}\, dz$, where the initial factor of 2 accounts for the full vertical extent of the disc) and pressure ($P = k_B n_{gas} T_{gas}$,

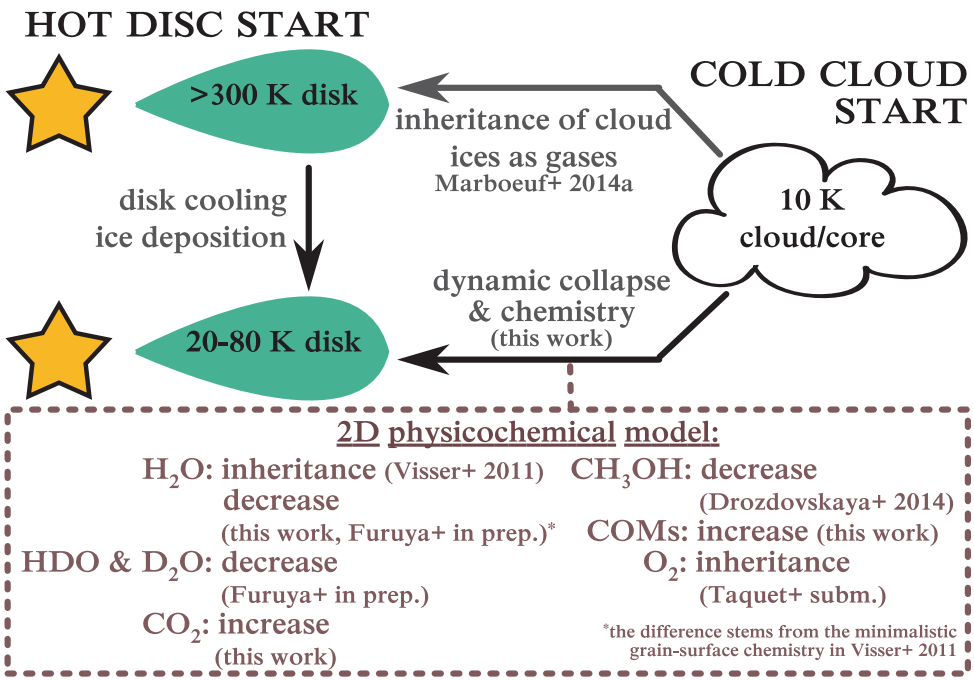

Figure 4.2: An illustration of the 'hot' and 'cold' start perspectives. The results obtained with this physical model in various publications, including this work, are also summarized.

where k_B is the Boltzmann constant and assuming $T_{gas} = T_{dust}$) of the midplane of the infall-dominated disc are higher than that of the spread-dominated disc. The surface density typically exceeds 100 g cm^{-2} (except for R $>$ 40 AU for the spread-dominated case) justifying the need for cosmic ray attenuation. The midplane pressure of each disc never exceeds 0.5 millibar (beyond 5 AU: P $< 10^{-7}$ bar).

4.3.1 *Dominant simple ices*

The left panels of Figs. 4.4a and 4.4b show the radial distribution of simple ices and gases in the inner 50 AU in an embedded disc for the spread-dominated and infall-dominated cases, respectively, at the final timestep of the evolution (2.46×10^5 yr since the onset of collapse). A number of snowlines/icelines are seen in both discs, e.g., a steep ice-to-gas transition for water (H_2O) and a more gradual transition for methane (CH_4). The sharpness of the transitions is set by the temperature gradient along the midplane of each disc, which is steeper closer to the protostar (Fig. 4.3). The order of the snowlines is set by the binding energies used in the chemical network (right column of Table 4.1). For both discs, the water snowline lies around $\sim$ 3 AU. The small spread-dominated disc lacks CH_4 and nitrogen (N_2) ices, and is low on carbon monoxide (CO) ice; while the infall-dominated disc is rich in all simple ices for R $\gtrsim$ 25 AU due to its overall lower temperature. Table 4.2 tabulates all the snowlines in both discs.

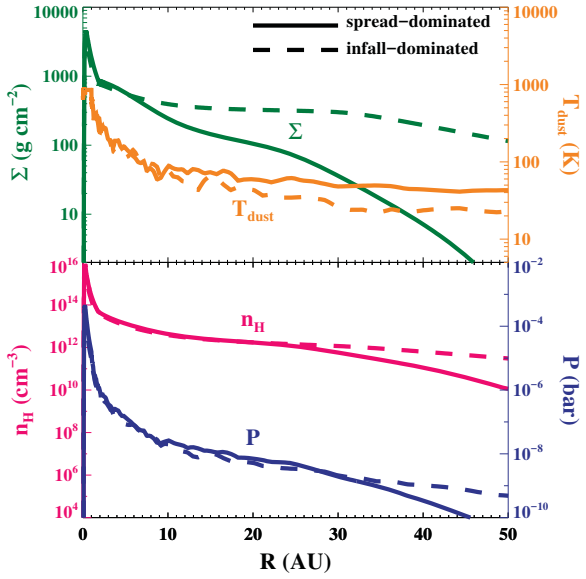

Figure 4.3: The midplane ($z \approx 0.01$ AU) physical conditions of the spread-(solid lines) and infall-dominated (dashed lines) discs at the end of the simulation (2.46×10^5 yr after the precollapse phase): dust temperature (T_{dust}), H nuclei number density (n_H), surface density (Σ) and pressure (P) as a function of disc radius (R). The infall-dominated disc extends out to 300 AU, only the inner 50 AU is shown.

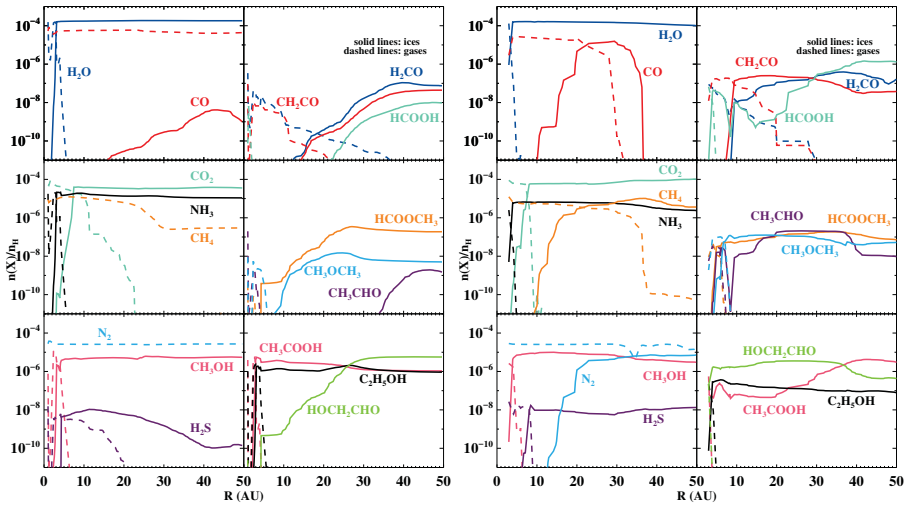

(a) Spread-dominated disc (b) Infall-dominated disc

Figure 4.4: The midplane abundances of volatiles (left column of each subfigure) and complex organics (right column of each subfigure) relative to the number of H nuclei (n_H) as a function of disc radius (R) in the gaseous (dashed lines) and solid (solid lines) phases at the end of the simulation (2.46×10^5 yr after the onset of collapse). Ice abundances beyond the respective snowlines (Table 4.2) are tabulated in Appendix 4.7.

Table 4.2: Snowlines[l] in the midplanes of the spread-dominated and infall-dominated discs at the end of the simulation (2.46×10^5 yr after the onset of collapse).

Species	R_{snow} (AU)	
	spread-dom.	infall-dom.
H_2O	3	3
CO	> 50	21
CO_2	7	7
NH_3	3	3
CH_4	> 50	23
CH_3OH	4	3
H_2S	7	8
N_2	> 50	36
H_2CO	20	11
CH_2CO	9	8
HCOOH	4	3
$HCOOCH_3$	5	4
CH_3CHO	7	5
CH_3OCH_3	7	6
C_2H_5OH	3	3
CH_3COOH	3	3
$HOCH_2CHO$	3	3

[l] Defined as the point when $n(X_{ice})/n(X_{gas}) = 0.5$ and rounded to the nearest AU. Note that these do not always correspond to a snowline in the traditional sense, for example, see the curve of HCOOH in the spread-dominated disc in Fig. 4.4a, which is set by chemistry.

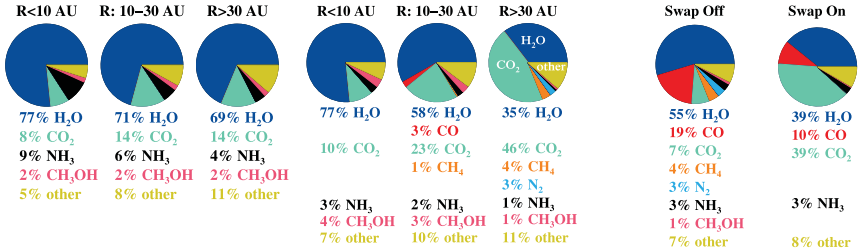

(a) Spread-dominated disc

(b) Infall-dominated disc

(c) Infall-dominated disc beyond 30 AU, as obtained with the three-phase chemical model of Furuya et al., (2015), for bulk and surface combined with and without the swapping mechanism

Figure 4.5: The percentage contribution of volatiles to the total ice content averaged over various radial ranges of the disc midplanes at the end of the simulation (2.46×10^5 yr after the precollapse phase). Only contributions of at least $\sim 1\%$ are shown. The 'other' category includes all ices that are not the following eight volatiles: H_2O, CO, CO_2, CH_3OH, CH_4, N_2, NH_3 and H_2S.

Figs. 4.5a and 4.5b show pie charts for three radial ranges, illustrating the percentage contribution of each species to the ice mantle. The values are number averages and are calculated according to

$$\frac{n\left(X_{ice}\right)}{\sum_X n\left(X_{ice}\right)}(\%) = 100\% \times \frac{\sum_{R_{min}}^{R_{max}} n\left(X_{ice}\right)_{(R,z)}\, dR}{\sum_{R_{min}}^{R_{max}} \sum_X n\left(X_{ice}\right)_{(R,z)}\, dR}, \tag{4.2}$$

which accounts for radial ranges dR between individual parcels, and where R_{max} and R_{min} are the maximum and minimum positions, respectively, of the radial range considered. The pie charts show that typically midplane ice is $\sim 70-80\%$ H_2O, $\sim 10-20\%$ carbon dioxide (CO_2), $1-10\%$ ammonia (NH_3) and $1-4\%$ methanol (CH_3OH). As mentioned above, CO, CH_4 and N_2 ices are only available in the cooler infall-dominated disc and are no more than a few per cent of the total ice content. However, this only holds as long as these species are not mixed with H_2O ice (see the discussion on trapping in Section 4.3.2.2), which would allow these molecules to be retained in the ice at a level of a few per cent. The contributions of various molecules show some radial dependencies, which are a reflection of certain species thermally desorbing at the respective snowlines along the midplane. Other ices, like complex organics and radicals make up no more than $\sim 10\%$ of the total.

For the infall-dominated disc, in Figs. 4.4b and 4.5b it can be seen that for $R > 30$ AU, CO_2 becomes more abundant than H_2O ice. This comes from a delicate balance of rehydrogenation of the OH radical (leading to H_2O) and its reaction with CO on the grain surface (producing CO_2 with an activation barrier of 400 K, Noble et al. 2011) according to the following scheme.

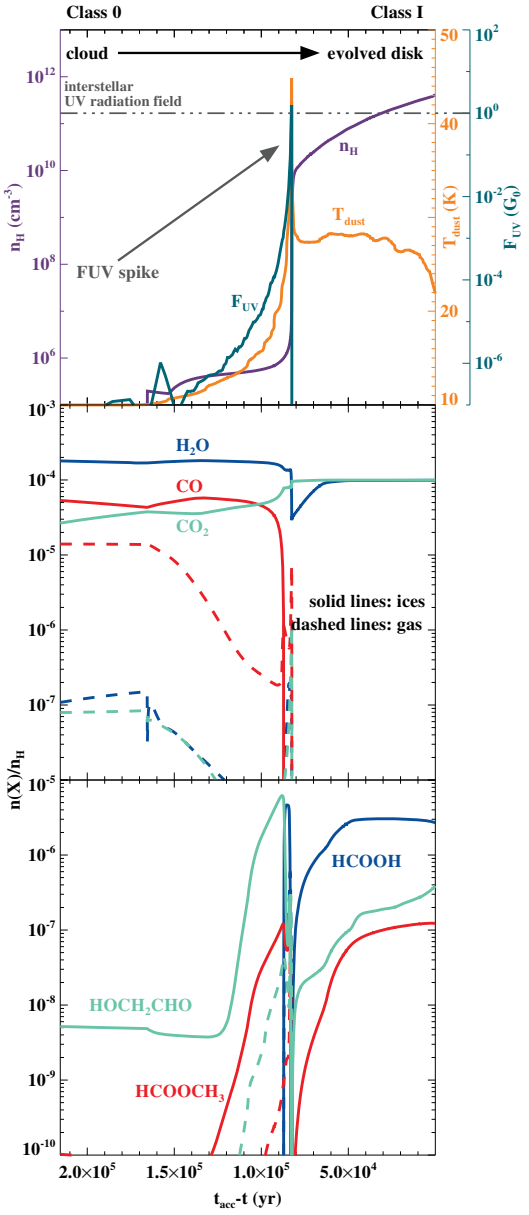

Figure 4.6: The physical parameters and chemical abundances as a function of time (t) for one trajectory (with a final radial position of ∼ 47 AU) in the case of the infall-dominated disc. The upper panel shows the H nuclei number density (n_H), the dust temperature (T_{dust}) and the FUV flux (F_{UV}, in units of G_0, which is the interstellar FUV radiation field of 1.6×10^{-3} erg cm^{-2} s^{-1}, Habing 1968). The middle panel shows the abundances relative to n_H of water, carbon monoxode and carbon dioxide in the solid and gasesous phases (solid and dashed lines, respectively). The lower panel displays the abundances of formic acid, methyl formate and glycolaldehyde. t_{acc} is the accretion time of 2.46×10^5 yr in this model run (see Drozdovskaya et al. 2014 for details). Evolution is from left to right. Note the transformation of CO to CO_2 ice and the build up of complex organics in the envelope upon the increase of FUV flux.

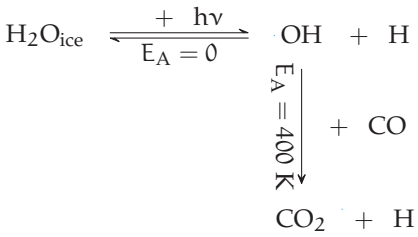

This effect comes into play only in the outer regions of the infall-dominated disc, where CO ice is available. The initial photodissociation of H_2O ice, producing the OH radical, stems from the exposure to stellar FUV photons in the envelope en route to the disc and partially from cosmic ray-induced FUV photons. It appears that the route towards CO_2 is favoured; and it is efficiently produced at the expense of H_2O and CO. This is clearly demonstrated when looking at the individual trajectories in detail, as in Fig. 4.6, which shows the physical parameters and chemical abundances as a function of time for a parcel that ends up at $R \approx 47$ AU along the midplane. The increase of CO_2 ice follows the profile of the FUV flux and is maximized once the FUV flux spikes at $\sim G_0$ (where G_0 is the interstellar FUV radiation field of 1.6×10^{-3} erg cm^{-2} s^{-1}, Habing 1968) immediately prior to disc entry. This effect persists under a static assumption (Section 4.3.4.2), but to a lesser degree, thus displaying the subdominant importance of cosmic ray-induced FUV photons towards the H_2O ice photodissociation process. Such efficient CO_2 production was already noticed in the molecular layer at intermediate heights of Class II protoplanetary disc models of Walsh et al., (2014b) (which also includes a discussion on the uncertainties in this reaction) and in the relatively cool disc around an M dwarf star in Walsh et al., (2015).

4.3.2 *Sensitivity of results to chemical parameters*

4.3.2.1 *Diffusion and quantum tunneling barriers*

To verify the robustness of the predicted CO_2 ice-rich zone in the infall-dominated disc, additional parameter tests were run to test the sensitivity of our results to the assumed grain-surface parameters. In the fiducial setup of our models, the diffusion barrier (E_{diff}) is related to the binding energy (E_{des}, also called the desorption energy) via $E_{diff} = 0.3 E_{des}$ (Hasegawa et al., 1992). The ratio between the two energies is uncertain. Off-lattice Monte Carlo simulations predict a value of $\sim 0.3 - 0.4$ for CO and CO_2 on amorphous water ice (Karssemeijer and Cuppen, 2014; Karssemeijer et al., 2014), while experiments suggest a range of $\sim 0.5 - 0.9$ for O and N on amorphous water ice (Minissale et al., 2016b); however, it is not excluded that this ratio may differ between molecules and atoms. Astrochemical models typically employ values in the $\sim 0.3 - 0.8$ range (e.g., Vasyunin and Herbst, (2013a). For the first test, the factor between the two energies is set to 0.5 to increase the diffusion barrier, thereby impeding radical-radical associations on grain surfaces and limiting the efficiency of the CO+OH surface reaction. For the second test, the fiducial barrier thickness of 1.5 Å is decreased, leading to a thinner barrier for quantum tunneling of H and H_2 between grain surface sites and, thus, the promotion of the OH+H surface reaction.

Both tests were computed for the same parcel with a final radial coordinate $R \approx 50$ AU at the end of the simulation (in the infall-dominated disc; this is not the same parcel as that shown in Fig. 4.6). The same initial molecular abundances as computed with

Table 4.3: Abundances ratios of selected solid species at the end of the simulation (2.46×10^5 yr after the precollapse phase) for a parcel in the infall-dominated disc with final R $\approx$ 50 AU with three different sets of parameters in the chemical model.

Species	Fiducial[g]	$E_{diff} = 0.5E_{des}$	$a = 1$ Å
CO_2/H_2O	1.04	1.28	2.76
CO/H_2O	8.3×10^{-8}	1.3×10^{-3}	4.5×10^{-3}

[g] In the fiducial setup, $E_{diff} = 0.3E_{des}$ and $a = 1.5$ Å.

fiducial parameters were used for all tests. Table 4.3 displays the final abundance ratios of the key species in relation to grain-surface chemistry of CO_2. For a higher diffusion barrier, the abundances of CO and radicals such as OH and HCO are higher in the solid phase, since radical mobility is reduced. However, an increase by $\sim$ 2 orders of magnitude in HCO abundance leads to more CO_2 ice formation via the atom-radical O+HCO reaction. For a thinner barrier for quantum tunneling, less atomic H is available on the grain, since it is easier for it to react with other species. This in turn reduces the availability of OH, reducing the amount of CO_2 ice produced via OH+CO. However, atomic H is not only used to reform H_2O, but to also hydrogenate other species, thereby reducing the amount of H_2O ice as well. The net result is that the ice remains CO_2-rich. Thus such a CO_2 ice-rich zone appears characteristic of the outer parts of the infall-dominated disc independent of the exact parameters used in the chemical model within the framework of the two-phase model considered here (although they do change the abundances quantatively). In fact, two additional pathways to CO_2 have recently been experimentally verified, namely CO+O with $E_A = 1000$ K and H_2CO+O with $E_A = 335$ K (Minissale et al., 2013, 2015). Currently, they are not included in the chemical network, but are expected to positively contribute to the CO_2 production.

4.3.2.2 *Binding energies*

The availability of specific ices in midplanes is set by their initial abundances, the temperature structure of the disc, and also by the binding energies of these species (Table 4.1). This is why in the warmer spread-dominated disc, CH_4 and N_2 ices are absent, and CO ice is low (Section 4.3.1, Fig. 4.4a). The adopted set of binding energies also sets the exact locations of the snowlines. In this work, the binding energies for molecules on amorphous water ice have been adopted for CO, NH_3, H_2S and CH_4. For the larger complex organic species and methanol, the binding energies for pure ices have been used. The binding energies of pure ices tend to be lower than those on H_2O ice, which is the dominant ice constituent (Fig. 4.5a). For example, for pure CO ice in the multilayer regime $E_{des} = 878$ K (Collings et al. 2015, which is within errors of measurements of Öberg et al., (2005), Bisschop et al., (2006), Cleeves et al., (2014) and Fayolle et al., (2016) for pure ices in the multilayer regime), while for CO on H_2O ice $E_{des} = 1150$ K (Collings et al. 2004; Garrod and Herbst 2006 or 1320 K, Cleeves et al. 2014).

In the laboratory, thermal desorption of CO ice deposited on top of H_2O ice is a multi-step process (Ayotte et al., 2001; Bisschop et al., 2006; Collings et al., 2003a,b; Sandford et al., 1988). At the cold ($10 - 15$ K) temperatures of prestellar cores, CO ice forms on top of the H_2O ice mantle (Öberg et al., 2011c; Pontoppidan, 2006); and the layers are frozen in place, since the mobility of such large species is minimal at these temperatures.

Upon heating, as much as 20% of CO ice can get trapped in amorphous H_2O ice as it undergoes phase transitions (Collings et al., 2003b). This implies that a single desorption energy is an oversimplification of the process of thermal desorption of CO. Visser et al., (2009a) (based on the approach of Viti et al. 2004) attempted to account for this effect by considering four flavours of CO with four different desorption energies, which allowed the authors to preserve ~ 15% of CO ice in a disc at the end of the simulation. Unfortunately, such an approach is not feasible in this work due to a much larger size of the chemical network and the inclusion of grain-surface reactions (thus making reaction-dependent CO-'flavouring' non-trivial). Deep trapping of CO in the inner layers is seen as a natural consequence in the multilayer models (Taquet et al., 2012).

Similar trapping mechanisms have also been seen experimentally for other volatiles, such as N_2, CH_4, CO_2, O_2, NH_3; and noble gases, such as Ar, Kr, Xe (Ayotte et al., 2001; Bar-Nun and Laufer, 2013; Bar-Nun et al., 2007; Fayolle et al., 2011; Fresneau et al., 2014; Gálvez et al., 2008; Notesco et al., 2003; Shi et al., 2009; Yokochi et al., 2012). It has also been suggested that irradiation of H_2O ice may collapse pores in the amorphous structure, thereby further enhancing trapping of volatiles (e.g., Shi et al. 2009). Such experimental findings imply that weakly bound volatiles can be preserved in the modelled discs at temperatures that are warmer than their respective thermal desorption regimes. However, this is expected to not exceed the level of a few per cent; thus the qualitative conclusions will remain unaltered. Additional observations of interstellar ices are necessary to verify the layering of ices and to quantify the degrees of mixing and segregation, which could imply a change of the trapping medium from H_2O ice to CO_2 or CH_3OH ices, for example.

4.3.2.3 *Comparison with a three-phase chemical model*

To further ensure that the production of a CO_2 ice-rich zone is not a feature of the two-phase chemical model, additional modelling has been carried out with the three-phase chemical model of Furuya et al., (2015). In the three-phase model, the ices are partitioned between a chemically active surface and an inert bulk at the expense of CPU time. For these comparative model runs, the surface is considered to consist of the uppermost 4 monolayers. The same binding energies and initial prestellar molecular abundances (for species common to both networks), as used in the results presented thus far in this work, are assumed. For the surface layers, $E_{diff} = 0.3E_{des}$ is used, similarly to the assumption made in the two-phase model. Further model details can be found in Furuya et al., (2015).

Fig. 4.5c shows the percentage contribution of volatiles to the total ice content averaged for the midplane beyond 30 AU of the infall-dominated disc at the end of the simulation (2.46×10^5 yr after the precollapse phase), as obtained with the three-phase model of Furuya et al., (2015). This figure is analogous to the right piechart of Fig. 4.5b. Model results with and without the swapping mechanism are shown, which allows the exchange of molecules between the surface layers and the inert bulk ice (according to the formalism of Garrod 2013). In the swapping-on model, bulk ice chemistry (two-body grain-surface reactions and photochemistry) is also included with $E_{diff} = E_{des}$. Thus, the swapping-off model corresponds to a fully inert bulk; while the swapping-on setup imposes marginal chemical reactivity in the bulk ice. Upon the inclusion of swapping, weakly bound species such as CH_4 and N_2 preferentially diffuse to the surface layers and are subsequently lost to the gas phase via thermal desorption. When swapping is excluded, the quantities are consistent between the two- and three-phase models for these

weakly bound species. The contributions of CH_3OH and other minor species are also in agreement.

Swapping enhances the supply of CO molecules available for reactions with OH in the surface, thus generating more CO_2 overall via the reaction with OH, as discussed earlier. This demonstrates that the same scheme that was responsible for CO_2 ice-dominance in the framework of a two-phase model persists with a three-phase model as well, once the assumption of total bulk inactivity is broken by allowing the bulk-surface exchange and marginal bulk reactivity. This implies that this is not a feature of the two-phase model, but rather a chemical effect consistent with the physical evolution of the system. The stellar FUV irradiation in the envelope during infall towards the disc is the driving force behind this CO_2 enhancement (see the spike in Fig. 4.6). Since the two-phase model assumes two chemically active monolayers of the same composition as the entire mantle, reactants which may not be available in the three-phase model are available in the two-phase model. Thus, the results tend towards each other when swapping is included. The two-phase model produces even more CO_2 (an additional 7%) than under the assumption of a marginally reactive bulk in the swapping-on case. Currently, there is no consensus on the chemical reactivity of the bulk ice mantle and further experimental verification is necessary.

4.3.3 *Trace complex organic ices*

Although simple ices dominate the ice composition, there is also a variety of complex organic ices present. Table 4.4 quantifies the abundance of such ices relative to methanol ice for both discs and in three radial ranges. Some complex organics may become close in abundance to methanol ice, i.e., at a level of up to a few per cent of the total ice mantle. Such trace species could potentially have prebiotic implications for the synthesis of amino acids by the Strecker mechanism (e.g., Fresneau et al. 2014, 2015). The right panels of Figs. 4.4a and 4.4b show the radial distribution of complex ices and gases in the inner 50 AU around a protostar for the spread-dominated and infall-dominated discs, respectively, at the final timestep of the evolution. Similar to the situation with simple ices, snowlines of complex organics are also recovered in the midplanes of both discs. Most are clustered near the water and methanol snowlines, as complex organics are tightly bound species (i.e., all those shown in the right panels of Figs. 4.4a and 4.4b except formaldehyde (H_2CO) and ketene (CH_2CO)).

For both discs, complex organic ices are most plentiful in the outer regions ($R > 30$ AU). In the infall-dominated case, complex organic ices survive closer to the protostar and as far in as their respective snowline. In the spread-dominated case, complex organic ices start decreasing around $R \sim 25$ AU (except for ethanol and acetic acid). Complex organic ice formation is facilitated by weak FUV irradiation (no more than a few orders of magnitude higher than the typical cosmic ray-induced FUV flux $\sim 10^{-7}$ erg cm^{-2} s^{-1}, Prasad and Tarafdar 1983, or $\sim 10^4$ photons cm^{-2} s^{-1}), such as that found for trajectories leading into more distant disc regions. Too strong FUV irradiation ($\sim G_0$) can quench complexity by photodissociation of complex organic ices. At the same time, luke warm temperatures are needed to enable radical mobility on grain surfaces; however, too high temperatures will result in the loss of radicals to the gas phase via thermal desorption. The warmer temperature profile of the spread-dominated disk is the main reason for the differences in complex organic abundances between the two disks. Higher temperatures explain also the larger abundance and sole survival of species like ethanol and acetic

acid in the spread-dominated disc, which are considered to only form via radical-radical associations (e.g., Walsh et al. 2014a,b). Meanwhile in the infall-dominated disc, the complex organic species which are efficiently formed via hydrogenation of solid CO and derivatives are also prevalent.

Table 4.4: Average abundances in disc midplanes of complex organic ices relative to methanol ice ($n(X_{ice})/n(CH_3OH_{ice})$) for three radial ranges at the end of the simulation (2.46×10^5 yr after the precollapse phase) for the spread- and infall-dominated discs. The values are given for the case of the fiducial dynamic simulation and under a static assumption (i.e., constant final disc physical parameters)[m]. Additionally, in the final line, the average abundance of methanol ice relative to the number of H nuclei is given for the respective radial ranges and models.

R (AU)	$1-10$				$10-30$				>30			
Species	spread-dom.		infall-dom.		spread-dom.		infall-dom.		spread-dom.		infall-dom.	
	dyn.	stat.	dyn.	stat.	dyn.	stat.	dyn.	stat.	dyn.	stat.	dyn.	stat.
H_2CO	4.7 (−7)	3.2 (−7)	3.4 (−4)	4.6 (−6)	1.4 (−2)	1.7 (−3)	7.1 (−5)	3.3 (−1)	1.4 (−2)	1.5 (−2)	2.4 (−1)	1.1 (−3)
CH_2CO	1.7 (−6)	1.1 (−6)	9.8 (−5)	2.1 (−5)	5.7 (−3)	1.4 (−2)	4.6 (−3)	3.9 (−2)	2.9 (−2)	7.7 (−2)	1.3 (−2)	2.0 (−2)
HCOOH	1.6 (−7)	3.9 (−7)	1.7 (−5)	2.2 (−7)	1.1 (−3)	3.7 (−5)	2.6 (−3)	3.0 (−3)	2.0 (−4)	4.8 (−3)	4.1 (−1)	7.0 (−4)
$HCOOCH_3$	2.7 (−4)	1.6 (−5)	2.4 (−2)	3.7 (−5)	3.9 (−2)	2.5 (−4)	5.1 (−3)	1.9 (−2)	1.2 (−2)	8.3 (−4)	2.4 (−2)	3.0 (−3)
CH_3CHO	1.7 (−9)	2.7 (−9)	1.7 (−8)	1.6 (−7)	1.6 (−4)	1.5 (−6)	1.1 (−3)	1.9 (−1)	1.3 (−2)	1.6 (−3)	7.7 (−3)	8.7 (−4)
CH_3OCH_3	1.4 (−6)	1.4 (−2)	1.6 (−3)	1.0 (−2)	1.1 (−3)	2.6 (−2)	6.8 (−3)	2.9 (−2)	1.5 (−2)	7.1 (−3)	1.5 (−2)	1.4 (−2)
C_2H_5OH	3.7 (−1)	1.8 (−2)	2.7 (−1)	1.8 (−2)	2.0 (−1)	3.1 (−2)	3.8 (−2)	2.2 (−2)	1.7 (−2)	2.2 (−2)	2.6 (−2)	1.3 (−2)
CH_3COOH	9.8 (−1)	3.3 (−1)	4.4 (−1)	3.5 (−1)	2.1 (−1)	2.0 (−1)	1.7 (−2)	2.6 (−2)	5.7 (−3)	2.4 (−3)	4.4 (−1)	2.1 (−3)
$HOCH_2CHO$	3.2 (−4)	1.0 (−3)	1.5 (−1)	1.1 (−2)	1.0 (0)	2.3 (−1)	2.3 (−1)	8.6 (−1)	4.2 (−1)	4.6 (−1)	2.1 (−1)	5.8 (−2)
$\frac{n(CH_3OH_{ice})}{n_H}$	2.8 (−6)	1.9 (−6)	5.1 (−6)	2.0 (−6)	5.2 (−6)	2.5 (−6)	8.5 (−6)	3.0 (−6)	5.4 (−6)	5.8 (−6)	1.7 (−6)	3.0 (−5)

[m] The notation a (b) stands for $a \times 10^b$.

For both discs an inner reservoir rich in gas-phase complex organics is recovered in these models. This zone appears to be the inner few AU of the disc midplanes, where the temperatures are high enough to thermally desorb all tightly bound species; and shielding by dust is sufficiently strong to preserve these molecules from the protostar's photodissociating FUV photons.

The abundances in Table 4.4 show that complex organic ices are plentiful in protoplanetary disks, especially in the outer regions. The current model is, however, tailored to the most favourable conditions for complex organic molecule production. This is achieved by assuming $E_{diff} = 0.3E_{des}$ (Hasegawa et al., 1992), which allows efficient radical-radical chemistry on grain surfaces. A two-phase model, additionally, assumes the same composition for the two chemically active monolayers as for the entire mantle, thus increasing the availability of species for radical-radical chemistry without accounting for, as an example, lower radical mobility deeper in the mantle. Hence, the presented abundances may be seen as upper limits on the quantities of complex organic ices in Class 0/I protoplanetary disk midplanes. These aspects are explored in a detailed parameter study in Drozdovskaya et al., (2015). On the other hand, the abundances of complex organic molecules may be enhanced by additional low ($\sim$ 15 K) temperature formation routes that are seen in recent laboratory studies even in the absence of FUV radiation (e.g., Chuang et al. 2016; Fedoseev et al. 2015).

The predicted ice reservoirs can potentially be traced indirectly via cometary studies, which are showing that comets are rich in large complex organic species. For example, the highly complex molecule glycine is detected at a ratio of 0.5 relative to methanol on 67P (Altwegg et al., 2016; Le Roy et al., 2015). This implies that the modelled abundances are not very different from such observational evidence. A more detailed comparison with comets is presented in Section 4.4.4. Observations of hot inner regions (so-called hot cores or corinos) place the gas-phase abundances of methyl formate, dimethyl ether, ethanol and glycolaldehyde at $\sim 1 - 10^{-2}, 1 - 10^{-2}, 10^{-1} - 10^{-2}, 10^{-2} - 10^{-3}$ relative to gaseous methanol, respectively (fig. 8 of Taquet et al. 2015). These values are comparable to those in Table 4.4 with the exception of glycolaldehyde, which is most likely caused by the lack of destructive chemical pathways in the network, while already including additional formation pathways via glyoxal (Drozdovskaya et al., 2015). Comparisons of the modelled complex organic ice abundances in disk midplanes with gaseous abundances in hot cores/corinos should, however, be made with caution since it remains unclear what the origin of the hot core emission is. In hot cores, thermal desorption leaves desorbed molecules intact, but the observed abundances are potentially modified by gas-phase reactions, since the temperatures and densities are high. Typically, ratios of isomers vary between hot core observations and models, which could indicate either missing chemical pathways in the network or the importance of gas-phase reactions in hot cores. Meanwhile, observed gases in (outer) disk regions are released via non-thermal desorption processes, which may break molecules apart (Bertin et al., 2016; Cruz-Diaz et al., 2016; Walsh et al., 2016).

4.3.4 *Comparison to planet population synthesis models*

Marboeuf et al., (2014a) studied the volatiles of planetesimals in a static cooling protoplanetary disc. The cooling occurs, because the disc surface density decreases with time, as a consequence of material accreting on to the star. As explained in Section 4.2.1, the models of Marboeuf et al., (2014a) assume a hybrid of the 'hot' and 'cold' start scenarios.

The volatiles are assumed to consist of H_2O, CO, CO_2, CH_3OH, CH_4, N_2, NH_3 and H_2S and are the sole potential ice constituents (if disc conditions allow the solid phase), because they are observed to be dominant interstellar and cometary volatiles. All other species are ignored, which means that as much as $\sim$ 10% of the total ice is possibly missed (Figs. 4.5a and 4.5b).

Taking these assumptions about volatiles, the hybrid start scenario, the use of phase diagrams and the differences in disc models into account, there are still some similarities in the findings of Marboeuf et al., (2014a) and the dynamic models presented in this work. Here, the inner discs in the embedded phase are somewhat more massive than those of Marboeuf et al., (2014a), where $\Sigma \lesssim 500$ g cm^{-2} at $R = 5.2$ AU, while here $\Sigma \sim 630$ g cm^{-2} and $\Sigma \sim 540$ g cm^{-2} for the spread-dominated and infall-dominated discs at $R = 5.2$ AU, respectively ($\Sigma \sim 110$ g cm^{-2} and $\Sigma \sim 300$ g cm^{-2} for the spread-dominated and infall-dominated discs at $R = 30$ AU; Fig. 4.3). First, similar trends in snowlines are observed. Most volatiles thermally desorb in the inner few AU ($\lesssim 10$ AU). The most volatile species, CH_4, CO and N_2, freeze out further out in the midplanes, if at all, such as in the hotter irradiated disc model of Marboeuf et al., (2014a) and the spread-dominated disc of this work. This consequently leads to the agreement in water being the dominant ice constituent in planetesimals at $\sim 55-75\%$ of the total ice content, with its contribution increasing with decreasing radius, as molecules that are more weakly bound thermally desorb in accordance with the midplane temperature profile (table 9 and figs. 15, 16 of Marboeuf et al. 2014a). The denominator used to obtain the values given in Marboeuf et al., (2014a) accounts only for 8 molecules, while in this work all available solids are summed to obtain the denominator. Further quantitative comparison of the planetesimal ice composition, as obtained via full prestellar inheritance by discs and subsequent disc cooling (Marboeuf et al., 2014a), versus that via full kinetic chemical modelling and dynamic collapse (this work) is not possible within the framework of our models.

Instead, the assumption of complete prestellar inheritance by discs can be tested by contrasting the assumed initial volatile abundances of Marboeuf et al., (2014a) with the midplane abundances obtained in this work. Table 4.5 shows the modelled midplane ice composition for three sets of initial abundances: the model-consistent fiducial prestellar phase abundances; and the CO-poor (CO:$CO_2 = 1:1$) and CO-rich (CO:$CO_2 = 5:1$) sets, which are based on observations of prestellar cores and protostellar sources as justified in Marboeuf et al., (2014a). Table 4.5 contains the results for both the spread- and infall-dominated disc midplanes. All values are number averages and focus on the most ice-rich outer regions of the midplanes beyond 30 AU. By comparing the tabulated initial and final disc values, it can be seen that the largest differences lie in the amount of CO_2 produced. In this work, more CO_2 is produced via the reaction of OH and CO mentioned earlier, which in turn eats away at the water and CO ice reservoirs. For the infall-dominated case with an excess of CO (CO:$CO_2 = 5:1$), this effect is at its most extreme as water ice is almost entirely converted to CO_2 ice. Another signficant change is seen for CH_3OH ice. If more than the fiducial prestellar quantity is injected into the system initially, as under the CO-poor and CO-rich conditions, then the final disc contribution is still $\lesssim 3$ per cent, as with the fiducial input. Methanol ice is chemical processed en route to the disc via photon-induced chemistry and used to build larger, more complex molecules, leading to a disc abundance of a few per cent that is independent of the initial abundance.

4.3.4.1 *Dependence on initial conditions*

Table 4.5 also gives insight into how the modelled disc abundances depend on the initial chemical conditions used. If all the gaseous volatiles in Marboeuf et al., (2014a) are assumed to deposit as ices, then, overall, more volatiles are frozen out than when a model-consistent prestellar phase is calculated. For the CO-poor abundances, the initial volatile quantities are increased by factors of 6.3, 4.3, 13, 17, 4.7, 49, 3.0×10^3, 7.5 for H_2O, CO, CO_2, NH_3, CH_4, CH_3OH, H_2S and N_2, respectively, relative to the fiducial presteller ice abundances. The largest increases, thus, are for CH_3OH and H_2S. The CO-rich abundances are extreme with CO ice being available at the level of H_2O ice.

For the spread-dominated disc, it is then seen that if more CO_2 is present initially with the CO-poor abundances, then that quantity is preserved and more CO_2 is made en route as also seen with the model-consistent prestellar phase abundances. If more CO is provided initially with the CO-rich abundances, then it is efficiently converted to CO_2 via the reaction with OH. In both situations, this leads to CO_2 occupying a more significant portion of the ice mantle than under those of the prestellar phase. This also holds for the infall-dominated disc. Since CO_2 was already abundant in the outer regions of that disc, under the CO-poor and CO-rich initial conditions favoring larger quantities of CO_2, the contribution of CO_2 to the ice mantle is even more extreme.

4.3.4.2 *Static scenario*

To further test the importance of dynamic motions in forming protostellar systems, a static scenario has also been computed. Material is assumed to be at the constant final physical conditions of the midplane for the entire duration of the evolution, i.e., for 2.46×10^5 yr, as is tradionally assumed for Class II disc models. For both discs, the largest impact is seen for complex organics (Table 4.4 for $R > 30$ AU). Fewer of the largest complex organic molecules are produced in both discs under a static assumption. By taking dynamic infall into account, protoplanetary disc materials are exposed to elevated temperature and increased FUV fluxes en route to the disc, which facilitates radical production and mobility on the grain surfaces, both of which are key to forming larger species in these models. This is clearly illustrated in Fig. 4.6, since the abundances of complex organics increase along with the FUV flux increase in the envelope. Under the static assumption for the infall-dominated disc in the $10 - 30$ AU range, the most favorable conditions for complex organic formation appear to be shifted from the outer disc to a more inner region. This in turn affects the availability of methanol ice, which is underproduced by a factor of 10 for this zone in comparison to the dynamic model runs (not shown).

The static assumption also shifts the balance of H_2O and CO_2 ices in the outer regions of the two discs (Table 4.5). For the spread-dominated disc, the static scenario means cooler temperatures for the duration of the simulation, leading to a higher availability of CO on the grains (if only transiently), which leads to more CO_2 ice at the expense of H_2O ice. For the infall-dominated disc, the static scenario means lower FUV irradiation, leading to less frequent H_2O ice photodissociation and thus a reduction of OH, on the contrary reducing the amount of CO_2 ice contribution in the outer disc. Other volatiles show variations of no more than a few per cent between the static and dynamic cases.

Table 4.5: Icy volatiles in outer ($R > 30$ AU) disc midplanes for different initial abundances at the end of the simulation (2.46×10^5 yr after the precollapse phase) for the spread- and infall-dominated discs for models including dynamic collapse and those for which static conditions were assumed.

Initial assumption	Species	Initial abundance[n]		$n(X_{ice}) / \sum n(X_{ice})$ (%)[o]				
		$n(X_{gas})/n_H$	$n(X_{ice})/n_H$	initial	spread-dom.		infall-dom.	
					dyn.	stat.	dyn.	stat.
Prestellar	H_2O	7.7×10^{-8}	1.9×10^{-4}	51	69	57	35	51
	CO	1.4×10^{-5}	5.9×10^{-5}	16	0[q]	0[q]	0[q]	1
	CO_2	7.9×10^{-8}	1.9×10^{-5}	5	14	27	46	21
	NH_3	2.1×10^{-7}	4.8×10^{-6}	1	4	3	1	4
	CH_4	1.2×10^{-7}	1.5×10^{-5}	4	0[q]	0[q]	4	3
	CH_3OH	2.0×10^{-10}	3.7×10^{-6}	1	2	2	1	10
	H_2S	5.3×10^{-10}	8.1×10^{-9}	0[q]	0[q]	0[q]	0[q]	0[q]
	N_2	1.3×10^{-5}	1.1×10^{-5}	3	0[q]	0[q]	3	2
$CO:CO_2 = 1:1$	H_2O	1.2×10^{-3}	-	57[p]	63	-	27	-
	CO	2.4×10^{-4}	-	11[p]	0[q]	-	0[q]	-
	CO_2	2.4×10^{-4}	-	11[p]	26	-	48	-
	NH_3	8.3×10^{-5}	-	4[p]	3	-	0[q]	-
	CH_4	7.1×10^{-5}	-	3[p]	0[q]	-	4	-
	CH_3OH	1.8×10^{-4}	-	8[p]	3	-	0[q]	-
	H_2S	2.4×10^{-5}	-	1[p]	0[q]	-	0[q]	-
	N_2	8.3×10^{-5}	-	4[p]	0[q]	-	5	-
$CO:CO_2 = 5:1$	H_2O	8.3×10^{-4}	-	39[p]	62	-	1	-
	CO	8.2×10^{-4}	-	39[p]	0[q]	-	16	-
	CO_2	1.6×10^{-4}	-	8[p]	27	-	73	-
	NH_3	5.7×10^{-5}	-	3[p]	3	-	0[q]	-
	CH_4	4.9×10^{-5}	-	2[p]	0[q]	-	0[q]	-
	CH_3OH	1.2×10^{-4}	-	6[p]	3	-	0[q]	-
	H_2S	1.6×10^{-5}	-	1[p]	1	-	0[q]	-
	N_2	5.7×10^{-5}	-	3[p]	0[q]	-	3	-

[n] Under the precollapse phase scenario, initial abundances are split over the gas and solid phases. Under the two sets of initial conditions adopted from Marboeuf et al., (2014a), the abundances are set for the gas-phase only in line with the 'hot' disc assumption.

[o] Number averages for $R > 30$ AU are given, as that region is the richest in ices. Note that the radial range considered for the infall-dominated disc is larger since the average is computed from $R = 30$ AU and out to the outer radius, which is much larger than for the spread-dominated disc.

[p] If all the gases deposit as ices.

[q] A few per cent can be trapped in H_2O ice (Section 4.3.2.2).

4.4 DISCUSSION

4.4.1 *Dynamics, chemistry and inheritance*

In this work, the importance of dynamic collapse and kinetic chemistry en route to protoplanetary disc midplanes has been assessed by considering two physical models and by running various test cases. The two modelled discs predominantly grow by different mechanisms, either via viscous spreading or by pure infall, leading to material being transported along different trajectories. The results have shown that there is a delicate balance between H_2O and CO_2 ices. Under cool ($\sim$ 20 K) temperatures, allowing the presence of CO ice, and weak FUV irradiation, producing the OH radical from the photodissociation of H_2O ice, a significant water-carbon dioxide imbalance can occur leading to large quantities of CO_2 ice at the expense of H_2O (and CO) ice(s). Such conditions are encountered at large radii ($R > 30$ AU) for the infall-dominated disc ($\sim$ 46% of the ice mantle is CO_2). Under an assumption of a static disc, this also occurs for the outer region of the spread-dominated disc, while the outer region of the infall-dominated disc becomes less imbalanced ($\sim$ 25% of the ice mantle is CO_2). If either the chemistry or the dynamic transport of volatiles was neglected, then these shifts in the ice mantle composition would be missed. This effect has been shown to be insensitive to chemical model parameters such as the diffusion and quantum tunnelling barriers, and binding energies. It also manifests when three-phase models are used. If the FUV field during the physical evolution would be modified, then the qualitative results would still hold; and the amount of CO_2 ice produced would only change quantitatively. In the case of a weaker FUV field, the amount of CO_2 produced would decrease (by at most $\sim$ 25 and $\sim$ 13 per cent for the infall- and spread-dominated cases, based on the static case without any FUV exposure in the envelope). In the case of a stronger FUV field, the amount of CO_2 is expected to increase, since more FUV photons are available to dissociate H_2O ice. The FUV field can also be harder or softer, and photodissociation cross-sections are wavelength-dependent, thus potentially shifting regional enhancements. Given the importance of the FUV flux demonstrated here, this should be explored in future work.

The trace complex organic species also show a strong dependence on dynamics. Their production is a delicate process balanced by dust temperatures that are warm enough to allow radical mobility on grain surfaces, but low enough to make radical thermal desorption inefficient; and by FUV irradiation that is sufficiently strong to produce radicals in the ice, but sufficiently weak to not efficiently photodissociate the complex organics back into radicals. As a result, dynamic infall leading to elevated temperatures and increased FUV exposure, facilitates complex organic molecule production, which would otherwise be impeded by the midplane physical conditions. This also influences the availability of methanol ice, which is a key parent species for many complex organics, making it sensitive to dynamic transport and the chemistry en route. The outer zones ($R > 30$ AU) of both the spread- and infall-dominated discs contain the most complex organic ices (at abundances as high as that of methanol ice, i.e., at a level of up to a few per cent of the total ice mantle), while the inner discs (inner few AU) are rich in gaseous complex organics. These molecules can only be modelled by using full kinetic chemical calculations.

Other volatiles are found to be insensitive to the dynamics and chemistry between the cloud and disc phases. The findings made with these physicochemical models are summarized in Fig. 4.2. The implication is that not all prestellar ices are simply inherited

by the midplanes of protoplanetary discs. The balance between dominating volatiles may change depending on the route taken by the material to get to the planetesimal- and comet-forming zones and the chemistry that occurs during that time. The variations seen in H_2O, CO_2 and CH_3OH ices are consistently obtained under different initial volatile abundances. The complex organic molecule production is facilitated by the favorable conditions in the envelope, thus determining the prebiotically-significant composition of planetesimals outside of the protoplanetary disc.

4.4.2 *Comparison to other disc models*

A large number of models exist for the Class II protoplanetary discs of varying physical and chemical complexity. Therefore, in this section, the models of young embedded discs will only be compared to the more evolved discs from studies including chemistry of complex organic molecules. The series of papers Walsh et al., (2014a,b), Walsh et al., (2015) have studied a full range of molecules in protoplanetary discs under static conditions, along accretion flows within the disc, and for various central irradiating protostars, using the same prescription for the chemistry as that used in this work.

Comparing with the midplane abundances of complex organics for the static Class II disc of Walsh et al., (2014b), it appears that the spead-dominated disc contains less acetaldehyde ($\sim$ 2 orders of magnitude) and more confined to the outer region ($R \gtrsim 30$ AU) rather than up to the thermal desorption front; less dimethyl ether ($\sim$ 1 order of magnitude), but more acetic acid ($\sim$ 2 orders of magnitude). The infall-dominated disc seems to be richer in complex organic molecules than the static Class II disc (more formic acid, methyl formate and acetic acid, all by $\sim$ 1 order of magnitude). These chemical variations stem from different physical conditions and time-scales of static Class II discs in comparison to these dynamically formed embedded Class I discs. Comparing with the $z = 0$ AU accretion flow through the disc of Walsh et al., (2014a), it seems that the spead-dominated disc abundances lie somewhere inbetween the isolated and extremely irradiated disc models (formic acid abundances are closer to the extremely irradiated disc, while methyl formate abundances are closer to the isolated disc, and acetaldehyde abundances lie inbetween the two models). The infall-dominated disc abundances are very similar to those in the midplane accretion flow of the isolated disc with only variations of factors of a few. Due to the inclusion of the additional pathway to glycolaldehyde via glyoxal in this work, more glycolaldehyde is made here by $\sim$ 2 orders of magnitude.

Comparing the spread- and infall-dominated discs to the results from turbulent disc models of Furuya and Aikawa, (2014), it appears that formaldehyde, methanol and ammonia agree within a factor of a few with the non-turbulent ($\alpha_z = 0$) model. However, there are subtle differences for complex organics such as methyl formate and dimethyl ether. Here, the outer disc in its entirety is rich in large complex species, however in the models of Furuya and Aikawa, (2014) the distribution of such species is highly localized. The abundances peak and match those obtained in this work only in a narrow radial range. This is most likely because Furuya and Aikawa, (2014) assume $E_{diff} = 0.5E_{des}$, which inhibits efficient complex organic molecule formation (see appendix A of Walsh et al. 2014b). These comparisons imply that current Class II disc models may be underestimating the complex organic content, since the initial chemical conditions set by the preceeding embedded phase could be much higher than currently assumed.

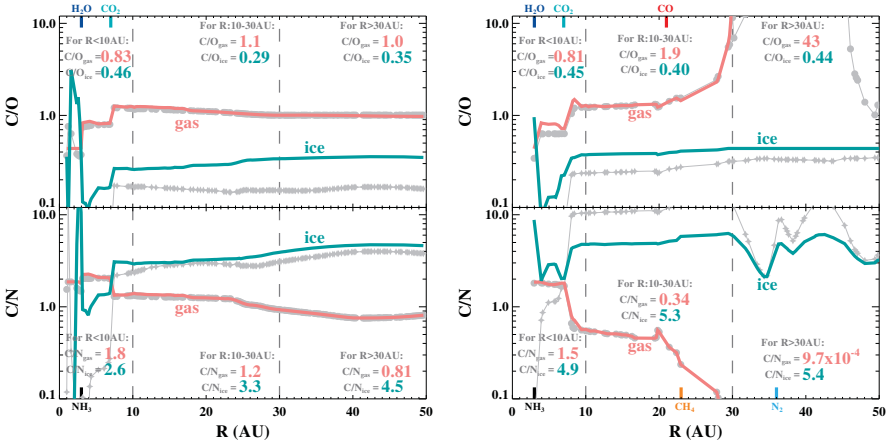

(a) Spread-dominated disc (b) Infall-dominated disc

Figure 4.7: The midplane C/O and C/N ratios as a function of disc radius (R) in the gaseous (coral colored lines) and solid (torquoise colored lines) phases at the end of the simulation (2.46×10^5 yr after the onset of collapse). The average ratios over three radial ranges (separated by grey dashed lines) are provided; and the locations of some snowlines are marked (the full list is in Table 4.2). The grey curves with dots and stars are the ratios in the gasesous and solid phases, respectively, as calculated with abundances of simple volatiles only (namely H_2O, CO, CO_2, CH_3OH, CH_4, N_2 and NH_3.)

4.4.3 *Implications for population synthesis models*

The results of these models on midplane volatiles have been compared to the initial volatile composition of planetesimals used in sophisticated planet population synthesis models of Marboeuf et al., (2014a,b), Thiabaud et al., (2014, 2015). The two sets of models and assumptions are put in perspective in Fig. 4.2. The main point is that complete inheritance of cloud volatiles by discs is not a valid assumption for species such as H_2O, CO_2 and CH_3OH for all regions of the disc, which have been shown to be affected by the dynamics and chemistry during transport. Thus, under current assumptions, planet population synthesis models are potentially overestimating the availability of CH_3OH by a factor of $\sim 2-4$ and could be missing large regional CO_2 reservoirs. Complete exclusion of complex organic ices means that as much as $\sim 10\%$ of the total ice may be currently omitted.

If the results of these models were to be used as the initial volatile abundances for population synthesis models, then the initial C/O and C/N ratios of planetesimals would be altered (the ratios denote the overall volatile carbon, oxygen, and nitrogen budgets). The midplane gaseous and solid C/O and C/N ratios are shown as a function of disc radius for the spread-dominated disc in Fig. 4.7a and for the infall-dominated disc in Fig. 4.7b. The first major point is that the two ratios in ices do not match those in gases, i.e., the two phases are decoupled in terms of these tracers. These findings are fairly consistent with those in fig. 1 of Öberg et al., (2011b), which were based on a much simpler adsorption-thermal desorption prescription for a static disc temperature profile, with the exception of the large gas-phase C/O jump seen in the outer regions of the infall-dominated disc.

For the spread-dominated disc, the gas-phase C/O ratio ~ 1. The ratio decreases to ~ 0.8 only in the inner 10 AU, once CO_2 and H_2O ices sequentially thermally desorb and increase the oxygen budget in the gas. The solid-phase C/O ratio in this warmer (~ 40 K) disc is subsolar at a value ~ 0.3, which reflects the ices being dominated by water and carbon dioxide setting C/O ~ 1/3. The ratio reaches towards the solar value of 0.5 in the inner few AU once CO_2 and H_2O are lost as gases. For the infall-dominated disc, the gaseous ratio is comparable to that of the spread-dominated disc for the inner 30 AU (with a value in the $\sim 0.8-2$ range). However, beyond that radius, the ratio increases by an order of magnitude as a result of CO adsorbing and locking away almost all oxygen carriers. The solid-phase ratio nearly matches the solar C/O ratio with values in the $0.4-0.45$ range along the entire extent of the disc, which stems from the larger CO_2 reservoir seen for in this disc, which drives the ratio towards 1/2.

The C/N ratio in the spread-dominated disc varies roughly between 0.8 and 1.8 in the gas and between 2.5 and 4.5 in the ice, thus below the solar value of 4.9 in both phases. The biggest variations are primarily driven by the thermal desorption events of the main icy carbon carrier CO_2 and the main icy nitrogen carrier NH_3 under the warm ~ 40 K conditions of this midplane. Beyond 30 AU, where complex organic ices are plentiful, the fraction of carbon stored in the solid phases increases and so does the C/N ratio in the ice. In the infall-dominated disc, the C/N ratio in the ice is approximately solar for all radii. The gas-phase ratio rapidly decreases beyond 20 AU, since the majority of both C and N carriers are frozen out at the cold ~ 20 K conditions of this disc. The solid phase C/N ratio in this disc is in agreement with the observed cometary value of ~ 7, however it does not explain the ratios on the order of ~ 50 for the Earth and chondrites in the inner few AU (see fig. 1 of Bergin et al. 2015).

In Figs. 4.7a and 4.7b, gray lines depict the C/O and C/N ratios as calculated based on the abundances of the main volatiles only, in contrast to the colored lines, which are calculated based on the full set of species in the network and model-consistent prestellar initial abundances. For the gas phase, the differences between the two calculations are minor (except the very inner $1-2$ AU). On the other hand, for the solid phase, variations by a factor of $2-3$ are seen. These differences reflect the quantities of C, O and N locked away in complex organic ices and demonstrate the importance of the ~ 10 per cent of the icy mantle labelled as 'other' in the earlier discussions. The implications of the volatile budget derived with these models for the planet populations are the subject of future collaborative work, which will account for drift beyond the traditional inner 30 AU planet-forming zone. Such work will show if chemical processing during the earlier dynamic phases of protoplanetary disc formation may help explain CO_2-rich exoplanet atmospheres, which cannot be replicated with chemical equilibrium models at atmospheric temperatures and pressures (Heng and Lyons, 2016), although chemical processing within the atmospheres themselves is non-negligible. The differences in the C/O and C/N ratios between the two phases could potentially be used to trace the contribution of ices from planetesimals to planetary atmospheres versus that of ambient disc gas.

4.4.4 *Comparison with comets*

Comets are thought to spend the dominant portion of their lifetime at large radii, far away from the heat and irradiation from the Sun. As a result, they are considered to be the most pristine probes of the composition of the young protosolar disc. Observed

chemical similarities between comets and protostellar environments are puzzling (see Mumma and Charnley 2011 and Caselli and Ceccarelli 2012 for reviews). It remains unclear whether the agreements signify comets inheriting materials from earlier phases of star and planet formation, or if it simply is a general coincidence caused by chemistry proceeding along similar pathways under astrophysical conditions. The modelled midplane volatile contributions relative to water ice generally agree with the observed ranges for cometary volatiles within a factor of 2 (comparing the values quoted in Figs. 4.5a and 4.5b with those in fig. 4 of Mumma and Charnley 2011). The dominating ice constituents are found to be H_2O, CO_2, NH_3, CH_4 and CH_3OH consistently. Only CO is underproduced in our models, but as mentioned earlier, this could be resolved by trapping in amorphous water ice (Section 4.3.2.2). The CO_2 ice-rich zone seen in this work can help explain CO_2-rich comets (fig. 4 of Mumma and Charnley 2011), and the CO_2-rich and H_2O-poor jets of comet 103P/Hartley 2 (A'Hearn, 2011).

Comets are rich in many complex organics; and the recent measurements for 67P with the *Rosetta* mission are revealing even more complexity than suggested by earlier observations (Capaccioni et al., 2015; Goesmann et al., 2015; Le Roy et al., 2015). Molecules as large as ethanol and glycolaldehyde have also been recently detected for comet Lovejoy (Biver et al., 2015), so chemical complexity seems to be characteristic to comets. The detected abundances are fractions of a per cent relative to water, however relative to methanol the abundances are as high as few per cent. This is consistent with the modelling outcomes of this work, where complex organics are shown to be efficiently formed relative to methanol (Table 4.4). This may imply that cometary complex organics formed en route in the envelope in the earliest embedded phases of star formation and were incorporated into planetesimals and cometary bodies in disc midplanes. Potentially, there are also contributions stemming from the prestellar phase, where complex organics have also been observed (Bacmann et al., 2012; Requena-Torres et al., 2007; Vastel et al., 2014). However, gas-phase processes have been proposed as the origin. Meanwhile, recent laboratory experiments indicate additional low-temperature pathways to complex organics (Chuang et al., 2016; Fedoseev et al., 2015). More detailed and quantitative comparisons between modelled midplane and observed cometary volatiles are the subject of future publications. In particular, the authors will aim to relate data on 67P obtained with the ROSINA instrument, which are free from temporal peculiarities (such as those discussed in Qi et al. 2015b) that could potential affect remote sensing observations, with the results of these models.

4.5 CONCLUSIONS

This paper builds on previous work by Visser et al., (2009a, 2011) and Drozdovskaya et al., (2014) and is focused on the midplane composition of protoplanetary discs in the embedded phase. State-of-the-art physicochemical models are employed to simulate the formation of discs from the initial prestellar phase for 2.46×10^5 yr. Two discs are studied that vary in their respective dominant disc-growth mechanism, either viscous spreading or pure infall. Subsequently, the path of material towards the midplanes of these discs differs, predominantly in-out or simply inwards, respectively. These routes in turn set the temperatures and UV fluxes during the transport of parcels from cloud to disc. More than 100 trajectories into each disc are computed to sample the disc midplane, and the icy content in the framework of such a dynamical model is analysed thereafter. The main conclusions are as follows:

- The typical main ice constituents in the midplanes are $\sim 70-80\%$ H_2O, $\sim 10-20\%$ CO_2, $1-10\%$ NH_3 and $1-4\%$ CH_3OH; however, CO_2 may dominate ($\sim 40\%$) in the outer disc when grown via pure infall.
- Trace complex organic ices are most abundant in the outer disc ($R \gtrsim 30$ AU). Some may be as plentiful as methanol ice in the midplane, at a level of $\sim 1\%$ of the total ice content, similar to that seen in comet observations. The inner disc is rich in complex organic gases.
- The positions of snowlines of volatiles and complex organics in the midplanes of protoplanetary discs, according to relative volatilities, are retained even when dynamics and chemistry during disc formation are taken into account.
- Dynamic infall and the chemistry en route to the midplane may enhance the amount of CO_2 and diminish CH_3OH ices in comparison to the prestellar phase. Not all volatiles are simply inherited by the midplane from the cloud. Icy planetesimals and cometary bodies reflect the provenances of the midplane ices.
- The elevated temperatures and additional FUV photons in the envelope facilitate the formation of prebiotically-significant molecules, which may consitute as much as $\sim 10\%$ of the icy mantles. Current Class II disc models may be underestimating the complex organic content, since the initial abundances set in the embedded phase could be much higher than currently assumed.
- The C/O and C/N ratios differ between the gas and solid phases. The two ratios in the ice show little variation beyond the inner 10 AU and both are nearly solar in the case of pure infall.

The latest theories and observations are suggesting much earlier planetesimal formation than previously thought. The results presented in this paper for the midplanes of protoplanetary discs around low-mass protostars in the embedded phase may probe the volatile and prebiotically-significant content of the pebbles that go on to feed exoplanet atmospheres and form comets. Future work will focus on deeper understanding of the consequences of these model results on cometary composition and planetary populations.

4.6 ACKNOWLEDGEMENTS

This work is supported by a Huygens fellowship from Leiden University, by the European Union A-ERC grant 291141 CHEMPLAN, by the Netherlands Research School for Astronomy (NOVA) and by a Royal Netherlands Academy of Arts and Sciences (KNAW) professor prize. C.W. acknowledges support from the Netherlands Organisation for Scientific Research (NWO, program number 639.041.335). U.M. and A.T. acknowledge the National Centre for Competence in Research PlanetS supported by the Swiss National Science Foundation.

4.7 APPENDIX

ICE ABUNDANCES

Table 4.6: Mean, minimum and maximum abundances of ices beyond their respective snowlines in the spread-dominated disc at the end of the simulation (2.46×10^5 yr after the onset of collapse).

Species	R_{snow} (AU)	$n(X_{ice})/n_H$			$n(X_{ice})/n(H_2O_{ice})$		
		mean	min	max	mean	min	max
H_2O	3	1.8 (−4)	1.6 (−5)	1.9 (−4)	1.0 (0)	1.0 (0)	1.0 (0)
CO	> 50						
CO_2	7	3.6 (−5)	1.0 (−6)	3.9 (−5)	2.0 (−1)	5.9 (−3)	2.3 (−1)
NH_3	3	1.3 (−5)	1.1 (−5)	2.1 (−5)	7.2 (−2)	6.0 (−2)	1.2 (−1)
CH_4	> 50						
CH_3OH	4	5.3 (−6)	1.1 (−6)	6.2 (−6)	2.9 (−2)	6.4 (−3)	3.3 (−2)
H_2S	7	3.2 (−9)	1.1 (−11)	2.1 (−8)	1.8 (−5)	6.5 (−8)	1.2 (−4)
N_2	> 50						
H_2CO	20	4.9 (−8)	4.7 (−11)	1.3 (−7)	2.7 (−4)	2.6 (−7)	6.9 (−4)
CH_2CO	9	1.6 (−8)	1.9 (−13)	4.4 (−8)	9.0 (−5)	1.1 (−9)	2.4 (−4)
HCOOH	4	3.0 (−9)	1.2 (−19)	1.0 (−8)	1.6 (−5)	6.9 (−16)	5.6 (−5)
$HCOOCH_3$	5	1.8 (−7)	3.5 (−19)	4.0 (−7)	9.6 (−4)	2.1 (−15)	2.1 (−3)
CH_3CHO	7	4.3 (−10)	2.5 (−17)	2.6 (−9)	2.4 (−6)	1.4 (−13)	1.4 (−5)
CH_3OCH_3	7	6.7 (−9)	1.5 (−12)	2.6 (−8)	3.7 (−5)	8.5 (−9)	1.4 (−4)
C_2H_5OH	3	1.3 (−6)	1.0 (−8)	2.6 (−6)	7.2 (−3)	6.6 (−4)	1.4 (−2)
CH_3COOH	3	1.9 (−6)	9.5 (−8)	5.5 (−6)	1.5 (−2)	5.9 (−3)	4.8 (−1)
$HOCH_2CHO$	3	3.1 (−6)	5.6 (−17)	5.8 (−6)	1.7 (−2)	3.3 (−13)	3.2 (−2)

Table 4.7: Same as Table 4.7, but for the infall-dominated disc.

Species	R_{snow} (AU)	$n(X_{ice})/n_H$			$n(X_{ice})/n(H_2O_{ice})$		
		mean	min	max	mean	min	max
H_2O	3	1.2 (−4)	9.0 (−7)	1.6 (−4)	1.0 (0)	1.0 (0)	1.0 (0)
CO	21	1.8 (−6)	1.9 (−17)	1.9 (−5)	1.2 (−2)	3.0 (−13)	1.2 (−1)
CO_2	7	8.8 (−5)	2.7 (−6)	1.1 (−4)	9.7 (−1)	1.7 (−2)	3.6 (0)
NH_3	3	3.6 (−6)	5.0 (−9)	6.6 (−6)	2.7 (−2)	3.4 (−4)	4.2 (−2)
CH_4	23	8.4 (−6)	1.7 (−8)	1.7 (−5)	1.1 (−1)	1.7 (−4)	4.0 (−1)
CH_3OH	3	4.6 (−6)	2.2 (−10)	1.2 (−5)	3.3 (−2)	2.4 (−4)	7.8 (−2)
H_2S	8	1.0 (−8)	5.6 (−15)	2.1 (−8)	9.7 (−5)	4.7 (−11)	3.8 (−4)
N_2	36	6.2 (−6)	6.5 (−11)	1.5 (−5)	7.4 (−2)	1.0 (−6)	3.8 (−1)
H_2CO	11	3.3 (−7)	6.6 (−12)	1.5 (−6)	4.2 (−3)	5.6 (−8)	2.3 (−2)
CH_2CO	8	8.6 (−8)	9.6 (−10)	2.9 (−7)	5.9 (−4)	9.2 (−6)	1.8 (−3)
HCOOH	3	5.8 (−7)	7.9 (−12)	2.8 (−6)	5.8 (−3)	1.5 (−7)	2.8 (−2)
$HCOOCH_3$	4	8.0 (−8)	5.5 (−13)	3.0 (−7)	6.3 (−4)	4.7 (−9)	2.3 (−3)
CH_3CHO	5	5.2 (−8)	1.3 (−13)	6.3 (−17)	3.8 (−4)	7.8 (−10)	4.4 (−3)
CH_3OCH_3	6	5.7 (−8)	3.9 (−11)	3.6 (−7)	4.2 (−4)	1.0 (−6)	3.0 (−3)
C_2H_5OH	3	1.0 (−7)	6.7 (−11)	3.7 (−7)	7.4 (−4)	1.7 (−6)	2.3 (−3)
CH_3COOH	3	1.1 (−6)	4.8 (−11)	5.4 (−6)	1.1 (−2)	9.9 (−7)	6.9 (−2)
$HOCH_2CHO$	3	1.3 (−6)	3.3 (−12)	6.3 (−6)	1.1 (−2)	2.8 (−8)	2.1 (−1)

5

THE ALMA-PILS SURVEY: THE SULFUR CONNECTION BETWEEN PROTOSTARS AND COMETS - IRAS 16293-2422 AND 67P/C-G

Maria N. Drozdovskaya, Ewine F. van Dishoeck, Jes K. Jørgensen,
Ursina Calmonte, Léna Le Roy, Kathrin Altwegg, PILS team
MNRAS, 2016b, in prep.

ABSTRACT

IRAS 16293-2422 is a one the most chemically rich low-mass protostellar system known to date and is likely one of the best Solar System analogues. ALMA Band 7 data from the large unbiased Protostellar Interferometric Line Survey (PILS) are searched for all sulfur-bearing molecules at the so-called "sweet spot" - a one beam offset position from source B. Species such as SO_2, OCS, CS, H_2CS and H_2S are either directly or indirectly detected via multiple isotopologues. Interferometric data permit spatial resolution of the emission and yields sufficient sensitivity to detect minor species. The search revealed a firm first-time detection of $OC^{33}S$ towards this source and a tentative first-time detection of $C^{36}S$ towards a low-mass protostar. A comparison in terms of molecular ratios with single dish observations reveals that single dish data are dominated by large scale outflow emission. Comets are thought to be the most pristine currently available tracers of the primitive Solar Nebula. Some of the best available data stemming from the ROSINA instrument aboard Rosetta are used to compare the sulfur budget of 67P/C-G with that of IRAS 16293-2422. Molecular ratios of 67P/C-G are shown to be significantly different from those towards the sweet spot with relatively more H_2S compared with OCS. This potentially indicates that our Solar System formed in a warmer, CO ice-poor environment that inhibits efficient OCS formation via grain-surface chemistry.

5.1 INTRODUCTION

Sulfur-bearing molecules have been detected in many interstellar environments from diffuse clouds to star-forming regions and rocky bodies in our Solar System. It is likely that the sulfur detected in cometary studies has its roots in the earliest diffuse phases of the interstellar medium. However, in comparison to diffuse clouds, observations show the total sulfur budget of dense cores to be depleted by several orders of magnitude. This puzzle remains unresolved and the missing sulfur is yet to be conclusively identified (e.g., Anderson et al. 2013). It has been postulated that sulfur may be a key element in linking the volatile and refractory components to a place of common origins, as it is found in both.

Some of the first detections of interstellar sulfur were in the gas phase towards Sgr B2 and Orion A in the 1970s - molecules such as CS, OCS, H_2S, SO, H_2CS and SO_2 were observed (Drdla et al., 1989; Jefferts et al., 1971; Minh et al., 1990; Pastor et al., 1991; Penzias et al., 1971). This also kicked off the studies of its chemistry, which suggested that in thin clouds sulfur is predominantly in the form of S^+ ions (Oppenheimer and Dalgarno, 1974) and likely undergoes partial incorporation into refractories. Meanwhile,

in dense clouds it is mostly neutral and gets incorporated into the observed volatiles via reactions with H_3^+ (Oppenheimer and Dalgarno, 1974) and grain-surface reactions (Duley et al., 1980). Subsequent chemical models quickly showed that the net sulfur budget as seen in volatiles is severely depleted in dense clouds (Prasad and Huntress, 1982). Some of the sulfur is incorporated into carbon chains such as CS, C_2S, C_3S and C_4S (Millar and Herbst, 1990; Smith et al., 1988; Wlodek et al., 1988). However, since the ionization potential of sulfur is lower than that of carbon, S^+ may exist in regions where most of carbon is neutral, which may lead to the formation of S_2 (suggested very early on by Duley et al. 1980). An important parameter is the initial elemental C/O ratio at time molecules start to form, which sets the ratio between oxygen- and carbon-containing S-bearing species (e.g., as seen in the ratio between SO and CS; Watt and Charnley 1985). Additional volatiles can be formed and/or enhanced via the passage of shocks, including HS, H_2S, S_2, SO^+ (Leen and Graff, 1988; Mitchell, 1984; Pineau des Forets et al., 1986; Turner, 1992). Species such as SO and SO_2 that are produced in the gas-phase via reactions with OH upon the liberation of S via sputtering, have become traditional shock tracers. Sulfur-bearing molecules have also been used to study disks via CS (e.g., Blake et al. 1992; Hasegawa et al. 1984) and as tracers of the centrifugal barrier via SO (e.g., Sakai et al. 2014).

Sulfur-bearing species also exist in the solid phase; and OCS ice was the first to be detected (Aikawa et al., 2012; Palumbo et al., 1995, 1997). Thereafter, the detection of solid SO_2 followed, but H_2S ice remains undetected (Boogert et al., 1997, 2015). The possible formation routes in ices towards species such as S_2 have already been investigated since Grim and Greenberg, (1987). In their experiments, ice mixtures containing H_2S are irradiated via ultraviolet (UV) photons and the production of sulfur chains is indirectly inferred. More recently, Chen et al., (2015) have shown energetic processing with UV of H_2S-CO ice mixtures leads to the formation of OCS and CS_2; and of H_2S-CO_2 mixtures to OCS and SO_2. It is thought that H_2S forms via the hydrogenation of atomic S and serves as a parent species for further synthesis of sulfur-bearing ices. It is suggested that SO forms on grain surfaces via oxygen addition to HS, and SO_2 forms via oxygen addition to SO and/or via the association of two SO molecules. OCS can potentially form via the addition of oxygen to CS, the addition of sulfur to CO and/or the association of HS and CO. Experiments also predict that H_2S_2 should be made on the grains via the association of two HS molecules. Further evidence on grain-surface chemistry of sulfur-bearing species is hidden in sulfur-bearing complex organics. The S-containing methanol analog, CH_3SH, has been detected towards the cold core B1 (Cernicharo et al., 2012); the hot core G327.3-0.6 (Gibb et al., 2000); Orion KL (Kolesniková et al., 2014); the O-type protostar IRAS 16547-4247 (Zapata et al., 2015); Sgr B2(N2) (Linke et al., 1979) and in the EMoCA survey (Müller et al., 2016). The S-containing ethanol analog, C_2H_5SH, has only been detected towards Orion KL; while searches towards Sgr B2(N2) remain uncertain (Müller et al., 2016). The network of sulfur chemistry on grain surfaces remains to be verified with detailed models and observations.

Sulfur-bearing species have also been detected in numerous places in the Solar System and several comets. A large reservoir of sulfur is found on Jupiter's moon Io, which has an atmosphere dominated by SO_2, as a result of active volcanic eruptions (e.g., Jessup et al. 2007). Contrary to the ISM, the majority of cometary detections of sulfur-bearing molecules belong to H_2S and S_2 (Ahearn et al., 1983; Mumma and Charnley, 2011). Only towards the brightest comet Hale-Bopp has a greater diversity been observed, including OCS, SO_2 and H_2CS. Currently, some of the most unique data to date are streaming in

from the *Rosetta* mission on comet 67P/Churyumov-Gerasimenko (67P/C-G hereafter). With the ROSINA instrument aboard the orbiter, the coma has been shown to contain H_2S, OCS, SO, SO_2, CS_2 and S_2 (and tentatively CS, as the mass spectrometer cannot distinguish it from CO_2) gases (Le Roy et al., 2015). Furthermore, S_3, S_4, CH_3SH, and C_2H_6S have now been detected (Calmonte et al., 2016, subm.) and information on isotopologues will be available soon (Calmonte et al. in prep.) It remains to be understood why surface sniffing of 67P/C-G by COSAC did not reveal any sulfur-bearing species (Goesmann et al., 2015). By piecing together the sulfur puzzle from the earliest diffuse phases to the oldest cometary probes, it may be possible to disentangle the history of volatiles and refractories simultaneously, as they are formed and assembled into larger bodies.

In this work, the sulfur trail is analyzed from the stance of the sulfur budget towards a low-mass protostar and how it compares to that of 67P/C-G, as unraveled by the ROSINA team. IRAS 16293-2422 is an embedded low-mass protostellar binary (Class 0/I) with a separation of 5.1″ or 620 AU (assuming a distance of 120 pc) and a combined luminosity of 21 ± 5 $L_\odot$. The system is associated with one collimated pair of outflow lobes in the NE-SW direction and one less collimated in the E-W direction. A full overview of the physical and chemical properties of the source are presented in Jorgensen et al. (2016, under rev.). There is a clear chemical differentiation between the A and B sources. Source A is significantly richer in sulfur-bearing species, as revealed with earlier interferometric studies (Jørgensen et al., 2011). Furthermore, the spatial distribution of the molecules varies, for example, CS is present on large scales in the envelope. The single dish survey with the CSO and JCMT telescopes detected CS, $C^{34}S$, SO, ^{34}SO, $S^{18}O$, SO, SiS, ^{29}SiS, HCS^+, OCS, $OC^{34}S$, $O^{13}CS$, ^{18}OCS, H_2S, HDS, o- and p-H_2CS, $H_2C^{34}S$, $H_2^{13}CS$, SO_2 (Blake et al. 1994; Dishoeck et al. 1995a and reanalyzed by Schöier et al. 2002), while the single dish TIMASSS survey with IRAM-30 m and JCMT-15 m facilities expanded the list with $^{34}SO_2$, ^{13}CS, $C^{33}S$, HDCS and C_2S (Caux et al., 2011). Interferometric observations with the SMA revealed the spatial distribution of CS, H_2CS, OCS, ^{33}SO, $^{33}SO_2$, $SO^{17}O$, ^{13}CS, $H_2C^{34}S$, $O^{13}CS$, ^{34}SO and $^{34}SO_2$ around the binary system (Jørgensen et al., 2011). IRAS 16293-2422 has been targeted with ALMA in Band 9 in terms of $^{34}SO_2$, $^{33}SO_2$ and SO (Baryshev et al., 2015).

This paper presents the full inventory of sulfur-bearing molecules towards IRAS 16293-2422, based on ALMA Band 7 data (Jorgensen et al. 2016, under rev.). Such interferometric observations make it possible to get away from the large scale outflow-dominated emission and spatially resolve the thermally desorbed molecules close to the central source. Subsequently, ratios between various molecules are compared to those deduced for the coma gases of 67P/C-G, as measured with the ROSINA instrument (Calmonte et al., 2016, subm.). Both sets of data are some of the best available for an extrasolar analogue of our Solar System and an innate Solar Nebula tracer - a comet. The differences and similarities between the two have implications for the formation history of our Solar System. Observational details are presented in Section 5.2 and the results are found in Section 5.3. Abundance ratios are computed and compared to cometary values in Section 5.4 and the conclusions are given in Section 5.5.

5.2 IRAS 16293-2422 OBSERVATIONS

This work is based on the large unbiased Protostellar Interferometric Line Survey (PILS; project-id: 2013.1.00278.S, PI: Jes K. Jørgensen) of IRAS 16293-2422 carried out with

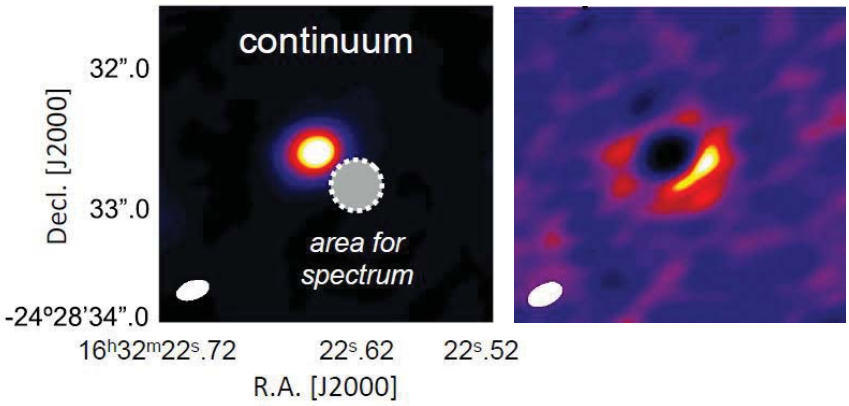

Figure 5.1: Left: ALMA Band 9 image at 690 GHz of IRAS 16293-2422 B from Baryshev et al., (2015). The circle indicates a 0.3″ beam used to extract the Band 9 spectrum shown in that paper. This position is close to the "sweet spot" used in this paper to extract the Band 7 spectrum in a 0.5″ beam by Jørgensen et al. (2016, under rev.). Right: Image of the $^{34}SO_2$ line near 686.6 GHz presented in Baryshev et al., (2015) showing the peak emission near the "sweet spot". Towards the strong continuum source itself, many lines are in absorption.

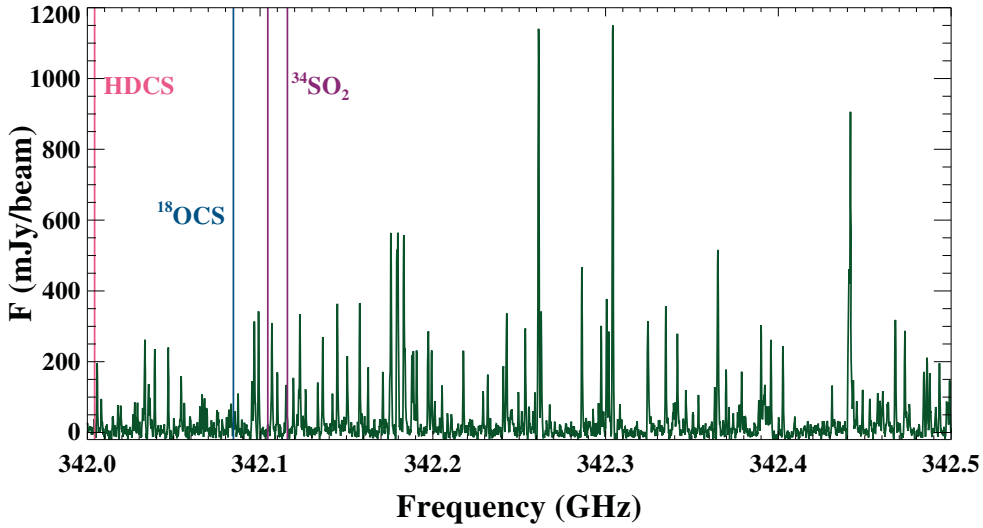

Figure 5.2: A section of the ALMA Band 7 spectrum at the "sweet spot" position illustrating the richness of the spectrum. The lines of some detected sulfur-bearing species that fall in this range are also shown.

ALMA in the $329 - 363$ GHz frequency range (Band 7) with a spectral resolution of 0.2 km s^{-1} and a beam size of $0.5''$ (or 60 AU in diameter, assuming a distance of 120 pc for the source). The local standard of rest (LSR) velocities assumed are 3.1 and 2.7 km s^{-1} for sources A and B, respectively. The data used here are continuum subtracted (based on the statistical method described in Jørgensen et al., 2016, under rev.) and are version 1.2 of the reduced dataset. The observations are a combination of the 12 and the 7 m dish arrays, thereby ensuring that the emission on large scales is recovered, while also spatially resolving the target. The root-mean-square (RMS) noise of the combined dataset is $\sim 7 - 10$ mJy beam^{-1} channel^{-1} (or $\sim 4 - 5$ mJy beam^{-1} km s^{-1} with beam sizes in the $\sim 0.4 - 0.7''$ range). Here, the dataset convolved with a uniform circular restoring beam of $0.5''$ is used. All further details on the PILS survey are available in Jørgensen et al. (2016, under rev.).

The spectral analysis presented in the subsequent section is carried out towards a single position of the dataset - one beam ($\sim$ 60 AU) offset from source B in the E direction (also called the "sweet spot"), which has also been the focal point of Coutens et al., (2016) and Lykke et al. (2016, subm.; twice as far as the position studied in Jørgensen et al. (2016, under rev.) in the same direction). The position is chosen to maximize emission at the higher densities that are on-source towards source B, while being sufficiently far from the source to avoid absorption against the strong dust continuum (Fig. 5.1; as seen in the Band 9 image in fig. 13 of Baryshev et al. 2015). The point also lies in the most outflow-free direction of the region to avoid any additional sources of heating. The spectrum at this "sweet spot" is rich in numerous lines from various species, as illustrated in Fig. 5.2. The recent analysis of complex organic emission in this direction from species such as glycolaldehyde, ethylene glycol, ethylene oxide, acetone and propanal indicate that the temperatures at this point are > 100 K, thus it is likely that the chosen position is probing hot inner envelope or face-on disk material heated by the protostellar B source. The choice to focus on source B has been made as its lines are much narrower than those observed towards source A, hence there is less line confusion and blending.

5.3 RESULTS

The one beam offset position (the "sweet spot") from source B of IRAS 16293-2422 in the PILS Band 7 dataset was searched for lines of all known sulfur-bearing species, especially those detected in 67P/C-G, and several that have been hypothesized to be present. The initial line searching and local thermal equilibrium (LTE) modeling have been carried out with CASSIS[2]. Thereafter, synthetic spectra have been generated with custom IDL routines. LTE is a good assumption in this case, because the densities are high at the chosen position and thus the molecules are expected to be thermalised. The detected species and the best-fitting parameters, assuming a constant $T_{ex} = 125$ K for all species, are tabulated in Table 5.1. This value for T_{ex} has been determined as best-fitting by eye based on a grid of synthetic spectra with 25 K steps. A value of 125 K is in agreement with what has been derived for acetaldehyde, ethylene oxide and propanal (Lykke et al., 2016, subm.), but is approximately a factor of 2 lower than the value of 300 K that has been derived for glycolaldehyde and ethylene glycol (Jørgensen et al., 2016, under rev.; however for a closer half beam offset position in the same direction) and isotopologues of formamide and isocyanic acid (Coutens et al., 2016). A constant source size of $0.5''$ (i.e., assuming that the emitting region equals the beam size) and a full width half-

2 CASSIS has been developed by IRAP-UPS/CNRS, http://cassis.irap.omp.eu

Table 5.1: Best-fitting parameters for detected species at the one beam offset position from source B of IRAS 16293-2422[a]

Species	# of clean lines (# of lines in range)	E_{up} (K)	N (cm^{-2})
SO_2, $v = 0$	13 (101)	$43 - 276$	1.5×10^{15}
$^{34}SO_2$	12 (107)	$35 - 185$	$4.0 \times 10^{14} \longrightarrow N(SO_2) = 5.9 \times 10^{15,e}$
SO, $v = 0$	0 (8)	$81 - 87$	$\leqslant 5.0 \times 10^{14,b}$
OCS, $v = 0$	0 (2)	$237 - 254$	$\geqslant 2.0 \times 10^{16,c}$
OCS, $v_2 = 1$	4 (4)	$986 - 1003$	2.0×10^{17}
$O^{13}CS$	2 (2)	$236 - 253$	$5.0 \times 10^{15} \longrightarrow N(OCS) = 3.5 \times 10^{17,d}$
$OC^{34}S$	3 (3)	$231 - 265$	$1.5 \times 10^{16} \longrightarrow N(OCS) = 3.3 \times 10^{17,e}$
$OC^{33}S$	2 (3)	$234 - 268$	$3.0 \times 10^{15} \longrightarrow N(OCS) = 3.8 \times 10^{17,f}$
^{18}OCS	3 (3)	$238 - 272$	$7.0 \times 10^{14} \longrightarrow N(OCS) = 3.9 \times 10^{17,g}$
$C^{34}S$, $v = 0, 1$	1 (2)	65	$3.0 \times 10^{14} \longrightarrow N(CS) = 6.6 \times 10^{15,e}$
$C^{33}S$, $v = 0, 1$	0 (2)	65	$\leqslant 1.0 \times 10^{14,b} \longrightarrow N(CS) \leqslant 1.3 \times 10^{16,f}$
$C^{36}S$	1 (1)	64	$2.0 \times 10^{13} \longrightarrow N(CS) = 9.5 \times 10^{16,h}$
H_2CS	9 (22)	$102 - 419$	1.5×10^{15}
HDCS	6 (23)	$98 - 322$	$1.5 \times 10^{14} \longrightarrow N(H_2CS) = = 1.5 \times 10^{15,i} - 1.5 \times 10^{16,j}$
HDS	1 (10)	35	$2.0 \times 10^{16} \longrightarrow N(H_2S) = = 2.0 \times 10^{17,i} - 2.0 \times 10^{18,j}$
$HD^{34}S$	1 (7)	35	$1.0 \times 10^{15} \longrightarrow N(HDS) = = 2.2 \times 10^{16,e} \longrightarrow N(H_2S) = = 2.2 \times 10^{17,i} - 2.2 \times 10^{18,j}$

[a] assuming a source size of 0.5″, FWHM of 1 km s^{-1} and $T_{ex} = 125$ K

[b] blended

[c] optically thick

[d] assuming $^{12}C/^{13}C = 70$

[e] assuming $^{32}S/^{34}S = 22$

[f] no estimate for local ISM is available, so a solar ratio of $^{32}S/^{33}S = 125$ is used

[g] assuming $^{16}O/^{18}O = 560$

[h] no estimate for local ISM is available, so a solar ratio of $^{32}S/^{36}S = 4747$ is used

[i] assuming D/H= 0.1, as measured with single-dish observations in HDS/H_2S (table 11 of Dishoeck et al. 1995a)

[j] assuming D/H= 0.01, as recent studies suggest that single dish observations may be overestimating deuteration as a result of underestimating optical depth

maximum (FWHM) of 1 km s^{-1} are assumed. Subsequent subsections describe the details of the detections on a molecule by molecule basis. Isotope ratios for the local interstellar medium (ISM) have been taken from Wilson and Rood, (1994) where available. Otherwise, solar ratios from Asplund et al., (2009) have been employed. A selection of the detected lines and fitted synthetic spectra are available as tables and figures in Appendix 5.7.

5.3.1 *SO_2*

Sulfur dioxide (SO_2) in the $v = 0$ state (CDMS entry 64502) has 101 lines in range of the PILS Band 7 dataset and 13 have been detected in a clean non-blended manner (with upper energy levels, E_u, up to 276 K and Einstein A coefficients $\geqslant 1.2 \times 10^{-4}$). The rest are blended with lines from the many other molecules emitting at this position. The best fitting column density is 1.5×10^{15} cm^{-2}. In the $v_2 = 1$ state (CDMS entry 64503), 83 lines are in range; but only 1 is detected cleanly, since all these lines have very high upper energy levels ($E_u \gtrsim 800$ K) and thus are not expected to be strong. In addition, 107 lines of $^{34}SO_2$ (CDMS entry 66501) are in range and 12 are detected cleanly (with $E_u < 185$ K and Einstein A coefficients $\geqslant 4.35 \times 10^{-5}$). The best fitting column density is 4.0×10^{14} cm^{-2}. For a ratio of $^{32}S/^{34}S = 22$, the column density of SO_2 should be 5.9×10^{15} cm^{-2}, which is no more than a factor of ~ 6 higher than the column density derived from the lines of SO_2 itself. The one beam offset position has also been searched for $^{33}SO_2$ (CDMS entry 65501, 471 lines in range), $S^{18}OO$ (CDMS entry 66502, 169 lines in range) and $S^{17}OO$ (CDMS entry 65502, 137 lines in range); however, all these lines are very weak and lie at most at the noise level of the dataset.

5.3.2 *SO*

Sulfur monoxide (SO) in the $v = 0$ state (CDMS entry 48501) has 8 lines in range. Only 2 are strong enough to be detected and are unfortunately blended with emission from C_3H_2 and C_2H_3CN. Therefore, the LTE fit for this molecule is less certain and only an upper limit can be derived on its column density at a value of 5.0×10^{14} cm^{-2}. This value reflects the maximal contribution SO can have in the observed blended lines. In the $v = 1$ state (CDMS entry 48502), 7 lines are in range, but all are predicted to be weaker than 1 mJy $beam^{-1}$ and are thus under the noise level of the dataset. The position has also been searched for ^{34}SO (CDMS entry 50501, 6 lines in range), ^{33}SO (CDMS entry 49501, 45 lines in range), ^{36}SO (CDMS entry 52502, 6 lines in range), $S^{18}O$ (CDMS entry 50502, 7 lines in range), $S^{17}O$ (CDMS entry 49502, 52 lines in range) and SO^+ (CDMS entry 48010, 2 lines in range); however, all these lines are very weak and are not detected above the noise level of the dataset.

5.3.3 *OCS*

Carbonyl sulfide (OCS) in the $v = 0$ state (CDMS entry 60503) has 2 lines in range ($E_u < 254$ K and Einstein A coefficients $\geqslant 1.15 \times 10^{-4}$); however, both are blended with lines from glycolaldehyde and ethanol. In the $v_2 = 1$ state, there are 4 lines in range, which are all cleanly detected ($E_u < 1003$ K and Einstein A coefficients $\geqslant 1.12 \times 10^{-4}$). Multiple isotopologues have also been detected: $O^{13}CS$ (CDMS entry 61502) with 2 clean lines in range ($E_u < 253$ K and Einstein A coefficients $\geqslant 1.14 \times 10^{-4}$); $OC^{34}S$

(CDMS entry 62505) with 3 clean lines in range ($E_u < 265$ K and Einstein A coefficients $\geqslant 1.07 \times 10^{-4}$); $OC^{33}S$ (CDMS entry 61503) with 3 lines in range and 2 cleanly detected ($E_u < 268$ K and Einstein A coefficients $\geqslant 1.11 \times 10^{-4}$); ^{18}OCS (CDMS entry 62506) with 3 lines in range and all cleanly detected ($E_u < 272$ K and Einstein A coefficients $\geqslant 1.06 \times 10^{-4}$). This is the first time $OC^{33}S$ has been detected towards this source. The presence of ^{33}S has been inferred previously via $^{33}SO_2$ (Jørgensen et al., 2012) and $C^{33}S$ (Caux et al., 2011). All the other isotopologues of OCS have been detected previously (Blake et al., 1994; Caux et al., 2011; Schöier et al., 2002). The dataset was also searched for ^{17}OCS (CDMS entry 61504), $OC^{36}S$ (CDMS entry 64510), $^{18}OC^{34}S$ (CDMS entry 64511), $^{18}O^{13}CS$ (CDMS entry 63503), $O^{13}C^{34}S$ (CDMS entry 63502), $O^{13}C^{33}S$ (CDMS entry 62507); however, the emission from these species is at the noise level of the dataset.

The best-fitting column density of OCS is 2.0×10^{17} cm^{-2} if inferred from the 4 lines of the $v_2 = 1$ state and is 2.0×10^{16} cm^{-2} if approximated from the 2 (blended) lines of the $v = 0$ state, but lines with this state are optically thick. Alternatively, its column density can be inferred indirectly via its optically thin isotopologues: based on $O^{13}CS$ and assuming that $^{12}C/^{13}C = 70$, the column density should be 3.5×10^{17} cm^{-2}; based on $OC^{34}S$ and assuming that $^{32}S/^{34}S = 22$, the column density should be 3.3×10^{17} cm^{-2}; and based on ^{18}OCS and assuming that $^{16}O/^{18}O = 560$, the column density should be 3.9×10^{17} cm^{-2}. These values agree within 30% and are within a factor two from the column density calculated from the $v_2 = 1$ state and a factor of 10 higher than that based on the $v = 0$ state confirming the optical thickness. The average of these 4 values is 3.2×10^{17} cm^{-2}. The average of the values based on the 3 isotopologues is 3.6×10^{17} cm^{-2} and is the best estimate of the column density of OCS at this position. As an additional check, the solar ratio of $^{32}S/^{33}S = 125$ can be used to derive the column density of OCS from its $OC^{33}S$ isotopologue, since no estimate for the local ISM is available. This yields a value of 3.8×10^{17} cm^{-2}, which is consistent with the average value derived from three other isotopologues.

5.3.4 *CS*

Carbon monosulfide (CS) in the $v = 0-4$ state (CDMS entry 44501) has 5 lines in range. Only 1 of them in $v = 0$, $J = 7-6$, is expected to be strong enough to be detected ($E_u = 66$ K and Einstein A coefficient of 8.40×10^{-4}), unfortunately there is some self-absorption in the line, which makes it hard to derive a column density. The $C^{34}S$ isotopologue in the $v = 0, 1$ state (CDMS entry 46501) has 2 lines in range. One is cleanly detected, while the second is too weak to detect as $E_u \sim 1880$ K. The best fitting column density is 3.0×10^{14} cm^{-2}. The $C^{33}S$ isotopologue in the $v = 0, 1$ (CDMS entry 45502) also has 2 lines in range. One is cleanly detected, while the second is again too weak to detect as $E_u \sim 1887$ K. The best fitting column density is 1.0×10^{14} cm^{-2}. The fourth S-isotopologue $C^{36}S$ (CDMS entry 48503) has 1 line in range and it is cleanly detected ($E_u = 64$ K and Einstein A coefficient of 7.66×10^{-4}), giving a best fitting column density 2×10^{13} cm^{-2}. This is the first time detection of ^{36}S towards a low-mass protostar. $C^{36}S$ has been previously detected towards high-mass hot cores (Mauersberger et al., 1996) as a first-time detection of interstellar ^{36}S. More lines are required to fully secure this detection; however, the isotopic ratios are in agreement with solar ratios. Other excitation states and isotopologues lack lines in the observed frequency range, specifically: CS in the $v = 1-0, 2-1$ (CDMS entry 44510) and $v = 2-0$ (CDMS entry 44511) states; $C^{34}S$ in the $v = 1-0$ state (CDMS entry 46510); ^{13}CS in the $v = 0, 1$ and $v = 1-0$ states

(CDMS entries 45501 and 45509); $^{13}C^{34}S$ (CDMS entry 47501) and $^{13}C^{33}S$ (CDMS entry 47501). Meanwhile, $^{13}C^{36}S$ (CDMS entry 49508) has 1 line in range, but it is a clear non-detection.

Assuming the local ISM ratio of $^{32}S/^{34}S = 22$ (Wilson and Rood, 1994), the column density of CS can be estimated at 6.6×10^{15} cm^{-2} from its $C^{34}S$ isotopologue. If this column density is used to fit the detected line of CS suffering from absorption, then the line width is consistent with the value derived from $C^{34}S$. Thus this is the best available estimate of the column density of CS. Again as an additional check, the solar ratio of $^{32}S/^{33}S = 125$ can be used to derive the upper limit on the column density of CS from its $C^{33}S$ isotopologue. This yields a value of 1.3×10^{16} cm^{-2}, which is consistent with the value derived from $C^{34}S$. Furthermore, the solar ratio of $^{32}S/^{36}S = 4747$ can be used to derive the column density of CS from its $C^{36}S$ isotopologue, since no estimate for the local ISM is available. This yields a value of 9.5×10^{16} cm^{-2}, which is only a factor of 1.4 larger than the value derived from $C^{34}S$.

5.3.5 *H_2CS*

Thioformaldehyde (H_2CS; CDMS entry 46509) has 22 lines in range and 9 are cleanly detected ($E_u < 419$ K and Einstein A coefficients $\geqslant 4.57 \times 10^{-4}$. The best fitting column density is 1.5×10^{15} cm^{-2}. In addition, its isotopologue HDCS (CDMS entry 47504) has 23 lines in range, of which 6 are detected cleanly ($E_u < 322$ K and Einstein A coefficients $\geqslant 4.74 \times 10^{-4}$. The best fitting column density is 1.5×10^{14} cm^{-2}. Assuming $D/H = 0.1$, as measured with single-dish observations in HDS/H_2S (table 11 of Dishoeck et al. 1995a), yields a column density of 1.5×10^{15} cm^{-2} for H_2CS, which is in exact agreement with the column density derived based on its own lines. However, recent studies suggest that single dish observations may be overestimating deuteration, either because of sampling colder material or as a result of underestimating optical thickness of the main species (Coutens et al. 2016, Jørgensen et al. 2016, under rev., Persson et al. 2016, in prep.). Thus, if $D/H = 0.01$ is assumed, as typically found in PILS data of other molecules, then the column density of H_2CS may be as high as 1.5×10^{16} cm^{-2}. Other isotopologues have not been detected: $H_2C^{34}S$, $H_2C^{33}S$ and $H_2^{13}CS$ (CDMS entries 48508, 47506 and 47505).

5.3.6 *H_2S*

Hydrogen sulfide (H_2S; CDMS entry 34502) has 1 line in the observed frequency range, however it is a clear non-detection due to a high upper energy level ($E_u = 758$ K) and line weakness (Einstein A coefficient of 6.28×10^{-9}). On the other hand, its isotopologue HDS (CDMS entry 35502) has 10 lines in range. One of those is a clear detection, while the others have upper energy levels that are too high ($E_u > 537$ K) and thus are not expected to be strong. The best-fitting column density is 2.0×10^{16} cm^{-2}. $HD^{34}S$ (CDMS entry 37503) has 7 lines in range. One is cleanly detected, while all others have upper energy levels that are too high ($E_u > 536$ K) to be strong. The best fitting column density is 1.0×10^{15} cm^{-2}. Assuming that $^{32}S/^{34}S = 22$, gives a column density of 2.2×10^{16} cm^{-2} for HDS, which closely agrees with the value derived based on its solo observed line. Other isotopologues are not detected. $H_2^{34}S$ and $H_2^{33}S$ do not have any lines in the observed frequency range (CDMS entries 36504 and 35503). D_2S (CDMS entry 36503) has 4 lines in range; however, only 2 are above the noise level and both

suffer from blending, thus no clear detection is available. $D_2\ ^{34}S$ (CDMS entry 38507) has 2 lines in range, but one is subject to strong absorption at that frequency and the other is blended with $C_2H_5\ ^{13}CN$; thus no confident detection can be claimed.

Assuming D/H= 0.1, as measured with single-dish observations in HDS/H_2S (table 11 of Dishoeck et al. 1995a), the column density of H_2S can be estimated at 2.0×10^{17} cm^{-2} from HDS and at 2.2×10^{17} cm^{-2} from $HD^{34}S$. The two values are in very close agreement and their average of 2.1×10^{17} cm^{-2} is our best estimate of the column density of H_2S at this position. If a ratio of D/H= 0.01 is assumed, as motivated above, then the best estimate increases to 2.1×10^{18} cm^{-2}.

The previously obtained SMA observations of IRAS 16293-2422 have detected a line of H_2S around ~ 216.71 GHz (see fig. 6 of Jørgensen et al. 2011). LTE modelling assuming a beam size of 3″, a spectral resolution of 0.56 km s^{-1} (as given in table 1 of Jørgensen et al. 2011), FWHM of 1 km s^{-1} and a source size of 0.5″ (as assumed for the ALMA observations) shows that the line is optically thick. In order to match the observed line intensity of ~ 2 Jy beam^{-1}, a larger source size is necessary. Upon the assumption of a source 1″ in size, the lower limit on the column density of H_2S is 4.0×10^{16} cm^{-2}. This illustrates the uncertainty in the emitting area of this molecule. Alternatively, a non-detection of the sole line in range of the SMA observations of $H_2^{34}S$ at ~ 226.70 GHz does not yield a strongly constraining column density estimate. Assuming the same parameters, then in order to be weaker than the 3σ noise level (where σ = 0.24 Jy beam−1 chan^{-1}; table 1 of Jørgensen et al. 2011), the column density of $H_2^{34}S$ must not exceed 4.0×10^{19} cm^{-2}. Assuming $^{32}S/^{34}S$= 22, the upper limit on the column density of H_2S is 8.8×10^{20} cm^{-2}. This is consistent with the limits obtained with the uncertain limit obtained from HDS, but is less constraining than the other. Dedicated high resolution ALMA observations are needed in order to constrain the spatial distribution and column density of H_2S.

5.3.7 *Other species*

Other species that were searched for and have lines in range of the dataset, but are not detected at this position include oxyhydroxysulfonium (cis-$HOSO^+$; CDMS entry 65510), sulfur chain species S_2, S_3, S_4 (JPL entries 64001, 96002, 128001), HS_2 (CDMS entry 65509), H_2S_2 (CDMS entry 66507), S_2O (CDMS entry 80503), cis-S_2O_2 (CDMS entry 96501), silicon monosulfide (SiS) and its isotopologues (CDMS entries 62508, 62509, 61508, 64514, 61506, 61507, 62510, 62511, 63504, 62512, 65507, 64513, 63505, 66505, 60506, 60507, 60508), HSiS (CDMS entry 61512), H_2SiS (CDMS entry 62513), OSiS (CDMS entry 76517), atomic S (CDMS entry 32511), $HOCS^+$ (CDMS entry 61510), $HSCO^+$ (CDMS entry 61509), t- and c-HC(O)SH (CDMS entries 62515 and 62516), SH^- (CDMS entry 33504), SH^+ (CDMS entry 33505), HSO (CDMS entry 49512), g- and a-C_2H_5SH (CDMS entries 62523 and 62524).

5.4 DISCUSSION

5.4.1 *Comparison with single dish observations*

The presented interferometric observations are capable of spatially resolving the hot inner regions near the continuum peak source B, which resolves issues such as beam dilution that plague single dish observations. Moreover, it is possible to detect weaker lines from multiple isotopologues, thereby allowing a better determination of the optical

Table 5.2: Abundance ratios relative to H_2S and OCS of IRAS 16293-2422 as measured with these interferometric ALMA observations and previous single dish work[k]

Species	N (cm^{-2})	Abundance ratio relative to H_2S (%)				Abundance ratio relative to OCS (%)			
		sweet spot[l]	constant	inner	outer	sweet spot[l]	constant	inner	outer
H_2S	$2.1 \times 10^{17,i} - 2.1 \times 10^{18,j}$	100	100	-	-	$58.3 - 583$	23	-	-
OCS	3.6×10^{17}	$171 - 17$	438	-	-	100	100	100	100
SO	5.0×10^{14}	$0.2 - 0.02$	275	-	-	0.14	63	100	117
SO_2	1.5×10^{15}	$0.7 - 0.07$	39	-	-	0.4	8.9	40	15
CS	6.6×10^{15}	$3.1 - 0.3$	188	-	-	1.8	43	-	-
H_2CS	1.5×10^{15}	$0.7 - 0.07$	13	-	-	0.4	3	1.2	3.3

[i,j] see footnotes of Table 5.1

[k] tables 5 and 6 of Schöier et al., (2002))

[l] one beam (~ 60 AU) offset from source B of IRAS 16293-2422 in the E direction

Table 5.3: Abundance ratios relative to H_2S and OCS of IRAS 16293-2422 in comparison to those of 67P/C-G[m]

Species	N (cm^{-2})	Abundance ratio relative to H_2S (%)		Abundance ratio relative to OCS (%)		
		sweet spot[l]	67P/C-G	sweet spot[l]	67P/C-G	W33A[n]
H_2S	$2.1 \times 10^{17,i} - 2.1 \times 10^{18,j}$	100	100	$58.3 - 583$	2257	$< 30 - 90$
OCS	3.6×10^{17}	$171 - 17$	4.43 ± 0.15	100	100	100
SO	5.0×10^{14}	$0.2 - 0.02$	7.06 ± 0.17	0.14	159	-
SO_2	1.5×10^{15}	$0.7 - 0.07$	12.5 ± 0.3	0.4	282	$3 - 7$
CS	6.6×10^{15}	$3.1 - 0.3$	-	1.8	-	-

[m] bulk coma ROSINA measurements corrected for photodissociation and ionization (table 3 of Calmonte et al., 2016, subm.)

[n] interstellar ice ratios for W33A - the strongest ice source; Boogert et al., (1997) and Tak et al., (2003)

depth. By comparing abundance ratios of interferometric and single dish observations, it is possible to disentangle whether molecules primarily emit on large scales or small inner scales near the source, or whether they are associated with outflows. For this purpose, Table 5.2 has been compiled with molecular ratios of the detected species relative to H_2S and OCS (where available), as obtained with the PILS survey with ALMA and with a compilation of single dish observations of (Schöier et al., 2002). Since single dish observations cannot spatially resolve the emission, three different sets of abundances are typically provided: one assuming a constant profile and one assuming a jump profile, giving an inner (hot) abundance and an outer (cold) one.

From Table 5.2 it can be seen that relative to H_2S the interferometric ratio for OCS is lower by a factor of $3-26$, for SO by $3-4$ orders of magnitude, and for SO_2, CS, and H_2CS by $2-3$ orders of magnitude than the ratio measured with single dish observations based on a constant abundance assumption. When measured relative to OCS, the interferometric ratio for H_2S is a factor of $2.5-25$ higher than the single dish value. Meanwhile, all other interferometric ratios are still lower: for SO by 3 orders of magnitude, for SO_2 by a factor of ~ 21, for CS by a factor of ~ 23 and for H_2CS by a factor ~ 7. When comparing relative to OCS with the inner and outer ratios, the differences are either comparable or exacerbated further. The inner ratio is expected to be most relevant as it is the closest estimate for the hot component. This implies that most of the emission from these sulfur-bearing species in single-dish measurements is dominated by large scales, i.e., those associated with outflows emanating from the source. This is in agreement with the largest differences being seen for SO - a well-known shock tracer that shows larger line widths in the single dish data.

The interferometric column density estimates for SO and SO_2 likely give limits on the maximal quantities of these species being produced via grain-surface reactions and then immediately thermally desorbed in the "sweet spot". However, SO and SO_2 can also be efficiently produced at high ($100\ K < T < 300\ K$) temperatures in the gas-phase via reactions of S and OH. OH is readily available at such high temperatures and seen in *Herschel* data (Wampfler et al., 2013). Single dish observations likely probe all these components at the same time due to the very large beam size. Furthermore, the position analysed in this work - the "sweet spot", is not the location with the strongest emission of sulfur-species. In fact, such species peak towards source A of IRAS 16293-2422, which powers stronger outflows in its vicinity. The analysis of a point near source A is the subject of future work. These will then also be compared with the results obtained by Oya et al., (2016), which suggest that OCS traces the infalling–rotating envelope, while H_2CS is associated with the centrifugal barrier of the disk and also with the envelope.

5.4.2 *Comparison with ROSINA data on 67P/C-G*

IRAS 16293-2422 is thought to be analogous to our innate Solar Nebula as it is one of the most chemically rich low-mass protostellar systems. Meanwhile, it has also been postulated that comets are the most pristine tracers of the protoplanetary disk that evolved into the Solar System that we have today. Therefore, it is interesting to compare the chemical inventories of comets to those of IRAS 16293-2422 in order to quantify the chemical budgets of Solar and extrasolar building blocks of planetary systems (Bockelée-Morvan et al., 2015; Schöier et al., 2002). The emission seen in the hot inner regions of this protostellar core could potentially be tracing solid species that are undergoing thermal desorption and thus is in fact probing the hidden solid reservoir of planet-building material.

Table 5.3 contains the abundance ratios relative to H_2S and OCS at the "sweet spot" of IRAS 16293-2422 in comparison to those of 67P/C-G, as obtained for the bulk coma with ROSINA measurements corrected for photodissociation and ionization (table 3 of Calmonte et al., 2016, subm.). It can be seen that for OCS the "sweet spot" ratio relative to H_2S is a factor of $\sim 3.8-39$ higher than that for 67P/C-G, for SO a factor of $\sim 3.5-35$ lower and for SO_2 a factor of $\sim 1.8-18$ lower. Relative to OCS the "sweet spot" ratio for H_2S is a factor of $\sim 3.9-39$ lower than that for 67P/C-G, for SO is ~ 3 orders of magnitude and for SO_2 is ~ 2 orders or magnitude lower. Such large differences are consistent with the fact that H_2S has not yet been detected in interstellar ices, but OCS has.

These results indicate that in the case of IRAS 16293-2422 there is significantly more OCS available, while for 67P/C-G more H_2S is present. Potentially, this has to be to do with the amount of solid carbon monoxide (CO) available in these systems. OCS is more easily produced via grain-surface chemistry when CO ice is abundant. CO undergoes thermal desorption into the gas-phase around 20 K and at that point the production of OCS is inhibited. Dedicated chemical models need to be run in order to quantify such effects. Nevertheless, this could be an initial indication of our Solar System being born in a somewhat warmer environment, i.e., > 20 K rather than in the $10-15$ K regime, which would lead to less CO being available on the grains for the synthesis of OCS. This scenario is also favored from the point of view of oxygen chemistry and the detection of O_2 on 67P/C-G (Bieler et al. 2015, Taquet et al., 2016, subm.). An enhanced availability of CO in the case of IRAS 16293-2422 is supported by the fact that the cold surrounding core is still observed in its current Class 0 phase. Such temperature differences should also be noticeable in terms of complex organics in these systems and the comparison in terms of sulfur-bearing and other complex organics are the topic of future publications.

Table 5.3 also contains the abundance ratios relative to OCS as observed towards W33A - the strongest ice source, which trace the interstellar ice content (Boogert et al., 1997; Tak et al., 2003). It is necessary to look towards the brightest available source in order to detect these trace species in the ISM ice, which is dominated by water ice. It can immediately be noted that for H_2S and SO_2, the ISM ice ratios relative to OCS are much closer to those of the "sweet spot" than for 67P/C-G. This could potentially be an indication that the 67P/C-G abundances are indeed indicating initial conditions that are different from those towards other protostellar sources.

Another stark difference between the IRAS 16293-2422 observations and 67P/C-G is that the former is shown to contain CS and H_2CS, both of which are not detected towards 67P/C-G. Both of these species have gas-phase routes to formation, as well as grain-surface pathways. Finally, the ROSINA team has also discovered sulfur chain fragments, such as S_2, S_3 and S_4 in their data on 67P/C-G (Calmonte et al., 2016, subm.). Such species have not been detected towards protostars and the search is ongoing (Martín-Doménech et al., 2016), as these species provide a link between the volatile sulfur-bearing molecules and the refractory component of cometary and protoplanetary materials.

5.4.3 *Comparison with models*

Efforts on chemical modelling of sulfur networks have recently been revived by Woods et al., (2015). The authors computed the abundances of sulfur-bearing species for hot core conditions upon the inclusion of recent experimental and theoretical data into their chemical network, including a refractory sulfur residue. The modelled abundance ratios

(relative to either H_2S or OCS; as tabulated in table 9 of Woods et al., (2015) for the standard model with the interstellar cosmic ray ionization rate of 1.3×10^{-17} s^{-1}) can be compared to those derived in this work for the "sweet spot" of IRAS 16293-2422 B. An agreement within one order of magnitude is found for OCS and CS, and the modelled ratios are in range of the observed "sweet spot" ratios for H_2S. The modelled ratios for H_2CS are three orders of magnitude higher, which maybe explained by the fact that the grain-surface network used in the models is fairly small and the grain-surface chemistry is not fully accounted for. H_2CS is expected to be involved in many grain-surface reactions and will likely be used up for synthesis of larger sulfur-bearing species, such as CH_3SH (analogous to the sequential hydrogenation of CO leading to CH_3OH with H_2CO as an intermediate).

The ratios for SO and SO_2 vary by many orders of magnitude between these observations and the models of Woods et al., (2015). This likely has to do with the fact that the models have been run for a very long time of 10^7 yr, which implies that many gaseous species are driven into SO and SO_2, leading to their overproduction. At earlier times (as seen in fig. 6 of Woods et al., (2015)), the model results have a closer agreement with observations of the "sweet spot" for SO. SO_2 remains too high nevertheless, which may have to do with thermal desorption being calculated via an efficiency factor. The development of a full gas-grain chemical network for sulfur, including grain-surface chemistry, is the topic of future research.

5.5 CONCLUSIONS

In this paper the sulfur inventory of the "sweet spot" in the vicinity of source B in the binary protostellar system IRAS 16293-2422 has been presented. The ALMA Band 7 data analyzed are part of the PILS survey towards this target. Sulfur is thought to be a unique simultaneous tracer of both the volatile and refractory components. By comparing molecular ratios observed towards IRAS 16293-2422 - a Solar System proxy, and those obtained for 67P/C-G - a most pristine available tracer of the innate Solar Nebula, the chemical links between the early embedded protostellar phases and the protoplanetary building blocks can be explored. The main conclusions of this paper are as follows:

1. The sulfur-bearing species previously detected towards IRAS 16293-2422 have now been firmly detected towards the "sweet spot" and spatially resolved with ALMA: SO_2 in the $v = 0$, $^{34}SO_2$, OCS in the $v_2 = 1$ state, $O^{13}CS$, $OC^{34}S$, $OC^{33}S$ (first-time detection towards this source), ^{18}OCS, H_2CS and HDCS. Furthermore, several are detected tentatively due to a lack of lines and/or blending: SO_2 in the $v_2 = 1$ state, SO in the $v = 0$ state, OCS in the $v = 0$ state, CS in the $v = 0 - 4$ state, $C^{34}S$, $C^{33}S$, $C^{36}S$ (tentative first time detection towards a low-mass protostar), HDS and $HD^{34}S$.

2. In comparison to earlier single dish observations, the molecular ratios determined from interferometric data can be several orders of magnitude lower. This implies that the single dish data are dominated by large scale outflow-dominated emission.

3. In comparison to ROSINA measurements of the coma gases of 67P/C-G, IRAS 16293-2422 molecular ratios differ significantly, potentially by as much as several orders of magnitude. In particular, IRAS 16293-2422 contains much more OCS than

H_2S, potentially indicating that our Solar System was born in a somewhat warmer ($T \sim 20$ K), CO ice-poor environment.

Future publications will explore the protostellar-cometary connection via isotopic ratios and a full set of complex organic species, thereby isolating chemical links formed during cold phases of evolution that are dominated by grain-surface chemistry.

5.6 ACKNOWLEDGEMENTS

The authors would like to thank Dr. Catherine Walsh, Dr. Vianney Taquet and Mr. Ko-Ju Chuang for useful discussions on sulfur chemistry. This work is supported by a Huygens fellowship from Leiden University, by the European Union A-ERC grant 291141 CHEMPLAN, by the Netherlands Research School for Astronomy (NOVA) and by a Royal Netherlands Academy of Arts and Sciences (KNAW) professor prize.

5.7 APPENDIX

A SELECTION OF LINES AND SYNTHETIC SPECTRA OF S-BEARING SPECIES IN THE PILS BAND 7 DATASET

Similar plots will follow for all the other detected molecules.

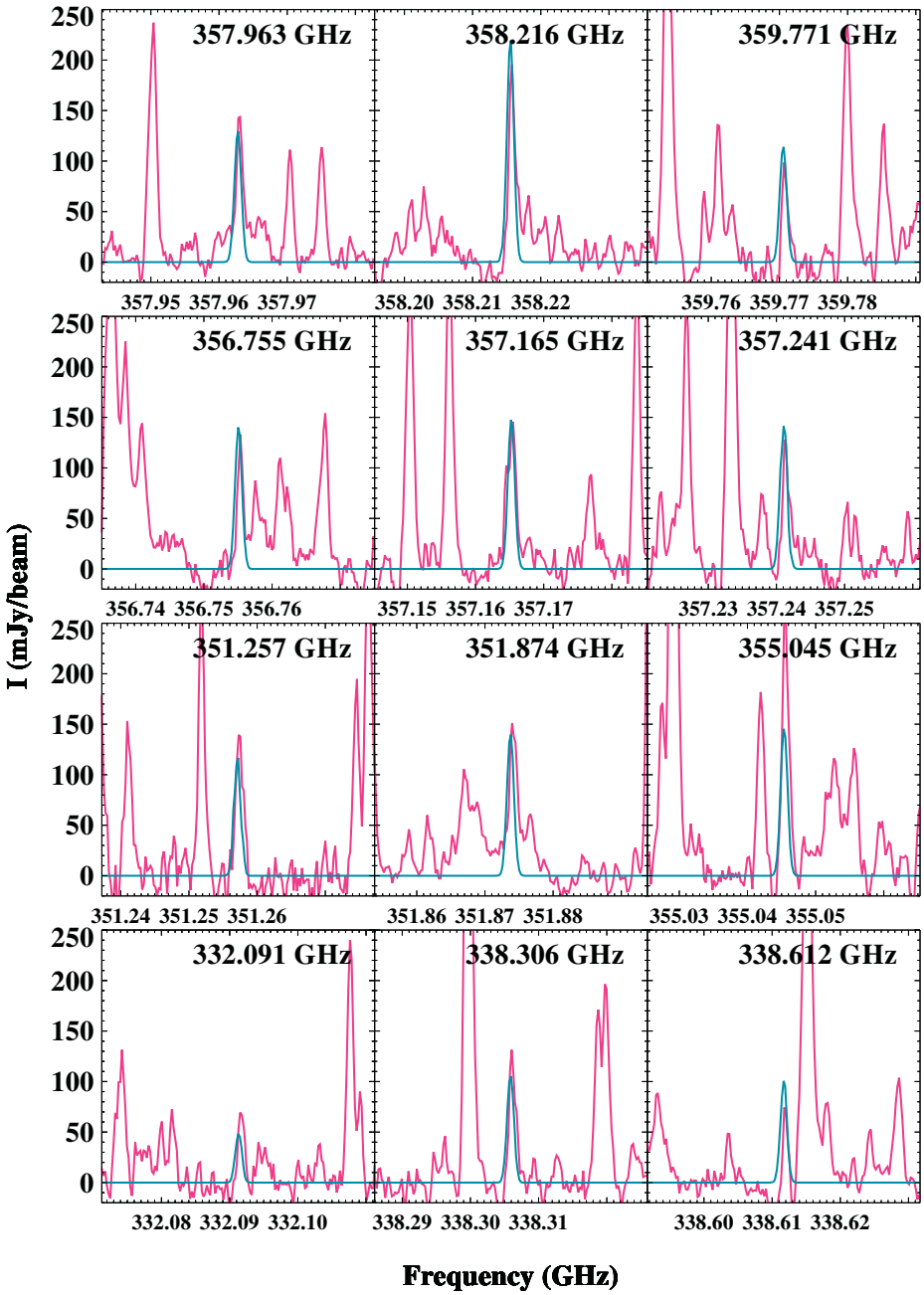

Figure 5.3: Twelve selected lines of SO_2 in the $v = 0$ state.

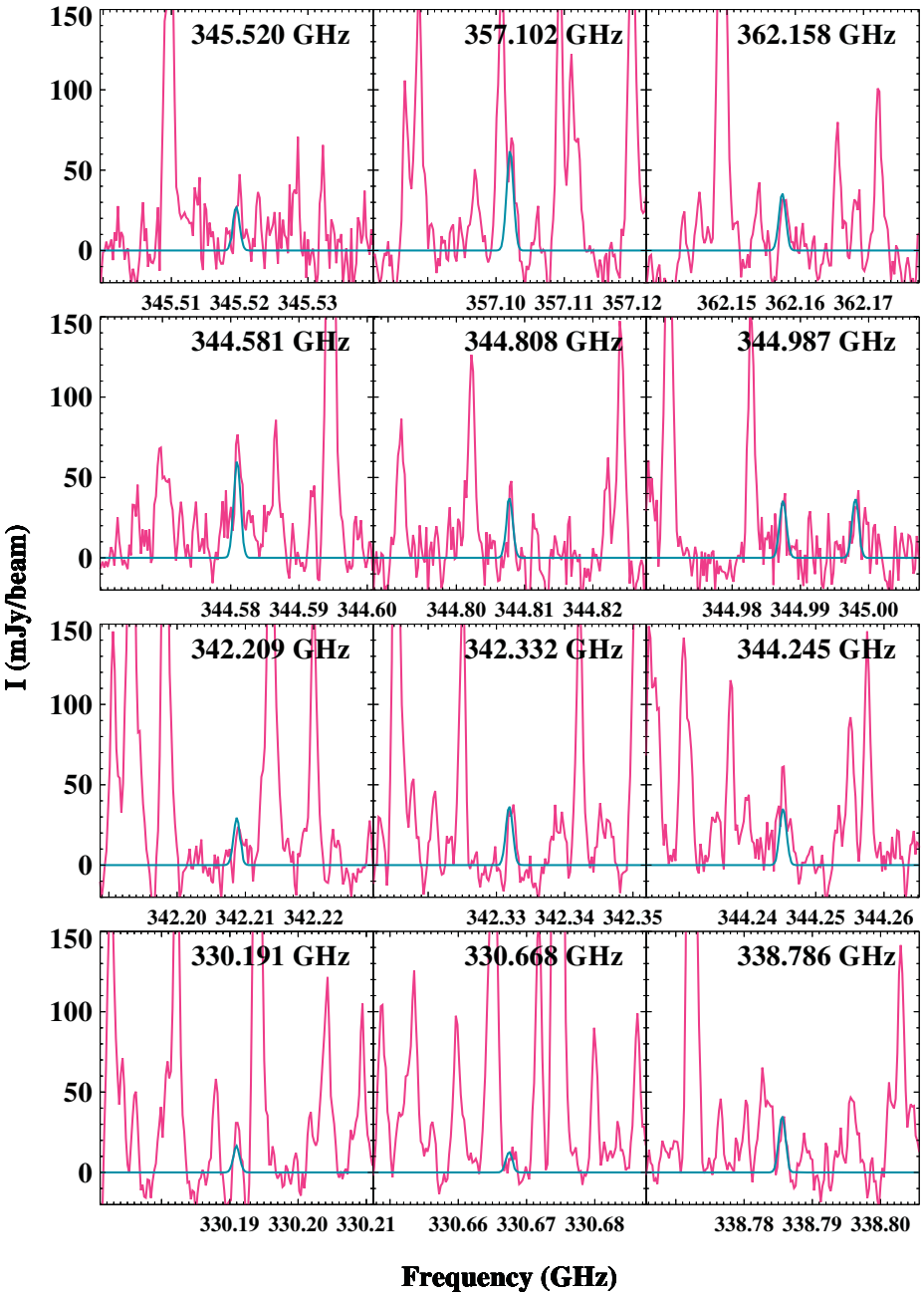

Figure 5.4: Twelve selected lines of $^{34}SO_2$.

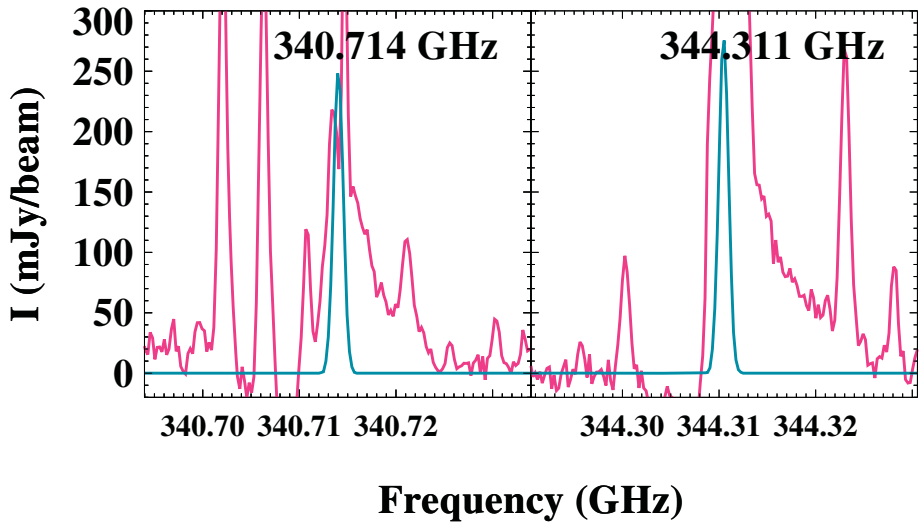

Figure 5.5: Two selected lines of SO in the $v = 0$ state.

SPECTROSCOPIC LABORATORY INFORMATION

The database sources, CDMS or JPL catalogs with their entry numbers, have been provided in the main text for all the species that we have searched for. In addition, the primary references on which these entries are based along with references for the dipole moments for all detected or possibly detected species are given below. Furthermore, the references with laboratory measurements in the range of our survey in cases in which the primary reference does not cover such data or if these data are an important contribution to the line list are also included.

SO_2

The $v = 0$ and $v_2 = 1$ entries for the main isotopic species are based on Müller and Brünken, (2005), those for $^{34}SO_2$ - on Belov et al., (1998). The dipole moment of SO_2 in several vibrational states was determined by Patel et al., (1979).

SO

The SO entry is based on Bogey et al., (1997). Its dipole moment was measured by Powell and Lide, (1964).

OCS

The main sources for the OCS entries are Golubiatnikov et al., (2005) (OCS, $v = 0$), Morino et al., (2000) (OCS, $v_2 = 1$), Dubrulle et al., (1980) ($O^{13}CS$, $OC^{34}S$, $OC^{33}S$). Dipole moment values were determined for OCS in various vibrational states and for several isotopic species by Tanaka et al., (1985).

CS

The CS entries are based on Müller et al., (2005), and the main sources of laboratory data are Bogey et al., (1982) and Ahrens and Winnewisser, (1999). The dipole moments of CS in $v = 0$ and 1 were measured by Winnewisser and Cook, (1968).

H_2CS

The H_2CS data are largely from Maeda et al., (2008), those of HDCS are from Minowa et al., (1997). Fabricant et al., (1977) determined the dipole moment of H_2CS.

H_2S

The H_2S entry is based to a considerable extent on Belov et al., (1995). The entries of HDS and $HD^{34}S$ are based on Camy-Peyret et al., (1985). The HDS transition frequencies with microwave accuracy were summarized by Helminger et al., (1971). Hillger and Strandberg, (1951) reported a small number of $HD^{34}S$ and HDS transition frequencies. Viswanathan and Dyke, (1984) determined dipole moments of H_2S, HDS and D_2S.

CH_3SH

The methyl mercaptan (methanethiol) entry is based on Xu et al., (2012) with transition frequencies in the range of our survey from Bettens et al., (1999). The information on the dipole moment components was provided by Tsunekawa et al., (1989).

BIBLIOGRAPHY

M. F. A'Hearn, ARA&A **49**, 281 (2011).

ALMA Partnership et al., ApJ **808**, L3 (2015).

ALMA Partnership et al., ALMA Cycle 4 Technical Handbook (2016).

F. C. Adams, ARA&A **48**, 47 (2010).

F. C. Adams and F. H. Shu, ApJ **308**, 836 (1986).

M. Agúndez and V. Wakelam, Chemical Reviews **113**, 8710 (2013).

M. F. Ahearn, D. G. Schleicher, and P. D. Feldman, ApJ **274**, L99 (1983).

V. Ahrens and G. Winnewisser, Zeitschrift Naturforschung Teil A **54**, 131 (1999).

Y. Aikawa, Chemical Reviews **113**, 8961 (2013).

Y. Aikawa and E. Herbst, A&A **351**, 233 (1999).

Y. Aikawa and H. Nomura, ApJ **642**, 1152 (2006).

Y. Aikawa et al., ApJ **486**, L51 (1997).

Y. Aikawa et al., Faraday Discussions **109**, 281 (1998).

Y. Aikawa et al., ApJ **552**, 639 (2001).

Y. Aikawa et al., A&A **386**, 622 (2002).

Y. Aikawa et al., ApJ **674**, 984 (2008).

Y. Aikawa et al., A&A **538**, A57 (2012).

V. Akimkin et al., ApJ **766**, 8 (2013).

R. Alexander et al., *Protostars and planets vi, volatiles in protoplanetary disks* (Univ. Arizona Press, Tucson, AZ, 2014), pp. 475–496.

Y. Alibert et al., A&A **434**, 343 (2005).

Y. Alibert et al., A&A **558**, A109 (2013).

L. J. Allamandola, A. G. G. M. Tielens, and J. R. Barker, ApJS **71**, 733 (1989).

K. Altwegg et al., Science Advances **2** (2016).

D. E. Anderson et al., ApJ **779**, 141 (2013).

S. Andersson and E. F. van Dishoeck, A&A **491**, 907 (2008).

S. Andersson et al., J. Chem. Phys. **124**, 064715 (2006).

P. André et al., *Protostars and planets vi, volatiles in protoplanetary disks* (Univ. Arizona Press, Tucson, AZ, 2014), pp. 27–51.

P. André et al., *Protostars and planets vi, volatiles in protoplanetary disks* (Univ. Arizona Press, Tucson, AZ, 2014), pp. 27–51.

C. Arasa et al., J. Chem. Phys. **132**, 184510 (2010).

C. Arasa et al., J. Chem. Phys. **134**, 164503 (2011).

C. Arasa et al., J. Chem. Phys. **117**, 7064 (2013).

H. G. Arce et al., ApJ **681**, L21 (2008).

P. J. Armitage, ARA&A **49**, 195 (2011).

M. Asplund et al., ARA&A **47**, 481 (2009).

M. Audard et al., *Protostars and planets vi, volatiles in protoplanetary disks* (Univ. Arizona Press, Tucson, AZ, 2014), pp. 387–410.

P. Ayotte et al., J. Geophys. Res. **106**, 33387 (2001).

A. Bacmann et al., A&A **541**, L12 (2012).

N. Balucani, C. Ceccarelli, and V. Taquet, MNRAS **449**, L16 (2015).

A. Bar-Nun and D. Laufer, Planet. Space Sci. **86**, 160 (2013).

A. Bar-Nun, G. Notesco, and T. Owen, Icarus **190**, 655 (2007).

A. M. Baryshev et al., A&A **577**, A129 (2015).

A. Belloche et al., Science **345**, 1584 (2014).

S. P. Belov et al., Journal of Molecular Spectroscopy **173**, 380 (1995).

S. P. Belov et al., Journal of Molecular Spectroscopy **191**, 17 (1998).

M. T. Beltrán and W. J. de Wit, A&A Rev. **24**, 6 (2016).

C. J. Bennett, C. Pirim, and T. M. Orlando, Chemical Reviews **113**, 9086 (2013).

W. Benz et al., *Protostars and planets vi, volatiles in protoplanetary disks* (Univ. Arizona Press, Tucson, AZ, 2014), pp. 691–713.

E. A. Bergin et al., Proceedings of the National Academy of Science **112**, 8965 (2015).

O. Berné and A. G. G. M. Tielens, Proceedings of the National Academy of Science **109**, 401 (2012).

M. Bertin et al., Phys. Chem. Chem. Phys. **14**, 9929 (2012).

M. Bertin et al., ApJ **817**, L12 (2016).

C. Bertout, G. Basri, and J. Bouvier, ApJ **330**, 350 (1988).

F. L. Bettens et al., ApJ **510**, 789 (1999).

A. Bieler et al., Nature **526**, 678 (2015).

S. E. Bisschop et al., A&A **449**, 1297 (2006).

S. E. Bisschop et al., A&A **488**, 959 (2008).

B. Bitsch, M. Lambrechts, and A. Johansen, A&A **582**, A112 (2015).

N. Biver et al., A&A **566**, L5 (2014).

N. Biver et al., Science Advances **1**, 1500863 (2015).

G. A. Blake et al., ApJ **315**, 621 (1987).

G. A. Blake, E. F. van Dishoeck, and A. I. Sargent, ApJ **391**, L99 (1992).

G. A. Blake et al., ApJ **428**, 680 (1994).

M. D. Boamah et al., Faraday Discuss. **168**, 249 (2014).

D. Bockelée-Morvan et al., A&A **353**, 1101 (2000).

D. Bockelée-Morvan et al., A&A **583**, A6 (2015).

M. Bogey, C. Demuynck, and J. L. Destombes, Journal of Molecular Spectroscopy **95**, 35 (1982).

M. Bogey et al., Journal of Molecular Spectroscopy **182**, 85 (1997).

R. C. Bohlin, B. D. Savage, and J. F. Drake, ApJ **224**, 132 (1978).

A. C. A. Boogert et al., A&A **317**, 929 (1997).

A. C. A. Boogert et al., ApJ **729**, 92 (2011).

A. C. A. Boogert et al., ApJ **777**, 73 (2013).

A. C. A. Boogert, P. A. Gerakines, and D. C. B. Whittet, ARA&A **53**, 541 (2015).

S. Bottinelli et al., ApJ **615**, 354 (2004).

S. Bottinelli et al., ApJ **617**, L69 (2004).

C. Brinch and J. K. Jørgensen, A&A **559**, A82 (2013).

C. Brinch, R. J. van Weeren, and M. R. Hogerheijde, A&A **489**, 617 (2008).

F. A. v. Broekhuizen et al., A&A **441**, 249 (2005).

W. A. Brown and A. S. Bolina, MNRAS **374**, 1006 (2007).

D. Brownlee et al., Science **314**, 1711 (2006).

S. Bruderer et al., ApJ **700**, 872 (2009).

S. Bruderer et al., ApJ **720**, 1432 (2010).

M. L. Cable et al., Chemical Reviews **112**, 1882 (2012).

J. Cami et al., Science **329**, 1180 (2010).

C. Camy-Peyret et al., Journal of Molecular Spectroscopy **109**, 300 (1985).

F. Capaccioni et al., Science **347**, aaa0628 (2015).

P. Caselli and C. Ceccarelli, A&A Rev. **20**, 56 (2012).

P. Cassen and A. Moosman, Icarus **48**, 353 (1981).

E. Caux et al., A&A **532**, A23 (2011).

S. Cazaux and A. G. G. M. Tielens, ApJ **604**, 222 (2004).

S. Cazaux et al., ApJ **593**, L51 (2003).

C. Ceccarelli, D. J. Hollenbach, and A. G. G. M. Tielens, ApJ **471**, 400 (1996).

C. Ceccarelli et al., A&A **355**, 1129 (2000).

C. Ceccarelli et al., *In henrik b., klessen r. s., dullemond c. p., henning t. eds, protostars and planets vi, deuterium fractionation: the ariadne's thread from the precollapse phase to meteorites and comets today* (Univ. Arizona Press, Tucson, AZ, 2014), pp. 859–882.

J. Cernicharo et al., ApJ **759**, L43 (2012).

R. Cesaroni et al., A&A **345**, 949 (1999).

S. B. Charnley, A. G. G. M. Tielens, and T. J. Millar, ApJ **399**, L71 (1992).

Y.-J. Chen et al., ApJ **798**, 80 (2015).

A. C. Cheung et al., Physical Review Letters **21**, 1701 (1968).

A. C. Cheung et al., Nature **221**, 626 (1969).

T.-L. Chou et al., ApJ **796**, 70 (2014).

K.-J. Chuang et al., MNRAS **455**, 1702 (2016).

F. J. Ciesla, ApJ **740**, 9 (2011).

F. J. Ciesla et al., ApJ **804**, 9 (2015).

L. I. Cleeves, F. C. Adams, and E. A. Bergin, ApJ **772**, 5 (2013).

L. I. Cleeves et al., Science **345**, 1590 (2014).

L. I. Cleeves et al., ApJ **799**, 204 (2015).

C. Codella et al., A&A **507**, L25 (2009).

C. Codella et al., MNRAS **449**, L11 (2015).

M. P. Collings et al., ApJ **583**, 1058 (2003).

M. P. Collings et al., Ap&SS **285**, 633 (2003).

M. P. Collings et al., MNRAS **354**, 1133 (2004).

M. P. Collings et al., MNRAS **449**, 1826 (2015).

M. A. Cordiner et al., ApJ **800**, L14 (2015).

S. Courteau et al., Reviews of Modern Physics **86**, 47 (2014).

A. Coutens et al., A&A **576**, A5 (2015).

A. Coutens et al., A&A **590**, L6 (2016).

A. Crapsi et al., A&A **486**, 245 (2008).

J. Crovisier et al., A&A **418**, L35 (2004).

G. A. Cruz-Diaz et al., A&A **592**, A68 (2016).

H. M. Cuppen and E. Herbst, ApJ **668**, 294 (2007).

H. M. Cuppen, L. J. Karssemeijer, and T. Lamberts, Chemical Reviews **113**, 8840 (2013).

F. D'Antona and I. Mazzitelli, ApJS **90**, 467 (1994).

A. Dalgarno, Proceedings of the National Academy of Science **103**, 12269 (2006).

E. Dartois et al., A&A **342**, L32 (1999).

A. M. Davis et al., *Protostars and planets vi, volatiles in protoplanetary disks* (Univ. Arizona Press, Tucson, AZ, 2014), pp. 809–831.

G. Dipierro et al., MNRAS **453**, L73 (2015).

E. F. v. Dishoeck et al., ApJ **447**, 760 (1995).

E. F. v. Dishoeck et al., ApJ **447**, 760 (1995).

E. F. v. Dishoeck, B. Jonkheid, and M. C. van Hemert, Faraday Discuss. **133**, 231 (2006).

E. F. v. Dishoeck, E. Herbst, and D. A. Neufeld, Chemical Reviews **113**, 9043 (2013).

E. F. v. Dishoeck et al., *Protostars and planets vi, volatiles in protoplanetary disks* (Univ. Arizona Press, Tucson, AZ, 2014), pp. 835–858.

C. L. Dobbs et al., *Protostars and planets vi, volatiles in protoplanetary disks* (Univ. Arizona Press, Tucson, AZ, 2014), pp. 3–26.

R. Dong, Z. Zhu, and B. Whitney, ApJ **809**, 93 (2015).

B. T. Draine, ApJS **36**, 595 (1978).

K. Drdla, G. R. Knapp, and E. F. van Dishoeck, ApJ **345**, 815 (1989).

M. N. Drozdovskaya et al., MNRAS **445**, 913 (2014).

M. N. Drozdovskaya et al., MNRAS **451**, 3836 (2015).

A. Dubrulle et al., Zeitschrift Naturforschung Teil A **35**, 471 (1980).

W. W. Duley, T. J. Millar, and D. A. Williams, MNRAS **192**, 945 (1980).

F. Dulieu et al., Scientific Reports **3** (2013).

C. P. Dullemond and C. Dominik, A&A **417**, 159 (2004).

C. P. Dullemond and J. D. Monnier, ARA&A **48**, 205 (2010).

M. M. Dunham et al., *Protostars and planets vi, volatiles in protoplanetary disks* (Univ. Arizona Press, Tucson, AZ, 2014), pp. 195–218.

M. M. Dunham et al., *Protostars and planets vi, volatiles in protoplanetary disks* (Univ. Arizona Press, Tucson, AZ, 2014), pp. 195–218.

A. Dutrey et al., *Protostars and planets vi, volatiles in protoplanetary disks* (Univ. Arizona Press, Tucson, AZ, 2014), pp. 317–338.

J. L. Edridge, «Adsorption and desorption of model interstellar ices on a dust grain analogue surface,» PhD thesis (University of London, University College London (United Kingdom), Dec. 2010).

P. Ehrenfreund et al., A&A **339**, L17 (1998).

C. Espaillat et al., *Protostars and planets vi, volatiles in protoplanetary disks* (Univ. Arizona Press, Tucson, AZ, 2014), pp. 497–520.

M. G. Evans et al., MNRAS **453**, 1147 (2015).

N. J. Evans II et al., ApJS **181**, 321 (2009).

B. Fabricant, D. Krieger, and J. S. Muenter, J. Chem. Phys. **67**, 1576 (1977).

E. C. Fayolle et al., A&A **529**, A74 (2011).

E. C. Fayolle et al., A&A **556**, A122 (2013).

E. C. Fayolle et al., ApJ **816**, L28 (2016).

G. Fedoseev et al., MNRAS **448**, 1288 (2015).

J. K. J. Fogel et al., ApJ **726**, 29 (2011).

A. Frank et al., *Protostars and planets vi, volatiles in protoplanetary disks* (Univ. Arizona Press, Tucson, AZ, 2014), pp. 451–474.

H. J. Fraser et al., MNRAS **327**, 1165 (2001).

A. Fresneau et al., MNRAS **443**, 2991 (2014).

A. Fresneau et al., MNRAS **451**, 1649 (2015).

P. Friberg et al., A&A **195**, 281 (1988).

G. W. Fuchs et al., A&A **505**, 629 (2009).

K. Furuya and Y. Aikawa, ApJ **790**, 97 (2014).

K. Furuya et al., ApJ **758**, 86 (2012).

K. Furuya et al., ApJ **779**, 11 (2013).

K. Furuya et al., A&A **584**, A124 (2015).

D. Galli and F. Palla, ARA&A **51**, 163 (2013).

Ó. Gálvez et al., Icarus **197**, 599 (2008).

R. T. Garrod, ApJ **765**, 60 (2013).

R. T. Garrod and E. Herbst, A&A **457**, 927 (2006).

R. T. Garrod and T. Pauly, ApJ **735**, 15 (2011).

R. T. Garrod and S. L. Widicus Weaver, Chemical Reviews **113**, 8939 (2013).

R. T. Garrod, V. Wakelam, and E. Herbst, A&A **467**, 1103 (2007).

R. T. Garrod, S. L. W. Weaver, and E. Herbst, ApJ **682**, 283 (2008).

R. Garrod et al., Faraday Discuss. **133**, 51 (2006).

W. D. Geppert and M. Larsson, Chemical Reviews **113**, 8872 (2013).

W. D. Geppert et al., Faraday Discuss. **133**, 177 (2006).

P. A. Gerakines, W. A. Schutte, and P. Ehrenfreund, A&A **312**, 289 (1996).

E. L. Gibb et al., ApJ **536**, 347 (2000).

E. L. Gibb et al., ApJS **151**, 35 (2004).

F. C. Gillett and W. J. Forrest, ApJ **179**, 483 (1973).

F. Goesmann et al., Science **349**, 020689 (2015).

G. Y. Golubiatnikov et al., Journal of Molecular Spectroscopy **234**, 190 (2005).

L. Gómez et al., A&A **529**, A161 (2011).

R. J. A. Grim and J. M. Greenberg, A&A **181**, 155 (1987).

S. Guerlet et al., Icarus **209**, 682 (2010).

H. J. Habing, Bull. Astr. Inst. Neth. **19**, 421 (1968).

W. Hagen, L. J. Allamandola, and J. M. Greenberg, Ap&SS **65**, 215 (1979).

T. Hama and N. Watanabe, Chemical Reviews **113**, 8783 (2013).

D. Harsono et al., A&A **555**, A45 (2013).

D. Harsono et al., A&A **562**, A77 (2014).

D. Harsono, S. Bruderer, and E. F. van Dishoeck, A&A **582**, A41 (2015).

L. Hartmann and S. J. Kenyon, ARA&A **34**, 207 (1996).

T. I. Hasegawa and E. Herbst, MNRAS **261**, 83 (1993).

T. I. Hasegawa, E. Herbst, and C. M. Leung, ApJS **82**, 167 (1992).

T. Hasegawa et al., ApJ **283**, 117 (1984).

P. Helminger, R. L. Cook, and F. C. De Lucia, Journal of Molecular Spectroscopy **40**, 125 (1971).

M. C. v. Hemert and E. F. van Dishoeck, Chemic. Phys. **343**, 292 (2008).

M. C. v. Hemert, J. Takahashi, and E. F. v. Dishoeck,

K. Heng and J. R. Lyons, ApJ **817**, 149 (2016).

T. Henning and D. Semenov, Chemical Reviews **113**, 9016 (2013).

T. Henning et al., ApJ **714**, 1511 (2010).

E. Herbst, Annual Review of Physical Chemistry **46**, 27 (1995).

E. Herbst and C. M. Leung, MNRAS **222**, 689 (1986).

E. Herbst and E. F. van Dishoeck, ARA&A **47**, 427 (2009).

V. J. Herrero et al., Physical Chemistry Chemical Physics **12**, 3164 (2010).

F. Hersant et al., A&A **493**, L49 (2009).

H. Hidaka et al., ApJ **614**, 1124 (2004).

A. E. Higuchi et al., ApJ **798**, L33 (2015).

R. E. Hillger and M. W. Strandberg, Physical Review **83**, 575 (1951).

U. Hincelin et al., ApJ **775**, 44 (2013).

U. Hincelin et al., ApJ **822**, 12 (2016).

K. Hiraoka et al., ApJ **577**, 265 (2002).

J. D. Ilee et al., MNRAS **417**, 2950 (2011).

J. D. Ilee et al., MNRAS **429**, 2960 (2013).

S. Inaba and M. Ikoma, A&A **410**, 711 (2003).

Z. Ivezic and M. Elitzur, MNRAS **287**, 799 (1997).

A. A. Jaber et al., ApJ **791**, 29 (2014).

K. B. Jefferts et al., ApJ **168**, L111 (1971).

K. L. Jessup, J. Spencer, and R. Yelle, Icarus **192**, 24 (2007).

A. Johansen et al., *Protostars and planets vi, volatiles in protoplanetary disks* (Univ. Arizona Press, Tucson, AZ, 2014), pp. 547–570.

K. G. Johnston et al., ApJ **813**, L19 (2015).

A. P. Jones et al., ApJ **433**, 797 (1994).

A. P. Jones et al., A&A **588**, A43 (2016).

J. K. Jørgensen and et al., (2016).

J. K. Jørgensen, F. L. Schöier, and E. F. van Dishoeck, A&A **389**, 908 (2002).

J. K. Jørgensen et al., A&A **507**, 861 (2009).

J. K. Jørgensen et al., A&A **534**, A100 (2011).

J. K. Jørgensen et al., ApJ **757**, L4 (2012).

A. Karska et al., A&A **552**, A141 (2013).

L. J. Karssemeijer and H. M. Cuppen, A&A **569**, A107 (2014).

L. J. Karssemeijer et al., ApJ **781**, 16 (2014).

C. Knez et al., ApJ **635**, L145 (2005).

W. Kofman et al., Science **349** (2015).

L. Kolesniková et al., ApJ **784**, L7 (2014).

J. Koning, G. J. Kroes, and C. Arasa, J. Chem. Phys. **138**, 104701 (2013).

S. Kraus et al., Nature **466**, 339 (2010).

L. E. Kristensen et al., A&A **516**, A57 (2010).

L. E. Kristensen et al., A&A **542**, A8 (2012).

M. R. Krumholz et al., *Protostars and planets vi, volatiles in protoplanetary disks* (Univ. Arizona Press, Tucson, AZ, 2014), pp. 243–266.

Y.-J. Kuan and Y.-L. Chuang, in 40th cospar scientific assembly. held 2-10 august 2014, in moscow, russia, abstract f3.2-6-14. Vol. 40, COSPAR Meeting (2014), p. 1676.

Y.-J. Kuan et al., ApJ **593**, 848 (2003).

J. C. Laas et al., ApJ **728**, 71 (2011).

R. B. Larson, MNRAS **145**, 405 (1969).

L. Le Roy et al., A&A **583**, A1 (2015).

J.-E. Lee and E. A. Bergin, ApJ **799**, 104 (2015).

J.-E. Lee, E. A. Bergin, and H. Nomura, ApJ **710**, L21 (2010).

T. M. Leen and M. M. Graff, ApJ **325**, 411 (1988).

X. Li et al., A&A **555**, A14 (2013).

Z.-Y. Li et al., *Protostars and planets vi, volatiles in protoplanetary disks* (Univ. Arizona Press, Tucson, AZ, 2014), pp. 173–194.

R. A. Linke, M. A. Frerking, and P. Thaddeus, ApJ **234**, L139 (1979).

H. Linnartz, S. Ioppolo, and G. Fedoseev, ArXiv e-prints: 1507.02729 (2015).

D. J. P. Lommen et al., A&A **515**, A77 (2010).

F. J. Lovas, D. R. Johnson, and L. E. Snyder, ApJS **41**, 451 (1979).

A. Luca, D. Voulot, and D. Gerlich, WDS'02 Proceedings of Contributed Papers **PART II**, 294 (2002).

K. L. Luhman, ARA&A **50**, 65 (2012).

J. I. Lunine and D. J. Stevenson, ApJS **58**, 493 (1985).

A. Maeda et al., ApJS **176**, 543 (2008).

S. Maity, R. I. Kaiser, and B. M. Jones, Phys. Chem. Chem. Phys. **17**, 3081 (2015).

U. Marboeuf et al., A&A **570**, A36 (2014).

U. Marboeuf et al., A&A **570**, A35 (2014).

R. Martín-Doménech et al., A&A **585**, A112 (2016).

G. S. Mathews et al., A&A **557**, A132 (2013).

B. C. Matthews et al., *Protostars and planets vi, volatiles in protoplanetary disks* (Univ. Arizona Press, Tucson, AZ, 2014), pp. 521–544.

R. Mauersberger et al., A&A **313**, L1 (1996).

A. J. Maury et al., A&A **563**, L2 (2014).

D. McElroy et al., A&A **550**, A36 (2013).

B. A. McGuire et al., Science **352**, 1449 (2016).

T. J. Millar and E. Herbst, A&A **231**, 466 (1990).

T. J. Millar and L. A. M. Nejad, MNRAS **217**, 507 (1985).

T. J. Millar, C. M. Leung, and E. Herbst, A&A **183**, 109 (1987).

Y. C. Minh et al., ApJ **360**, 136 (1990).

M. Minissale and F. Dulieu, J. Chem. Phys. **141**, 014304 (2014).

M. Minissale et al., A&A **559**, A49 (2013).

M. Minissale et al., A&A **577**, A2 (2015).

M. Minissale, E. Congiu, and F. Dulieu, A&A **585**, A146 (2016).

M. Minissale et al., A&A **585**, A24 (2016).

M. Minissale et al., MNRAS (2016).

H. Minowa et al., ApJ **491**, L63 (1997).

A. Miotello et al., A&A **567**, A32 (2014).

G. F. Mitchell, ApJ **287**, 665 (1984).

I. Morino, K. M. T. Yamada, and A. G. Maki, Journal of Molecular Spectroscopy **200**, 145 (2000).

O. Mousis et al., ApJ **751**, L7 (2012).

H. S. P. Müller and S. Brünken, Journal of Molecular Spectroscopy **232**, 213 (2005).

H. S. P. Müller et al., Journal of Molecular Structure **742**, 215 (2005).

H. S. P. Müller et al., A&A **587**, A92 (2016).

M. J. Mumma and S. B. Charnley, ARA&A **49**, 471 (2011).

N. M. Murillo et al., A&A **560**, A103 (2013).

D. A. Neufeld and D. J. Hollenbach, ApJ **428**, 170 (1994).

J. A. Noble et al., ApJ **735**, 121 (2011).

K. Nomoto, C. Kobayashi, and N. Tominaga, ARA&A **51**, 457 (2013).

H. Nomura et al., A&A **495**, 183 (2009).

G. Notesco, A. Bar-Nun, and T. Owen, Icarus **162**, 183 (2003).

K. I. Öberg, Chemical Reviews, in press (2016).

K. I. Öberg et al., ApJ **621**, L33 (2005).

K. I. Öberg et al., A&A **504**, 891 (2009).

K. I. Öberg et al., ApJ **693**, 1209 (2009).

K. I. Öberg, E. F. van Dishoeck, and H. Linnartz, A&A **496**, 281 (2009).

K. I. Öberg et al., ApJ **716**, 825 (2010).

K. I. Öberg et al., ApJ **718**, 832 (2010).

K. I. Öberg et al., ApJ **740**, 14 (2011).

K. I. Öberg, R. Murray-Clay, and E. A. Bergin, ApJ **743**, L16 (2011).

K. I. Öberg et al., ApJ **740**, 109 (2011).

K. I. Öberg et al., ApJ **771**, 95 (2013).

K. I. Öberg et al., ApJ **810**, 112 (2015).

K. I. Öberg et al., Nature **520**, 198 (2015).

K. I. Öberg et al., in The molecular universe, Vol. 7, Proceedings of the International Astronomical Union (June 2011), pp. 65–78.

N. Ohashi et al., ApJ **796**, 131 (2014).

S. Okuzumi et al., ApJ **821**, 82 (2016).

M. Oppenheimer and A. Dalgarno, ApJ **187**, 231 (1974).

C. W. Ormel and H. H. Klahr, A&A **520**, A43 (2010).

Y. Oya et al., ApJ **824**, 88 (2016).

M. Padovani, P. Hennebelle, and D. Galli, A&A **560**, A114 (2013).

L. Pagani et al., Science **329**, 1622 (2010).

M. E. Palumbo, A. G. G. M. Tielens, and A. T. Tokunaga, ApJ **449**, 674 (1995).

M. E. Palumbo, T. R. Geballe, and A. G. G. M. Tielens, ApJ **479**, 839 (1997).

M. E. Palumbo et al., ApJ **685**, 1033 (2008).

J. Pastor et al., A&A **252**, 320 (1991).

D. Patel, D. Margolese, and T. R. Dyke, J. Chem. Phys. **70**, 2740 (1979).

M. Pätzold et al., Nature **530**, 63 (2016).

T. Pauly and R. T. Garrod, ApJ **817**, 146 (2016).

M. V. Penston, MNRAS **144**, 425 (1969).

A. A. Penzias et al., ApJ **168**, L53 (1971).

T. G. Phillips et al., A&A **518**, L109 (2010).

G. Pineau des Forets, E. Roueff, and D. R. Flower, MNRAS **223**, 743 (1986).

C. Pinte et al., ApJ **816**, 25 (2016).

A. L. Plunkett et al., ApJ **774**, 22 (2013).

A. L. Plunkett et al., Nature **527**, 70 (2015).

K. M. Pontoppidan, A&A **453**, L47 (2006).

K. M. Pontoppidan et al., A&A **408**, 981 (2003).

K. M. Pontoppidan et al., A&A **404**, L17 (2003).

K. M. Pontoppidan, E. F. van Dishoeck, and E. Dartois, A&A **426**, 925 (2004).

K. M. Pontoppidan et al., ApJ **656**, 980 (2007).

K. M. Pontoppidan et al., *Protostars and planets vi, volatiles in protoplanetary disks* (Univ. Arizona Press, Tucson, AZ, 2014), pp. 363–385.

F. X. Powell and D. R. Lide Jr., J. Chem. Phys. **41**, 1413 (1964).

S. S. Prasad and W. T. Huntress Jr., ApJ **260**, 590 (1982).

S. S. Prasad and S. P. Tarafdar, ApJ **267**, 603 (1983).

C. Qi et al., ApJ **813**, 128 (2015).

C. Qi et al., ApJ **799**, 110 (2015).

L. Reboussin et al., MNRAS **440**, 3557 (2014).

B. Reipurth et al., *Protostars and planets vi, volatiles in protoplanetary disks* (Univ. Arizona Press, Tucson, AZ, 2014), pp. 267–290.

M. A. Requena-Torres et al., ApJ **655**, L37 (2007).

L. Ricci et al., A&A **512**, A15 (2010).

J. F. Roberts et al., MNRAS **382**, 733 (2007).

S. D. Rodgers and S. B. Charnley, ApJ **546**, 324 (2001).

M. Ruaud et al., MNRAS **447**, 4004 (2015).

D. P. Ruffle and E. Herbst, MNRAS **324**, 1054 (2001).

N. Sakai and S. Yamamoto, Chemical Reviews **113**, 8981 (2013).

N. Sakai et al., Nature **507**, 78 (2014).

T. Sakai et al., ApJ **775**, L31 (2013).

S. A. Sandford et al., ApJ **329**, 498 (1988).

J. Schneider et al., A&A **532**, A79 (2011).

F. L. Schöier et al., A&A **390**, 1001 (2002).

W. A. Schutte et al., A&A **343**, 966 (1999).

K. R. Schwarz et al., ApJ **823**, 91 (2016).

D. Semenov and D. Wiebe, ApJS **196**, 25 (2011).

D. Semenov, D. Wiebe, and T. Henning, ApJ **647**, L57 (2006).

D. Semenov et al., A&A **522**, A42 (2010).

R. J. Shannon et al., Nature Chemistry **5**, 745 (2013).

C. J. Shen et al., A&A **415**, 203 (2004).

J. Shi, B. D. Teolis, and R. A. Baragiola, Phys. Rev. B **79**, 235422 (2009).

F. H. Shu, ApJ **214**, 488 (1977).

F. H. Shu, F. C. Adams, and S. Lizano, ARA&A **25**, 23 (1987).

D. Smith et al., A&A **200**, 191 (1988).

I. W. M. Smith, ARA&A **49**, 29 (2011).

L. E. Snyder et al., Physical Review Letters **22**, 679 (1969).

L. E. Snyder et al., ApJ **619**, 914 (2005).

M. Spaans et al., ApJ **455**, L167 (1995).

M. Sugimura et al., PASJ **63**, 459 (2011).

F. F. S. v. d. Tak et al., A&A **412**, 133 (2003).

J. C. Tan et al., *Protostars and planets vi, volatiles in protoplanetary disks* (Univ. Arizona Press, Tucson, AZ, 2014), pp. 149–172.

K. Tanaka, T. Tanaka, and I. Suzuki, J. Chem. Phys. **82**, 2835 (1985).

V. Taquet, C. Ceccarelli, and C. Kahane, A&A **538**, A42 (2012).

V. Taquet et al., ApJ **804**, 81 (2015).

V. Taquet, E. S. Wirström, and S. B. Charnley, ApJ **821**, 46 (2016).

S. Terebey, F. H. Shu, and P. Cassen, ApJ **286**, 529 (1984).

L. Testi et al., *Protostars and planets vi, volatiles in protoplanetary disks* (Univ. Arizona Press, Tucson, AZ, 2014), pp. 339–361.

A. Thiabaud et al., A&A **562**, A27 (2014).

A. Thiabaud et al., A&A **574**, A138 (2015).

K. Thürmer et al., Surface Science **641**, 216 (2015).

A. G. G. M. Tielens, ARA&A **46**, 289 (2008).

A. G. G. M. Tielens, Reviews of Modern Physics **85**, 1021 (2013).

A. G. G. M. Tielens and S. B. Charnley, Origins of Life and Evolution of the Biosphere **27**, 23 (1997).

A. G. G. M. Tielens and W. Hagen, A&A **114**, 245 (1982).

J. J. Tobin et al., Nature **492**, 83 (2012).

J. J. Tobin et al., ApJ **771**, 48 (2013).

J. J. Tobin et al., ApJ **805**, 125 (2015).

W. Tsang and R. F. Hampson, J. of Phys. and Chem. Ref. Data **15**, 1087 (1986).

S. Tsunekawa et al., Journal of Molecular Spectroscopy **134**, 63 (1989).

B. E. Turner, ApJ **396**, L107 (1992).

N. J. Turner et al., *Protostars and planets vi, volatiles in protoplanetary disks* (Univ. Arizona Press, Tucson, AZ, 2014), pp. 411–432.

T. Umebayashi and T. Nakano, PASJ **33**, 617 (1981).

C. Vastel et al., ApJ **795**, L2 (2014).

A. I. Vasyunin and E. Herbst, ApJ **762**, 86 (2013).

A. I. Vasyunin and E. Herbst, ApJ **769**, 34 (2013).

A. I. Vasyunin et al., ApJ **727**, 76 (2011).

T. Velusamy, W. D. Langer, and K. A. Marsh, ApJ **668**, L159 (2007).

R. Visser and E. A. Bergin, ApJ **754**, L18 (2012).

R. Visser and C. P. Dullemond, A&A **519**, A28 (2010).

R. Visser et al., A&A **495**, 881 (2009).

R. Visser, E. F. van Dishoeck, and J. H. Black, A&A **503**, 323 (2009).

R. Visser, S. D. Doty, and E. F. van Dishoeck, A&A **534**, A132 (2011).

R. Visser et al., A&A **537**, A55 (2012).

R. Visser, E. A. Bergin, and J. K. Jørgensen, A&A **577**, A102 (2015).

R. Viswanathan and T. R. Dyke, Journal of Molecular Spectroscopy **103**, 231 (1984).

S. Viti et al., MNRAS **354**, 1141 (2004).

V. Wakelam, H. M. Cuppen, and E. Herbst, ArXiv e-prints: 1309.7792 (2013).

V. Wakelam et al., MNRAS **445**, 2854 (2014).

C. Walsh, T. J. Millar, and H. Nomura, ApJ **722**, 1607 (2010).

C. Walsh et al., ApJ **747**, 114 (2012).

C. Walsh et al., Faraday Discuss. **168**, 389 (2014).

C. Walsh et al., A&A **563**, A33 (2014).

C. Walsh, H. Nomura, and E. van Dishoeck, A&A **582**, A88 (2015).

C. Walsh et al., ApJ **823**, L10 (2016).

S. F. Wampfler et al., A&A **552**, A56 (2013).

N. Watanabe and A. Kouchi, ApJ **571**, L173 (2002).

N. Watanabe et al., ApJ **616**, 638 (2004).

N. Watanabe et al., ApJ **714**, L233 (2010).

G. D. Watt and S. B. Charnley, MNRAS **213**, 157 (1985).
R. J. v. Weeren, C. Brinch, and M. R. Hogerheijde, A&A **497**, 773 (2009).
J. C. Weingartner and B. T. Draine, ApJS **134**, 263 (2001).
D. C. B. Whittet et al., A&A **315**, L357 (1996).
K. Willacy et al., ApJ **644**, 1202 (2006).
J. P. Williams and L. A. Cieza, ARA&A **49**, 67 (2011).
T. L. Wilson and R. Rood, ARA&A **32**, 191 (1994).
G. Winnewisser and R. L. Cook, Journal of Molecular Spectroscopy **28**, 266 (1968).
S. Wlodek, D. K. Bohme, and E. Herbst, MNRAS **235**, 493 (1988).
P. Woitke et al., A&A **586**, A103 (2016).
P. M. Woods et al., ApJ **777**, 90 (2013).
P. M. Woods et al., MNRAS **450**, 1256 (2015).
D. E. Woon, ApJ **569**, 541 (2002).
L.-H. Xu et al., J. Chem. Phys. **137**, 104313 (2012).
R. Yokochi et al., Icarus **218**, 760 (2012).
H. W. Yorke and P. Bodenheimer, ApJ **525**, 330 (1999).
N. Ysard et al., A&A **588**, A44 (2016).
L. A. Zapata et al., MNRAS **447**, 1826 (2015).
K. Zhang, G. A. Blake, and E. A. Bergin, ApJ **806**, L7 (2015).
B. Zhao et al., MNRAS **460**, 2050 (2016).

NEDERLANDSE SAMENVATTING

INLEIDING

Astrochemie is één van de meest interdisciplinaire onderzoeksgebieden binnen de theoretische en observationele sterrenkunde met raakvlakken aan de experimentele en theoretische chemie. Astrochemici bestuderen de vorming van moleculen in de ruimte en hun chemische evolutie tot uiteindelijk complexe organische moleculen, waar het onderzoek samenkomt met het gebied van de astrobiologie. De grote vraag die centraal staat bij dit onderzoek is hoe planeten en leven gevormd kunnen worden uit stof en atomen. Daarnaast willen de onderzoekers begrijpen welke omstandigheden het meest geschikt zijn voor leven, ook al staat de definitie van leven nog ter discussie.

Nederland is gezegend met vier universiteiten met gespecialiseerde sterrenkunde afdelingen verenigd in de Nederlandse Onderzoekschool voor Astronomie (NOVA; Netherlands Research School for Astronomy). Astrochemie zelf is een van de programma's die worden gefinancierd door de Nederlandse Organisatie voor Wetenschappelijk Onderzoek (NWO), wat het centrale belang van dit onderzoeksgebied binnen de Nederlandse wetenschapsgemeenschap aangeeft. Bij de Universiteit Leiden werken vier grote groepen op dit gebied onder één dak: prof. dr. Xander Tielens, dr. Michiel Hogerheijde, prof. dr. Harold Linnartz en de promotor van de auteur - prof. dr. Ewine van Dishoeck. Dit 'powerhouse' maakt Leiden de kern van het astrochemisch onderzoek in Nederland.

CHEMIE IN DE RUIMTE

Het eerste meer-atomige molecuul dat in de ruimte gedetecteerd werd was ammoniak in 1968, gevolgd door water en het eerste organische molecuul, formaldehyde, in 1969. Vijftig jaar later worden er steeds complexere moleculen ontdekt. In 2012 werd met behulp van de Atacama Large Millimeter/submillimeter Array (ALMA) glycolaldehyde, een suikermolecuul, waargenomen in het gas rond de jonge, zonachtige ster IRAS 16293-2422. Twee jaar later werd isopropyl cyanide gedetecteerd in Sagittarius B2, een stervormingsgebied nabij het centrum van onze Melkweg. Deze ontdekking was bijzonder omdat dit de eerste keer was dat een molecuul met een zijtak werd waargenomen in de ruimte. Dit jaar, 2016, hebben onderzoekers in Sagittarius B2 het eerste chirale molecuul ontdekt. Polycyclische aromatische koolwaterstoffen worden overal in de interstellaire ruimte gevonden. Zulke moleculen spelen een belangrijke rol in allerlei biologische processen. Dankzij ALMA en andere nieuwe telescopen worden er nog veel nieuwe ontdekkingen van complexe moleculen verwacht in het komende decennia.

Moleculen zijn het makkelijkst te identificeren wanneer ze zich in het gas bevinden. Enerzijds omdat ze dan meer unieke emissielijnen bezitten en anderzijds zijn de meeste faciliteiten geschikt voor dit soort waarnemingen. Maar er is ook een grote chemische diversiteit in interstellair ijs. Waterijs werd gedetecteerd in 1973 en sindsdien zijn er ook een aantal andere moleculen aangetoond in de vaste fase. Het is moeilijk om de grootste moleculen in het ijs te bestuderen omdat er relatief weinig van deze moleculen aanwezig

Figure .6: Donkere koude interstellaire wolken en bipolaire straalstromen in HH 901/902 in zichtbaar licht als gezien door *The Hubble Space Telescope*. Jonge sterren en protoplanetaire schijven vormen binnen deze wolken (NASA, ESA, and M. Livio and the Hubble 20th Anniversary Team, STScI).

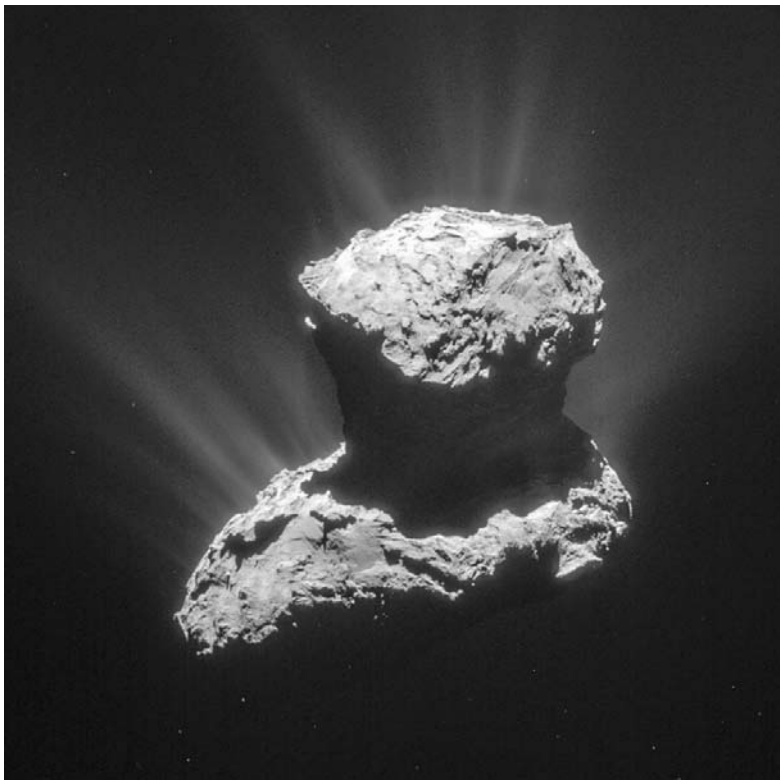

Figure .7: Komeet 67P op 25 maart 2015 genomen met de Navigation Camera (NavCam) van *Rosetta* op 86,6 km afstand vanaf het centrum van de komeet. De gas 'jets' zijn het gevolg van sublimatie van het ijs op en onder het oppervlakte van de komeet en vormen de koma van de komeet (ESA/Rosetta/NAVCAM-CC BY-SA IGO 3.0).

zijn. Bovendien hebben ze minder unieke vibraties, wat het lastig maakt ze onderling te onderscheiden.

Desondanks voorspellen moderne experimentele studies en complexe fysico-chemische modellen dat de chemische processen in de vaste fase een cruciale rol spelen in de ontwikkeling van de chemische diversiteit in de ruimte. Grote complexe moleculen kunnen gevormd worden uit kleinere moleculen en atomen via chemische reacties op het oppervlak van met ijs bedekte stofdeeltjes in interstellaire wolken. Op deze manier kan de chemische ontwikkeling al plaatsvinden onder de heel koude omstandigheden in de vroegste stadia van ster- en planeetvorming, wanneer reacties in het gas nog inefficient zijn door de te lage temperaturen en dichtheden. De stofdeeltjes zelf groeien tot grotere lichamen door middel van verschillende mechanismen en vormen uiteindelijk kometen en planeten. Op deze manier worden moleculen van biologische belang automatisch opgenomen in de grotere objecten die een volwassen planeetstelsel vormen.

VORMING VAN EEN ZONNESTELSEL

De interstellaire ruimte is niet leeg, maar gevuld met donkere koude wolken van ver-

schillende gassen en stofdeeltjes (afb. .6). Op een gegeven moment kunnen deze wolken instorten onder de invloed van de zwaartekracht en een jonge ster is dan geboren. Door de rotatie van het systeem vormt er zich een schijf rond de ster. Hierin zullen de kometen en planeten vormen en daarom heet zo'n schijf een protoplanetaire schijf. In eerste instantie is het ster-schijf systeem ingebed in de resterende wolk materie. Door bipolaire straalstromen (meerderen zijn te zien in afb. .6) wordt de omgeving schoongeveegd en uiteindelijk blijven alleen de ster en schijf over. Als het systeem verder ontwikkelt verdwijnt het gas uit de schijf en worden de stofdeeltjes gebruikt voor de vorming van grotere lichamen of weggeblazen. Uiteindelijk blijft er een volwassen zonnestelsel over die vergelijkbaar is met het onze. Zo'n zonnestelsel bestaat uit een aantal planeten en zit vol met achtergebleven kleinere planetaire bouwstenen, zoals kometen (afb. .7) en asteroiden.

De *Rosetta* missie is een unieke in situ poging om de komeet 67P de bestuderen. De orbiter volgt de komeet sinds 6 augustus 2014 en zal nog tot 30 september 2016 67P blijven volgen. Hierdoor kunnen de gassen en stofdeeltjes in de koma bestudeerd worden gedurende meer dan twee jaar, inclusief het moment waarop de komeet zich het dichtst bij de zon bevindt (perihelium op 13 augustus 2015). De *Rosetta* orbiter ging gepaard met een lander *Philae* die op 12 november 2014 een historische landing op een komeet heeft gemaakt. De data van de orbiter en de lander worden nog onderzocht, maar er zijn al meerdere ontdekkingen gedaan. Bijvoorbeeld de eerste detectie van moleculair zuurstof en glycine in een komeet. Daardoor is dit de ultieme tijd voor onderzoekers op het gebied van chemische inventarisatie van zonnestelsels.

CHEMISCHE PROCESSEN

De vorming van een zonnestelsel is een ingewikkeld dynamisch, fysisch proces met een grote variatie in temperatuur, dichtheid en hoeveelheid straling gedurende de evolutie. Simultaan vinden de chemische reacties plaats, die op hun beurt afhankelijk zijn van de fysische condities en de tijd die beschikbaar is voor verschillende chemische processen. Buiten ons zonnestelsel bevinden de meeste complexe moleculen zich in andere stervormingsgebieden. Dit is de reden waarom andere zonnestelsels zo interessant en belangrijk zijn om te begrijpen hoe en wanneer het leven op Aarde zou hebben kunnen ontstaan. Chemische processen zijn universeel, maar het is nog onduidelijk of het leven hier uniek is.

De synthese van grotere complexe moleculen begint met de vorming van kleine simpele moleculen in de interstellaire wolken. Tijdens de instorting van de wolk tot een ster en schijf zal de chemie verder ontwikkelen door hogere temperaturen, sterkere straling en grotere dichtheden. Belangrijke pre-biologische moleculen kunnen al vormen voordat de materie zich in de schijf bevindt (afb. .8). In de protoplanetaire schijf zal de vorming van kometen en planeten plaatsvinden in het centrale gedeelte waar de dichtheid het hoogst is. Daar kunnen de grote complexe moleculen opgenomen worden in de bouwstenen voor grotere lichamen. Op deze manier zijn de vroegste stadia van ontwikkeling (zoals de wolken in afb. .6) verbonden met de oudste componenten van een zonnestelsel (zoals de kometen in afb. .7).

DIT PROEFSCHRIFT

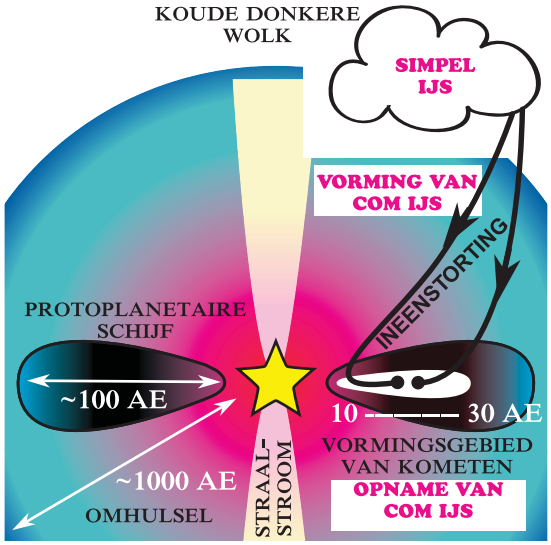

Figure .8: Een afbeelding die aangeeft hoe complexe organische moleculen vormen uit kleinere simpele moleculen in de wolken tijdens de ineenstorting van het systeem tot een ster en een protoplanetaire schijf. In de schijf zullen deze moleculen opgenomen worden in de bouwstenen voor kometen en planeten. 'COM' staat voor 'complex organisch molecuul'. 'AE' staat voor Astronomische Eeenheid, wat gelijk is aan de gemiddelde afstand tussen de Aarde en de Zon.

In dit proefschrift staat de jongste fase van ster- en planeetvorming centraal. Het doel is om de oorsprong van op kometen aanwezige complexe organische moleculen te vinden. De grote motivatie is het begrijpen van ons interstellaire erfgoed. Drie hoofdstukken van dit proefschrift hebben betrekking op fysico-chemische modellen van deze eerste fase van de vorming van een jong ster-schijf systeem. Het laatste hoofdstuk gaat over ALMA-waarnemingen van zo'n systeem, IRAS 16293-2422, en de zwavelhoudende moleculen daarin.

In hoofdstuk 2 wordt aangetoond dat methanol, één van de belangrijkste bouwstenen voor andere complexe organische moleculen, niet direct vanuit de donkere wolk fase naar de protoplanetaire schijf getransporteerd wordt. Onderweg naar de schijf wordt meer methanol gemaakt, maar uiteindelijk ook vernietigd, wat uiteindelijk leidt tot minder methanol in de schijf dan in de wolk aanwezig was. In hoofdstuk 3 tonen modellen aan dat verschillende complexe organische moleculen worden geproduceerd in het ijs dat zich in een ringvormig gebied rond een jonge ster bevindt, en in het gas langs de holte gemaakt door de bipolaire straalstromen. In hoofdstuk 4 wordt de volledige ijssamenstelling in protoplanetaire schijven geanalyseerd, die belangrijk is voor het opbouw van grotere lichamen zoals kometen. De modellen laten zien dat er meer kooldioxide ijs en complexe organische ijzen kunnen ontstaan in de schijf dan in de wolk, dankzij de ineenstorting van het systeem en de chemische evolutie gedurende die tijd. Het laatste hoofdstuk maakt een vergelijking tussen de aanwezige zwavelhoudende moleculen in 67P, als gedetecteerd door *Rosetta*, en een jonge protoster op de schaal van ons eigen

zonnestelsel. De chemische verschillen zouden kunnen betekenen dat ons zonnestelsel gevormd is in een warmer gebied dan meestal wordt aangenomen. Alles tezamen is dit een poging om de chemische link tussen wolken, schijven en kometen te kwantificeren. *De hoofdconclusie van dit proefschrift is dat het onvermijdelijk is dat een jong zonnestelsel geboren wordt met de complexe organische bouwstenen voor leven.*

VOORUITBLIK

Verder onderzoek van de auteur zal zich richten op de latere stadia in de evolutie van schijf tot kometen en planeten. De modellen zullen aangepast worden zodat ze beter te vergelijken zijn met ons jonge zonnestelsel, en het chemische netwerk zal uitgebreid worden met de nieuwe moleculen die *Rosetta* op 67P ontdekt heeft. Dit onderzoek zal verricht worden aan het Center for Space and Habitability (CSH) aan de Universiteit van Bern.

ACKNOWLEDGEMENTS

People are shaped by their experiences with the surrounding environment and their interactions with those around them. A researcher is shaped by those that guide him/her and those that one meets during their scientific path. Thereby, I am sincerely grateful to my supervisor Prof. Dr. Ewine van Dishoeck for providing me with the necessary balance between supervision and freedom in terms of my PhD research project. I have learned numerous valuable lessons from her. She will always remain a figure of aspiration. Scientifically, I grew a lot from my interactions with Dr. Catherine Walsh and Dr. Ruud Visser. I am very grateful for everything you have taught me about chemical and physical models. Many thanks also to Dr. Daniel Harsono, who has helped me with getting things running during my very first weeks as a PhD student and has since also been there for all my various computational questions. Thanks to the computer group of the Leiden Observatory as well for their technical assistance.

I am further unmeasurably grateful to Dr. Lars Kristensen and Dr. Ruud Visser for making an astrochemist out of me. They were the first to introduce and convert me to the research area, while I was still a master student. I appreciate all that you have taught me during the minor master project and thereafter. I know that you always have my best interest in mind.

I could not have asked for better office mates! Dr. Daniel Paardekooper and Dr. Alan Heays, I will always cherish the memories that I have from the three and a half years that we shared HL504 together. Sierk van Terwisga we were happy to have you join us as well.

My gratitude also extends to Prof. Dr. Xander Tielens for valuable lessons on what it takes to be a scientist during my major master research project and our interactions thereafter. I would also like to thank Prof. Dr. Harold Linnartz for the right guidance on specializing when he was my bachelor study adviser and also subsequent chats. Additionally, I am grateful for the introduction to astronomical research that I received from Prof. Dr. Vincent Icke as a bachelor student.

I have had the pleasure of working with some brilliant and reliable collaborators: Dr. Amaury Thiabaud, Dr. Ulysse Marboeuf, Dr. Vianney Taquet, Dr. Kenji Furuya. Thank you all very much for the valuable discussions! Besides all those directly involved in my work, there was also the army of PhD students and postdocs in our group during my four years that have all shaped me as a scientist through our weekly group meetings, annual group retreats and random chats in the hallway. Thank you all very much!

Many thanks to Heather Andrews Mancilla for being a friend with whom I could share the inevitable PhD frustrations!

This thesis is dedicated to my parents, both of whom are responsible for the person that I am today. I am beyond grateful for all that you have provided me with and all that you have taught me. If it was not for your life choices and decisions, I could potentially have been in a very different place right now.

Most recently my gratitude also extends to Benoît Fournier. The last chapter would not have been here if it was not for your support on a Saturday. You have also been able to keep me sane during the madness of the last few months of my PhD.

Finally, I would like to thank my funding sources for making this research project possible: Huygens fellowship from Leiden University, the European Union A-ERC grant 291141 CHEMPLAN, the Netherlands Research School for Astronomy (NOVA) and a Royal Netherlands Academy of Arts and Sciences (KNAW) professor prize.

PUBLICATIONS

PUBLISHED PAPERS

Drozdovskaya M. N., Walsh C., Visser R., Harsono D., van Dishoeck E. F., 2014, MNRAS, 445, 913
Methanol along the path from envelope to protoplanetary disc

Karska A., Kristensen L. E., van Dishoeck E. F., Drozdovskaya M. N., Mottram J. C., Herczeg G. J., Bruderer S., Cabrit S., Evans II N. J., Fedele D., Gusdorf A., Jørgensen J. K., Kaufman M. J., Melnick G. J., Neufeld D. A., Nisini B., Santangelo G., Tafalla M., Wampfler S. F., 2014, A&A, 572, A9
Shockingly low water abundances in *Herschel*/PACS observations of low-mass protostars in Perseus

Drozdovskaya M. N., Walsh C., Visser R., Harsono D., van Dishoeck E. F., 2015, MNRAS, 451, 3836
The complex chemistry of outflow cavity walls exposed: the case of low-mass protostars

Coutens A., Jørgensen J. K., van der Wiel M. H. D., Müller H. S. P., Lykke J. M., Bjerkeli P., Bourke T. L., Calcutt H., Drozdovskaya M. N., Favre C., Fayolle E. C., Garrod R. T., Jacobsen S. K., Ligterink N. F. W., Öberg K. I., Persson M. V., van Dishoeck E. F., Wampfler S. F., 2016, A&A, 50, L6
The ALMA-PILS survey: First detections of deuterated formamide and deuterated isocyanic acid in the interstellar medium

Drozdovskaya M. N., Walsh C., van Dishoeck E. F., Furuya K., Marboeuf U., Thiabaud A., Harsono D., Visser R., 2016, MNRAS, in press
Cometary ices in forming protoplanetary disc midplanes

Jørgensen J. K., van der Wiel M. H. D., Coutens A., Lykke J. M., Müller H. S. P., van Dishoeck E. F., Calcutt H., Bjerkeli P., Bourke T. L., Drozdovskaya M. N., Favre C., Fayolle E. C., Garrod R. T., Jacobsen S. K., Öberg K. I., Persson M. V., Wampfler S. F., 2016, A&A, in press
The ALMA Protostellar Interferometric Line Survey (PILS): First results from an unbiased submillimeter wavelength line survey of the Class 0 protostellar binary IRAS 16293-2422 with ALMA

PAPERS SUBMITTED AND IN PREPARATION

Drozdovskaya M. N., van Dishoeck E. F., Jørgensen J. K., Calmonte U., Le Roy L., Altwegg K., Calcutt H., Bjerkeli P., Bourke T. L., Coutens A., Favre C., Fayolle E. C., Garrod R. T., Jacobsen S. K., Lykke J. M., Müller H. S. P., Öberg K. I., Persson M. V., van der Wiel M. H. D., Wampfler S. F., 2016, MNRAS, in prep.

The sulfur connection between protostars and comets: IRAS 16293-2422 and 67P/C-G

Drozdovskaya M. N., Tan J. C., Zhang Y., Visser R., Walsh C., 2016, MNRAS, in prep.
Complex organic chemistry around high-mass protostars

Mottram J. C., van Dishoeck E. F., Kristensen L. E., Karska A., San José-García I., Khanna S., Herczeg G. J., André Ph., Bontemps S., Cabrit S., Carney M. T., Drozdovskaya M. N., Dunham M. M., Evans N. J., Fedele D., Green J. D., Harsono D., Johnstone D., Jørgensen J. K., Könyves V., Nisini B., Persson M. V., Tafalla M., Visser R., Yıldız U. A., 2016, A&A, under rev.
Outflows, infall and evolution of a sample of embedded low-mass protostars: The William Herschel Line Legacy (WILL) Survey

Furuya K., Drozdovskaya M. N., Visser R., van Dishoeck E. F., Walsh C., Harsono D., Hincelin U., Taquet V., 2016, A&A, subm.
Water delivery from cores to disks: deuteration as a probe of the prestellar inheritance of H_2O

Lykke J. M., Bourke L., Coutens A., Calcutt H., Jørgensen J. K., Drozdovskaya M. N., Persson M. V., van der Wiel M. H. D., Favre C., van Dishoeck E. F., Wampfler S. F., Garrod R. T., Fayolle E. C., Jacobsen S. K., Müller H. S. P., Öberg K. I., 2016, A&A, under rev.
The ALMA-PILS survey: First detections of ethylene oxide, acetone and propanal toward the low-mass protostar IRAS 16293-2422

PROCEEDINGS

Drozdovskaya M., Walsh C., Visser R., Harsono D., van Dishoeck, E., 2013, Protostars and Planets VI Posters, 73

Drozdovskaya M., van Dishoeck E., Walsh C., Visser R., Harsono D., 2014, 40th COSPAR Scientific Assembly, COSPAR Meeting, 40, 749

Drozdovskaya M., Walsh C., Visser R., Harsono D., van Dishoeck E., 2015, IAU General Assembly, 22, 57257

Drozdovskaya M., Walsh C., Visser R., Harsono D., van Dishoeck E., 2015, IAU General Assembly, 22, 57335

Drozdovskaya M., Walsh C., van Dishoeck E., 2015, IAU General Assembly, 22, 58173

Furuya K., Drozdovskaya M. N., Walsh C., van Dishoeck E. F., 2016, EAS Publications Series, 75, 259

BIOGRAPHICAL SKETCH

I was born on September 14th, 1989 in Moscow, U.S.S.R. My parents, Liudmila Mikhaylovna Drozdovskaya and Nikolay Valeriyevich Drozdovskiy, were both engineers by profession with PhD degrees from the Moscow Power Engineering Institute. I will never know whether my interest for sciences is a result of genetics, the scientific at-home environment or a combination of the two. Nevertheless, I was intrigued by astronomy from a very young age. When I was a little girl, my dad would take me to look at the moon at night with the simplest binoculars and point out the various dark craters. A future astronomer was created.

Throughout my childhood, my parents and I moved countries several times. After completing advanced pre-school and 1st grade at UVK Phoenix, N1666, in Moscow; we moved to Sagamihara, Japan when I was 7 years old. We spent one year in Japan, during which I attended the 3rd grade at a regular Japanese school, Kyowa Elementary School in Sagamihara, and additionally once a week (as an extern) the 2nd grade at the School at the Russian Embassy in Tokyo. I have the fondest memories of our life in Japan and I am very grateful to all the kind people that my family met there. This is also where I was exposed to an environment that was even richer in astronomy, as my dad worked at the Institute of Space and Astronautical Science (ISAS) and we lived on campus of the institute, which means that I was able to enjoy the rockets displayed on the grounds daily. Thereafter, my family returned to Moscow for another year where I completed 3rd grade at the same school in my neighborhood that I attended previously.

At the age of 10, my parents and I moved to Rosemont, Pennsylvania in the U.S. First, I attended 5th grade at the Ithan Elementary School in Wayne and subsequently the 6th grade at the Radnor Middle School in Radnor. My dad was employed at Villanova University for the duration of our stay in the U.S., and my mom had also worked at the same place for a period of the time. Thanks to the one and a half years that we spent in the area of Philadelphia, I am now able to speak English on equal footing with Russian. After this, my family spent another year in Russia where I completed 7th grade at the same school as before. On the 2nd of August, 2002, we moved to the Netherlands. My dad has since been working at the European Space Research and Technology Centre (ESTEC); yet again, exposing me to astronomy.

For the first few years, my family lived in Oegstgeest and then in 2007 we moved to Leiden. I attended the international school Het Rijnlands Lyceum Oegstgeest for 5 years in total (8th through 12th grade), where I first obtained the International Baccalaureate (IB) Middle Years Programme (MYP) diploma, and subsequently graduated with the IB Diploma Programme (DP) diploma and a 7th IB subject certificate. During my high school years, I tailored my track towards sciences by taking higher level Physics, Chemistry, Mathematics and English. Furthermore, I participated in numerous Model United Nations (MUN) conferences in the Netherlands in the 2004-2007 period. At my final conference in January 2007, the largest in the world - The Hague International Model United Nations (THIMUN), I was chosen to hold the position of the Deputy Secretary General. MUN has taught me what it is like to attend large international meetings, how to approach new people and most importantly, how to speak in public.

The first time I got involved with Leiden University was through the Pre-University College, a selection-based 2-year program during the final years of high-school, from which I graduated with honors. In pursuit of a scientific career, I embarked on a double bachelor of astronomy and mathematics at Leiden University. Having always been interested in many things, I diversified the scientific courses by additionally following Painting (Schilderen; part-time fall 2007-spring 2008) and Painting 1 and 2 (Schilderen 1 and 2; part-time fall 2008 and spring 2009) at the Royal Academy of Art (Koninklijke Academie van Beeldende Kunsten; The Hague, The Netherlands; supervisor Michel Snoep) and Introduction to Psychology (fall 2007 at Leiden University). For my dual Bachelor thesis, I carried out a combined astronomy and mathematics research project entitled "Voronoi Diagrams and Their Application in the DTFE Reconstructions of the Cosmic Web" under the supervison of Prof. Dr. Vincent Icke and Dr. Dion Gijswijt, which involved computing Voronoi diagrams with Brown's algorithm and assessing the quality of the Delaunay Tessellation Field Estimator (DTFE) reconstructions of the Cosmic Web. I was awarded two BSc diplomas - one in astronomy and one in mathematics. As a result of an accident, my mom passed away in 2010. I will always continue to miss her, but also cherish and appreciate all the guidance and support that she provided me with.

Having always been enticed by astronomy, I decided on my specialization and continued with a masters program in astronomy. At Leiden, an astronomy master student on the research track needs to carry out two research projects. My minor research project (with a duration of 8 months) was entitled "CO Emission in C-Type Shocks", which I carried out under the supervison of Dr. Lars Kristensen, Dr. Ruud Visser and Prof. Dr. Ewine van Dishoeck. This was my first introduction to star formation and astrochemistry. After the project was complete, I knew I wanted more. My major research project (with a duration of 12 months) carried the title of "*Spitzer* and *Herschel* Study of RCW 49" and was supervised by Prof. Dr. Xander Tielens and Dr. Olivier Berné. During this time, I was taught several valuable lessons about the drive it takes to be independent researcher. In 2012, I was awarded the MSc diploma in astronomy. From September 2011 to September 2012, I have additionally worked as a Student Assistant at Leiden University, which included various administrative jobs and tasks at public outreach events.

For the past four years, as of September 2012, I have been working in the group of Prof. Dr. Ewine van Dishoeck as a PhD student under the Huygens Fellowship on the topic of synthesizing complex organic molecules in star-forming regions. The research is relevant to the hunt for answers to the questions dealing with the emergence of life on Earth and is presented in this thesis. During this time I have also held three teaching assistant assignments for MSc-level courses: Stellar Structure and Evolution in spring 2013 with Prof. Dr. Joop Schaye and in spring 2014 with Prof. Dr. Xander Tielens; and Star Formation in spring 2014 with Prof. Dr. Ewine van Dishoeck. I have also become acquainted with public outreach in relation to astronomy by giving a public lecture (two talks of 45 min) at the Christiaan Huygens Astronomy Club in Papendrecht, the Netherlands. I have given 9 contributed talks, 9 seminars and presented 7 posters at national and international meetings, other institutes and universities, and my home university. I have had the opportunity to obtain hands-on observational experience at the JCMT and have also been submitting proposals for ALMA during the last two cycles (cycles 3 and 4), both as the principal investigator (PI) and co-investigator (co-I).

As of November 1st, 2016, I will start working at the Center for Space and Habitability (CSH) at the University of Bern, Switzerland, as a combined CSH and International

Astronomical Union (IAU) The Gruber Foundation (TGF) Fellow. My PhD research was focused on complex organic chemistry at the earliest phases of star and planet formation. My research as a postdoc fellow will extend the study towards the later phases once larger bodies, such as comets and planetary embryos, have formed.